The Development of a Novel Method for the Raman Spectroscopic Non-Destructive Analysis of Tissue Engineered Bone Cell Cultures

Lens Vibration Lock-In Amplified Raman Spectroscopy for Bone Tissue Engineering

The University Of Sheffield.

Rachel Louise Thompson BSc (Hons)

School of Clinical Dentistry

University of Sheffield

A thesis submitted in partial fulfilment of the requirements for the degree of

Doctor of Philosophy

March 2017

The University Of Sheffield.

Access To Thesis.

A fully completed copy of this form must be submitted to Research & Innovation Services prior to the award of your degree. If you are submitting a hard copy of the thesis the form should be bound into the front of the thesis

SECTION 1: STUDENT DETAILS			
Family Name	Thompson	First Name	Rachel
Registration Number	110228622	Department	Clinical Dentistry
Thesis Title	The Development of a Novel Method for the Raman Spectroscopic Non-Destructive Analysis		

SECTION 2: THESIS SUBMISSION DETAILS – PLEASE SELECT ONE OF THE FOLLOWING OPTIONS	
☐	I am submitting in print format only for deposit in the University Library **(Note: this option only applies to students who initially registered prior to 2008)**
☑	I am submitting an eThesis only to the White Rose eTheses Online server. I confirm that the eThesis is a complete version of my thesis and no content has been removed
☐	I am submitting an eThesis to the White Rose eTheses Online server and also submitting in print format because I have removed some content from my eThesis

SECTION 3: EMBARGO DETAILS – PLEASE SELECT FROM THE FOLLOWING OPTIONS

Each Faculty has agreed a pre-approved embargo threshold (Arts & Humanities – 1 yr; Engineering – 1 yr; Medicine, Dentistry & Health – 2 yrs; Science – 5 yrs; Social Sciences – 3 yrs. Requests for embargoes that exceed the Faculty threshold will require Faculty approval. If you wish to request a longer embargo, please complete and submit the form available at: www.shef.ac.uk/ris/pgr/code/embargoes

Please note that if no boxes are ticked, you will have consented to your thesis being made available without any restrictions.

Should the thesis be embargoed? If 'Yes', please specify the length of embargo requested (in years)	Print Thesis	☐ No	☑ Yes	2 Years
	eThesis	☐ No	☑ Yes	2 Years

Reason for the embargo (please select from the following options):

☐	Third party copyright	☐	Commercial confidentiality
☐	Contains personal data	☐	Could prejudice national security
☐	Could endanger health and safety	☐	Exempt under another category listed in the FOI Act 2000
☑	Planned publication	☐	Other

SECTION 4: COPYRIGHT LICENCE OPTIONS – PLEASE SELECT ONE OF THE FOLLOWING

This thesis is protected by the Copyright Design and Patents Act 1988. No reproduction is permitted without consent of the author. It is recommended that you make your thesis available using a Creative Commons Licence http://creativecommons.org/about/license/. This Licence protects you as the author of the work and also clarifies the uses that others may make of your work.

☑	Creative Commons Attribution-Non-Commercial-No-derivatives **(recommended)**	☐	Creative Commons Attribution-Non-Commercial
☐	Creative Commons Attribution	☐	Creative Commons Attribution-No-derivative-Works
☐	Creative Commons Attribution-Non-Commercial-Share Alike	☐	Other/Do not apply a Licence

SECTION 5: THESIS DEPOSIT AGREEMENT - STUDENT		
1. I, the author, confirm that the Thesis is my own work, and that where materials owned by a third party have been used, copyright clearance has been obtained. I am aware of the University's *Guidance on the Use of Unfair Means* (www.sheffield.ac.uk/ssid/exams/plagiarism).		
2. I confirm that all copies of the Thesis submitted to the University, whether in print or electronic format, are identical in content and correspond with the version of the Thesis upon which the examiners based their recommendation for the award of the degree (unless edited as indicated above).		
3. I agree to the named Thesis being made available in accordance with the conditions specified above.		
4. I give permission to the University of Sheffield to reproduce the print Thesis (where applicable) in digital format, in whole or part, in order to supply single copies for the purpose of research or private study for a non-commercial purpose. I agree that a copy of the eThesis may be supplied to the British Library for inclusion on EThOS and WREO, if the thesis is not subject to an embargo, or if the embargo has been lifted or expired.		
5. I agree that the University of Sheffield's eThesis repository (currently WREO) will make my eThesis (where applicable) available over the internet via an entirely non-exclusive agreement and that, without changing content, WREO and/or the British Library may convert my eThesis to any medium or format for the purpose of future preservation and accessibility.		
6. I agree that the metadata relating to the eThesis (where applicable) will normally appear on both the University's eThesis server (WREO) and the British Library's EThOS service, even if the eThesis is subject to an embargo.		
Student's name (PLEASE PRINT): Rachel Thompson	Signature:	Date

SECTION 6: THESIS DEPOSIT AGREEMENT - SUPERVISOR		
I, the supervisor, agree to the named Thesis being made available in accordance with the conditions specified above.		
Supervisor's name (PLEASE PRINT): Paul Hatton	Signature:	Date:

SECTION 6: TO BE COMPLETED BY RESEARCH & INNOVATION SERVICES		
Does the embargo exceed the agreed Faculty length? FCA - 1YR; FCE - 1YR; FCM - 2YRS; FCP - 5 YRS; FCS - 3 YRS	☐ Yes* if 'yes' please attach embargo extension request form	☐ No
University stamp		

For Matt, Mum, Dad, Nana and Granddad. We got here together.

"A straight line may be the shortest distance between two points, but it is by no means the most interesting."

- The Doctor,

Doctor Who: The Time Warrior (Series 11 Serial 1) by Robert Holmes

Declaration

I hereby declare that except where specific reference is made to the work of others, the contents of this dissertation are original and have not been submitted in whole or in part for consideration for any other degree or qualification in this, or any other university. This thesis is my own work and contains nothing which is the outcome of work done in collaboration with others, except as specified in the text and Acknowledgements.

Rachel Louise Thompson BSc (Hons)
March 2017

Acknowledgements

I would like to acknowledge everyone who's help, knowledge, advice and support made this thesis possible. Firstly, I would like to thank my supervisors Prof. Paul Hatton, Prof. Ben Varoce and Dr Aileen Crawford for their guidance and support throughout my course of study. I would also like to thank my examiners Prof. Hugh Byrne and Dr Frederik Claeyssens for all their advice and feedback which significantly improved this work.

I would like to thank Dr Martin Eduardo Santocildes Romero for providing my mesenchymal stem cells, help with teaching me how to culture my cells, and his advice and help throughout the PhD. Thanks also to Matthew Everitt with his help and advice on my laser set up and for always being a willing ear for me to sound out problems with. Thank you to Dr Katie Bardsley and Dr Abigal Pinnock for help with sectioning and staining of the biological samples. Thanks to Freya Wilson and Beth Newton for letting me pick their brains when I had problems which needed working out. Thanks to Matt Goodyear and Matthew Everitt for helping me with debugging the computational aspects of this work. Thanks to Amanda McDonnell and Steph McKay for proof reading in times of desperate need. Thank you also to Dr Alison Voice for helping gather images from the department's Raman spectrometer and Dr Mingzhou Chen and Prof. Kishan Dohlakia for their time and use of their Raman system. Immense thanks to the coffee club: Freya, Amanda, Chris, Joe and Matthew. I couldn't have finished without your support and shoulders to cry on. Also, many, many thanks to my ~~prof~~ proof reading party Matt, Amanda, Adam, Matthew, Steph, Rhiannon, Oz, Em, Phoebe, Steven, Mark and Claire, my thesis wouldn't be a thesis with out you all.

I am exceptionally thankful for the financial support of the ESPRC through the White Rose DTC in Tissue Engineering and Regenerative Medicine, without that support this project would not have been possible. I would also like to thank Reinnervate Ltd. for their material support of this project in providing 3D scaffolds for the cell culture aspect and Kirkstall Ltd. for their support in 3D culture training.

I must also thank Matthew Mercer and Vox Machina, this thesis could not have been finished this without Critical Role keeping me smiling while I wrote it. Lastly, I would like to thank my all of friends and family (including the ones already

mentioned above). Thank you for all the encouragement, being pillars of strength, and willing ear's in times of need.

Abstract

Raman spectroscopy is a burgeoning area in biological research and is of particular interest in providing a way to analyse tissue engineered constructs. However, current Raman spectroscopic methods are often suboptimal for use in biological spectroscopy and new instrumentation methods may be useful. This work proposes a new spectrometer design using lens vibration lock-in amplified Raman spectroscopy, which uses the principle that modulating the position of the laser focal spot generates a signal which is suitable for lock-in amplification. The key aim of the design was to enable low irradiance Raman spectroscopy using a maximum laser power of 20 mW at 788 nm, to minimise the risk of causing cell damage. The application of lock-in amplification to this signal allows for phase selective amplification, selectively amplifying the Raman signal above the background.

The spectrometer design was tested and validated initially by producing spectra from silica and 3 forms of hydroxyapatite. Next, cultures of mesenchymal stromal cells cultured in proliferation and differentiation media, and prepared for scanning electron microscopy were analysed. The spectra collected demonstrated that the application of lock-in amplification improved spectral quality compared to spectral collection without lock-in amplification. Interestingly the spectral signals collected from the cell cultures were also stronger than those collected from silica and hydroxyapatite with similar collection settings, suggesting that the preparation of the cells for scanning electron microscopy generated a surface-enhanced Raman effect.

Raman mapping was then performed across the proliferative cell culture, generating a map across the sample at a wavenumber shift of 2149.1 cm^{-1}, which demonstrated improvement with lock-in amplification.

Finally, this work attempted to apply lens vibration lock-in amplification to a commercial CCD compact spectrometer. This effort, while not completely successful, represents a positive step towards producing commercially viable lens vibration lock-in amplified Raman spectroscopy.

Table of contents

Table of contents **xiii**

List of figures **xv**

List of tables **xvii**

1 Introduction **1**

2 Literature Review **5**

2.1 Bone Tissue Engineering and the Need for Non-Destructive Analysis . 5

2.1.1 Bone Tissue: Function and Repair 5

2.1.2 Bone Tissue Engineering 6

2.1.3 Analysis of Tissue Engineered Constructs 13

2.2 Raman Spectroscopy 16

2.2.1 The Raman Effect 16

2.2.2 Parameters Which Impact Upon the Raman Effect 26

2.2.3 The Raman Effect as a Tool 28

2.3 Applications of Raman Spectroscopy in Biological Research 30

2.3.1 General Biological Applications 30

2.3.2 Raman Spectroscopy for Cancer Detection 35

2.3.3 Raman Spectroscopy of Bone 39

2.3.4 Raman Spectroscopy in Tissue Engineering 45

2.3.5 Raman Spectroscopy *in vivo* 55

2.3.6 Challenges in Using Raman Spectroscopy for Biological Analysis 57

3 Aims and Objectives **59**

4 Materials and Methods **63**

4.1 Bone Cell Cultures 63

4.1.1 Bone Marrow MSC Isolation 64

4.1.2 MSC Culture Protocols 65

4.2 Background and Theory of the Spectrometer 74

4.3 Preliminary Study 80
4.4 Spectrometer Design 90
4.5 Spectral Collection Using Lock-In Amplification 96
4.5.1 Silica Raman Spectra 96
4.5.2 Hydroxyapatite Raman Spectra 100
4.5.3 SEM Prepared MSC Culture Raman Spectra 102
4.5.4 Scanning System Design 103
4.6 Development of a CCD Lens Vibration Raman Spectrometer 106

5 Results **111**
5.1 Conventional Analysis of MSC Cultures 111
5.1.1 Analysis of Statically Seeded MSC Cultures on Uncoated Scaffolds 111
5.1.2 Analysis of Dynamically Seeded MSC Cultures on Collagen Coated Scaffolds 123
5.2 Raman Spectrum of Silica 132
5.3 Raman Spectrum of Hydroxyapatite 137
5.4 Raman Spectra of SEM Prepared MSC Cell Cultures 140
5.5 Raman Mapping of SEM Prepared MSC Cell Cultures 155
5.6 Raman Spectra Collected with the Compact CCD Spectrometer . . . 161

6 Discussion **171**
6.1 Conventional Analysis of MSC cultures 171
6.1.1 Analysis of Alvetex® Scaffolds Statically Seeded with MSCs . 171
6.1.2 Analysis of Collagen Coated Alvetex® Scaffolds Dynamically Seeded with MSCs 175
6.2 Raman Analysis of Synthetic Materials 178
6.2.1 Analysis of Silica Spectra 179
6.2.2 Analysis of Hydroxyapatite Spectra 183
6.3 Raman Analysis of Fixed MSC Cultures 190
6.4 Raman Optical Activity 199
6.5 Potential Surfaced Enhanced Raman Spectroscopy via SEM Preparation 200
6.6 Analysis of Experiments with the CCD Spectrometer 201

7 Conclusions **203**

8 Future Work **207**

References **211**

Appendix A Supporting Custom Programs 237
A.1 LabView Programs for Spectral Collection 237
A.1.1 Basic Collection of Lock-In Amplified Raman Spectra 237
A.1.2 Scanning System for the Collection of Spectral Data in 2D . . 242
A.1.3 Single Spectral Point Raman Mapping 247
A.1.4 CCD Spectrometer Data Collection 252
A.1.5 Processing of CCD Spectra and Lock-In Amplification Data Construction, Output and Collection 252

List of figures

4.1 Diagram of the initial basic Raman spectrometer in reflection mode. . 81

4.2 Diagrams describing linear polarisation of an EM wave 82

4.3 Diagrams describing the circular polarisation of an EM wave. 83

4.4 Diagram denoting parameters used to calculate wavenumber values. . 84

4.5 Graph of silica spectrum captured via chopping the laser and lock-in amplification with a sensitivity of 5 mV and time constant of 100 ms, averaged over 50 measurements per point with error bars representing standard deviation. 87

4.6 This graph presents the silica Raman signal (4.6a) and laser line signal (4.6b) at different displacements from the back face of silica. Raman data was collected at a lock-in sensitivity of 5 mV and time constant of 100 ms and the laser signal was collected at a lock-in sensitivity of 500 mV and time constant of 100 ms, with both data sets averaged over 50 measurements in each case and error bars representing standard deviation. 88

4.7 These graphs demonstrate the percentage change in maximum voltage in the Raman signal with displacement from the back face of silica at a lock-in sensitivity of 5 mV and time constant of 100 ms in 4.7a and the laser signal with the same displacement and lock-in sensitivity of 500 mV and time constant of 100 ms in 4.7b, averaged over 50 measurements in each case and error bars representing standard deviation. 89

4.8 These graphs present the hydroxyapatite Raman signal (4.8b) and laser line signal (4.8c) at different displacements from the front face of a fused hydroxyapatite sample. Raman data was collected at a lock-in sensitivity of 5 mV and time constant of 100 ms and the laser signal was collected at a lock-in sensitivity of 500 mV and time constant of 100 ms, with both data sets averaged over 50 measurements in each case and error bars representing standard deviation. 89

4.9 These graphs demonstrate the percentage change in maximum voltage in the Raman signal with displacement from the front face of fused hydroxyapatite at a lock-in sensitivity of 5 mV and time constant of 100 ms in 4.9a and the laser signal with the same displacement and lock-in sensitivity of 500 mV and time constant of 100 ms in 4.9b, averaged over 50 measurements in each case and error bars representing standard deviation. 90

4.10 Graph of diffracted laser voltage output from photodiode with lens vibrating with no amplification. 91

4.11 Diagram of optics set up for the lens vibration lock-in amplified Raman spectrometer. 92

4.12 First silica spectrum collected with the lens vibration lock-in amplified spectrometer. The spectrum was collected at 5 mV sensitivity and 100 ms time constant, with a single measurement made at each photodiode position. 92

4.13 The graphs show the Raman spectrum of silica collected at 50 measurements per point, 2 mV lock-in amplifier sensitivity and 200 ms lock-in amplifier time constant. The red line is an adjacent average with a window of 11 points, designed to produce a smoothed spectrum to allow spectral features to be easily identified. Figure 4.13a shows the full spectrum, with Figure 4.13b showing the same spectrum with over the range $0 - 0.0675\ V$ 93

4.14 The graphs show the Raman spectrum of silica and glass collected from separate time points at 20 measurements per point, 500 μV lock-in amplifier sensitivity and 200 ms lock-in amplifier time constant. The red line is an adjacent average with a window of 11 points, designed to produce a smoothed spectrum to allow spectral features to be easily identified. 4.14a shows a glass spectrum, 4.14b shows a silica spectrum and 4.14c shows the glass and silica spectra on the same axis for direct comparison. 94

4.15 Spectrum of the ThorLabs LDM785 laser reflected straight from the PBS to the diffraction grating. The spectrum was captured with lock-in amplification to a chopped laser signal at 5 mV sensitivity and with a 200 ms time constant and is generated from an average of 20 measurements per spectral point. The red line in Figure 4.15b is an adjacent averaging smoothing function with a window of 11 points. 95

4.16 Spectrum of the ThorLabs LDM785 laser reflected from a mirror placed in the z translation sample mount. 96

4.17 Graph of the laser wavelength variation with time over 53 minutes immediately after initial laser start up. 97
4.18 Photograph of the translation stage set up used to translate the cell cultures and acquire Raman signals from across their surfaces. 104
4.19 Diagram of final spectrometer build with Thorlabs CCS compact spectrometer. 107
4.20 Example square wave. 108

5.1 Microscopy images of cells with no staining in 2D well cultures of MSCs.112
5.2 Microscopy images of alkaline phosphatase staining in 2D well cultures of MSCs. 112
5.3 Microscopy images of cells with alizarin red staining in 2D well cultures of MSCs. 112
5.4 Microscopy images of the first slice of a scaffold cultured in proliferation medium 5.4a & 5.4c 20× magnification and 5.4b & 5.4d at 10× magnification. 113
5.5 Microscopy images of a slice 50 μm into a scaffold cultured in proliferation medium at 5.5a & 5.5c 20× magnification and 5.5b & 5.5d 10× magnification. 114
5.6 Microscopy images of the first slice of a scaffold cultured in osteogenic medium 5.6a & 5.6c 20× magnification and 5.6b & 5.6d at 10× magnification. 114
5.7 Microscopy images of a slice 50 μm into a scaffold cultured in osteogenic medium at 5.7a & 5.7c 20× magnification and 5.7b & 5.7d 10× magnification. 115
5.8 μ-CT maximum z projection data from the 3 successfully imaged scaffolds. 116
5.9 Example cross sectional CT slices through the imaged scaffolds. . . . 117
5.10 CT images with a threshold of 195 applied to isolate mineral candidates for each scaffold. 118
5.11 Microscopy images of MSCs in Alvetex® scaffolds stained with alizarin red. MSC cells in Alvetex® at 10× magnification cultured with 5.11a proliferation medium and 5.11b osteogenic medium. MSC cells in Alvetex® at 20× magnification cultured with 5.11c proliferation medium and 5.11d osteogenic medium. 119
5.12 Microscopy images of MSCs in Alvetex® scaffolds stained with alkaline phosphatase. 120
5.13 Microscopy images of MSCs in Alvetex® scaffolds stained with hematoxylin and eosin. 121

5.14 Microscopy images of MSCs in Alvetex® scaffolds stained with toluidine blue. . . . 122
5.15 SEM images of MSCs in Alvetex® scaffolds cultured in proliferation medium. . . . 123
5.16 Higher magnification SEM images of MSCs in Alvetex® scaffolds cultured in proliferation medium. . . . 124
5.17 SEM images of MSCs in Alvetex® scaffolds cultured in osteogenic medium. . . . 124
5.18 Higher magnification SEM images of MSCs in Alvetex® scaffolds cultured in proliferation medium. . . . 125
5.19 Standard light microscopy images of MSCs stained for alkaline phosphatase cultured in 2D with osteogenic medium (5.19a and 5.19b) and proliferation medium (5.19c and 5.19d) as a control for dynamic scaffold seeding . . . 125
5.20 Standard light microscopy images of MSCs stained for calcium deposition via alizarin red cultured in 2D with osteogenic medium (5.20a and 5.20b) and proliferation medium (5.20c and 5.20d) as a control for dynamic scaffold seeding . . . 126
5.21 Graph of the standard concentration curve for p-nitrophenol at 405 nm, with the calculated line of best fit given in red. . . . 127
5.22 Graph of average concentration of p-nitrophenol produced from alkaline phosphatase activity at 405 nm from MSCs on Alvetex® scaffolds cultured in osteogenic and proliferative medium 800 s and 960 s of exposure. . . . 128
5.23 Photograph of calcium and alkaline phosphatase staining on dynamically seeded collagen coated Alvetex® . . . 129
5.24 Photographs of calcium and alkaline phosphatase staining on collagen coated and uncoated non-seeded Alvetex® . . . 130
5.25 Microscopy images of calcium and alkaline phosphatase staining on collagen coated and uncoated non-seeded Alvetex® at 10× magnification . . . 131
5.26 Microscopy images of calcium staining on collagen coated Alvetex® dynamically seeded with MSCs and cultured in osteogenic medium. . . 132
5.27 Microscopy images of calcium staining on collagen coated Alvetex® dynamically seeded with MSCs and cultured in proliferative medium. 133
5.28 Microscopy images of alkaline phosphatase staining on collagen coated Alvetex® dynamically seeded with MSCs and cultured in osteogenic medium. . . . 133

5.29 Microscopy images of alkaline phosphatase staining on collagen coated Alvetex® dynamically seeded with MSCs and cultured in proliferative medium. 134
5.30 SEM images of Alvetex® scaffold. 135
5.31 SEM images of collagen coated Alvetex® scaffold. 136
5.32 SEM images of collagen coated Alvetex® scaffold cultured with MSCs in proliferation medium. 137
5.33 SEM images of collagen coated Alvetex® scaffold seeded with MSCs and cultured with osteogenic medium. 138
5.34 SEM images of collagen coated Alvetex® scaffold cultured with MSCs in proliferation medium focusing on the bulk of the scaffold. 139
5.35 SEM images of collagen coated Alvetex® scaffold seeded with MSCs and cultured with osteogenic medium focusing on the bulk of the scaffold. 140
5.36 SEM images of collagen coated Alvetex® scaffold cultured with MSCs in proliferation medium focusing on the rolled up cell layer. 141
5.37 Initially collected lens vibration Raman spectra from silica in terms of photodiode position. 142
5.38 Graph of Gaussian fit to the raw reflected silica laser line, used to find the laser line position to calculate the wavenumber scale for the silica spectrum given in Figure 5.37 143
5.39 Initially collected lens vibration Raman spectra from silica in terms of wavenumbers. 143
5.40 Silica spectrum collected through lock-in amplification at 500 μV, with a 200 ms time constant with the Raman peak to be measured for stability indicated. The spectrum is an average of 10 spectral measurements per point with the error bars representing the measurement standard deviation. 144
5.41 Graph of the stability of the lock-in amplified Raman signal at 789.87 cm^{-1} wavenumber shift over 90 minutes with measurements made at a rate of 1 s^{-1}. The red line denotes the linear fit to the data. 144
5.42 Graph displaying the location of maximum measured voltage from the laser used to determine the required photodiode position for stability measurement of the laser line. 145
5.43 Graph displaying the raw photodiode output voltage at the position of maximum laser signal over time. The red line denotes a linear fit to the data, as calculated by OrignPro 8.6. 145

5.44 Graph displaying the lock-in amplified output voltage of the environmental background processed at 500 μV sensitivity and 200 ms time constant. The red line denotes a linear fit to the data, as calculated by OrignPro 8.6. 146
5.45 Spectra of silica over time to assess spectrometer stability in terms of absolute position data and wavenumber. 146
5.46 Lens vibration lock-in amplified spectra of silica over time to assess spectrometer stability in terms of absolute position data and wavenumber. 147
5.47 Silica spectra collected with the focal point at varying depth positions using lens vibration lock-in amplification. 148
5.48 Initial fused hydroxyapatite Raman spectra 149
5.49 Fused hydroxyapatite spectra with 5.49a collected with lock-in amplifier set to 200 μV sensitivity and a 2 s time constant and 5.49b being the same spectrum collected with no LIA. 150
5.50 Fused hydroxyapatite spectra with 5.50a collected with lock-in amplifier set to 50 μV sensitivity and a 5 s time constant and 5.50b being the same spectrum collected with no LIA. 150
5.51 Graph of the non-lock-in amplified porous hydroxyapatite spectrum, with the red line representing the Gaussian fit to the data set. 151
5.52 Porous hydroxyapatite spectra with 5.52a and 5.52b collected with lock-in amplifier set to 100 μV sensitivity and a 1 s time constant and 5.52c being the same spectrum collected with no lock-in amplification. 151
5.53 Porous hydroxyapatite spectrum collected with, (5.53a) the lock-in amplifier at 50 μV sensitivity and 2 s time constant and (5.53b) without the lock-in amplifier. 152
5.54 Powdered hydroxyapatite spectrum without lock-in amplification, with respect to detector position. 152
5.55 Spectra collected from powdered hydroxyapatite collected with (5.55a, 5.55b) and without (5.55c) lock-in amplification at 200 μV sensitivity with a 0.5 s time constant. 153
5.56 Spectra collected from an osteogenically differentiated cell culture prepared for SEM analysis 153
5.57 Spectra collected from an osteogenically differentiated cell culture prepared for SEM analysis 154
5.58 Spectra collected from just the gold coated carbon sticker used for SEM preparation and gold coated Alvetex®. 155
5.59 Spectra collected from an non-differentiated cell culture prepared for SEM analysis 156

5.60 Spectra depth dependence for osteogenic differentiated cell culture prepared for SEM analysis 156
5.61 Spectra collected after removal of the beam compressor. 157
5.62 Initial spectra collected along a line of an osteogenic cell culture . . . 158
5.63 Line profiles across an osteogenic sample at a range of spectral positions 159
5.64 High resolution 1D line profiles across an osteogenic sample. 160
5.65 High resolution 2D Raman map across an osteogenic sample 162
5.66 Normalised high resolution 2D Raman map across an osteogenic sample 163
5.67 Initial spectra captured with the compact spectrometer 164
5.68 Simulated lock-in amplification to simulated chopped signal with pre-averaging 166
5.69 Silica spectra collected at 45 V and 75 V lens displacement using the CCD spectrometer 167
5.70 Lock-in amplified silica spectrum with simulated lens vibration. . . . 168
5.71 Dual phase lock-in amplified chopped and lens vibration spectra from the CCD spectrometer 169

6.1 Photograph of 2D control cultures at experiment termination. 172
6.2 Silica spectrum used for SNR and contrast calculations. The spectrum in black denotes the lock-in amplified spectrum, with the red trend line representing adjacent averaging with a window of 11 points. The red spectrum denotes the raw spectrum, with the black trend line representing adjacent averaging with a window of 11 points. The lock-in amplified spectrum was processed with a sensitivity of 500 μV and a time constant of 200 ms. 180
6.3 Silica spectrum with a different alignment The lock-in amplified spectrum was processed with a sensitivity of 200 μV and a time constant of 200 ms. 181
6.4 (a) Silica spectrum labelled with approximate wavenumber assignments, collected with the lock-in amplifier at 500 μV sensitivity and 200 ms time constant with an average of 10 spectral measurements per point as previously shown in figure 5.40.(b) Reference spectrum of silica produced by Logunov and Kuchinsky using a custom spectrometer with excitation at 633 nm, reprinted from *S. Logunov and S. Kuchinsky, "Experimental and theoretical study of bulk light scattering in CaF2 monocrystals", Journal of Applied Physics, vol. 98, no. 5, pp.053501, 2005* with the permission of AIP Publishing. . . . 182
6.5 Normalised lock-in amplified silica spectrum with normalised non-lock-in amplified spectrum subtracted. 183

6.6 Fused hydroxyapatite spectrum used for SNR, SNR_{Diff} and contrast with and without lock-in amplification, using a sensitivity of 50 μV and a time constant of 5 s. 184
6.7 Porous hydroxyapatite spectrum used for SNR, SNR_{Diff} and contrast with and without lock-in amplification, using a sensitivity of 50 μV and a time constant of 2 s. 185
6.8 Powdered hydroxyapatite spectrum used for SNR, SNR_{Diff} and contrast with and without lock-in amplification, using a sensitivity of 200 μV and a time constant of 0.5 s. 186
6.9 Fused hydroxyapatite spectrum labelled with approximate wavenumber assignments. 187
6.10 Porous hydroxyapatite spectrum labelled with approximate wavenumber assignments. 188
6.11 Powdered hydroxyapatite spectrum labelled with approximate wavenumber assignments. 188
6.12 Reference raman spectra of hydroxyapatites produce via 3 different synthesis routes by collected by Koutsopoulos using an FRA 106/S FT-Raman, Bruker spectrometer operating at 1064 nm. Reprinted from *S Koutsopoulos,"Synthesis and characterization of hydroxyapatite crystals: A review study on the analytical methods", Journal of Biomedical Materials Research Part A, vol. 62, no. 4, pp. 600-612, 2002* with permission from Wiley Periodicals, Inc. Copyright © 2002 Wiley Periodicals, Inc. 189
6.13 Spectra of fused hydroxyapatite shifted so that the highest voltage peak is at 964 cm^{-1}, this was achieved by shifting the grating line by (6.13a) changing the grating angle to 25.1° or by (6.13b) changing the laser line position to 284.3 cm. 190
6.14 Spectra of hydroxyapatite, normalised to the peak of the non-lock-in amplified feature and with the non-lock-in amplified spectra subtracted from the lock-in amplified spectra for (6.14a) fused HA, (6.14b) porous HA, and (6.14c) powdered HA. 191
6.15 Spectrum of gold coated MSCs on Alvetex® cultured in proliferative medium labelled with approximate wavenumber assignments. 193
6.16 Spectrum of gold coated MSCs on Alvetex® cultured in osteogenic medium labelled with approximate wavenumber assignments. 193

A.1 Block diagram of basic spectrometer Labview control code. 238

List of tables

2.1 A summary of early literature documenting the application of Raman spectroscopy to biological molecules and processes. 31

6.1 SNR, SNR_{Diff} and contrast data for all peaks with and without lock-in amplification for a spectrum of silica. The positions marked * are the the locations of the peaks in the non-lock-in amplified spectrum. . 180

6.2 SNR, SNR_{Diff} and contrast data for all peaks with and without lock-in amplification for a spectrum of fused HA. Wavenumber marked with a * represents the peak in the non-lock-in amplified spectrum. 184

6.3 SNR, SNR_{Diff} and contrast data for all peaks with and without lock-in amplification for a spectrum of porous HA. Wavenumber marked with a * represents the peak in the non-lock-in amplified spectrum. . 186

6.4 SNR, SNR_{Diff} and contrast data for all peaks with and without lock-in amplification for a spectrum of powdered HA. Wavenumber marked with a * represents the peak in the non-lock-in amplified spectrum. . 186

6.5 SNR, SNR_{Diff} and contrast data for all peaks with and without lock-in amplification for a spectrum from MSCs cultured in proliferation medium. 192

6.6 SNR, SNR_{Diff} and contrast data for all peaks with and without lock-in amplification for a spectrum from MSCs cultured in osteogenic medium. 192

6.7 Raman features observed during the culture of human MSCs observed during the culture of human MSCs by McManus et al. 194

6.8 Tentative wavenumber assignments for additional spectral features in the spectra of differentiated and undifferentiated MSCs. 196

6.9 Spectral quality metrics over the line profile of an osteogenic sample at approximately 1194.6 cm^{-1} wavenumber shift with 10 μm resolution, lock-in amplified at 200 μV sensitivity and 200 ms time constant, averaged over 100 measurements per point. 197

6.10 Spectral quality metrics over the line profile of an osteogenic sample at approximately 2149.1 cm^{-1} wavenumber shift with 1 μm resolution, lock-in amplified at 200 μV sensitivity and 200 ms time constant, averaged over 100 measurements per point. Values of exactly zero represent a negative calculated value. 198

6.11 SNR, SNR_{Diff} and contrast data for major peaks with and without lock-in amplification for the spectral map of MSCs cultured in proliferative medium at 2149.1 cm^{-1} using lock-in amplification at 200 μV sensitivity and 200 ms time constant. 198

Abbreviations

Roman Symbols

α-MEM	Minimal Essential Medium - Alpha Modification
$\Delta\overline{\nu}$	Wavenumber shift
ΔE_{States}	Difference in energy between the initial and final molecular energy states
ϵ_0	Vacuum Permittivity
$\mathcal{I}$	Irradiance (Power per unit area)
μ-CT	μ-Computed Tomography
ν_i	Frequency /Hz of a light source
$\overline{\nu}$	Wavenumber
c	The speed of light in a vacuum
E_f	Energy of final molecular energy state in a Raman transition
E_i	Energy of initial molecular energy state in a Raman transition
E_p	Initial Photon Energy
E_p	Photon Energy
E_s	Scattered Photon Energy
h	Planck's Constant
I	Intensity (Time averaged power per unit solid angle)
Q	Normal Coordinates
BCIP/NBT	5-Bromo-4-chloro-3-indolyl phosphate/Nitro blue tetrazolium
C	Contrast

CARS	Coherent Anti-Stokes Raman Spectroscopy
CCD	Charge-Coupled Device
CCD	Charge-Coupled Device
CHO	Chinese Hamster Ovary
DMEM	Dulbecco's Modified Eagle's Medium
DMSO	Dimethylsulfoxide
ECM	Extracellular Matrix
FCS	Foetal Calf Serum
FWHM	Full Width at Half Maximum
IMS	Industrial Methylated Spirits
MRI	Magnetic Resonance Imaging
MSCs	Mesenchymal Stromal Cells
NADH	Nicotinamide Adenine Dinucleotide
OCT	Optimal Cutting Temperature
OD	Optical Density
PBS	Polarising Beam Splitter
PCA	Principal Component Analysis
PCR	Polymerase Chain Reaction
ROA	Raman Optical Activity
SERDS	Shifted Excitation Raman Difference Spectroscopy
SNR	Signal to Noise Ratio
SNR_{Diff}	Differential Signal to Noise Ratio
SRS	Stimulated Raman Spectroscopy

Chapter 1

Introduction

Tissue engineering is a field with great promise to transform the face of modern medicine. We are only just beginning to see the impact of tissue engineered therapies and the field is still growing rapidly. As well as having a direct clinical application, tissue engineering also has the potential to have a significant impact on the modelling of biological systems. Such models are of extreme importance for many reasons. Firstly, in a fundamental research context, the ability to create and maintain complex 3D tissue cultures will enable the detailed examination of key biological processes in a research laboratory [1]. Currently, a large amount of important research on the basics of biology relies on 2D cell cultures. Tissue engineering could allow the use of 3D tissue cultures with multiple cell types to be created, allowing researchers to interrogate a more physiologically relevant system [2]. Additionally, these systems could also have a profound impact on drug discovery processes. Much initial drug testing is performed on 2D cell cultures meaning that 3D cultures may improve initial drug studies. Furthermore, animal testing represents a large challenge for the pharmaceutical industry. Other than the ethical issues with animal testing, there is a profound problem in that they are not very good predictors of a drugs efficacy in a human patient [3], and that there are legislatory requirement to replace, reduce, and refine the use of animal testing[4]. Therefore, in order to increase the speed and reduce the cost of the drug development pathway, there is a great need to generate a reliable laboratory based model of a functional human being for pre-clinical drug testing in the place of animals.

Bone is a vital tissue in the human body. As well as providing mechanical strength, stability and structure, the bone marrow is a key location for the generation of blood cells and the maintenance of the adult population of mesenchymal stem cells [5]. Bone fractures are a frequent occurrence and although many fractures can be easily fixed via setting, there are many more serious fractures which can be debilitating for the patient and require permanent repair, currently provided through metal pins and plates [6, 7]. Therefore, in a clinical context, there is a

need to create tissue engineering solutions to repair such bone defects or even to develop tissue engineered therapies for arthritis. One of the most popular proposed methods of tissue regeneration in a bone defect is the implantation of a bioactive scaffold which will be integrated into the bone [8–10]. However, there is a need to fully understand the interactions of these scaffolds with bone tissue. Therefore, 3D laboratory based tissue engineered models of bone are of great importance in creating a well understood effective scaffold. A laboratory based model would be highly useful as it allows for tight modulation of experimental conditions and thorough characterisation of the bone-implant interaction [10].

Current biological research methods rely on post construct sacrifice interrogation [11][12]. Therefore, large numbers of replicate systems are needed in order to complete thorough time point studies and in order to interrogate a variety of different factors. Although this technique has been very effective, it has its problems. Firstly, each system will include some inherent biological variability, so it is difficult to disentangle what quantities were an inherent feature of a culture and which have been modulated. Therefore, there would be an immediate impact on biological research if it were possible to individually monitor cell cultures all the way through a time point study through the use of non-destructive analysis. Non-destructive analysis becomes even more valuable in the event of widespread use of tissue engineered models. This is because 3D tissue models require large numbers of cells and therefore culture media and treatments in order to produce the same number of replicates as in a 2D system. This, combined with scaffold costs and long culture times makes it less financially viable to have large numbers of replicates [13, 14]. Therefore, in order to introduce tissue engineered models into widespread biological research, the application of non-destructive analytical techniques is vital. As well as being non-destructive, there are other potential features of non-destructive analysis which could be highly valued in biological research. If an analysis method allowed multiple molecular signatures to be detected at once, it would be possible to save time in research by not having to interrogate samples again and again for different pieces of information.

Another driver for the use of non-destructive analysis techniques is the need for quality assurance for tissue engineered products [12]. Tissue engineered products will be highly invasive interventions. Therefore, it will be crucial that every product is manufactured to the highest quality. Due to the current need to destructively analyse a tissue culture, in a situation where products are being delivered to patients, producers will only be able to batch test constructs. This means that out of a number of produced constructs only a small sample will be sacrificed and analysed for quality. It will then be assumed that the remaining products have the same properties as the sacrificed ones. This could be problematic as there could be untested constructs

with quality issues that will slip through the net. Therefore, there is a clear need for an industrially scalable method of non-destructive analysis for tissue engineered products destined for use in clinical therapy.

Research into the development of non-destructive analytical methods for tissue engineering models and for tissue engineered products is increasing. One possible method for cell culture analysis is Raman spectroscopy, a technique based on the scattering of light from the cells themselves and detecting changes in the scattered light [15]. This technique requires the application of a laser and a spectrometer to collect and analyse the light. Therefore, there is an associated risk of cellular damage by the action of the laser light. This risk is created by a combination of photochemical, photothermal and photodegredation processes in the case of Raman spectroscopy. Photochemical processes occur shorter wavelengths in the visible and ultraviolet ranges, at low irradiences when electronic bonds are excited by interactions with a laser [16]. This process can lead to the breaking of molecular bonds, which may alter cell biochemistry [16], potentially resulting in cell damge [17]. Photothermal processes occur over the visible and infra-red range [18] for power densities from $10^{-3}\ Wm^2$ depending on laser wavelength [19]. In the effect, energy from laser photons is deposited as kinetic energy in a sample which is inturn converted to heat raising the sample temperature, and potentially causing damage [16]. Photodegredation processes occur when materials containing a chromophore or photosensitiser are exposed to visible or ultraviolet radiation, in the presence oxyden, which leads to the breaking of polymer chains and the production of free radiacals [20, 21]. This process has been associated with the mechanisms for the formation of age-related cataracts and age-related macular degeneration due to photodegredation of proteins and lipids [21]. In addition, the laser light, like any light, is a form of electromagnetic radiation that can cause direct DNA damage [22]. Such risks can be reduced and mitigated by the use of a long excitation wavelength outside the visible spectrum, low power and a large laser spot size [22]. However, doing so results in a drastic reduction in the amount of characterisable light returning from a sample [23]. Therefore, many commercial Raman spectroscopy systems, optimised for the analysis of non-live samples, use high powers and short wavelengths to get the best signal possible [24–29]. Where they do not, they use computational subtraction algorithms to remove background components. However, this leaves a question of the effectiveness of the algorithms under scrutiny. There is a risk of artefact generation, which could lead to misleading information being produced [30]. Therefore, a physical method of noise reduction is vitally needed in order to provide a more reliable noise removal method [30]. There are a number of current methods to do this [29–32]. However, these methods, while effective, are either not viable for application on cell cultures due to their application of force, and need for a heterogeneous sample [29, 31, 32], or

could be too expensive for industrial scale up due to the costs of the rquired optics equipment [30].

These combined factors highlight a great technological need in the field of tissue engineering. Thus, the aim of this research is to develop and test a cost effective non-destructive method of analysing tissue engineered bone. On completion of this work, a new Raman spectroscopy method for tissue engineering applications will be developed and tested to meet the unmet challenge of online non-destructive analysis in bone tissue engineering. Prior to beginning work on the novel spectrophotometry system, a literature review was carried out on previous work in the field of biological Raman spectroscopy. Previous works have shown that Raman spectroscopy has great potential to provide detailed analytical information for many biological processes. However, Raman spectroscopy of live cell cultures has focused on the use of high laser irradiance and computational background subtraction and data processing methods. High laser irradiance can induce damage in cells and computational background subtraction is a suboptimal signal recovery method for small signals. This work presents a novel system which allows background subtraction through manipulation of the underlying physics and low laser powers to be applied without compromising on signal quality, potentially overcoming previous problems with non-destructive Raman analysis.

Chapter 2

Literature Review

2.1 Bone Tissue Engineering and the Need for Non-Destructive Analysis

2.1.1 Bone Tissue: Function and Repair

Bone is a very important tissue; as well as providing structural function it also has roles in synthesis and metabolism. The structural role of bone is two fold, as well as supporting the loads exerted on the body, it is also responsible for redistributing stress. Additionally, bone has a second structural function in protecting key organs, by allowing energies created by impacts to be absorbed. Beyond structural functionality, bone has a role in synthesis of hematopoietic cells and metabolism through the secretion of several hormones [33].

There are many cases in which a patient may experience a loss of bone tissue, through both deliberate (e.g. joint replacement surgery) and accidental circumstances (e.g. the non-union of a fracture) [34]. In total there are over 2 million bone graft procedures performed worldwide every year [35]. Where bone repair is needed, the gold standard treatment is an autograft where the patient's own bone is used to repair a defect [36]. Such grafts are often harvested from the illiac crest, but other areas of the skeleton can also be used, including Gerdy's tubercle, the distal radius and the distal tibia if cancellous bone is required or the fibula and rib for a cortical bone graft [37]. Unfortunately, although autografts are the ideal choice, as they have the correct mechanical and functional properties, they are imperfect in practice. Key problems with autografts are donor site morbidity, which can lead to pain for the patient, and the fact that only a limited amount of bone can be harvested [34, 35]. Therefore, there is a pertinent need for another graft source. One possible source is an allograft where bone from a living or deceased donor is implanted into the defect site. In the UK, National Health Service Blood and Transplant remove allogenic

material and sterilise bone grafts prior to implantation and currently run a surplus of grafts stored to grafts used [38]. However, demand for allografts would easily outstrip supply if all surgeons moved to using allografts as the preferred method for filling bone defects [39]. As a result, an alternative to allogenic and autologous grafts is required.

2.1.2 Bone Tissue Engineering

Clinical medicine has been rapidly advancing over the past 100 years with the pioneering work of clinicians and researchers to develop organ transplants, replacement joints, cancer treatments and more. Tissue engineered therapies represent yet another potential medical revolution which could help clinical medicine in numerous ways over the coming decades. However, this aim is not without its challenges and many researchers are grappling with questions of cell sources, growth environments and appropriate scaffold materials.

Tissue engineering was initially defined as a concept in 1993 by Langer and Vacanti as "an interdisciplinary field of research that applied the principles of engineering and the life sciences towards the development of biological substitutes that restore, maintain, or improve tissue function [40]". Therefore, tissue engineering focuses on using cells, scaffolds, growth factors or a combination of these to enable the regeneration of tissue function [41]. Current allogenic organ replacements are often very successful in terms of patient outcomes. However, demand for donated organs on the whole outstrips supply [42]. In the UK there are currently around 7000 people on the transplant list [43], but every year around 1000 of those waiting for an organ die, including a number who die after being removed from the transplant list as they are too ill to undergo the operation [44]. Therefore, one motivating factor behind tissue engineering is to remove the need for a transplant list. If the promise of tissue engineering comes to fruition then the transplant list will no longer be required and suitable replacement organs will be engineered for the patient which will improve on organ donation by removing the allogenicity of the transplanted organ [42].

Replacement organs are by no means the only target for tissue engineered solutions. There are many tissues which suffer a loss of function through injuries or disease, with no or sub-optimal current repair strategies, which may have large potential socio-economic cost to them as well as a detrimental effect on the patient involved [45, 46]. For example, diabetes is a condition which is managed rather than cured, with a large economic cost. In diabetic patients, β - cells in the pancreatic islets undergo cell death, leading to insufficient regulation of glucose [40, 47]. Diabetes has a large economic and human impact. The cost of diabetes to the NHS was £9.8 billion in 2010/2011, a figure which is expected to rise to £16.9 billion

by 2035, with an additional cost implication to GDP through disabilities caused by the condition [48]. Additionally, there are 24,000 early deaths annually in the UK among diabetics [48]. Tissue engineering has the potential to provide a cure for diabetes via producing healthy pancreatic islets for implantation into a patient, restoring function, curing diabetes and reducing the financial and social burden of the disease [40]. Another good example is in the development of tissue engineering technologies to regenerate cartilage. Current repair strategies are sub-optimal, with many procedures leading to the need for further surgery. Therefore, there is a great deal of interest in producing scaffolds which mimic the properties of cartilage and foster chondrocyte growth and extracellular matrix (ECM) secretion [49]. This example is just one of the many potential applications of tissue engineering in a clinical setting, with other potential uses as diverse as the tissues present in the human body.

Bone tissue engineering is an extremely active area of tissue engineering research. However, despite years of work in the field, very few tissue engineered bone therapies are available in the market [50]. One of the most popular tissue engineering approaches in bone regeneration is to create an implantable scaffold which will become infiltrated with cellular material and integrated into the new bone structure, or will be degraded over time[51]. There are many potential tissue engineered bone grafts currently under test, whereby the main aim is to provide an environment to encourage cellular regrowth into the structure [51, 52]. Scaffolds for bone tissue engineering can be made from a range of different materials which can be either synthetic or natural in origin, the most popular materials being ceramics, glasses and polymers [51, 52]. Natural materials may seem like an optimal material for use in scaffolds as they are fully biocompatible, can be remodelled by cells and are able to interact with cells [51]. However there are often challenges associated with them such as insufficient mechanical properties and high degradation rates [52]. In contrast, although synthetic materials do not posses inherent bioactivity, they can be produced under controlled conditions, leading to highly reproducible scaffolds which can then be functionalised by coatings or ligand addition. It is also possible to modify the mechanical properties of a synthetic polymer which is highly desirable in the context of bone tissue engineering [51, 52]. The main down side of synthetic polymers is that they are naturally hydrophobic, which is not conducive to cell attachment [51, 52]. Ceramic scaffolds are often made of calcium carbonate or hydroxyapatite components, which mimic the mineral component of bone and are said to be bioactive [51].

The main challenge being faced in bone tissue engineering is the creation of a mechanically competent material with minimal immunogenicity. Firstly, the material must be able to withstand physiological loading and stresses, and yet retain a level

of porosity which allows for the graft to be infiltrated with sufficient vascularisation to support the cell population necessary for full graft integration into the host's bone structure. Secondly, the material must integrate without causing an immune response which leads to sub-optimal implant integration, such as the encapsulation of the implant in fibrous tissue [53].

In addition to the diverse range of scaffolds being used for bone tissue engineering, there are also differences in approaches to seeding scaffolds with cells. Some groups are focusing on creating scaffolds which will be pre-seeded with cells prior to implantation, whereas others are designed to encourage autologous cell ingrowth without pre-seeding [53]. Although there are complexities in creating solutions for bone tissue engineering, it has the potential to reach clinical use faster than other tissue engineered therapies. This is because in many cases substitute bone grafts are regulated as a medical device rather than as a biologic by the Federal Drug Authority. This means that the regulatory pathway has the potential to be less arduous than for other tissue engineered products [54]. As a result, there are bone tissue engineering solutions on the market, such as the Infuse Bone Graft [39, 55]. However, such solutions are currently approved only for limited applications [55]. Therefore, the full potential of clinical bone tissue engineering is yet to be seen.

The path to creating any tissue engineered treatment is far from clear. There are many key challenges which must be overcome before the widespread clinical use of tissue engineering is possible. Such challenges include vascularisation of constructs, finding a suitable cell source, optimising biodegradability, dealing with contamination and the analysis of tissue engineered constructs.

Vascularisation of tissue engineered constructs is a key challenge for the engineering of large scale organs. Within tissues, the diffusion limit of nutrients means that only cells within 200 μm of a nutrient source (blood *in vivo* or culture medium *in vitro*) will receive the nutrients they require for life [56]. Evidently, if tissue engineers want to supply constructs of a clinically relevant size for transplantation, this is a critical issue. If a scaffold is to be implanted with cells then it is vital that there is a natural or artificial vessel equivalent population within the scaffold that can be surgically or naturally integrated quickly into the native blood vessel population [56]. Also, if a non-cellular scaffold is implanted, designed to allow the patient's cells to infiltrate and regenerate *in vivo*, it must also encourage adequate vascularisation in order to support the infiltration of cells and secretion of ECM [57, 58].

Cell sources are also a cause for concern in the development of tissue engineered therapies. Autologous cells are the ideal source as they come from the patient requiring treatment and so are completely compatible. However, there are difficulties in harvesting and expanding an adequate population, along with a high cost to do this for each individual [58]. Additionally, in the case of primary cells, the harvested

population from a patient could be diseased [59, 60]. The use of xenogenic cells is another option. However, these would elicit an immune reaction and there are strong concerns over disease transmission [58, 59]. Allogenic cells are currently a very attractive option for use in tissue engineering as they could be used to create products ready for use off the shelf. However, they still produce immunogenic reactions within the patient [58]. Therefore, the challenge of immunogenicity needs to be overcome in the long run [59].

As well as there being multiple possible cell donor sources, there are several different cell types in contention for producing tissue engineered therapies. Primary cells are the ideal cell type for use in tissue engineering as they are the cells found natively within the tissue being engineered [61]. However, some primary cells are found to lose their functionality in culture. Therefore, they may lose their key properties before reaching the patient, thus providing an insufficient construct [61]. Additionally, primary cell types generally exhibit poor *in vitro* proliferation, leading to difficulties in generating a sufficient cell population to seed a scaffold [61, 62]. Embryonic stem cells have been linked with a great deal of promise for use in medicine, thanks to their pluripotent nature and ability to potentially continually proliferate in culture [63]. However, there are concerns about the use of embryonic stem cells because of their inherent allogenicity and tumorigenicity [63–65]. Therefore, there are technical hurdles to be overcome before embryonic stem cells can be safely used in tissue engineering. One possible method could be to use differentiated embryonic stem cells which are believed to be non tumorigenic [59]. Additionally, there are moral issues surrounding the use of embryonic stem cells as they are sourced from harvested or induced human embryos. This means that the use of embryonic stem cells in research and medicine is highly regulated or even banned in many countries [66]. Consequently, it is questionable how freely available embryonic stem cells will be for therapeutic use.

A potential alternative to embryonic stem cells are adult stem cells such as mesenchymal stromal cells (MSCs). Adult stem cells are multipotent rather than pluripotent, so they can be induced to become one of a limited number of cell types [67]. Another difference in comparison to embryonic stem cells is that adult stem cells are believed to be less tumorgenic than embryonic stem cells, and differentiate more predictably [59] (although they have been linked to normal cancer formation [68]). Potential benefits of using adult stem cell populations are that they can be harvested from the patient, circumventing the problem of immunogenicity [58, 69]. Unfortunately, adult stem cells do not strongly proliferate *in vitro*, making it more likely that a bank of donor stem cells would be needed to provide therapies [59, 69]. Therefore, adult stem cells are currently a front runner as a cell source in tissue engineering due to their potential safety and reduced ethical burden [59]. However,

there are still problems with immunogenicity, expansion [59], characterisation and identification of adult stem cells [70].

A final possible alternative cell source is the induced pluripotent stem cell. These are cells which are engineered to have pluripotency via gene manipulation and are of interest as it may be possible to take a small biopsy of a patient's cells and induce them into a pluripotent state. Therefore, inducing pluripotency would provide autologous cells with the proliferation and differentiation potential of embryonic stem cells [71]. However, there are safety concerns with induced plouripotent stem cells; they are derived from retrovirus transcription methods, not all reprogrammed cells have pluripotency [71], they are not exactly identical to embryonic stem cells and they are more tumorigenic than embryonic stem cells [72].

Biodegradability can be a challenging property to optimise in a tissue engineered construct. Tissue engineering often seeks to have the body's own cells foster regeneration and replace the implant over time. Therefore, the scaffold needs to be degradable into non-toxic products by the body [73]. Creating a safe biodegradable material is not overly complex. However, engineering a biodegradable substance which has a tissue's required mechanical properties and a degradation rate which matches well with the tissue regeneration rate is much more difficult [74, 75].

Contamination of the materials used in tissue engineered constructs is another issue for tissue engineering to overcome. Many proposed tissue engineered products use scaffold materials harvested from animals and a possible donor cell component [58, 60, 76]. Purity and safety of the base materials is therefore paramount. There are possible risks of disease transmission from cell donors or pathogenic transfer from scaffold materials [76–78]. Contamination of constructs could be a result of harvesting from a diseased donor or source, but contamination may also be introduced during manufacture. Furthermore, the use of xenogenic serum in cell culture may need to be replaced as it has been shown to cause immunological reactions and can be a disease transmission vector [59]. As a result of these possible issues, manufacturing processes will need to be closely regulated and stringent screening applied to constructs and their components [79].

Analysis of tissue engineered constructs is a key challenge in bringing tissue engineered therapies into the clinic. Currently, the vast majority of analytical methods require a construct to be sacrificed in order for a full analysis to be conducted. This has a range of associated problems; namely in quality assurance of constructs prior to implantation and in evaluating the outcome of a therapy *in vivo* to assess how well the construct is performing in a patient. These issues are a difficult barrier for tissue engineering to overcome as it makes it difficult to ensure safety, and to fully understand the performance of a therapy [80].

Although the challenges listed above are not easy to overcome, they are far from

impossible and a great deal of active research is being performed in order to scale these barriers and bring tissue engineered therapies into the clinic.

Another use for tissue engineering which is often neglected is in the development of model biological systems *in vitro*. Current *in vitro* models are widely utilised for a variety of applications from drug screening to cosmetics testing to disease modelling and many more [81–84]. Most of these models are formed from conventional monolayer tissue culture techniques, in which cells are in 2D on tissue culture plastic. However, the use of such methodologies is sub-optimal; as research has demonstrated that there are detrimental effects to the validity of *in vitro* model if the cells are cultured in 2D and in the presence of only one phenotype [81]. Comparatively, cells cultured in 3D produce a model which is more physiologically relevant [81, 82]. Therefore, the use of 3D cell culture models instead of 2D monolayers can improve the results of a vast range of research systems from pharmaceutical testing to materials testing [81, 82].

In vitro bone models created using tissue engineering techniques will be an important part of 3D biological modelling for research and development. Bone models will be particularly useful in modelling implant tissue interfaces, which have great utility for evaluating new biomaterials and fully understanding mechanisms of interaction with existing medical implants [85]. Additionally, bone *in vitro* models are an important part of postulated "human on a chip"/"human on the bench devices" which seek to accurately simulate human physiology in order to move towards the aim of improved *in vitro* pre-clinical testing and the replacement of animal testing [86–89].

Whatever tissue is being modelled, simulation of the *in vivo* environment is key, with 3D tissue culture representing a vital part in simulating *in vivo* systems *in vitro*. The importance of 3D culture has only recently begun to be taken into account, but the principle of culturing cells in 3D is surprisingly old. Very early research on 3D cell culture was performed in 1951 by Leighton [90], who used cellulose sponges as a substrate for culturing cancerous cells and a set of embryonic tissues. As part of the study, Leighton compared the migration and attachment of cells from an explant into the sponge with migration and attachment onto a standard glass substrate. Upon analysing the cultures, it was demonstrated that the cells in 3D migrated and adhered differently in the cellulose sponge compared to the 2D glass plate culture [90]. Therefore, this work highlighted that 3D culture had an impact on cellular behaviour. Leighton continued to perform research on 3D sponge models, including using a collagen sponge to examine the morphology of a number of strains of cancer [91], modelling how normal cells and cancerous cells interact [92], examining cancer cell aggregation [93], as well as modelling the invasion of HeLa cells into a variety of embryonic tissues and fibroblasts [94, 95].

When cells are cultured in 2D monolayers, there are a number of differences that are readily apparent between the cells in an organ *in vivo* and the cells in a tissue culture flask. These are:

1. Standard 2D tissue culture imposes growth on a flat and rigid surface, often a very different environment to *in vivo* biology. These conditions can lead to a loss of typical cell functional behaviour and can force cells to adapt to the flat 2D environment [96].

2. 2D culture conditions impose polarity on cells in culture, whereby differences arise between the top and bottom surfaces of the cell. The imposed polarity can impact on the cell's biological functionality and its sensitivity to apoptosis [97].

3. The cell-cell contacts present in a 2D culture are significantly different to the contacts present in 3D systems [83]. These differences can lead to changes in cell signalling interactions which are an important part of many biological processes.

4. *In vivo* tissues are subject to chemical gradients as a result of the diffusion of nutrients and other chemical factors into 3D structures. These gradients can induce differences in cell function as a result of differences in chemical concentration in the environment the cell is exposed to. However, 2D cultures remove concentration gradients from the system, removing a feature of *in vivo* systems [81].

The use of 3D cell culture has been found to be important in many situations and the use of a 3rd dimension has been seen to change the outcome of experiments [81, 82]. For example, the 3D environment has been found to be of vital importance to the behaviour of tumour cells which interact with a highly complex 3D environment *in vivo*. Co-culture can be used in tandem with 3D systems to model tumour biology *in vitro* in order to provide a simulation of the interactions between cells and between cells and the ECM in tumorogenesis [13, 82, 83, 98]. Furthermore, it has been well documented that the behaviour and function of hepatocytes is different in 2D compared to 3D, which leads to a change in their metabolic properties in 2D culture compared to *in vivo* [82, 99]. Therefore, in order to properly model drug metabolism processes in the screening of new potential drug compounds 3D culture is essential[82].

In summary, for as long as there is a reliance on 2D models, the true potential of *in vitro* models will never be realised. If the validity of tissue models could be improved this could have an impact on medicine in a number of ways. Firstly, improved models could help with improved understanding of both healthy and diseased tissue

functions which could help inform treatments. Secondly, if *in vitro* models which could accurately predict a human response, this could make the drug discovery process cheaper and quicker. Currently, one of the main problems with drug discovery is the number of drugs which start the clinical trial process and fail [3]. If more failures could be indicated sooner, this would save vast amounts of time and money. Another aspect which could improve drug discovery is that if *in vitro* models were a better analogue to a human, safety tests would be able to be fully characterised in the laboratory, removing the need for animal trials, which would relieve a financial and ethical burden. Furthermore, there is a legal obligation for moving towards the use of *in vitro models* under The Animals (Scientific Procedures) Act 1986 which requires the reduction, refinement and replacement of animal models in scientific research [4].

2.1.3 Analysis of Tissue Engineered Constructs

Even though the production of tissue engineered medical devices and *in vitro* models is very achievable, they have a significant challenge associated with them. Namely, how do we monitor them? Classic biological methods of analysis are not optimised for work in 3D or are not suitable for use *in vivo*. This is because many analytical methodologies require the construct under test to be sacrificed. As a result, in a research context, numerous duplicate tissue constructs must be created to allow a system to be analysed at multiple time points. This has multiple downsides; firstly, there is great variation between cell cultures [100]. Therefore, when analysing different cell cultures at discrete time points, it becomes difficult to determine whether a change observed is due to inherent biological variation, or the passage of time. If it were possible to track a single cell culture through all time points it would be possible to begin to rule out inter-sample error in experimental results. Secondly, if a study requires the comparison of 3 samples at 6 time points, 18 samples must be generated. If a non-destructive analysis method were applied this figure would drop to 3 samples. Such a reduction in the minimum required number of samples will save money, time and also allow for it to be more practical to increase the number of repeats per time point, improving the quality of the results biological research can generate.

Moreover, there are also clinical drivers to develop non-destructive analysis methodologies. In a clinical context, the requirement for sacrifice means that it would not be possible to fully test each and every biologic containing tissue engineered product before it goes into a patient, making safety reliant on batch testing. This is not an ideal situation due to the fact that if faulty members of a batch are not caught via testing a small sample, the consequences of implanting an unsafe

product in a patient could be life threatening. Also, there may be a requirement for the effectiveness and integration of a tissue engineered therapy to be measured *in vivo*. Without non-destructive imaging, this will be almost impossible in a patient as, in order to generate detailed information on the microstructure of an engineered tissue, a biopsy will be required leading to secondary procedures and tissue morbidity. Therefore, non-destructive analysis techniques will be essential in bringing tissue engineered therapies into clinical use through the provision of thorough quality assurance, as well as by reducing research costs. Furthermore, an additional motivator is the need to move away from qualitative analysis methods to quantitative methods.

Therefore, new methods of analysis are required for analysis of *in vitro* tissue models and *in vivo* implants. This may help improve understanding of base biological processes and the safety and efficacy of tissue engineered therapies. There are a number of contenders to meet this need, such as magnetic resonance imaging, micro-computed tomography, optical coherence tomography, multiphoton imaging and Raman spectroscopy.

Magnetic resonance imaging (MRI) is widely used for clinical medical imaging. However, it can also be adapted for use in microscale imaging on a sub-cellular scale [101]. MRI is a very promising technique thanks to it being non-invasive, non-ionising and online imaging. It operates by applying a strong magnetic field to a patient or sample, followed by radio frequency waves to stimulate the protons within a sample to undergo a change in energy state, which causes them to emit radio waves. By measuring the radio frequencies emitted by the sample or patient, high contrast images can be obtained [102]. However, due to the large magnetic fields required for use, MRI scanners are extremely expensive to purchase and maintain [103–105], along with taking a long time for image acquisition which significantly limits their use [106].

μ-computed tomography (μ-CT) is a high resolution analogue to x-ray CT techniques used in diagnostic imaging, with a potential resolution of the order of microns [107–109]. In μ-CT, a sample is illuminated with x-rays, which are then attenuated by the sample and the transmitted rays are measured by a detector. In CT, a set of projections is collected from a set of angles around a sample and slices through the object of interest are reconstructed [110]. The contrast in CT arises from changes in density. However, the density variation across a cell or within many tissue types is relatively small. Therefore, CT will not produce clear images of a tissue in many situations without contrast agents [107]. Additionally, μ-CT uses ionising radiation to produce an image, making it a sub-optimal choice for online imaging due to the potential for tissue damage, cell death and cancerous transformation [107, 109, 111].

Optical coherence tomography is a technique which uses the reflection of light from boundaries between materials to create an image of a test sample in methods similar to those of ultrasound. In this technique, the reflection of light from boundaries between materials in a sample is measured and the strength and time between the reflections is measured in order to build up an image of the sample. Optical coherence tomography is an improvement over using ultrasound for high resolution imaging as, in such techniques, the resolution is proportional to the wavelength used [112, 113]. Optical coherence tomography systems are beginning to provide sub-cellular resolution imaging capabilities, improving the applicability of optical coherence tomography, but there are still challenges associated with poor depth penetration and its difficulty with imaging strongly scattering materials [113]. Therefore, optical coherence tomography could be seen as a complementary analysis technique which provides morphological information alongside a technique which provides chemical information [114].

Multiphoton imaging is a specialised form of fluorescence microscopy which uses stimulated multi-photon excitations of molecular labels to image a sample. Due to the technique of selecting specific photon emissions from a sample, this technique is able to remove the unfocused background from the image and penetrate up to 3 times deeper into a tissue sample than confocal microscopy [115]. Multiphoton microscopy is able to use not only fluorophores prepared and added into a tissue but potential fluorophores already in the tissue. For example, nicotinamide adenine dinucleotide (NADH), a key molecular component of cellular metabolic processes, can be used as a multiphoton fluorophore in the UV range. Fluorescent markers are also not necessary in the analysis of highly ordered tissue components such as collagen due to second harmonic effects [115]. However, in a majority of cases, fluorophore addition is still needed to be able to obtain a full tissue analysis with multiphoton techniques which can render tissues unsuitable for implantation into a patient [115].

Raman spectroscopy is a relatively simple molecular analysis technique applied in the identification of unknown samples. It uses the changes in wavelength induced in a scattering event between a photon and molecule to generate data on the energy level structures of the molecules in a sample under test, which can be used to identify the components of a sample [116]. Raman spectroscopy can be used in high resolution, limited only by the Abbe limit which is proportional to the wavelength divided by twice the numerical aperture of the lens (of the order of 100s of nm). However, techniques such as tip enhanced Raman spectroscopy allow for resolution of the order of nm [117]. Therefore, Raman has a suitable resolution to examine constructs on both a tissue and cellular level. Furthermore, it doesn't use ionising radiation or molecular tags, so has the potential to be non-destructive and non-

invasive, resulting in an analysed construct suitable for further use [118]. Raman can be used in a quantitative capacity to analyse processes in the cells [27, 118–120] and ECM [121–123]. It can also be used to develop images of a sample through mapping the presence of a certain Raman peak across a biological sample [121]. Raman does have its limitations, incuding the weakness of the Raman signal [124] and the Mie scattering background [125], often misconstrued as fluorescence [125], which may mask the Raman signal [30, 126, 127]. However, there are methods to overcome these difficulties [30, 124, 126, 127]. A more serious limitation of the technique is the laser penetration depth into a 3D tissue sample, which can vary significantly depending on the tissue being examined and the wavelength used [15], but efforts are being made to extend the penetration depth [128]. Despite these limitations, Raman spectroscopy is a multifaceted tool for biological applications.

It could be argued that infrared spectroscopy could be a candidate for biological analysis in this context, as it is very similar in function to Raman spectroscopy. However, water dominates in infrared spectroscopy, making biological sample analysis difficult and the resolution of the technique is limited to around 10 μm [122]. Both of these factors make Raman spectroscopy the superior of the two techniques in a biological context.

In this work the use of Raman spectroscopy to interrogate tissue engineered bone is investigated. Bone cell cultures are particularly interesting to explore with Raman spectroscopy, firstly, as there is still academic debate over the pathway of hydroxyapatite synthesis, a research question which can be probed with Raman spectroscopy. Also, Raman spectroscopy could have a role in the testing of tissue engineered therapies, where the form of the bone formation generated via tissue engineering techniques can be compared to bone synthesised *in vivo* [129]. Raman spectroscopy has been extensively used to study tissues and cells [124, 130], as discussed in Section 2.3 . However, researchers in the field are yet to optimise the technique for online biological analysis, where tisse constructs are analysed in the laboratory while they are growing. Therefore, research is needed to take the base technique and improve it for use in online monitoring of live tissue engineered constructs.

2.2 Raman Spectroscopy

2.2.1 The Raman Effect

In 1927, C. V. Raman and K. S. Krishnan wrote a letter to Nature, describing a "new type of secondary radiation" [131]. When a sample is illuminated with monochromatic light which is off resonance, so no direct excitation between molecular energy

levels take place, the light is scattered by the molecules of the sample. The scattering event can either be elastic, as in the Compton effect, where an incident photon is scattered by a molecule at the same wavelength at which it was incident, or it can be inelastically scattered via the Raman effect. During the inelastic scattering event, the photon can exchange the energy required to excite the molecule between rotational or vibrational energy states. This leads to a spectrum returned from the sample which consists of light at the incident frequency and a small amount of frequency shifted light. This secondary radiation from a form of inelastic scattering came to become known as the Raman effect in honour of Raman's discovery. The discovery, and subsequent work on this form of radiation, led to Raman being awarded a Nobel Prize in Physics in 1930[132].

To explain the Raman effect in more detail, it is necessary to examine the relationship between the photons and a molecular sample. In a monochromatic light source, such as a laser, the energy of each photon is given by

$$E_p = h\nu_i[133], \tag{2.1}$$

where E_p is the energy of the photons , where ν_i is the frequency of the photons and h is Planck's constant. An important feature of the Raman effect is that it is not an absorption process. In an absorption process, the incident photons of light must have the correct energy to excite a state transition between electronic, vibrational or rotational states [134]. However, scattering is in essence a process characterised by the interaction between light photons and the changing electromagnetic field of molecules and atoms, which can occur at any wavelength [134].

In a scattering event of any form, the underlying process of the event is the interaction of the electric field of the photons with the electric field of the molecule's electrons. This interaction causes a polarisation and resulting electric dipole moment of the electrons, leading to the molecule and photon forming a "complex" during a transition to a very unstable high energy state. This state, known as a virtual state, has an associated electron geometry which does not map to any other electronic state[134]. The geometric properties and energy of the virtual state are dictated by the energy of the incident photon, along with the original energy state of the molecule before the interaction. As a result, different frequency photons applied to the same molecular state result in different virtual states being produced. Conversely, photons of the same frequency being applied to molecules in different energy states also results in different virtual states being produced [134]. If during the interaction, molecule's dipole oscillates at the same frequency as the incident radiation, the scattered photon is released in a Rayleigh scattering event. However, if the molecular dipole oscillates at a frequency equal to the inident radiation, plus

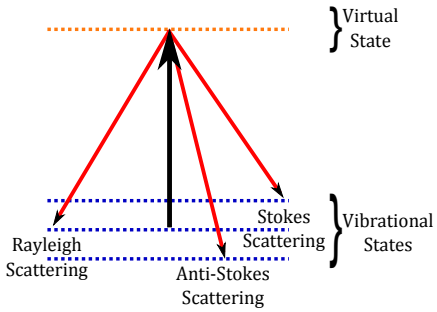

Fig. 2.1 Diagram of scattering processes in a molecule adapted from reference [134].

or minus a transition frequency, Raman scattering occurs [23].

In this situation, when the molecule decays from the virtual state, it decays to an energy level which is different to the one it was excited from and the photon exhibits an appropriate change in energy according to

$$E_s = E_p \pm \Delta E_{States}[134], \tag{2.2}$$

where E_p is the initial photon energy, E_s is the scattered photon energy and ΔE_{States} is the difference in energy between the initial and final state of the molecule. There are two forms of possible Raman scattering events: Stokes and Anti-Stokes scattering. In Stokes scattering, a molecule undergoes a transition in which the energy of the final state is greater than the energy of the initial state, i.e. $E_f > E_i$, where E_f is the energy of the final state and E_i is the energy of the initial state. The second form of possible transition is an Anti-Stokes scattering event, in which the final state of the molecule has a lower energy than the initial state of the molecule, so $E_f < E_i$ [134]. This is possible due to the action of previous scattering events or due to the fact that molecules in a system have a range have a range of energies as described by the Boltzmann distribution [133], and a certain number of molecules will have enough thermal energy to be in an excited energy state. Rayleigh scattering, Stokes Raman scattering, and Anti-Stokes Raman scattering processes are summarised in Figure 2.1.

To gain further insight into this scattering process, it is necessary to look at the mathematical behaviour of the system. Although the Raman effect is quantum in nature, a classical description can provide a framework which allows for a good basis for understanding the effect. The classical approach is built on the foundation of the wave description of EM radiation. In order to describe the Raman effect, the classical description examines the induced electric dipole vectors when a wave of EM radiation is incident in a molecule with a certain degree of polarisability. The standard equation used to describe the electric field of an EM wave is given by

$$\mathbf{E} = \mathbf{E_o} cos\omega_i t[23], \tag{2.3}$$

where $\mathbf{E}$ is the electric field vector, $\mathbf{E_o}$ is the electric field amplitude vector and t is the time and ω is equivalent to $2\pi\nu_i$ [23]. As described above, when a molecule is illuminated with light, a dipole moment is induced within the molecules. The relationship between the induced dipole moment and the light's EM field is linear [135] and can be described as,

$$\mathbf{p}^{(1)} = \boldsymbol{\alpha} \cdot \mathbf{E}[23], \tag{2.4}$$

where $\mathbf{p}^{(1)}$ is the induced dipole moment and $\boldsymbol{\alpha}$ is the polarisability tensor of a molecule. The dominant induced dipole moment in the molecule due to the application of light is a electric dipole, formed from the periodic motion of two charges $\pm q$, in a harmonic motion. It is the amplitude of this motion which denotes the dipole moment created by this oscillation. The properties of the induced dipole within a molecule is determined by both the electric field applied by the EM wave and the intrinsic molecular properties, as described by the inherent polarisabilty, where polarisability is simply a measure of the responsiveness of a molecule to the applied electric field [23, 134].

In the event of a molecule being free only to vibrate and not rotate, the polarisability tensor is characterised as a Taylor expansion, approximated to the first order [135]. The expansion is required in order to account for the fact that, even in a ground state geometry, the atoms present in a molecule vibrate around their equilibrium positions, which in turn causes small perturbations to molecules and therefore a corresponding perturbation to $\boldsymbol{\alpha}$ [135]. This leads to a description of the polarisability components when the molecule is vibrating in a way described by a normal mode. A normal mode is defined as a mode of vibration where the vibration is a simple harmonic oscillation [136]. Therefore, it is a sinusoidal motion whereby the phase of each atom of the molecule is the same, which means that the molecules will be at maximum displacement or pass through the equilibrium point at exactly the same time [136]. In reality the vibrations of atoms within molecules is much more complicated than that of a normal mode. However, if the amplitude of the vibration within a molecule is limited, then the motion of the atoms can be described as a sum of normal modes with a number of phases[137]. In order to help describe the normal mode vibrations a coordinate system known as normal coordinates (Q) is invoked, which relates to the position of the nuclei during the course of a vibration and the relevant displacement of the nuclei from their equilibrium positions [23]. For the normal mode k of the molecule, we can define the polarisbility in the following way, through use of a Taylor Expansion:

$$(\alpha_{\rho\sigma})_k = (\alpha_{\rho\sigma})_0 + \left(\frac{\delta\alpha_{\rho\sigma}}{\delta Q_k}\right)_0 Q_k[23]. \tag{2.5}$$

where $\alpha_{\rho\sigma}$ is a component of the polarisability tensor, $(\alpha_{\rho\sigma})_0$ is the equilibrium value of $\alpha_{\rho\sigma}$ when no molecular vibration occurs, with the subscript 0 indicating the equilibrium, and Q_k is the single normal mode vibration coordinates associated with a vibration at ω_k. To simplify the expression it is defined that,

$$(\alpha'_{\rho\sigma})_k = \left(\frac{\delta\alpha_{\rho\sigma}}{\delta Q_k}\right)_0. \tag{2.6}$$

Therefore, the derived polarisability tensor from the derivatives of the normal coordinates is $\boldsymbol{\alpha}'_k$ in vector form. Equation 2.5 can now be transformed to give the the overall tensor $\boldsymbol{\alpha}_k$ as

$$\boldsymbol{\alpha}_k = \boldsymbol{\alpha_0} + \boldsymbol{\alpha}'_k Q_k [23]. \tag{2.7}$$

If it is assumed that the motion within the molecule is of a simple harmonic form, then the time dependence of Q_k is given by

$$Q_k = Q_{k_0} cos(\omega_k t + \delta_k) [23], \tag{2.8}$$

where Q_{k_0} is the amplitude of the normal coordinate and a phase factor is represented by δ_k, which represents the phase difference between the incident photons and the normal mode of the molecule [23]. This expression for Q_k is then substituted into equation 2.7 to give

$$\boldsymbol{\alpha}_k = \boldsymbol{\alpha}_0 + \boldsymbol{\alpha}'_k Q_{k_0} cos(\omega_k t + \delta_k) [23]. \tag{2.9}$$

Now that an expression for polarisability has been obtained in equation 2.9, it is possible to begin to calculate the induced dipole moment by inserting the expression for $\boldsymbol{\alpha}_k$ into equation 2.4, along with the mathematical description of the EM wave (equation 2.3). This produces the following expression for the induced dipole moment of

$$\mathbf{p}^{(1)} = \boldsymbol{\alpha}_0 \mathbf{E}_0 cos(\omega_i t) + \boldsymbol{\alpha}'_k \mathbf{E}_0 Q_{k_0} cos(\omega_k t + \delta_k) cos(\omega_i t) [23]. \tag{2.10}$$

Equation 2.10 above is an unwieldy expression which does not help to create an impression of the behaviour of a molecule being irradiated with EM radiation. However, it can be further manipulated through application of the trigonometric identity

$$cosAcosB = \frac{1}{2}\left[cos(A+B) + cos(A-B)\right] [23], \tag{2.11}$$

which allows equation 2.10 to be expressed as

$$\begin{aligned}\mathbf{p}^{(1)} =& \boldsymbol{\alpha}_0 \mathbf{E}_0 cos(\omega_i t) + \\ & \frac{1}{2}\boldsymbol{\alpha}'_k \mathbf{E}_0 Q_{k_0} \left(cos(\omega_i t - \omega_k t - \delta_k) + cos(\omega_i t + \omega_k t + \delta_k)\right). \end{aligned} \tag{2.12}$$

Equation 2.12 can now be further simplified by defining the following factors,

$$\boldsymbol{\alpha}^{Ray} = \boldsymbol{\alpha}_0, \tag{2.13}$$

$$\boldsymbol{\alpha}^{Ram} = \frac{1}{2}\boldsymbol{\alpha}'_k Q_k [23], \tag{2.14}$$

which are substituted back into equation 2.12 to produce a final expression for $\mathbf{p}^{(1)}$ of

$$\begin{aligned}\mathbf{p}^{(\mathbf{1})} =& \boldsymbol{\alpha}^{Ray} \cdot \mathbf{E_0} cos\omega_i t + \\ & \boldsymbol{\alpha}^{Ram} \cdot \mathbf{E_0} cos(\omega_i t - \omega_k t - \delta_k) + \\ & \boldsymbol{\alpha}^{Ram} \cdot \mathbf{E_0} cos(\omega_i t + \omega_k t + \delta_k) [23]. \end{aligned} \tag{2.15}$$

This expression is very important because an oscillating electric dipole, such as the one described by equation 2.15, radiates an EM wave with a frequency equal to the frequency of the dipole oscillation. In equation 2.15, it can be seen that there are 3 different frequencies at which the dipole induced by an incident EM wave will vibrate. Therefore, the dipole will emit EM radiation at ω_i and $\omega_i \pm \omega_k$. The radiation emitted at ω_i is said to be elastically scattered via Rayleigh scattering as it has the same frequency as the incident EM wave. In contrast, radiation emitted at $\omega_i \pm \omega_k$ has a different frequency to the incident EM wave, so it has been scattered inelastically in a Raman scattering event [23][135]. This treatment only considers a simplified classical model of Raman scattering via vibration and therefore gives an incomplete description of Raman scattering. However, a full quantum mechanical treatment of Raman scattering gives a very similar mathematical result to the one derived in equation 2.15 [23], and the overall description of the effect as a transition between vibrational energy states via a virtual state holds.

The change in rotational energy level exhibited during the Raman effect can be broadly explained classically in the following qualitative way, as it is not possible to obtain a full mathematical description of rotational transitions classically. This is because, in classical theory, molecules do not have discrete rotational frequencies [23]. However, it is possible to state that, as in vibration, the key to rotational Raman scattering is to have a changing polarisability. This can occur if the molecule has an anisotropic polarsability tensor such that a rotation of the molecule causes a change in its polarisability, stimulating a related oscillating dipole moment. In

rotation, due to symmetry, the modulation of the dipole moment is at a frequency of $2\omega_{rot}$, where ω_{rot} is the frequency of rotation, as the modulation of the dipole will be repeated for every 180° the molecule rotates. The anisotropy of the polarisiblity can be summarised by the principle polarisabilities $\alpha_{\parallel}$ and $\alpha_{\perp}$ being unequal to one another. [138].

Normal modes play a key part in the Raman scattering process, and in general for a molecule of N atoms there are 3N-6 vibrational normal modes for the molecule, which is calculated from the fact that a molecule has 3N degrees of freedom, which include 3 translational and 3 rotational degrees of freedom in a general case [116]. However, if a molecule is linear, which means that the atoms are in a straight line spatially, then the molecule has 3 translational degrees of freedom, but only 2 of rotation, meaning that there are 3N-5 normal modes [116].

There are many possible molecular vibrations which may be induced by Raman scattering processes. These motions are often highly complex, but can be reduced to combinations of simple vibrations known as normal modes for analysis. Normal modes are independent vibrations of a system (in this case of molecules) at the natural frequency of the system where the entire system vibrates in synchronous unison. For example, the vibration of the air within an organ pipe that produces a sound wave at a specific note is a vibration at the natural frequency of the pipe and is therefore a normal mode of the system [133]. The concept of normal mode analysis can be applied to many different systems in mechanics. In particular, it is used to describe the possible motions of masses on springs. When molecules are considered, they are treated very much in the same way as simple spring-mass systems, with the nuclei being the masses and the bonds between the atoms the springs. The set of approximations of molecular motion, i.e. the treatment of molecules as a collection of masses on springs and the fact that the motion is a form of simple harmonic oscillation, is called the harmonic approximation[133].

It is possible to define a normal coordinate to describe the vibrational movement of a normal mode of any polyatomic molecule. The calculation of normal coordinates can be typified by the following simple example. Consider a generic diatomic molecule, which is linear in form. It consists of 2 different atoms of differing masses linked by a bond. When the molecule is in the ground state the atoms will remain a constant displacement, which can be described as the equilibrium distance. When the molecule is given energy and begins to vibrate, the atoms will experience movement away from their equilibrium positions and will be subject to a force which can be modelled by Hooke's law [116], the equation which describes the force acting on an elastic material, such as a spring while it is extended (or compressed) away from

its equilibrium position [139]. Hooke's law is defined mathematically as

$$F = -k(x)[133], \tag{2.16}$$

where F is the restoring force experienced by the molecules, k is the spring constant, which describes the stiffness of the bond, and x is the extension of the bond away from equilibrium. In the diatomic molecule, when the atoms are at equilibrium, the first molecule with mass M_1 is at a position p_1, and the second molecule with mass M_2 is at a position p_2. When the molecule vibrates, the positions of the atoms change to $p_1 + a_1$ and $p_2 + a_2$ respectively, where a_1 and a_2 are the distances of each atom from its equilibrium position. These positions can now be translated into the centre of mass reference frame, where the atomic masses and positions are given with reference to the centre of mass of the whole molecule. In this situation, we define all positions relative to the centre of mass so that so p_1 and p_2 are simply the distances from the centre of mass to each of the particles. Using the definition of centre of mass, it can then be found that

$$M_1 p_1 = M_2 p_2[116]. \tag{2.17}$$

This holds true when the molecule vibrates, as well as at equilibrium. So, when the atoms are displaced during the virbration to $p_1 + a_1$ and $p_2 + a_2$, it follows that, $M_1(p_1 + a_1) = M_2(p_2 + a_2)$. If equation 2.17 is substituted into this formula it is found that

$$\begin{aligned} M_1 p_1 + M_1 a_1 &= M_1 p_1 + M_2 a_2, \\ M_1 a_1 &= M_2 a_2. \end{aligned} \tag{2.18}$$

Next, the displacement parameters are inserted into equation 2.16. This produces the results $F = -k(a_1 + a_2)$ and $a_2 = \dfrac{M_1}{M_2} a_1$. Therefore, we can now create the expression

$$\begin{aligned} F &= -k\left(a_1 + \frac{M_1 a_1}{M_2}\right), \\ &= -k\left(\frac{M_1 + M_2}{M_2} a_1\right), \end{aligned} \tag{2.19}$$

for the molecule of mass M_1 and

$$F = -k\left(\frac{M_1 + M_2}{M1} a_2\right), \tag{2.20}$$

for the molecule of mass M_2. Through Newton's second law $F = m\dfrac{d^2x}{dt^2}$ [133] where

m is the mass and $\frac{d^2x}{dt^2}$ is acceleration of that mass, it is possible to generate 2 equations of motion for the diatomic molecule

$$\begin{aligned} M_1\frac{d^2a_1}{dt^2} &= -k\left(\frac{M_1+M_2}{M_2}a_1\right), \\ \frac{d^2a_1}{dt^2} &= -k\left(\frac{M_1+M_2}{M_2M_1}a_1\right), \end{aligned} \tag{2.21}$$

$$\begin{aligned} M_2\frac{d^2a_2}{dt^2} &= -k\left(\frac{M_1+M_2}{M_1}a_2\right), \\ \frac{d^2a_2}{dt^2} &= -k\left(\frac{M_1+M_2}{M_1M_2}a_2\right). \end{aligned} \tag{2.22}$$

Adding these equations of motions together gives

$$\begin{aligned} \frac{d^2a_1}{dt^2}+\frac{d^2a_2}{dt^2} &= \left[-k\left(\frac{M_1+M_2}{M_1M_2}a_1\right)\right]+\left[-k\left(\frac{M_1+M_2}{M_1M_2}a_2\right)\right], \\ \frac{d^2a_1}{dt^2}+\frac{d^2a_2}{dt^2} &= -k\left(\frac{M_1+M_2}{M_1M_2}\right)(a_1+a_2), \\ \frac{d^2}{dt^2}(a_1+a_2) &= -k\left(\frac{M_1+M_2}{M_1M_2}\right)(a_1+a_2). \end{aligned} \tag{2.23}$$

Equation 2.23 can be simplified as $\frac{M_1M_2}{M_1+M_2}$ is known as the reduced mass of a particle, μ, and a_1+a_2 can be expressed as a displacement q such that

$$\frac{d^2q}{dt^2} = -\frac{k}{\mu}q[116]. \tag{2.24}$$

The above equation is known as the wave equation. This can be solved to demonstrate that the molecule will vibrate in a periodic simple harmonic fashion with a frequency f_{Vib} given by

$$f_{Vib} = \sqrt{\frac{k}{\mu}}[133]. \tag{2.25}$$

Equation 2.24 can be extended into 3D using the following equation for q as a vector quantity

$$\mathbf{q} = \mathbf{R} - \mathbf{R}_0[116], \tag{2.26}$$

where $\mathbf{R}_0$ is given by,

$$\mathbf{R}_0 = \mathbf{r^{eq}}_1 - \mathbf{r^{eq}}_2[116]. \tag{2.27}$$

Therefore, $\mathbf{R}_0$ describes the vector between the equilibrium molecular positions $\mathbf{r^{eq}}_1$ and $\mathbf{r^{eq}}_2$ with respect to the center of mass. Similarly, $\mathbf{R}$ is given by

$$\mathbf{R} = \mathbf{r}_1 - \mathbf{r}_2[116], \tag{2.28}$$

where $\mathbf{r}_1$ and $\mathbf{r}_2$ are the displaced molecular positions with respect to the center of mass. In the example of the diatomic molecule vibrating in 1D, described above $\mathbf{r^{eq}}_1 = p_1\mathbf{i}$ and $\mathbf{r^{eq}}_2 = -p_2\mathbf{i}$, where $\mathbf{i}$ is the unit vector and we take the positive direction to be towards molecule 1. Similarly, $\mathbf{r}_1 = (p_1 + a_1)\mathbf{i}$ and $\mathbf{r}_2 = -(r_2 + a_2)\mathbf{i}$ which are the molecular positions with respect to the centre of mass after extension or compression. As a result, in this case of the diatomic molecule in 1D, $\mathbf{q}$ is given by

$$\begin{aligned}\mathbf{q} &= (p_1 + a_1 - (-p_2 - a_2) - (p_1 - (-p_2)))\mathbf{i}, \\ &= (p_1 - p_1 + p_2 - p_2 + a_1 + a_2)\mathbf{i}, \\ &= (a_1 + a_2)\mathbf{i},\end{aligned}$$

and thus is identical to the scalar value of q derived in equation 2.24. It is highly useful to condense the description of molecular displacement into a single vector. The direction of $\mathbf{q}$ is constant, for all possible vibrations of the diatomic molecule, no matter how the molecule rotates as it is defined with reference to the molecule and not the surrounding space. Therefore, all vibrations can be stripped down to a magnitude, in a direction described by a unit vector $\mathbf{q}$, which defines a normal mode of the molecule [116].

It is important to note that, through the spring and mass model, the equations of motion match those of a simple harmonic oscillator. This provides a link between the classical and quantum description of the Raman effect, as the quantum harmonic oscillator is a solved problem of quantum mechanics [133]. Using this basic quantum mechanical formulation, we can derive the energy structure for the diatomic molecule by substituting the potential energy of the simple harmonic oscillator($\frac{1}{2}kx^2$) into the Schrodinger equation and solving for the total energy[133]. Ultimately, the solutions of the equation describes the vibrational energy levels as

$$E_n = \left(n + \frac{1}{2}\right) h\nu_k[133], \tag{2.29}$$

where E_n is the energy of excited state n and $\nu_k = \omega_k/2\pi$. Thus, we can see that the energy levels are quantised and that there are discrete transitions between permitted energy levels in a Raman scattering process. This is an approximation to the physical reality, which deviates from this model. However, it provides a simple demonstration of the quantum nature of the underlying process [133].

One very important consideration of vibrational analysis in Raman spectroscopy is that Raman activity does not automatically arise just because there is a vibrational mode. In order for a vibrational mode to be induced in a Raman transition, the vibration must change a component of the polarisability of the molecule over a

small vibration. Therefore, we can define that for a vibration to be Raman active $\left(\frac{d\alpha_i}{dq_j}\right)_0 \neq 0$ which means that the rate of change of a polarisbility tensor component in the motion of the mode described by the relevant normal coordinate q_j around the equilibrium position must be non-zero [116]. Whilst the analysis of normal modes, their vibrations and effect on polarisability is possible for simple molecules, it is not feasible for large molecules or those with complex structures. Additionally, although normal modes are excited in Raman scattering, there are many more complex vibrations which are also excited, which are made from the superpositions and/or harmonics of normal modes [116].

2.2.2 Parameters Which Impact Upon the Raman Effect

There are many factors that have an impact on what Raman shifts occur and on the number of Raman scattered photons. In order to gain an appreciation of the nuances of the technique it is important that these factors are both understood and taken into account. Firstly, there are factors which relate to the nature of the light used to stimulate Raman scattering processes from the molecule. The first factor of this nature is the irradiance of the light applied to a sample being analysed by Raman spectroscopy. The irradiance of a light source is defined as the energy flux passing though a defined area per unit time. Therefore, it can be defined as

$$\mathcal{I} = \frac{E}{tA}[23], \tag{2.30}$$

where $\mathcal{I}$ is the irradiance, E is the energy deposited, t is the time for the deposition, and A is the area over which the power is deposited. However, as energy per unit time is the definition of power, irradiance can more easily be described as

$$\mathcal{I} = \frac{P}{A}[23], \tag{2.31}$$

where P is the power of the electromagnetic radiation over an area A and has the units Wm^{-2}. In comparison, intensity, I, is the power averaged over time over a solid angle, and is applicable when a point source is radiating in conical beam shape. Therefore, intensity is defined as the power averaged over time incident on a solid angle and can be expressed as

$$I = \frac{d\Phi}{d\Omega}[23], \tag{2.32}$$

where $d\Phi$ is time averaged power in Watts and $d\Omega$ is the solid angle over which the power is incident in steradians (sr). Many references treat intensity as a simple measure of Wm^{-2}, i.e. as the same as intensity, but although the quantities are similar, this is strictly incorrect [23]. The radiated intensity of a source through the

Raman effect is linearly proportional to the irradiance of the incident laser source; the bigger the irradiance, the bigger the intensity of the scattered radiation [23][140].

The second factor which impacts on the intensity of the Raman signal is the frequency of the scattered EM radiation. Firstly, the frequency of the scattered light depends linearly on the frequency of the incident EM radiation for a given vibration [141]. Additionally, it can be shown that the intensity of the Raman scattered light is directly proportional to the 4th power of the frequency of the EM wave used to illuminate the sample [141]. This is because the intensity radiated from an oscillating dipole in a direction θ is given by

$$I = \frac{(\omega_i \pm \omega_k)^4 \, sin^2\theta}{32\pi^2\epsilon_0 c^3} \left(\left(\overline{\mathbf{p}^{(1)}} \right)^2 \right) [141]., \tag{2.33}$$

where $\left(\overline{\mathbf{p}^{(1)}} \right)^2$ is the magnitude of the induced dipole oscillation, $\omega_i \pm \omega_k$ is the frequency of Raman emission as before, θ is the scattering angle, ϵ_0 is the vacuum permittivity and c is the speed of light. Therefore, the higher the frequency of the exciting light source, the greater the excited Raman intensity. As a result, one possible method to increase the intensity of the emitted Raman light is to use a high frequency light source such as an ultraviolet or visible laser. However, in the case of biological analysis, this is not a feasible option. Firstly, light in the ultraviolet region, is often resonant with biomolecules, which can generate emissions which may mask weak Raman signals [125]. At visible wavelengths, cells and intracellular structures are of a size such that, Mie scattering occurs. Mie scattering is an eleastic scattering process, where scattered light has the same wavelength as the incident light, but due to its diffuse nature it is not fully removed by wavelength dependent optical componets, and spreads across spectral collection optics, giving the appearance of a background signal [125]. In addition, photochemical and photodegredation processess, as discussed in Chapter 1, are more likely to occur at shorter wavelengths in the ultraviolet and visible wavelengths [16, 20, 21], with ultraviolet and visible light is more likely to cause DNA damage to cells [15, 22]. In the infra-red region of the EM spectrum, Mie scattering is reduced [125], and the risks of damage to a sample from photochemical and photodegreative processes is significantly reduced [16, 20, 21]. Therefore, infra-red excitation is the optimal choice for biological Raman spectroscopy [125], even though the inherrent intensity of the Raman signal is reduced [141].

Another property which has an impact on Raman spectra is the polarisation of the incident light source. The induced dipole moment, as described in equation 2.14, is dependent on the direction of the electric field vector and, therefore, the scattered light intensity is dependent on this property, which is also known as the polarisation of the light wave. If light has a linear polarisation, meaning the electric field oscil-

lates in a single defined direction, then the intensity of the scattered radiation will alter with different linear polarisations thanks to the change in the induced dipole generated. However, if light without a single linear electric field vector is used, this dependence can be negated, as the light molecule interactions can occur in any and all electric field vector directions [142].

The second factor that can affect a spectrum is the phase of the sample under examined. In a gas form, a molecule would produce an ideal spectrum, including peaks arising from both vibrational and rotational energy transitions, but rotational peaks often appear merged into a continuum due to limited instrument resolution [141]. If the molecule was in a liquid state, the rotational bands are smeared out due to more frequent collisions broadeding the spectrum [143]. In a solid, crystalline state, in general only vibrational transitions can occur [116, 144]. However, as there is relative motion of the molecules within the structure, extra spectral features appear, along with features due to symmetries and the movement of the molecules relative to the unit cell [141].

The chemical environment under which the spectrum was collected also impact the spectral features [141]. Vibrational features in a Raman spectrum can often relate to the motion of a group of atoms in a molecule, rather than an individual bond. As a result, the local molecular environment, with respect to the bonds and symmetries in the molecule, has an effect on the possible vibrations that can occur. Therefore, a carbon-hydrogen bond will vibrate in different ways depending on the other molecules or atoms bonded to the carbon atom. This means that the spectral features relating to various bonds may appear within a range of wavenumber shifts in a Raman spectrum, with the actual position of the feature depending on the molecular environment in the molecule [134].

2.2.3 The Raman Effect as a Tool

The discovery of the Raman effect is now over 90 years old, and in that time it has been harnessed as a powerful tool for the characterisation of molecules. The Raman effect centres around the scattering of photons at different wavelengths due to the molecule-photon interaction resulting in a change of molecular state. Therefore, as energy level structures are unique to individual molecules, so are Raman spectra. Of course, if two samples have similar molecular groups, there will be similarities in regions of their Raman spectra but the overall spectrum will exhibit differences. Therefore, since the detection of the Raman effect, there has been extensive cataloguing of molecules and molecular groups so that it is now possible to use Raman spectroscopy to both look for a certain molecule in a sample, and to identify an unknown sample.

Raman photons intrinsically carry information about the molecular energy levels of the sample being illuminated. If these photons are collected and their frequencies measured, it is possible to build up information about the energy states of a molecule and in turn use this information to identify molecular components in an unknown sample. For a particular energy transition in a particular molecule, the scattering removes an amount of energy from the scattered photon which is constant regardless of the initial frequency properties of the monochromatic light. For example, consider a scattering event where a molecule transitions from a ground state to an excited state with 0.0397 eV more energy after being illuminated by light of 384.35 THz (and thus a wavelength of 780 nm). The Raman scattered photon will have a frequency of 374.74 THz (a wavelength of 800 nm). However, if the same transition is excited by a photon with a frequency of 459.10 THz (a wavelength of 653 nm), the Raman scattered photon will have a frequency of 449.50 THz (a wavelength of 666.94nm). In each case, the same amount of energy is transferred, even though the incident and scattered frequencies are different. Therefore, a relative scale is required to measure this frequency shift effectively. The value used to quantify the change in energy from the Raman scattering is called the wavenumber shift. In this measurement, absolute frequencies are converted into wavenumbers, a wave property representing the number of waves per unit length [145]. The wavenumber shift can be calculated as

$$\overline{\nu} = \frac{\nu}{c}[23], \tag{2.34}$$

where $\overline{\nu}$ is the wavenumber, ν is the frequency of the light, and c is the speed of light . The wavenumber, $\overline{\nu}$, is a measure of the spatial frequency of a wave so it has units of inverse distance. InRaman spectroscopy the convention is to measure wavenumbers in cm^{-1}, the number of wavelengths per cm [145]. Raw frequencies are converted into a wavenumber shift by simply finding the difference between the absolute wavenumber values of the incident and scattered photons using the equations

$$\begin{aligned} \Delta\overline{\nu} &= \overline{\nu}_i - \overline{\nu}_s, \\ \Delta\overline{\nu} &= \frac{1}{c}(\nu_i - \nu_s)[116], \end{aligned} \tag{2.35}$$

where $\Delta\overline{\nu}$ is the wavenumber shift. As wavenumber shift is conventionally quoted in units of cm^{-1}, it is often more convenient to calculate $\Delta\overline{\nu}$ from the wavelengths of the incident and shifted photons (as $\nu = \frac{c}{\lambda}$, where λ is the wavelength) using the formula

$$\Delta\overline{\nu} = (\frac{1}{\lambda_i} - \frac{1}{\lambda_s})10^7[116], \tag{2.36}$$

where λ_i is the wavelength of the incident photon and λ_s is the wavelength of the

scattered photon.

Due to the relative nature of the Raman effect, theoretically any excitation wavelength can be applied to stimulate Raman transitions. However, one must consider Mie scattering, the relationship between Raman intensity and wavelength, and resonances due to electronic transitions. There are many different experimental set ups that can be used to create a Raman spectrometer to measure the scattered photons produced by the Raman effect. However, there are common elements between these instruments: a well defined monochromatic light source (normally provided by a laser), a lens to focus the light onto the sample and collect the scattered photons, a dispersive element to divide the light into its constituent wavelengths, and a detector to measure the wavelengths of the scattered light. Using these simple elements, Raman spectra can be collected from a sample and used to help determine its composition.

2.3 Applications of Raman Spectroscopy in Biological Research

Raman spectroscopy has a long history of use in the biological sciences. The application of Raman spectroscopy to analyse biologically relevant samples began in 1932, when Kutzner collected the Raman spectra of a collection of sugars in crystalline form [146]. Over time, the catalogue of biological samples analysed via Raman spectroscopy grew, and eventually the first tissue analysis was performed in 1970 by Walton and collaborators [147]. Raman spectroscopy has since been applied broadly to analyse many kinds of complex biological systems and in many fields from cancer detection to non-destructive imaging as discussed below [15, 124, 148].

2.3.1 General Biological Applications

There are many ways in which Raman spectroscopy can be applied to the biological sciences, from the broad use of Raman to characterise individual molecules of interest to examining the biochemistry of whole cell populations. The original application of Raman spectroscopy to biology was in characterising specific individual molecules. Although this work now appears very simplistic, this initial groundwork was necessary to allow the characterisation and identification of more complex systems today. The primary work performed on biological molecules is summarised in table 2.1.

Authors	Year	Summary
C.V. Raman & K.A Krishnan	1928	Raman's original publication in which the Raman effect is documented. [131]
W Kutzner	1932	The first paper to successfully collect Raman spectra of biological molecules. In this work, the spectra of several crystallised sugars were collected, but only a limited number of peaks were resolved [146].
FH Spedding & RF Stamm	1942	This work by Spedding and Stamm significantly improved on Kutzner's work with studies of hydrous and anhydrous α- and β-D-glucose with Raman spectroscopy. [149]
RC Lord & GJ Thomas	1967	This paper records the first Raman spectra of RNA bases, base derivatives and ribose derivatives both in the solid phase and in solutions of variable pH [150].
MC Tobin	1968	This work reports the first Raman spectra of proteins, with lysozyme, pepsin and chymotrypsin in crystalline forms analysed by Raman spectroscopy. [151]
M Smith, AG Walton & JL Koenig	1969	Although Tobin analysed proteins in a crystalline form first, this paper records the first Raman spectra of proteins in a solution. Smith et al. obtained spectra from glycine, diglycine, triglycine, tetraglycine, and pentaglycine, both in solid phase and in a solution [152]. Later that year, further work was published collecting and analysed the spectra of poly-L-proline in solution [153].
AG Walton, MJ Deveney & JL Koenig	1970	This paper documents the first Raman spectrum collected from a tissue sample. The work presents and analyses *ex vivo* ox bone and include identification of the now well known phosphate and amide peaks found in bone [147].
SJ Webb	1976	In 1976, Webb documented one of the first examinations of cells using Raman spectroscopy and attempted to use Raman spectroscopy to quantify changes in cellular processes [154]. Webb followed this work with numerous other papers in the same year [155, 156]. Webb et al. also collected spectra from suspensions of cells of *ex vivo* tumour cells and cultured Chinese hamster ovary (CHO) cells, maintained in culture medium in 1977. This work was the first measurement of *in vitro* cell culture [157].
P Jeannesson, M Manfait & J-C Jardiller	1983	In this work, Jeannesson et al. followed Webb's initial work and used Raman spectroscopy to examine the changes in cellular processes caused by an anti-tumour agent on tumour cells [158].

Table 2.1 A summary of early literature documenting the application of Raman spectroscopy to biological molecules and processes.

Thanks to the groundwork laid down pre-1990, it has been possible for the field to expand dramatically in the last 25 years. In fact, many of the most highly cited papers have been published since 1990 and searching the topic search term "Raman spect** tissue" on "Web of Science" shows only 115 out of over 8000 papers were published before 1990. Many of the papers which have garnered the most citations were published after 1990, showing how the new potential of Raman spectroscopy is being explored in biology. There are vast amounts of research focussed on classifying cells and tissues using Raman spectroscopy. Therefore, this discussion of the field, will focus on the key developments and innovations rather than an exhaustive list of every experiment using Raman spectroscopy as a tool to analyse cell cultures and tissues as it has little value to this research. Rather, the focus will be on the key milestones in Raman spectroscopy research, which include: the use of Raman spectroscopy as a live/dead assay, Raman spectroscopy to determine cell cycle state, online monitoring with Raman spectroscopy, examination of ECM in culture, the proof of concept cancer detection and the initial use of Raman spectroscopy *in vivo*. Additionally, there will be a focus on key research in the examination of *ex vivo* and *in vitro* bone and bone cell culture.

As well as demonstrating the potential of Raman as a live/dead assay, in 2003 Notingher et al. [159] also demonstrated that Raman spectra of cells in different phases of the cell cycle exhibited subtle spectral differences [159]. In this experiment, cells from a human lung cell line were set up in a layered configuration to produce cells in the G0/G1 phase in the bottom layer, due to a reduced nutrient supply, and a population of cells in a variety of cell cycle states in the top layer due to free access to nutrients. Analysis of average spectra from these discreet populations revealed that the majority of variation between the populations arose from the spectral peaks associated with DNA. In general, cells in the lower layer exhibited larger DNA peaks. This theoretically confirms that the cells in this layer are in G1/G0 phase of the cell cycle and the cells in the upper layer are moving through the cell cycle [159]. However, it would be very difficult to confirm that all the cells of the upper layer are in the same phase of the cycle. Therefore, this study is a promising indicator that Raman spectroscopy can distinguish static cells from actively dividing cells, rather than a conclusive result. Since 2003, more studies on cell cycle analysis have been performed, offering more evidence as to the cell cycle staging potential of Raman spectroscopy. In 2005, Huang et al. [160] presented evidence that Raman spectroscopy could identify the phase of yeast cells [160], and in 2008, Swain et al. [161] monitored the phase of MG63 human osteosarcoma cells [161].

As well as generating spectra to analyse the biochemistry of a cellular sample, Raman spectra can be used to map the distribution of molecules across a sample. This is achieved by simply collecting spectra at multiple points across a sample

and representing the intensity of a Raman peak at each point across the sample using a colour scale. This simple process allows maps of molecular distribution to be obtained, which allows an image of a sample to be created. A recent study using Raman imaging was performed by Ichimura et al. [162] to examine the state transition of myogenic and embryonic stem cells as they differentiate. In the Raman images, several peak intensities are plotted using different colours. Although the colour maps do not clearly elucidate the differentiation process, possibly because the study doesn't look for or analyse specific differentiation markers, it does show clear, unsurprising differences between the nucleus and cytoplasm. Therefore, the next logical stage in this work would be to analyse the changing spectral components in detail through differentiation in order to improve mechanistic understanding of the process and to produce the maps of key differentiation markers. However, some separation of populations was also found by the application of prinicpal component analysis (PCA) [162]. One key consideration that is often ignored in the generation of Raman maps for biological analysis is the criteria used to create colour mappings to translate intensity information into false colour images. This issue has been recently considered by Ashton et al. [163], who highlight that different colour map intensity ranges can vastly change the information conveyed in a Raman image. In the study they compared different colour map generation schemes for the tracking of a drug within a cell population. As well as demonstrating the drug tracking prospects of Raman spectroscopy, this study demonstrates that transparency in how the colour map was chosen is vital. They go on to suggest that the best approach to presenting false colour images is to provide distribution plots of the intensity values overlaid with the colour map selected to show the reasoning behind selecting the colour map in question, as well as illuminating the meaning of the scale provided [163].

An exciting area of Raman research is in real time analysis of cells that are exposed to an external factor. Recently, Morita et al. [164] and Takanezawa et al. [25] examined cellular dynamics of MCF-7 cancer-derived cells exposed to growth factors using Raman spectroscopy in a set of studies. In this portfolio of work, cells were exposed to either heregulin or epidermal growth factor and compared to cells without a growth factor. Heregulin causes cells to form oil droplets in the cytoplasm, whereas epidermal growth factor stimulates proliferation. The main technique used in this investigation is PCA, which is employed to examine cell population changes over time through the changing forms of cell distributions in PCA component space. In the first instance, cells exposed to heregulin were monitored over 12 days, followed by a shorter study of cells under heregulin and epidermal growth factor over 24 hours. In each instance, clear time-dependent changes in the PCA distributions and Raman spectra were identified, whereas the untreated control exhibited no real change in PCA distribution and spectra. The key finding of this work is that there appear

to be different resting populations of cells which undergo changes into different end states under 24 hour exposure to heregulin, whereas, when cells are exposed for 24 hours to epithelial growth factor, the different resting populations transition into a single state. This work is an excellent proof of concept and shows how PCA can be used with Raman not just to identify two different populations of cells, but to help understand and monitor cellular processes [25, 164]. The only disadvantage of the initial study was the use of independent cell cultures at different time points, meaning, different cells are measured at each time point, which could contribute to broadening the PCA distributions and creating uncertainty in the experiment [164]. However, in the second, more detailed study, the same cell cultures were tracked throughout the experiment, with the authors noting no evidence of photodamage at a slightly reduced incident power than used in the first experiment [25].

One of the pressing issues with Raman spectroscopy is how to sufficiently extract information from the collected spectra in order to identify spectral differences between cells. In 2005, Notingher et al. [165] worked towards providing clarity regarding which analytical methods should be used to provide the required level of information from the spectra [165]. The authors recommend that for applications where small differences in biochemical composition need to be identified, such as in early disease detection, the optimal choice is PCA analysis combined with linear discriminant analysis. However, when the aim of Raman spectroscopy is to analyse and interrogate the biology of a cell or tissue, the authors conclude that a classical least squares approach is optimal, as it fits the spectra of individual biochemical components to the overall spectrum [165]. Unfortunately, the authors neglect to fully consider partial least squares regression in their analysis [165]. Partial least square regression is another tool for multivariate analysis which can produce models to describe how spectra change as the result of an alteration to a specific environmental variable [166]. Therefore, Notingher's work [165] may not provide a complete solution for optimal spectral analysis.

There is a strong level of interest in using Raman spectroscopy to complement or even replace standard histology techniques in biological and medical applications. A recent work by Bonetti et al. [167] in this area compared Raman imaging to traditional histology techniques to analyse calcified stenotic aortic valves. In the study, Raman maps were created from hydroxyapatite, collagen, phospholipids, cholesterol, and carotenoid peaks, and compared to von Kossa staining for calcium, Movat pentachrome for ECM, and Nile blue for lipids. The Raman maps were highly consistent with standard histological staining and confirmed the form of hydroxyapatite present in calcified valves as a type B apatite, which forms in heterophic ossification. It was concluded that Raman spectral maps generate extra information on top of histological investigation, suggesting that there is a strong potential for using Raman

spectroscopy in interrogating disease pathologies [167].

The biological Raman spectroscopy community is extremely active, with new applications for the technology being explored all the time. The studies mentioned above are a fantastic representation of the diversity of research being performed in the community. However, there is still a long way to go before Raman techniques enter standard use in biological research. In many cases, studies need to be performed with increased numbers of samples in order to show that the effects observed over a small number of repeats or only over one cell culture, are reproducible over a statistically significant population [25, 118, 159, 161, 164, 167]. Furthermore, there needs to be more rigour in examining the effects of Raman irradiance on cells over longer time periods if Raman is to be used as more than an endpoint assay.

2.3.2 Raman Spectroscopy for Cancer Detection

Research into using Raman spectroscopy to identify tumours has been greeted with a great deal of interest from the academic community at large. The development of possible screening processes has the advantage that it can be easily validated by histology, could provide a greater depth of information about the tumour and its biological profile, and has the added attraction of the possibility of being able to diagnose tumours without a biopsy. Additionally, it is hoped that Raman spectroscopy may have a role in guiding surgery with real time *in vivo* measurements, allowing surgeons to see if they have removed all of a tumour or not [93]. In many ways, cancer screening is a fantastic test bed to show the potential power of Raman spectroscopy and highlight the areas where more advances are needed. The key aims of the spectroscopic measurement of tumours are to catalogue and characterise tumour spectra such that they may be identified by Raman spectroscopy in future diagnostics and, secondly, to further develop our understanding of tumour processes in biology. In this review, the focus will be on introducing the field of cancer detection in Raman spectroscopy, and then on the key research in this area that has an impact on the application of Raman spectroscopy to tissue engineering.

The very first studies performed on cancerous cells with Raman spectroscopy were those of Schmidt-Ullrich et al. [168] in 1975. In this early work, Raman spectroscopy was used to monitor the changes in isolated plasma membranes under exposure to viral agents. The key aim of this work was to highlight the potential viral element in tumourogenesis [168]. In a later, similar work Verma et al. [169] in 1977 examined the effect of temperature on transitions of isolated normal membranes compared to virally transformed tumourogenic membranes [169]. However, the first incidence of examining tumour cells with Raman spectroscopy can be traced to Webb et al. [154–156] in 1976 and 1977. Over a period of a few years, Webb

and collaborators focussed on examining tumourgenic transformations in cells [154–156], while in 1977 they published a key study examining isolated breast tumour cells compared to normal cells and looked at transformed BHK cells in comparison to normal cells [157]. After this initial work, progress on tumour cell analysis stalled. However, in recent years there has been a strong resurgence in research exploring the potential of Raman spectroscopy in cancer detection.

A very important work in the area of cancer detection is that of Frank et al. [170, 171] between 1994 and 1995. Over a set of studies, Frank and collaborators found the optimal laser wavelength for Raman spectral collection from breast tumour biopsies, and performed a pilot study with attempts to classify the Raman bands present in terms of the lipids giving rise to the signal [170]. After this initial study, Frank et al. proceeded to perform a robust characterisation of breast tumours in comparison to normal healthy breast tissue. Using a relatively large data set of 123 spectra collected from 47 samples across 12 patients, Frank et al. were able to identify the key Raman bands which indicate a tumour with histological backing. Additionally, they created a robust frame work for identifying spectral changes across samples. Frank et al. were very rigorous in their methods. They looked for changes in the average cancer spectra that were outside the 5% standard deviation of the average health spectrum. The difference found in the ratio of the 1654/1439 cm^{-1} peaks between healthy and cancerous samples was found to be around 100%, much greater than the standard deviation of the healthy spectra of 5%. This variation is a clear demonstration that not all tumours are alike and that large data sets are required to define tumour criteria, as, if only a small data set is taken, the definition of a 'typical tumour' could exclude many abnormal pathologies. Additionally, a proof of concept study focusing on fibre optic probes use is performed, showing that the probe's silica background can be subtracted to provide spectra of healthy and cancerous tissues that retain their key features. Therefore, this study demonstrated that Raman biopsies *in vivo* could be a useful tool in breast cancer diagnosis [171]. The work performed by Frank et al. has a great deal of importance, not just for Raman spectroscopy as a cancer diagnosis tool, but for Raman spectroscopy as a tool in all of biology. Their research, clearly defined a baseline case, and that diagnostically relevant changes must not fall within the margin of observed instrumental or inherent biological variation. This concept is clearly applicable in all forms of biological Raman spectroscopy, from classifying stem cells to observing differentiation and extracellular matrix growth. If one were to observe spectral changes, but not have a robust 'normal' population average with an associated standard deviation formed from many, many measurements, variations in spectra due only to population inhomogeneity could be incorrectly identified as a marker of a pathology, process, or cell. Using these methods, Frank et al. note

that although they observe some differences between benign and malignant tumour spectra, they do not have large enough sample sizes to make a conclusive judgement on the discrimination ability of Raman spectroscopy in this sense [171].

In 2002 Schafer-Peltier et al. [172] performed a Raman imaging study of breast cancer biopsies in efforts to work towards the use of Raman spectroscopy as an *in vivo* biopsy tool. In their work, frozen tissue samples were examined in order to attempt to avoid introducing fixation artefacts from the use of chemical substances to preserve biological samples [172]. This is an important area of research as if Raman spectroscopy was used *in vivo*, the collected spectra could be different to those from chemically preserved tissue samples [172]. Another interesting aspect of this study is the discussion of PCA analysis. The authors note that whilst PCA is a valuable technique, it requires larger data sets than they have for the analysis to be reliable, and that it does not provide identification of spectral components, only differences between different spectra. Therefore, the authors use an algorithm to match 'known' spectra to the features of the experimental spectral data sets. This work was mainly based on identifying the key spectral contributors and validating their use as a model. The benefits of this work are that, after validation, the model can be used to identify the percentage composition of a sample of each of the components and to produce Raman images mapping each component. This study also highlights how calcium compounds have a key role in the diagnosis of malignant breast lesions. Therefore, there are applications in understanding biological mineral content far beyond simply performing bone analysis. The key feature of this work is that, by creating a model that describes all forms of breast pathology, it allows for the identification of breast cancer by quantifying the percentage of each fit component applied to a spectrum. Therefore, not only does it allow for discrimination between different pathologies, it also highlights the source of those differences in a physically tangible way, allowing for an increased understanding of the fundamental chemical markers associated with normal and diseased states [172]. The main limitation of this work is the assumption that all breast samples are similar, an assumption used in order to produce the basis spectra. As other works in this review discuss, this is not the case, and therefore, although in these measurements inter-patient variation is not found or considered, a more robust examination and classification of variation is necessary [171]. Other work has also been performed on the use of Raman spectroscopy as a replacement for histology in biopsy analysis in bone cancer. Chiang et al. [24] recently demonstrated the ability of Raman spectroscopy to distinguish between osteosacrcoma cells of different stages through measurement of mineral to matrix ratio [24]. However, as they used controls of foetal osteoblasts and MSCs rather than primary osteoblasts further work needs to be done to verify whether Raman spectroscopy can distinguish cancerous osteoblasts at different stages from healthy primary osteoblasts as well as

from each other and the inherent MSC population [24].

One of the key challenges in the use of Raman in cancer diagnosis is the ability to produce well defined criteria for diagnosis. There are numerous methodologies that can be used to perform this discrimination. One interesting method by Sigurdsson et al. [173] tested for skin cancer through the application of a neural network for automatic classification of lesions. Classification of skin lesions is currently a key challenge in medicine, with malignant melanoma being correctly classified by experienced practitioners at a rate of 65% to 75%. Therefore, there is a clinical need driving the development of Raman technologies in this area. By applying neural network analysis to Raman spectra of a range of normal and diseased skin pathologies, the classification rate of malignant melanoma was found to be 75.2% to 85.8%, an increase on clinician-led identification. The overall classification rate covering a range of pathologies was found to be 91.8% to 97.8%. Therefore, this work presents a strong argument for the further development of Raman spectroscopic diagnosis methodologies [173]. In the same year, the same research group published a paper by Gniadecka et al. [174] reporting correct malignant melanoma diagnosis rates of between 80% and 90%, using a very similar biopsy test set [174]. This improvement in classification rate could be due to the use of a first derivative background subtraction, rather than a regression and simple subtraction method as used previously [173, 174]. However, Gniadecka's study notes that *in vitro* analysis, as used in both these works, induces less variation in spectra than is present *in vivo* which may cause the true classification rate with neural networks to be reduced in clinical practice [174]. PCA is also a promising technique to allow for the discrimination of cancerous and normal tissues. Recently, Raman spectroscopy with PCA been applied to the analysis of oral cancers by Carvalho et al. [175]. In this work, PCA analysis could be shown to provide discrimination between a primary culture of mucoperiosteal tissue and malignant and dysplastic cell lines, the nucleus providing particularly clear differentiation between cell types [175]. Additionally, Raman spectroscopy with PCA analysis has been shown to clearly differentiate between normal tissue and pre-cancerous changes in the cervical epithelium of both low and high grades [176]. Both studies using PCA exhibit strong results, but both also require further testing on greater sample sizes to ensure that they can provide robust metrics for diagnosis of cancer and pre-cancerous changes in a population. However, these developments in the use of Raman spectroscopy with PCA and/or neural networks present promising evidence that clear diagnostic criteria can be derived from Raman spectra.

Although the use of Raman spectroscopy in tumour detection and removal has great potential. It is important to remember that Raman spectroscopy of cancerous tissues is still in the research phase and there is a good deal of work to do before

Raman in instrumentation becomes a standard part of the cancer diagnosis pathway.

2.3.3 Raman Spectroscopy of Bone

Raman investigations of bone have often been a pioneering research area in biological Raman spectroscopy. The very first recorded whole tissue spectra came from the work of Walton et al. in 1970 [147] as described in Section 2.3.1. In this work Walton, and collaborators performed a comparative study between infrared spectroscopy and Raman spectroscopy of an ox tibia. In the experiment, the sample was treated with acetone and chloroform in order to remove the fatty component. In the spectroscopic investigation, the phosphate bands were identified as the key component of the spectrum and the authors suggested that the strength of the phosphate bands and other inorganic components could lead to possible uses of Raman spectroscopy for producing information on the form of the crystal in a calcified tissue [147]. Since this initial *ex vivo* work, there has been a great deal of activity in the field of Raman analysis of *ex vivo* bone in a range of situation. Firstly, there have been many studies examining the mineral form of biological hydroxyapatite [123]. Raman spectroscopy has been applied to analyse harvested bone samples in order to examine bone development pathways, to investigate the properties of bone, to examine bone-implant interfaces [177], and to assess the potential of Raman spectroscopy for clinical use in distinguishing bone pathologies [178].

Other applications of Raman *in* or *ex vivo* include the analysis of bone structure in terms mapping the components of bone and determining the orientation of the collagen fibres which form the majority of the collagen matrix. One such work examining this aspect of Raman spectroscopy is that of Kozielski et al. [179] in 2011. After capturing Raman spectra from trabecular bone over a 90×90 μm^2 area, Raman maps were computed for a variety of quantities which indicate matrix composition. In addition, by applying linearly polarised light to the sample and measuring scattered light at certain polarisations, it was possible to uncover the direction of collagen fibril orientation using the polarisation dependent ratio of the phosphate ν_1 peak to the amide I peak [179]. Furthermore, in additional to attempting to determine mechanical properties from Raman spectra, work has been performed to examine the molecular changes induced in bone by damage mechanisms. For example, in the 2003 work by Carden et al. [180], spectral changes after permanent deformation by indentation were examined [180]. Through examining spectra across the created indents, it was found that the spectra at the edges indicated a rupture of collagen cross links. Additionally, the indented region exhibited spectral changes which possibly indicate that the mineral component has gone through a change in structure, potentially due to the pressures applied in indentation [180].

Applications such as these have helped to further the understanding of the biology of bone and to advance new research. However, examining *ex vivo* bone has its limitations. The bone is in a static state and is not metabolically active, and *ex vivo* bone is often chemically processed to allow for analysis to take place. Therefore, the chance to study the vital metabolism of bone is lost and there is a chance that processing can lead to spectral artefacts.

Analysis of bone and bone cell cultures with Raman spectroscopy can generate a vast amount of detailed information about the sample being analysed. As well as providing information of the pure molecular composition of the tissue, Raman spectroscopy can also provide information about key properties of the ECM of the sample being tested. Firstly, the level on mineralisation of the ECM can be ascertained through the mineral to matrix ratio by calculating the ratio of the phosphate ν_1 peak to the amide I peak [181]. The mineral found in bone is not a pure hydroxyapatite, it is a substituted apatite with carbonate and hydroxide groups substituted into the lattice [182]. Therefore, Raman spectroscopy can be applied in order to analyse the extent of lattice substitutions through calculation of the ratio of carbonate to phosphate ν_1 peak size. Furthermore, it has been postulated that crystallinity of the mineral could be linked to the value of the full width at half maximum of the phosphate ν_1 peak, but this link still requires further study to allow for a greater understanding of this relationship [183, 184]. The application of Raman spectroscopy to bone analysis is not limited to mineral studies, it can also be used to analyse the collagen component in terms of quality through analysis of amide I peaks. However, this is of limited applicability due to difficulties obtaining a high enough signal to noise ratio (SNR), meaning that there is information Raman spectroscopy can access which is currently unobtainable due to spectral collection difficulties [181]. The framework for determining these properties was developed through spectroscopy of *ex vivo* bone [181–184], but they can be applied as metrics to the developing ECM in cell culture.

Penel and collaborators have produced several key works on the Raman spectra of bone. Their comprehensive 1998 work [123] is one of the most important papers in the field of Raman spectroscopy of bone and is commonly used as a reference for band assignments. This key work compared biological apatites with hydroxyapatites with different forms of carbonate substitution, known as type A and B respectively. Through application of Raman spectroscopy, it was possible for Penel et al. to show that biological apatites as found in bone, dentine, and enamel produce Raman spectra consistent with a mixture of carbonate substitutions. Additionally, this study highlighted the presence of acidic phosphate species in biominerals [123].

In order to provide more specific and detailed spectra, there has been a large amount of work performed on osteogenic cell cultures *in vitro*. This work is of

great importance as it allows researchers to rigorously investigate bone formation pathways, cell differentiation and to model systems of cells or cells and chemicals in a well controlled environment. The initial reported spectral measurement of osteogenic cells in culture with Raman spectroscopy was made by Silve et al. in 1992 [185], with the aim of demonstrating the effect of bone and a biomaterial on the mineralisation of an osteoblastic culture. The experiment used osteoblasts cultured from bone chips, with additional biomaterial added to the cell cultures. For analysis, the cells were fixed and sectioned, so that sections of tissue formed between bone and biomaterial chips could be analysed. It was observed that the Raman spectra from mineralising nodules in the new tissues displayed a calcium carbonate component [185]. The work described by Silve et al. is a relatively basic use of Raman spectroscopy. However, since 1992 there has been a vast increase in the number of Raman studies on *in vitro* samples.

Key work on the Raman spectroscopy of cell cultures was performed by McManus et al. in 2011 and 2012 [122, 186]. In 2011 McManus and collaborators investigated the ossification of human MSCs grown on silica in the presence of growth medium or osteogenic medium over a period of 28 days. In this study, Raman spectroscopy was used to analyse cell development over time and it was found that the culture grown in osteogenic medium expressed ECM and mineralised with the ECM, changing over time [122]. Later, in 2012, a further study was performed where the mineralisation of primary human osteoblasts and U20S cell line osteoblasts, cultured in an osteogenic or growth medium for 28 days was studied. Using Raman spectroscopy, McManus et al. were able to show that the mineralisation process and mineral composition was different for the different cell types. This demonstrates that cell lines are not always applicable either in models or as a cell choice in tissue engineering [186]. Therefore, it is very important to properly evaluate cell lines before using them in research or therapies. In both of McManus' experiments, the cells were fixed prior to performing Raman spectroscopy [122, 186], which can induce some spectral artefacts [172] . However, the key result that there are differences between the cell populations in each experiments is not undermined, as both are preserved in the same way. This means that any observed differences should be due to biology, not different preparation regimes [122, 186].

Prior to McManus' work, in 2009, Gentleman et al. [129] performed an important study on the properties of the mineral produced by different cells with osteogenic potential. Raman spectroscopy was used as one of several modalities to study the mineral deposited by embryonic stem cells, MSCs, and osteoblasts cultured in an osteogenic medium *in vitro*. This work is very important as osteoblasts, MSCs, and embryonic stem cells have all been posited as potential cell sources for use in tissue engineering. Therefore, it is vital that the mineral these cells produce

has comparable properties to hydroxyapatite found *in vivo*. In this study, Raman spectroscopy was applied at day 14 and day 28, and was utilised in order to evaluate the secreted matrix in a non-destructive way. The day 14 time point demonstrates the early, pre-mineralisation ECM secretion of the cultures and highlights differences between the embryonic stem cells and the other phenotypes. Embryonic stem cell cultures expressed a range of protein features, but osteoblasts and MSCs produced type II collagen and less nucleic acid and phospholipids. This trend of difference continued into day 28, at which point the cells had formed mineralised nodules. The MSCs and osteoblast cultures had formed the three mineral factors found in natural bone, associated to collagen I strands as *in vivo*. However, embryonic stem cells only produced two mineral factors, with mineral unbound and present in fibrous structures. With additional analytical methods, the Raman data enabled Gentleman et al. to conclude that while MSCs and osteoblasts form mineral and matrix similar to that found in native bone under osteogenic conditions, embryonic stem cells do not [129]. Therefore, embryonic stem cells cultured simply with osteogenic medium would not be suitable as a cell source for tissue engineered bone. This is an important finding given the excitement around embryonic stem cells and shows that they may not be the optimal choice in all tissue engineering applications.

A similar vein of study to that of Gentleman was performed by Notingher et al. in 2004 [187]. In this study, the aim was to distinguish the differences between primary osteoblasts, MG63 osteosarcoma derived cells and immortalised alveolar bone transfected with SV40. This study was motivated by the need to characterise cells and to obtain more information on the biochemical differences between the immortalised cells and normal osteoblasts, which may shed light on the difference in phenotype between the osteosarcoma cells and osteoblasts. Raman spectroscopy was successfully applied with PCA to be able to identify the differences between the cancerous MG63 cells and osteoblastic cells of transfected or primary lineages. However, even after application of linear discriminant analysis, a non-significant population separation was recorded between osteoblasts and the transfected cells. This work suggests that, whilst osteosarcoma cells have clear differences to osteoblasts and are therefore not a good option for tissue engineering, transfected cells may be a better option. However, this feels somewhat short sighted as there was some discrimination between transfected cells and osteoblasts and there was no attempt made to examine the difference spectra. Therefore, there is a possibility that some subtle Raman cues are being missed in this investigation [187]. Additionally, there are various concerns with using virally transfected cells for tissue engineering, which Notingher proposes the system be used for. However, this work could help inform the creation of more physiologically relevant cell models through the choice of a more suitable immortalised cell phenotype.

There have been numerous studies examining osteogenic MSC differentiation using Raman spectroscopy *in vitro*. An example of this work is that of Hung et al. in 2013 [188], in which a proof of concept live cell online monitoring approach was employed to monitor osteogenic differentiation over 24 days. In this study, octocalcium phosphate and $\beta-$tricalcium phosphate were identified as hydroxyapatite precursors and that hydroxyapatite only begins to form after nine days in culture, with standard differentiation markers assessed to show the validity of the measurements. Interestingly, although this study is about proving real time *in situ* Raman spectroscopy is possible, the samples are fixed and stained after each measurement. Therefore, although live analysis is performed in phosphate buffered saline, there is no way to verify the cells continued to grow and differentiate without perturbation after Raman analysis [188].

As in most forms of biological Raman spectroscopy, many researchers are very keen to move into using Raman spectroscopy as an *in vivo* tool for a variety of applications. Such applications include in cancer screening, intra-operative assessments during surgery, monitoring drug transport *in vivo*, histological screening, and the *in vitro* analysis of biological constructs [189]. The first recorded *in vivo* spectra of bone were generated through the study of the rat palate with the aim of measuring cancer indicating dysplasia by Bakker Schut et al. in 2000 [190]. In this study, live rats were treated with a carcinogen, with palate Raman spectra collected over time whilst dysplasia developed. Although the study was focussed on the soft tissues in a primary sense, the spectra collected included components from the soft palate and the bone and one indicator of dysplasia was found to be the amplitude of the bone signal which became more obscured the greater the dysplasia became [190]. Although this experiment records the first example of *in vivo* bone spectra, the examination of this spectrum is not the key focus of the study. The first *in vivo* study to truly examine bone in deliberate detail is that of Penel et al. [191] in 2005, where intravital microscopy was used to examine bone and biomaterial interactions with the bone via the use of an implanted titanium bone chamber with a silica window. The chamber was implanted at the calvaria with the bone intact or with a sham defect created and filled with hydroxyapatite or β-tricalcium phosphate. Raman spectra were then collected over the course of several months to monitor changes in natural bone and to observe the integration of the biomaterials. Over time, natural bone exhibited Raman fluctuations, with a lipid fluctuation marked out as a possible healing or maturation process. Additionally, it was found that while the hydroxyapatite spectrum stayed relatively constant with time, the β-tricalcium phosphate PO_4 ν_1 double peak exhibited a reduction and replacement by bone. Also, the infiltration of blood vessels into both biomaterials was observed. This study indicates several key factors. Firstly, it found that the spectra of *in vivo* bone is different from that

of pre-processed *ex vivo* bone, an unanswered question prior to this study. Secondly, the study recognises the dynamic nature of *in vivo* bone, and finally, is a proof of concept for the use of Raman spectroscopy as a method for online *in vivo* analysis of the integration of biomaterials, or indeed other implants [191].

Raman spectroscopy offers the opportunity to analyse the biochemical effects of applied stimuli on cell cultures. This idea was applied to MSC cell differentiation in 2006 by Azrad. et al. [192] in order to examine the effect of an elk velvet antler extract as a supplement in comparison to dexamethasone supplemented medium. Using surface enhanced Raman spectroscopy, via culturing MSCs on a gold substrate, allowed the investigators to collect high quality spectra at low powers on live samples. The collected spectra demonstrated that, over 14 days, the cells exposed to the antler extract differentiated more than cells supplemented with dexamethasone, through earlier emergence of hydroxyapatite precursors and hydroxyapatite itself over the 14 day culture period [192].

Yet another first in Raman spectroscopy that can be attributed to bone is the analysis of human cell differentiation. In 2007, Jell et al. [193] used Raman spectroscopy to analyse the differentiation of human foetal osteoblasts via exposure to bioglass ions dissolved in cell culture medium. The study attempted to show what influence a conditioned medium had on foetal osteoblast differentiation compared to a standard medium and some small differences were found between the media types. However, Raman spectroscopy was able to track changes with time in both cell types, showing that Raman spectroscopy can analyse differentiation in a human model and in other cell types than embryonic stem cells [193].

One possible use for Raman spectroscopy in clinical orthopedic practice could be in fracture risk analysis. Carretta et al. [194] used Raman spectroscopy to try to improve fracture risk analysis for patients in 2015. Current fracture risk analysis through dual x-ray absorptiometry is a good indicator of fracture risk for populations, but not individuals. Therefore, there is a clinical need to create better tools for risk indication. In the study, Caretta and collaborators attempted to map Raman spectra of trabecular bone samples to the local ultimate strain, and toughness. Results of the study showed a correlation between carbonate substitution and collagen cross-link ratios and ultimate strain, suggesting that the quality of bone mineral and the organisation of collagen have a key role in the failure properties of bone. The work does not develop a model linking ultimate strain and the measured ratios. However, there is potential for a larger sample size to create a useful clinical model [194]. Other investigators have also been attempting to develop models to describe mechanical properties using Raman spectroscopic measurements. Another recent study by Ojanen et al. [195] found a link between mineral crystallinity, as measured by Raman spectroscopy, and the viscoelastic properties of bone. In the study, crys-

tallinity was measured as the reciprocal of the full width at half maximum (FWHM) of the phosphate ν_1 vibration. Nanoindentation was also performed to measure the mechanical properties of a variety of bone samples, and Raman spectroscopy was performed on these samples. After analysis, it was found that the reciprocal of the ν_1 FWHM was correlated with creep parameters, and that carbonate substitution and mineralisation are correlated with age, although age had no correlation with nanoindentation measurements. Overall, this is an encouraging study with significant, if weak correlations between parameters [195]. Although correlations are being found between various Raman peaks and mechanical properties, they tend to be weak and are rarely significant in a statistical sense [194, 195]. Therefore, there is a need to investigate the features of larger populations, to use standardised mechanical testing methods and to use more powerful Raman spectroscopy techniques to fully characterise any relationships to a significant degree.

The process of biomineralisation is not fully understood and remains a key research question in bone biology and Raman spectroscopy is being applied to improve understanding of these processes. In 2006 Crane et al. [196] cultured calvaria organ culture with fibroblast growth factor two coated beads compared to those exposed to a control bead and applied Raman spectroscopy to analyse mineralisation occurring in the organ cultures. Over 72 hours of growth, a variety of intermediary mineral phases were observed, including octocalcium phosphate phases. However, this study demonstrated the presence of intermediate phases which are postulated as possibly having a β tricalcium phosphate component and calcium salts. This study was an important step in bone development as it was the first time transient minerals have been detected in culture [196].

2.3.4 Raman Spectroscopy in Tissue Engineering

Raman spectroscopy clearly has large potential benefits demonstrated in a range of fields, and one of the areas which could benefit the most from the development of Raman spectroscopy is tissue engineering. One of the fundamental roadblocks to the further development and introduction of Raman spectroscopy is the lack of non-destructive analysis practices available to provide online information about a tissue engineered construct and quality assurance by methods which do not rely on batch testing. In addition, there is a key potential to apply Raman spectroscopy to the evaluation and monitoring of *in vitro* tissue engineered models. This would help to improve the analysis pathway of 3D constructs in terms of time, money and efficacy, by allowing a study to follow a single construct through all time points. Therefore, a sample's baseline properties could be characterised, and the action of a drug or process to be clearly extracted, and identified. Although Raman is not yet

in routine use in tissue engineering, there are many studies which utilise it or focus on its potential in the field.

One of the key aspects of Raman spectroscopy which makes it attractive for the analysis of tissue engineered constructs is the ability to map cellular components across a sample. In 2003, Uzunbajakava et al. [197] presented the first example of mapping the distribution of cellular proteins using spontaneous Raman spectroscopy [197]. There were several factors which were key to the success of this work; an increase in the laser power applied to cells, an increase in the time for spectral collection, and an overall increase in instrument sensitivity, compared to other works, in addition to the use of a confocal set up [148]. In this work, the protein distribution present in peripheral blood lymphocytes was compared to that of eye lens epithelial cells. This cell selection was made to allow for two very different cell types to be analysed. Lymphocytes do not replicate and have a low level of transcription activity, whereas eye lens cells are metabolically active in lens homoeostasis, replicate, and have a larger nuclear size than lymphocytes. Protein content was mapped in a confocal set up using a 647.1 nm laser. Comparing cell spectra, the lymphocyte cells exhibited a stronger DNA signal, due to it being present in a smaller nucleus and in a condensed form, whereas in the lens cells, DNA will be less closely packed thanks to the increased levels of transcription and large nuclear volume. However, the general protein signal is greater in the lens cells. Raman mapping was performed by analysing the intensity of scattered radiation in the 2800-3030 cm^{-1} region , a recognised protein band [197], over an area of the order of 10 μm^2 in steps of the order of 100 nm covering the cell nucleus. In lymphocytes, the nucleus contained vastly more protein than the cytoplasm, with clear variation across the nucleus. In contrast, the eye lens cells exhibited more protein in the cytoplasm and a more homogeneous distribution across the nucleus. This study is a good example of the power of Raman spectroscopy to provide detailed analytical and imaging of biological constructs, even with a very simple set up. In this study, the key limitations are the use of fixed cells, the time taken to image the cells and the power used. The authors acknowledge that the limit for exposure before spectral changes to the cell is 70 mW for 100 s, but then use 120 mW of power for 1 s per point for analysis of the lymphocyte protein distribution [197]. With a more advanced spontaneous Raman system, these limitations can be overcome, using longer wavelengths and lower power [198][32]. In Perlaki's [148] 2014 review of Raman spectroscopy in TERM, the need to work towards faster and more efficient spectral collection is highlighted in reference to the work by Uzunbajakava et al. [148].

A key paper which is often referenced in the application of Raman spectroscopy in tissue engineering is the work of Krishna et al. in 2005 [199]. This work is often cited as a demonstration of the capability of Raman spectroscopy to distinguish

between cells in a mixed population. However, this description of the work is not quite correct. Krishna and collaborators in fact find that the principle components of the spectra from mixed cell population form a distribution distinct from the populations of the individual cell types. Even though the paper is misrepresented, it is still important. The paper shows that it is possible to identify differences between pure and impure cell samples so it could be possible to identify cancer cells in a heterogeneous healthy background by looking for a deviation from the healthy normal population. In a tissue engineering context, this could be used to identify the differentiation of cells into different terminal states by looking for a population distinct from that of primary cells using PCA [199].

A recent body of work has been produced by Khmaladze et al. on using Raman spectroscopy to asses *ex vivo* produced oral mucosa equivalent (EVPOME) development [200, 201]. In both studies, the aim was to probe whether Raman spectroscopy could identify compromised EVPOME constructs in the *in vitro* and *in vivo* environments. In the initial study, EVPOME was engineered and a number of constructs were exposed to high temperature or calcium ion concentrations as a stressor. Raman spectra and histology were then collected from stressed and control tissues, and markers of stressed tissue were derived from the Raman spectra. In the case of both thermal and calcium stress, EVPOME exposed to the stressor exhibited an increased ratio of the CH_2 peak to the phenylalanine peak, along with morphological changes in other Raman bands [201]. In a later study, the ability of Raman spectroscopy to identify competency of EVPOME constructs upon implantation *in vivo* was measured. EVPOMEs were implanted into mice and analysed after one or three weeks. Prior to implantation, a number of constructs were exposed to thermal stress to provide 'known' incompetent samples of the tissue. At both time points, clear spectral differences could be identified between the stressed and unstressed samples and the study allowed a number of non-viable Raman peak parameters to be identified [200]. The main limitations of the above studies are their limited range of considered stress factors. Although it is important to be able to identify heat and calcium related damage, they are not the only possible damage sources in cell culture. Other potential stressors could be mechanical in nature, due to low temperatures, caused by acidic build up, or due to another source. Therefore, although these studies present some very interesting results, they do not account for all mechanisms of causing cell stress and Raman cannot yet be relied upon to identify tissues damaged by any and all stresses. It is also worth noting that, while the results of measurement of Raman peaks intra sample showed clear differences between stressed and unstressed populations, the differences between the averages of all control batches against all thermally stressed batches and all calcium stress batches do not show significant differences [200, 201]. Therefore, the need to con-

sider inherent biological and inter-patient variation is vital. Research focusing on failure screening is not limited to EVPOME. Kerney et al. [202] have investigated the potential of using surface enhanced Raman spectroscopy in order to use Raman spectroscopy to screen for the risk of calcification and therefore failure in vascular grafts. This work is in a very early stage and may be a sub-optimal technique due to its use of antibody-conjugated nano-particles. Nevertheless it is an interesting proof of concept study [202].

In the area of tissue engineered models, one key concern is ensuring parity between the engineered model and the system it is trying to mimic. In order to test the properties of a model against a natural tissue sample, histology is commonly used, which is a sub-optimal method due to its destructive nature. Raman spectroscopy may be able to analyse a tissue engineered model and provide comparison with native tissue in a non-destructive way. Therefore, there is active research being conducted on applying Raman spectroscopy to asses the validity of tissue engineered models. One of the most investigated tissues in this respect is in tissue engineered epidermal models, where numerous groups have compared skin models to native skin. In 2010, Lo et al. [203] analysed an oral mucosa model formed from karatinocytes in EVPOME to a natural oral mucosa sample [203]. Raman spectroscopy was applied as an online monitoring technique alongside immunohistochemistry over a 21 day period. It was found that Raman spectroscopy allowed for a quantitative measurement of maturity due to the linear relationship between the ratio of amide I and phenylalanine peak areas, suggesting that Raman spectroscopy could be used to monitor sample maturity [203]. More recently, Leroy et al. [204] have applied Raman spectroscopy to the comparison of a skin model formed from sheets of dermal fibroblasts seeded with keratinocytes and cultured for 21 days to natural skin. After fixation and sectioning, Raman spectra were collected from natural skin samples and synthesised skin samples. Raman spectroscopy was able to illuminate similarities and differences between the natural and engineered skin, proving itself to be a useful analytical technique for this application [204]. Useful future work could be to see if Raman spectroscopy can be applied as successfully in an online confocal set up with the skin model to see if online non-destructive monitoring of it can be performed, and whether this provides the same level of useful information.

Skin models are not the only *in vitro* model to have Raman spectroscopy applied to them. Recently, Hashimoto et al. [205] produced a study using Raman spectroscopy to analyse the maturation of a nerve model *in vitro*. Nerve models have many applications, this one being focussed on studying the development of neural networks. Over a 120 day period, Raman spectra were collected along side immunohistochemistry data and the results of PCA analysis of the spectra compared to previous electrophysiological studies of a similar model. The work finds that PCA

identifies four different populations of the neural cells with time, which roughly map to three observed states in electrophysiological measurement and appear to be consistent with immunohistochemistry. However, the PCA groupings only exhibit weak separation and the degree of difference is not quantified. Therefore, although this is an interesting experiment, it could be argued that further work is needed to fully understand and interpret the Raman spectra changes through the maturation of this form of model. One way to do this could be through quantifying the changes with time in the peaks that have strong PCA loading and thus contribute to variance in the data set. Additionally, this work has the issue that different systems are analysed at different time points, which could add inherent biological variation into the analysis, making the PCA separation less clear. Therefore, a worthwhile investigation could be to follow several duplicate systems through all time points and to see if PCA separation improves inter or intra cell populations [205].

Another possible application of Raman spectroscopy for tissue engineering is in the screening and quality control of materials and cells used to create tissue engineered models. This is an important application because the use of contaminated materials or, an unintended cell type, could compromise the efficacy of the model. One example of using Raman spectroscopy as a cell screening tool is the work of Stenke et al. in 2014 [206], where the ability of Raman spectroscopy to screen human tracheobronchial cells for signs of cancer was tested by comparing the spectra of the donated tracheobroncal cells and epithelial carcinomas. This study was focussed on the development of airway tissue models, which are of importance in investigating bacterial infection and biotoxin transport. As cell function is key in this environment, non-destructive cell screening would be highly beneficial, as destructive methods are commonplace in testing the cell population. In this study, clear differences were recorded in the Raman spectra of the two cell populations, including the presence of 'known' tumour makers in the cell line, which were absent in the donor tissue. Therefore, this proved the potential of Raman spectroscopy as a screening technology in this context[206].

A key aspect of quality control and screening in tissue engineering is the identification and classification of cells. Many conventional methods of identifying cells are sub-optimal for tissue engineered purposes, namely because they can be time consuming or destructive in nature. A recent study by Pudlas et al. [207] examined the potential for Raman spectroscopy to distinguish between fibroblasts and MSCs. This is a key challenge as MSC populations can be contaminated with fibroblasts in an isolation protocol, and the traditional MSC differentiation assay is destructive and time consuming. By applying Raman spectroscopy, this work found clear differences in the spectra between fibroblasts and MSCs, which can be identified from a difference spectrum and take the form of changes in the fluorescence background

and through PCA analysis [207].

A similar application to cellular identification for Raman spectroscopy in tissue engineering is using Raman spectroscopy for online monitoring of stem cell differentiation *in vitro*. In 2004, Notingher and collaborators demonstrated the use of Raman spectroscopy for following the differentiation of murine embryonic stem cells [208, 209]. This work was later followed for human embryonic stem cells by Schulze et al. [210]. In the first study by Notingher et al. on the analysis of embryonic stem cells by Raman spectroscopy, the initial finding through PCA loading analysis was that the ratio of 813 cm^{-1} RNA peak to the 1005 cm^{-1} peak of phenylalanine could be used as a marker of embryonic stem cell differentiation. When comparing undifferentiated cells to differentiated cells at 16 days onwards, it was found that RNA concentration and therefore 813 cm^{-1} to 1005 cm^{-1} peak ratio decreased. The main failing of this study was that it relied on the definition of differentiation by morphology alone [209], and that there was no corroboration of the result by conventional means, such as via the polymerase chain reaction technique (PCR) [211], except through comparison to the literature. However, this study was a proof of concept which then triggered much more detailed work into understanding and characterising the ability of Raman spectroscopy to non-destructively detect cell differentiation *in vitro* [209]. The later work of Notingher et al. demonstrates decreases in nucleic acid content in spectra over 16 days of differentiation [208]. In the study by Schulze et al. nucleic acids were also found to be more prominent in undifferentiated cells [210], with proteins being more prominent in differentiated cells. The study also goes on to identify ratios of Raman band intensities that are optimal for assessing cell differentiation, along with showing population separation with principal component analysis [210]. The first study of human embryonic stem cell differeniation was in the context of producing cardiac cells by Chan et al. in 2009 [212]. In this work, undifferentiated human embryonic stem cells, embryonic stem cells differentiated down a cardiomyocyte lineage, and human cardiomyocytes were analysed with Raman spectroscopy. Difference spectra were initially used to demonstrate a difference in chemical composition between the cell types, then PCA analysis was performed. Using a linear discriminant analysis informed by PCA, a leave one out cross validation procedure, a predictive model was created for identifying cells of different types. The model was 98% effective for embryonic stem cells, 96% effective for isolated cardiomyocytes, and 66% effective for cardiomyocytes differentiated from embryonic stem cells. This drop in sensitivity of measurement is speculated to be a result of the embryonic cell culture containing cells at different stages of maturity, which PCA analysis confirmed to a degree by showing the differentiated population overlapping with the discrete embryonic stem cell population and cardiomyocite population. However, overall, Chan et al. produced a

strong proof of concept for monitoring human embryonic stem cell differentiation [212]. Therefore, Raman spectroscopy demonstrates a strong potential for online assessment differentiation of stem cells *in vitro*, potentially marking it as a suitable technique for assessing the maturation of tissue engineered constructs prior to implantation. However, these studies are rather short term and do not follow the cells through to a terminally differentiated state. Therefore, there is more to be done on characterising the full differentiation pathway of a stem cell using Raman spectroscopy.

Tissue engineering has strong prospects for creating better *in vitro* models and therefore, for use in testing both drug testing and toxicological screening. Raman spectroscopy potentially has a key role to play in these fields through providing real-time monitoring of changes induced in a cell culture, or to monitor bio-processes and cellular changes to identify toxic compounds. Several works by Notingher and collaborators [26, 213, 214] have focused on the possibility of combining the use of Raman spectroscopy to monitor the activities of cells during exposure to toxic agents. Although these works have been performed on a very simple model, the proof of concept is an interesting one and highlights the potential of Raman spectroscopy to help produce multifunction sensors for toxic compounds. In 2004 Notingher et al. published their first paper on biosensors based on a combination of cells and Raman spectroscopy. In the study they exposed a lung cell line to toxic Triton X and observed the changes in the cells with Raman spectroscopy over 7 hours, with additional information provided by Western blotting and the MTT assay. Over time, the cell viability decreased and clear changes occurred in the Raman spectrum of the cells, including a reduction in some protein and DNA peaks and an increase in some phospholipid peaks. On conclusion of this work, Notingher et al. postulate that, as different toxins cause different biochemical effects, Raman spectroscopy of cells exposed to a toxin may allow for toxin identification through monitoring the differences in spectral changes over time during exposure [213]. In order to work towards proving this hypothesis, a study was performed by Notingher et al. comparing spectral changes in a lung cell line exposed to sulphur mustard or ricin using a 300 mW laser 785 nm. Sulphur mustard acts to trigger apoptosis at low concentrations, with necrosis occurring at high concentrations, whilst ricin causes apoptosis. Additionally, the ability of Raman spectroscopy to identify a cell treated with low concentration of sulphur mustard or ricin was tested. In order to verify that cell death had been initiated or occurred, an MTT assay and fluorescence microscopy was used. There were clear, identifiable differences between the spectra of high and low sulphur mustard concentration, but differences between ricin and low concentration sulphur mustard were not immediately evident. Therefore, PCA and LDA analysis was performed to find discrimination factors. Applying the discrimination

factors to test data sets, it was found that one factor could discriminate damaged cells with 98.9% sensitivity and 87.7% specificity, using another factor to identify the ricin or low concentration sulphur mustard classified ricin treated cells correctly in 71.4% of the time and sulphur mustard treated cells 88.6% of the time. Cells treated with different sulphur mustard concentration could be correctly identified over 90% of the time. Therefore, Notingher et al. have presented strong evidence showing that Raman spectroscopy of cells treated with toxic agents could be a good biosensor for a range of toxins [214]. Finally, a proof of concept drug screening study was performed by Owen et al. [26] (from the same group as Notingher) examining the toxicology of etoposide, a cancer drug, on the A549 human lung cancer cell line. The cells in this study were exposed to 100 μM and were analysed after 24 and 48 hours, with MTT and Western blot assays to provide additional results validation. Raman spectroscopy was performed using a Raman microscope with 100 mW power at the sample at 785 nm. The spectra were analysed using a classical least squares technique which treated each spectrum to be formed from the spectra of each of its component molecules, developed using reference spectra recorded by the investigators. Before analysis, the cell spectra after etoposide exposure exhibited an increase in lipid components and a decrease in DNA peaks, as observed by the group previously [213, 214]. After the classical least squares model was applied, PCA was performed and clear discrimination between untreated and treated cells after 48 or 24 hours was achieved. However, there was no clear distinction between the 24 hour or 48 hour population [26]. Even though these are interesting proof of concept studies, their use of cell lines and 2D tissue culture limit them if a true biological response was to be modelled. This is of particular relevance to the testing of drugs, as to get a valid result the system should be as representative of the *in vivo* situation as possible. However, in the case of toxicological screening, having a consistent marker for a toxin is of vital importance. Therefore, using the immortalised cells may be the best way to keep measurements consistent.

With reference to tissue engineering there are key drawbacks to using many common Raman signal enhancing methodologies. The very popular signal enhancement technique coherent anti-stokes Raman spectroscopy uses a pump probe system to directly excite a particular Raman transition [148]. However, this technique can be complex and expensive to implement, making it a less attractive option for widespread biological use. Resonance Raman spectroscopy can also enhance Raman scattering effects via applying a laser frequency which will stimulate electronic transitions in a sample. Unfortunately the wavelengths required to create this effect in biological samples are in the ultraviolet range [148] and could induce photochemical damage or photdegredation in a sample [16, 20–22]. Surface enhanced Raman spectroscopy has been very effective in amplifying Raman signals due to the stimulation

of plasmon effects in metals situated near to the molecules in question. Unfortunately, in order to use this technique there is a requirement for the sample to be on a metal surface or surrounded by metallic nano particles [148]. This is sub-optimal for biological samples as nano particles are potentially toxic and the effects of nanoparticles on cellular behaviour are not fully understood [215]. Also, the magnitude of the enhancement decreases with distance from the surface so the use of a metallic plate would only enhance the signal from the surface of a tissue engineered construct [148].

One of the key challenges for Raman spectroscopic analysis of tissue engineered constructs is the analysis substrate [216]. Many systems use bottom-up analysis systems which require silica or glass windows for proper observation [30, 198]. Additionally, a tissue culture substrate can dominate the spectrum of a cell culture or tissue engineered sample even when the laser is incident directly on the cells [213, 214, 216]. This could be problematic in tissue engineering, not only for analysing cells, but because cell interactions with the substrate upon which they are grown impact on cell behaviour [217].

The potential of tissue engineering for producing model systems has been highlighted several times in this review. A key enabling technology in this area of research is the bioreactor. Briefly, bioreactors are specialised cell culture chambers designed to provide the cells cultured within them with an environment which is as similar as possible to that found *in vivo* in order to promote the development of cell biochemistry and associated ECM secretion which is as representative of the ECM and cell behaviour *in vivo*, thus providing an improved biological model *in vitro* [218] [219]. Bioreactors are often employed to run for long periods of time with minimal interference [220]. Therefore online monitoring systems are of particular interest for use with bioreactor systems. This is because it would allow the researcher to not only confirm that the cells are alive and physiologically active, but also to maximise the amount of data that can be collected from the model system to aid in increasing understanding of the biological processes at work. Furthermore, bioreactor culture can be very expensive, making the use of replicate systems at multiple time points fiscally infeasible. Therefore, online monitoring could allow thorough analysis of a small number of replicates at all time points in a research study[221]. Currently, there has been relatively little work performed focussing on the use of Raman spectroscopy in bioreactor systems. Additionally, most of the work performed has been in non-tissue engineering applications. However, they are relevant in highlighting that Raman spectroscopic monitoring is possible in the bioreactor environment.

The first study assessing the feasibility of using Raman spectroscopy to aid in monitoring bioreactor systems was performed by Xu et al. in 1997 [222], where concentration measurements of relevant biomolecules were performed using Raman

spectroscopy in order to assess the feasibility of applying Raman spectroscopy to provide data about the molecular environment within a bioreactor [222]. However, it wasn't until 2003 when Raman spectroscopy was first used to monitor a live bioreactor process by Cannizzaro and collaborators [223]. Finally, in 2007, Varma et al. [224] reported the first use of Raman spectroscopy to monitor mammalian cell culture in a bioreactor, thorough monitoring metabolites, total cell count and viable cell count using Raman spectroscopy for a culture of Chinese Hamster Ovary cells [224]. One of the most developed works was performed by Pulley et al. [225] in 2010, when two bioreactors designed to allow for online monitoring of human MSCs with Raman spectroscopy were created. The first bioreactor was fabricated from poly(dimethylsiloxane) with a CaF_2 substrate for cell growth and to act as the optical window. However, this design was found to be incompatible with Raman spectroscopy due to the spectrometer being unable to focus on the cells through the thick CaF_2 window [225]. An alternative design was developed using a proprietary flow chamber sealed with a coverslip to act as an optical window using parafilm. Using this bioreactor design, cells were successfully analysed with Raman spectroscopy after four days of culture [225]. Unfortunately, cells cultured in the second bioreactor were only analysed once with Raman spectroscopy. Therefore, there is no proof of concept for online monitoring over a time course [225].

Later, in 2011, Abu-Absi et al. [226] performed a proof of concept study for using Raman spectroscopy as an in-line biosensor to monitor various metabolite concentrations as well as the total cell density and density of viable cells [226]. The study attempted to build a model to quantify concentrations of metabolites and measure cell densities from Raman spectra by creating a model set of data and validating the model using a culture of Chinese Hamster Ovary cell line in bioreactor culture. The deviation in the concentration values measured by Raman spectroscopy from those measured with a reference method was greater than the standard deviation of the referenced method in most cases. However, the Raman model captured the general behaviour of the system and could be improved by using a wider set of data to form the initial model. Therefore, this study provides an interesting test of Raman spectroscopy for detailed chemical analysis in bioreactor systems [226]. A similar experiment to Abu-Absi et al. was performed by Whelan et al. [227] in 2012, also on Chinese Hamster Ovary cells, where metabolites and cell densities were measured using Raman spectroscopy of a model developed from reference methods [227]. Once again, the Raman measurements of concentration followed the trends identified in the reference methods, but in most cases the difference between the Raman measurement and standard method was greater than the standard measurement error [227]. Fortunately, *in situ* Raman concentration measurements are improving. In 2015 Berry et al. [228] reported a strong model for deriving metabo-

lite concentration and cell counts using Raman spectroscopy in a Chinese Hamster Ovary cell culture [228]. Models developed on a small test volume had some issues when scaled up [228]. However, this is a positive piece of research demonstrating a further improvement in Raman spectroscopy for *in situ* measurement.

In 2013, Pascut et al. [229] performed a study using online Raman monitoring of embryonic stem cell differentiation into a cardiac phenotype in a bioreactor, arguably the first clear study in tissue engineering to use a bioreactor with Raman monitoring [229]. In the study, differentiation of the embryonic stem cells was monitored using Raman spectroscopy every 24 hours in day 5 to 9 of the differentiation process, during which the cells were cultured in a bioreactor. Spontaneous beating of the cells began at day 7 and throughout the experiment spectral changes in the cell cultures occurred alongside differentiation processes. This study provides a strong case for the potential to use Raman spectroscopy for online monitoring *in situ* thanks to the clear results obtained. However, over the culture period a peak at 505 cm^{-1} developed, which is not a common feature in embryonic or cardiomyocyte culture. This peak was thought to be induced through stressing the cells by not refreshing the culture medium during the investigation, but the chance of it being caused by laser interaction with the sample is not fully explored and should be investigated further. Apart from the possible stress the cells were exposed to, the key disadvantage of this study is that the 'bioreactor' in question was a static sealed culture vessel with an optical window rather than an active environment used to enhance function and differentiation. Therefore, although this is a strong proof of concept for online monitoring using Raman spectroscopy, it does not demonstrate that Raman is applicable in a dynamic culture environment [229].

In tissue engineering, the key need is to analyse the biochemistry of a sample and to detect changes over time. Therefore, the 2005 work of Notingher et al. [165] examining optimal analysis methods, as discussed in 2.3.1, would suggest that rather than using PCA, a classical least square model would be a preferable method in order to attempt to fully understand a sample's spectrum [165]. However, in certain experiments, PCA could be a strong addition for population discrimination. There are many common components across different cell types, as can be seen in much of the literature difference spectra between different cell populations are often unclear which confounds the need for processing methods. An ideal situation would be to generate sufficiently intense and resolved spectra such that difference methodologies produce clear results to allow differences between cell types to be more easily accessed.

2.3.5 Raman Spectroscopy *in vivo*

A branch of research into medical applications of Raman spectroscopy, which is highly complementary to the use of Raman spectroscopy in cancer detection is the development of systems to allow Raman spectroscopy to be used *in vivo* in a clinical context. There is also the possibility that *in vivo* Raman spectroscopy could be used to analyse the integration of implanted tissue engineered therapies overtime in a minimally invasive way to ensure their competency within a patient. Raman could be used as a methodology for the interrogation of animal disease models to help advance understanding of pathological processes, or to investigate the exact mechanisms of drug interactions with diseases and their symptoms in an *in vivo* setting. The general approach of *in vivo* Raman focuses on the use of fibre optic systems, and with improvements in the miniaturisation and alignment of fibre probes there is an increased suitability for using Raman in a range of situations.

In 2002, Knudsen et al. [230] performed a important study examining spectral variations in healthy skin with time, position, repetition, participant and with skin pigmentation variation [230]. The Raman bands examined in this study where the amide I and III bands, with reference to the 1450 cm^{-1} CH band and the water band at around 3250 cm^{-1} with respect to the 2940 cm^{-1} CH band. In the study, potential variations in band intensity and position were recorded in order to fully catalogue variation (if any) across the different epithelial sites. Variations were found to exist within repeat measurements taken at the same time in amide I intensity, between people in amide I and water intensity, with time of day in water intensity, day to day in amide III and water intensity and in amide III wavenumber, and finally with skin pigmentation through background intensity. The authors note that the differences observed in this experiment are small, but use a variety of statistical tests (data set dependent) which indicate each of these variations are significant. Therefore, this work emphasises to the need to study a wide population set to define the bounds of healthy normal spectra *in vivo* [230]. In a similar area, Pence et al. [231] looked at the challenges of performing *in vivo* Raman measurements by examining the spectral variation of the vitamin E and the spectrum of skin between instruments, with changing probe angle and pressure, with physiology, between operators and at two different times on the same day [231]. Over time, between operators and different instruments induced no change in the collected spectrum. For skin, there were no inter-instrument variations detected. However, spectra were shown to vary with probe angle, probe pressure, over different skin locations, and importantly over time. The key finding was that, *in vivo*, one must be aware that there can be significant intra-patient variation, so with this in mind, creating general classification rules for Raman spectra from tissues is difficult. However, Pence et al. suggest that patient

specific controls and consistency checks should allow for suspicious tissue signals to be correctly identified [231]. Once again, the work of Pence et al. has implications for a vast range of implementations of Raman spectroscopy for biological applications.

2.3.6 Challenges in Using Raman Spectroscopy for Biological Analysis

In all applications of Raman spectroscopy, the spectroscopist will aim to generate the highest quality of spectrum. One way to do this is to use a high irradiance on the test sample [23]. As described in Section 2.2.2 the irradiance of the laser exciting a Raman transition is directly proportional to the intensity of Raman photons emitted from the sample. Therefore, the greater the irradiance, the more Raman scattered photons there are and the better the measurement, as detection systems have more photons to count. However, in a biological context, increasing irradiance to increase the photon yield is a poor option. This is because strong light sources can cause damage to tissues by many mechanisms. The key factors that increase the risk of laser damage are unfortunately the opposite of those which lead to higher quality Raman spectra. Shorter wavelengths increase the Raman return, as the emitted intensity is inversely proportional to the 4th power of the wavelength [141]. However, shorter wavelengths also increase the risk of cellular damage occuring, as previously described in Section 2.2.2, but this risk can be redused by using longer wavelengths of light, such as in the infrared region of the EM spectrum [22].

The second factor to be considered is the laser power. Raman intensity is proportional to incident power applied to a sample. However there is a strong relationship between laser power and an increase in DNA damage [22]. Therefore, although the ideal way to increase Raman return at infrared wavelengths to counteract the inverse wavelength dependence is to increase the laser power, this increases the risk of damage to the cells exposed to the laser light. The final factor which influences irradiance and therefore the damage risk of the spectrometer is the resolution of the instrument at the sample. The resolution of the spectrometer in terms of the variations in molecular composition it can measure spatially is due to the spot size of the laser. The higher the spectrometer resolution, the smaller the spot size and the better the Raman image quality achievable. As irradiance is inversely proportional to laser spot size on the sample, in turn, Raman intensity is inversely proportional to spot size [23]. Therefore, a smaller laser spot size improves Raman return as well as instrument resolution. Unfortunately, like Raman return, laser damage is also related to irradiance and a reduced laser spot size, the greater the risk of laser induced damage [22].

The key mechanism associated with Raman spectroscopy is thermal damage.

Many researchers in Raman spectroscopy associate this damage mechanism with large scale burning and immediate changes to the cell morphology and spectra due to clear catastrophic damages [118, 209]. Therefore, there is a tendency within the community to postulate that if the spectra or cell morphology does not alter over the exposure time, there is no damage [118, 209]. However, this does not account for subtle DNA damage induced by the EM radiation [22]. Such damage may not immediately be apparent and, over time could lead to cancer formation and/or cell death [232]. This is evidently not an issue over a short timescale where Raman is being used as part of a cell of terminal cell and tissue assays. However, if the overall headline aim to use Raman spectroscopy in order to analyse constructs over prolonged culture times is to be met, or if Raman is to be used in quality assurance for tissues destined for implantation into patients, there is a strong argument that DNA damage mechanisms should not be ignored, firstly, because DNA damage could result in the results of an experiment being modulated or a construct with a carcinogenic risk factor being implanted into a patient [232, 233]. There are three key parameters which contribute to thermal damage severity; wavelength, time and laser irradiance. Firstly, the shorter the wavelength the stronger biological tissue has been found to absorb laser light, leading to a greater transference of energy into a construct and an increased damage risk [118]. Therefore, in order to protect tissues from damage, lasers with wavelengths in the infrared should be used. Exposure time also impacts on thermal damage. The longer the exposure time the more energy deposited in a tissue and the greater the damage risk [16]. Irradiance is a measure of power per unit area and therefore relates to the laser power applied to a sample and the area over which the laser is focussed [23]. The greater the power and the smaller the area of the laser, the more damaging the laser light is to a sample [22]. Therefore, there is a need to minimise these factors. Further challenges in applying Raman spectroscopy biological settings are also present. The use of substrates suitable for cell growth and spectroscopy can be a challenge [213, 214, 216], as well as clinical requirements for speed and reproducibility of results.

It is clear that all the research methodologies listed above would benefit from a low irradiance Raman technique, especially in the field of *in vivo* Raman where it is not only an experiment which could be compromised, but where it is possible to induce harm to a patient. In addition, there is also a need to develop technologies which better meet the requirements of the clinical and biological community. Therefore, in this research, the ability of low power laser technologies to analyse biological samples will be addressed. In addition, consideration will be paid to the need for fast, commercially viable analytical techniques.

Chapter 3

Aims and Objectives

The existing base of literature, clearly demonstrates that there is a demand for non-destructive analysis in tissue engineering. Raman spectroscopy is a promising technology which could meet this need, producing positive data with regard to the analysis of cell differentiation, cancer detection and live/dead assaying. However, collecting Raman spectra from biological samples can be challenging, high laser powers combined with high spatial resolution, to allow analysis on a cellular or sub-cellular scale, risk inducing damage in cell samples. Additionally, computational background subtraction methods when lower irradiances are applied are sub-optimal, as the background may completely mask the signal of interest. Furthermore, in order to generate enough data for analysis, long timescales are required. As a result, it is clear that although Raman spectroscopy is a very promising technology, it is not a complete solution to the problem of non-destructive analysis in its current form. More powerful methods of Raman spectroscopy, optimised for biological analysis are currently lacking and require development to extend the usage and potential of Raman spectroscopy further. Therefore, the aim of this PhD project was the design, construction and evaluation of a new Raman spectrometer for the low irradiance interrogation of live bone cell cultures in order to specifically identify regions of mineralisation within a cell culture and follow the development of mineralised sites over time.

The specific objectives of this work were to:

1. Design and build a spectrometer with physial amplification capabilities, optimised for biological analysis. The spectrometer will allow low power and high spatial resolution working to minimise irradiance, with lock-in amplification applied. Completion of this objective will provide a novel stand alone Raman spectrometer designed with the analysis of biological materials in mind.

2. Evaluate the performance of the Raman spectrometer using silica as a test standard. Silica is selected as an initial test standard because it forms the

backbone of the optical components and therefore, must be well studied and understood.

3. Produce a set of viable bone cell cultures. Mineralised and non-mineralised samples will be generated based on the rat MSC model in order to allow for comparison of spectra from cellular samples with different properties.

4. Analyse a range of calcium phosphates and cell cultures in order to determine the value of the new Raman spectrometer design for applications in life science, medicine and bone tissue engineering.

5. Produce a proof of concept spectrometer demonstrating that the new spectrometer key technologies could be applied to existing Raman spectroscopy systems or implemented using standard techniques. This will demonstrate the universality of the spectrometer, making the technology accessible non-specialist users.

Upon completion of this research, a novel Raman spectrometer will have been described and developed. The spectrometer will be capable of analysis of biological samples with minimal irradiance and will provide spectra which could be clearly distinguishable from each other, allowing easier sample differentiation using spectroscopy. The final instrument will have tremendous potential in a wide range of medical research fields and could aid in bringing Raman spectroscopy into more routine use in the biological community. The eventual integration of Raman spectroscopic techniques into research could save money and time in analysis, improve the results produced from *in vitro* model systems by allowing all repeats to be followed through all time points and potentially provide quality assurance for biological products and tissue engineered constructs for use in medicine.

This work is a feasability study, with a focus on developing a new methodlogy. Therefore, this work does not represent, at this stage, a comprehensive comparison between the spectrometer developed here and other technologies. As a result, the main criterion for success is the production of spectra using a low irradiance arangement, which has no need of computational background subtration. To verify that any signals collected result from the Raman effect, the spectra produced will be compared with spectra previously reported in the literature. Consequently, the spectrometer's basic function will be assessed as successful if the data produced by the spectrometer matches that in the literature, within the accuracy of the initial design.

Considering the production of biological samples, this area of work will be considered successful if the cell cultures are successfully maintained for the full expansion and differentiation period, and stain for markers of mineralisation. In the case of

cultures grown on 3D scaffolds, the ideal outcome would be to demonstrate that the cells have fully infiltrated the scaffolds through applying conventional analysis techniques for biological samples. However, if the cells do not fully infiltrate the scaffold, but form mineralised cultures on the scaffold surface, these samples will still be useful for analysis, even if they do not exhibit an optimal morphology.

Chapter 4

Materials and Methods

4.1 The Growth of Bone Cell Cultures

Bone cell cultures were prepared in order to provide a live substrate for analysis using the Raman spectrometer. The foundation for the cell cultures was the use of mesenchymal stromal cells in order to produce a mineralised cell culture. The Mesenchymal stem cells are an attractive choice of cell for use in this project due to a number of factors. Firstly, as a primary cell, MSC biology *in vitro* is more representative of *in vivo* than that of an immortalised cell line. Secondly, primary MSCs are relatively easy to isolate through the aspiration of bone marrow.

In preparing the cell cultures for analysis with the spectrometer, the ideal culture morphology would be a 3D system. As described in Section 2.1, 3D culture has many advantages over 2D cell culture, and future 3D tissue models and therapies will be developed in 3D. Therefore, by demonstrating that the spectrometer can be applied to 3D samples, this assures that the spectrometer will be useful in a tissue engineering context. There are many possible scaffold options available for the culture of MSCs, from electrospun scaffolds to porous ceramics, but these can often be difficult to manipulate using standard tissue culture techniques. In this work, it was decided that the proprietary Alvetex® scaffold [234] would be used as a 3D substrate for the growth of MSCs. Alvetex® is designed to be a 3D scaffold which is compatible with standard tissue culture methods in order to make the transition from standard 2D laboratory practice to 3D very simple. The scaffold is formed via the polymerisation of high internal phase emulsions of styrene, divinylbenzene, and sorbitan to produce a porous sheet 200 μm thick, with pores of the order of 36 to 40 μm in size [234]. Therefore, Alvetex® could provide a well defined, easy to use environment for 3D MSC culture.

4.1.1 Bone Marrow MSC Isolation

In this study MSCs were obtained from 4 to 5 week old wistar rats and isolated using a protocol developed by Martin Eduardo Santocildes Romero [235], based on work by Maniatopoulos et al. [236]. During the isolation process, the rats were dissected using aseptic methodologies in a class 2 biosafety cabinet and the femurs were removed and isolated from any surrounding tissues. After isolation, the femurs were placed in vials of Dulbecco's Modified Eagle's Medium (DMEM) (Sigma Aldrich, UK) , supplemented with $100 units/ml$ of penicillin (Sigma Aldrich, UK) and $1\ mg/ml$ of streptomycin (Sigma Aldrich, UK) to help ensure the cells contained within the bone are free of infection. After immersion, the ends of each femur are removed and the bone marrow is flushed out of the bone using a 20 gauge needle filled with 5 ml cell culture medium consisting of DMEM (Sigma Aldrich, UK) with 10% foetal calf serum (FCS) qualified for use with MSCs (Biosera, UK), 20 mM L-alanyl glutamine, 10 $units/ml$ of penicillin (Sigma Aldrich, UK), and $100 \mu g/ml$ of streptomycin (Sigma Aldrich, UK). The collected bone marrow aspirate was then transferred into a standard T75 tissue culture flask, with 1 flask used for each dissected femur, and incubated in cell culture medium of $15\ ml$ total volume at $37°C$ for 24 hours [235]. After this initial incubation, the cell culture plates were checked for infection and cell attachment, following which the culture medium was aspirated and replaced with fresh medium. There are several kinds of cell types which can be found within bone marrow, including MSCs, hematopoietic cells, and mononuclear cells; all of which will be present within the incubated flasks. MSCs are well known as an adherent cell type with some hematopoietic cells adhering to MSCs and tissue culture plastic [237]. When the flask's medium is changed, the non-attached cells will be removed, leaving a population of MSCs and a number of hematopoietic cells remaining. Therefore, there is a strong likelihood that the MSC population was impure, but population purity is not of importance in the context of this experiment. When cell lineage is of vital importance to an experiment, specific testing may be used to ensure the multipotency of the cell population obtained, and confirm that a population which may be classed as MSCs has been obtained [238][239]. However, in this case, the aim of the experiment is to simply obtain a mineralised cell culture and multipotency is not required. Therefore, cell adhesion is sufficient to define an MSC population for this application [237]. After the initial medium change, the MSCs were incubated at $37°C$ and 5% CO_2 with medium changes every 48 to 72 hours until the cells were between 80% to 90% confluent. The cells can then be stored or passaged for further use. When cryopreservation was required, the culture medium was aspirated from the flasks, then the cells were washed twice with approximately 5 ml of sterile phosphate buffered saline. Next,

the cells were released from the flasks via application of 4 ml 0.05% trypsin/0.02% EDTA solution (Sigma Aldrich, UK) and incubation at $37°C$ with 5% CO_2 for 3 minutes, which was extended to 5 minutes when the cells failed to detach after the initial incubation. After the cells had detached, the trypsin/EDTA solution was inactivated by application of FCS at 10% of the volume of the trypsin/EDTA solution (i.e 0.5 ml). The generated solution was washed over the surface of the flask to ensure the maximum number of cells was captured by the solution then transferred into a sterile vial for centrifuge. A cell pellet was formed by centrifuging at 1000 RPM, the supernatant was pipetted off and the cells were resuspended in 10 ml standard cell culture medium. The cells were then counted and aliquoted into vials at a volume such that each vial contained 2×10^6 cells. These vials were then centrifuged at 1000 RPM to generate vials each containing a cell pellet, which were then resuspended in 1 ml of dimethylsulfoxide (DMSO) (Sigma Aldrich, UK) at a concentration of 10% by volume. The cell/DMSO solution from each vial was then transferred to a 2 ml cryovial and frozen overnight at $-80°C$, after which the cells were stored in liquid nitrogen until use.

4.1.2 MSC Culture Protocols

Expansion of MSC Population

Before each experiment, the freshly isolated or cryopreserved MSC population needed to be expanded. The expansion step was required in order to ensure an adequate number of cells were generated for the experimental use as only a small number of cells can be obtained from each rat. Therefore, to minimise the number of rats sacrificed, expansion is necessary. Expansion was performed by seeding 1 million cells per T75 flask and supplying proliferation medium consisting of 15 ml of minimal essential medium with α modification (α-MEM) (Sigma Aldrich, UK) supplemented with 10 $units/ml$ of penicillin (Sigma Aldrich, UK), 100 $\mu g/ml$ of streptomycin (Sigma Aldrich, UK), 20 mM L-alanyl glutamine, and 10% FCS (Biosera, UK). The cells were cultured to between 80% and 90% confluence, then were detached from the flasks using the same protocol of trypsin/EDTA application as for crystorage. After the detached cells had been centrifuged and resuspended in 10 ml standard cell culture medium, they were counted and seeded into T75 tissue culture flasks at a density of 1×10^6 cells per flask, and the volume of medium topped up to a total medium volume of 13 ml. The cells were then replaced in an incubator at $37°C$ and 5% CO_2 and replenished with fresh medium every 48 to 72 hours until reaching 80% to 90% confluence at which point the cells were detached, counted and passaged or seeded for experimental use if the required cell number was reached.

Alvetex® MSC Culture with Static Seeding

The cells and scaffold were prepared for seeding in order to attempt to produce 3D mineralised and non-mineralised cell culture. In all cases of 3D culture, a 2D control was also produced in order to aid in the identification of failure sources in the event of problems occurring with the cell cultures. The first step in seeding the proprietary Alvetex® scaffold (Reinnervate, UK) was to prepare the scaffold by treatment with ethanol to make the scaffold hydrophillic. As per the manufacturer's instructions, a 70% ethanol solution was prepared by using a syringe to pass the solution through a Millex GP 0.22 μm filter (SLGP033RS, Millex GP, UK) into a sterile sample tube. Six Alvetex® scaffolds in 12 well plate insert format were removed from their packaging and placed in a 12 well plate using sterile tweezers. The extra-long arms of the insert were removed using sterile instruments, then each scaffold was treated with 2 ml of sterile 70% ethanol for approximately 2-3 minutes. In order to ensure parity of treatment between 2D and 3D cultures, the wells used for 2D MSC culture were treated in the same way. The ethanol was then removed from each scaffold or well and two washes of 2.5 ml of α-MEM were applied for 2 to 3 minutes to each treated scaffold and well. Each scaffold required seeding with 1×10^6 cells and it was decided each well would receive 2.5×10^5 cells, leading to a total of 7×10^6 cells required to seed six scaffolds and four wells. The required volume of suspended expanded MSC cells at passage 4 were isolated into a sterile centrifuge tube and spun down at 1000 RPM to form a cell pellet, the supernatant was removed from the pellet and the cells were resuspended as per the manufacturers instructions to produce a MSC solution at a concentration of 1×10^6 cells per 100 μl or 10×10^6 cells per ml. 100 μl of cell suspension were pipetted onto each of the 6 scaffolds and 25 μl was pipetted into each of the 6 control wells. The plate was then immediately placed in an incubator at $37°C$ and 5% CO_2 for 20 to 30 minutes to allow the cells to begin to attach to the scaffold. After the initial incubation, each well was supplied with 4 ml of proliferation medium and incubated at $37°C$ and 5% CO_2 for 72 hours to allow the cells to fully attach to the scaffold or plate.

After the initial 72 hours, the medium for each scaffold and well was changed. Two of the scaffolds and two of the wells were provided with more proliferation medium, four scaffolds and two wells being provided with an osteogenic medium consisting of α-MEM (Sigma Aldrich, UK) supplemented with 10 $units/ml$ of penicillin (Sigma Aldrich, UK), 100 $\mu g/ml$ of streptomycin (Sigma Aldrich, UK), 20 mM L-alanyl glutamine (Sigma Aldrich, UK), 50 mg/ml ascorbic acid (Sigma Aldrich, UK), 10 mM β-glycerophosphate (Fluka Biochemika, UK), 10^{-8} M dexamethasone (Sigma Aldrich, UK), and 10% FCS (Biosera, UK). In the case of each medium type, the scaffolds were provided with 4 ml of medium and the wells were provided

with 2 ml. After this initial medium change, the cells received an osteogenic or proliferation medium change (4 ml for scaffolds, 2 ml for wells) every 48 to 72 hours over a culture period of 31 days.

On day 4 after osteogenic medium addition, it was noticed that cells had begun to grow on the bottom of the wells containing suspended scaffolds. In order to ensure that cells were still present in the scaffolds and that they were receiving sufficient nutrition, on day 9 the scaffolds were transferred to a fresh 12 well plate and the experiment continued with the scaffolds receiving 4 ml of medium each and the wells containing cells that had leached from the scaffolds, along with the original 2D controls, were supplied with 2 ml for the remaining culture period of 22 days.

After 31 days, the scaffolds and 2D conventional well plate MSC cultures were fixed and analysed with a variety of modalities. Before fixation, the scaffolds were removed from the 12 well plate, placed into a Petri dish and washed twice in phosphate buffered saline to remove excess proteins from the cultures. The scaffolds were freed from the insert holders and then cut into four equal pieces with a scalpel blade. Each piece of the scaffold was fixed, then analysed using four different methodologies; two sections from each scaffold were fixed in 4% neutral buffered formalin for μ-CT analysis and wax embedded histology, one section from each scaffold was cryopreserved in optimal cutting temperature (OCT) medium and one section from each scaffold was fixed and prepared for SEM analysis. The 2D control cultures of MSCs were also fixed and analysed, utilising methanol fixation and standard staining methods.

Conventional Analysis of Statically Seeded MSC Cultures on Alvetex®

The 2D control MSC cultures were fixed with a cold methanol solution. A 70% methanol solution (Fisher Scientific, UK) was produced with distilled water and chilled down to $-20°C$ in a spark free freezer. 2 ml of the methanol solution was added to each well of cells and the plate was then stored for 30 minutes at $-20°C$ to fix the cells. After the 30 minute fixation process, the methanol was removed, leaving samples ready for staining. After fixation, the plates containing the samples were wrapped in parafilm and stored in a $-20°$ freezer. The 2D MSC cultures were analysed by simple staining and light microscopy techniques. Staining was performed for calcium via the alizarin red stain [240] as a marker of osteogenic differentiation through the demonstration of mineral deposition in mineralising nodules [241] and for alkaline phosphatase enzyme activity through the SIGMA FAST™ BCIP/NBT (5-Bromo-4-chloro-3-indolyl phosphate/Nitro blue tetrazolium)(Sigma Aldrich, UK) stain; which is also a marker of mineralisation [242, 243]. Staining for alkaline phosphatase activity was performed by adding 1 ml of the SIGMA FAST™ BCIP/NBT reagent in 10 ml of distilled water as per the manufacturers instructions, to 2 wells containing mineralised cells and 1 well of non-mineralised cells for 10 minutes. The

stain was then removed and the wells were washed with distilled water. The stain was then imaged using a light microscope, with areas of alkaline phosphatase activity stained blue-black. Staining for calcium deposits was performed by alizarin red staining. The alizarin red stain was prepared by dissolving 342 mg of Alizarin Red S (Sigma Aldrich, UK) per 25 ml of distilled water and adjusting the pH of the resulting alizarin red solution to 4.2 using 1 M NaOH. 1 ml of alizarin red was applied to the remaining wells for 10 minutes, at which point the stain was removed and the wells were washed 3 times with distilled water. As alizarin red is an unstable stain, the cell cultures were imaged immediately after staining with a light microscope to ensure that a true image of the stain distribution could be obtained.

Formalin fixation was performed by decanting 4% neutral buffered formalin in phosphate buffered saline into 5 ml sample tubes, with one tube prepared for each scaffold sample. Two quarters of each scaffold were placed into each individual tube and labelled as required. The sample tubes were placed in a 4° fridge for at least an hour. The samples were then stored at room temperature in the formalin solution. One of each of the formalin fixed samples from each scaffold was sent for wax embedded histological processing and the other section from each scaffold underwent analysis by μ-CT.

Wax embedded histology was performed by Orla Gallagher at the Mellanby Centre for Bone Research Bone Analysis Laboratory at the University of Sheffield, making use of their wealth of expertise in histological processing. The formalin fixed scaffold sections were automatically processed by a tissue processor through stepwise dehydration with alcohol, cleared with xylene and embedded in histological grade paraffin wax. Next, the scaffolds were sectioned into 5 μm slices on a microtome, then placed on a water bath to flatten the sections. The sections were then fixed to electrostatically charged slides and dried overnight in an oven. After drying, the tissue sections were rehydrated by passing the sections through xylene twice, then through industrial methylated spirits (IMS) of 99% twice, through 95% IMS once, through 70% IMS once, and finally immersed twice in tap water. Each pass through xylene and IMS lasted for 5 minutes, with the tap water immersion steps lasting 1 minute each. Next the slides were staining in Gill's II haematoxylin (Merck Millipore, UK) through immersion in the stain for 90 to 120 s, followed by a 3 minute wash with tap water. Then, a 1% aqueous eosin stain (VWR, UK) with 1% calcium carbonate (Sigma Aldrich, UK) was applied for 5 minutes, followed by a short 30 s wash in tap water. The slides were dehydrated once again for storage via immersion in 70% IMS for 10 s, 95% IMS for 10 s, 99% IMS for 30 s twice and immersion in xylene for 1 minute remove any remaining IMS then a 3 minute immersion to clear the slides. Finally, the slides were treated with Distyrene Plasticizer Xylene (VWR, UK) mounting medium to mount the scaffold section on the slide and a cover slip

was fixed on top to protect the sample.

Imaging of the stained section was performed by a light microscope. Haematoxylin is a basic purple dye which stains the acidic components of a cell, namely DNA and RNA. Therefore, the nucleus along with RNA in ribosomes and endoplasmic reticulum are stained purple, along with other acidic species. Eosin is an acidic dye and therefore stains basic structures pink. Many proteins in the cytoplasm are basic, along with intracellular membranes and some extracellular matrix components, so all these areas are stained pink [244].

In order to produce 3D information on the distribution of mineral through the MSC cultures, μ-CT images were captured from formalin fixed scaffold segments using a SkyScan 1172 μ-CT (Bruker, BEL). μ-CT analysis was performed on two mineralised samples and two non-mineralised samples of MSCs on Alvetex® . The scaffold sections were mounted between 2 sections of radiolucent polystyrene to prevent movement during the scan duration and the polystyrene was glued onto the μ-CT mount. CT data was generated with a pixel size of 6.05 μm, 147 ms exposure time, 167 μA and 59 keV x-ray beam energy with no filter in the beam. The μ-CT instrument collected images through the cross section of the scaffold, which can then be reconstructed to form a 3D data set and images in the transverse plane across the scaffold surfaces. Image reconstruction was performed using the NRecon (Bruker, BEL) reconstruction software Image reconstruction image reconstruction 8 pixels were combined to produce each voxel, with a height of 6 μm and lateral pixel size of 24.19 μm. The first imaged scaffold, a mineralised sample, exhibited an artefact in the form of fibrils extending from the scaffold surface. This was caused by excess liquid remaining in the scaffold being absorbed into the polystyrene. Therefore, further scaffolds were blotted on tissue paper before mounting in the CT scanner. After all the data sets had been collect and reconstructed with NRecon, further image processing was performed in ImageJ (U.S. National Institutes of Health, USA) image processing software to produce z-stack images and combined projections of the reconstructed image slices [245].

Cryopreservation was performed on one of the sections of each of the scaffolds. Moulds for the process were made by attaching tubes of tin foil to labelled cork boards using optimal cutting temperature (OCT) medium and a needle was inserted into the cork board. To fix the cork board and foil together, the mould was placed in a small beaker of chilled isopentane to form a sealed mould. The foil mould was then filled with OCT medium and a scaffold section was placed into the mould of OCT medium. The mould is then placed in the beaker of isopentane (Fisher Scientific, UK), which in turn is placed in a dewar of liquid nitrogen to freeze until the medium had turned fully white and solid. The newly frozen sample was removed from the beaker of isopentane, the needle removed from the cork, and the mould

was then placed directly in the dewar of liquid nitrogen. After all scaffolds had been frozen and prepared, the samples were removed from the liquid nitrogen, the tinfoil removed, and the OCT medium mounted scaffold samples placed in a $-20°$ freezer for storage. After cyropreservation, the mounted scaffolds were sectioned using a cryostat and attached to coated slides [246]. Multiple sections from a single scaffold were applied to each slide to account for sections which may be damaged during sectioning or washed off during the fixation and staining. Sections were taken from two of the scaffolds cultured in osteogenic medium and one scaffold cultured in proliferation medium with four slides were prepared from each scaffold. After attachment of the scaffold sections to the slides, the slides were left to dry overnight at $4°C$.

Immunohistochemical staining was then performed on the sectioned scaffolds. Alizarin red staining was performed for calcium via the alizarin red stain as a marker of osteogenic differentiation through the demonstration of mineral deposition [240, 241], staining for alkaline phosphatase enzyme activity was conducted through the SIGMA FAST™ BCIP/NBT stain [242, 243], haematoxylin and eosin staining was performed to stain cell nuclei and extracellular matrix components, and Toluidine Blue O (Sigma Aldrich, UK) staining was performed to stain acidic tissue components staining DNA and RNA blue and glycosaminoglycans purple [247].

Samples to be stained with haematoxylin and eosin staining or toluidine blue were fixed in 4% paraformaldehyde a $4°C$ for 30 minutes and samples for staining with alizarin red and SIGMA FAST™ BCIP/NBT were fixed in $-20°C$ for 30 minutes. After fixation, the scaffolds were washed three times in distilled water. Unfortunately, during the fixation process, all of the sections from one of the scaffolds cultured osteogenic medium were washed off their coated slide. This could have been due to poor sectioning and adhesion to the slides due to the high temperatures on the day sectioning was performed. However, scaffolds from one osteogenic cultured sample and scaffolds from two proliferation cultured samples were retained on their coated slides. To stain with Toluidine Blue O (Sigma Aldrich, UK), the scaffolds were ringed with an Immedge Hydrophobic Barrier Pen (Vector Laboratories, UK,) and the stain applied with for 10-30 seconds. Scaffolds to be analysed with Alizarin red (Sigma Aldrich, UK) and SIGMA FAST™ BCIP/NBT stain (Sigma Aldrich, UK) were prepared in the same way, the stains made using the same method as for the 2D well cultures, and applied for 10 minutes. Haematoxylin and eosin staining was performed via a sample processing machine in the School of Clinical Dentistry at the University of Sheffield, which automates the process of hydrating a sample, staining with haematoxyin and eosin, and dehydrating the sample as described above. After staining, the alizarin red stained samples were mounted in Aqua Pertex®aqueous mounting medium (Histolab®, Sweden) and the samples stained

with haematoxylin and eosin, Toluidine Blue O, and SIGMA FAST™ BCIP/NBT were mounted in Distyrene Plasticizer Xylene mounting medium (Sigma Aldrich, UK). The sections were then imaged by a light microscope.

The final section of the scaffolds was fixed and prepared for SEM analysis. The scaffold sections were placed in individual wells of a 12 well plate, then 2 ml of 0.1 M cacodylate buffer at $4°C$ was added to each well containing a scaffold with a glass pipette in a fume cupboard. The cacodylate buffer was applied to each scaffold for 3-5 minutes, then removed. Next, each scaffold was covered with gluteraldehyde for fixation and left at room temperature for 30 minutes. The gluteraldehyde was then removed from each scaffold, and each scaffold was washed with 1 ml of cacodylate buffer. A small amount of osmium tetra-oxide was then added to each well, to just cover the scaffolds (approximately 0.5 ml) and allowed to react with the scaffolds for 1-2 hours. The osmium tetra-oxide was then removed from each sample and each scaffold was washed with 2 ml of cacodylate buffer for 10-15 minutes. The scaffolds were then stored at $4°C$ in fresh 0.1 M cacodylate buffer until one day prior to SEM analysis.

The dehydration process was performed by applying serially higher percentage ethanol to the scaffolds. Firstly, the cacodylate buffer was removed, then 75% ethanol was applied for 15 minutes, followed by 95% ethanol for 15 minutes, 100% ethanol was applied for 15 minutes, then 100% ethanol over anhydrous $CuSO_4$ was applied by 15 minutes, finally the samples were left to air dry in a fume hood. After drying the scaffold, samplers were applied to carbon SEM adhesive discs (Agar Scientific, UK) on 11 mm diameter SEM stubs (Agar Scientific, UK) and sputter coated with gold. SEM analysis was performed on a Philips XL-20 Scanning Electron Microscope with an electron beam energy of 20.0 keV.

The results produced from each analysis technique can be found in Chapter 5 Section 5.1.

MSC Culture on Alvetex® with Dynamic Seeding and Collagen Coating

In the first round of MSC culture on Alvetex® , it was found that the MSCs mainly remained on the scaffold surface, forming a cell layer rather than infiltrating the entire scaffold and forming a truly 3D culture (as detailed in Section 5.1). Therefore, a mainly 2D culture sample was produced via static seeding of the Alvetex®. It was hypothesised that the failure of the cells to infiltrate the scaffold could be due to the fact that in the initial culture the cells were delivered in a highly concentrated solution, meaning that the cells could have adhered to each other forming cell agglomerates of sizes greater than the pore size, preventing infiltration into the scaffold. Therefore, a second protocol for preparing and seeding the scaffolds was proposed. Firstly, the scaffolds would be coated with collagen to attempt to improve

cell adhesion. Secondly, a dynamic seeding methodology would be applied, utilising a dilute cell solution and shaker plate culture to improve initial cell distribution and potentially reduce the chance of large cell aggregates blocking the pores of the scaffold.

After expanding an MSC population using the methods previously described, the scaffolds were prepared for seeding by applying a coating of collagen I. Firstly, each Alvetex® scaffold was treated with 2 ml of filter sterilised 70% isopropanol (Fisher Scientific, UK) for 5 minutes, like in the initial cell culture period. After application of isopropanol, the scaffold was washed three times in sterile phosphate buffered saline. A solution of collagen I from freeze dried bovine dermis(APCOLL-PD, Australia) was prepared in 0.1 M filter sterilised acetic acid at a concentration of 4 mg/ml, which was then diluted on ice to 0.4 mg/ml using filter sterilised water and 500 μl of the solution was added to each scaffold. The scaffolds were left to soak in the collagen for around 4 hours at room temperature, then at 4°C for around 30 minutes.

Six scaffolds were prepared for seeding with 1 million cells each as per the manufacturers instructions. For seeding, the cells were suspended at a concentration of 5.7×10^5 $cells/ml$ in α-MEM (Sigma Aldrich, UK) supplemented with 10 $units/ml$ of penicillin (Sigma Aldrich, UK) and 100 $\mu g/ml$ of streptomycin (Sigma Aldrich, UK), 20 mM L-alanyl glutamine, 10% FCS (Biosera, UK), and 10^{-8} M dexamethasone (Sigma Aldrich, UK). 12.476 ml of medium and cells were added to two Petri dishes containing three scaffolds each. The Petri dishes were placed on an orbital shaker plate at 30 RPM in an incubator at 37°C and 5% CO_2 for 48 hours to allow attachment to occur. Alongside scaffold seeding, six wells of a 12 well plate were seeded with 4.174×10^4 cells each in 1.15 ml of α-MEM (Sigma Aldrich, UK) supplemented with 10 $units/ml$ of penicillin (Sigma Aldrich, UK) and 100 $\mu g/ml$ of streptomycin (Sigma Aldrich, UK), 20 mM L-alanyl glutamine, 10% FCS (Biosera, UK) and 10^{-8} M dexamethasone (Sigma Aldrich, UK).

After the initial 48 hour period of seeding and attachment, the scaffolds were transferred from Petri dishes into a 12 well plate and a medium change was conducted. Three scaffolds and three wells received a proliferative medium containing α-MEM (Sigma Aldrich, UK) supplemented with 10 $units/ml$ of penicillin (Sigma Aldrich, UK) and 100 $\mu g/ml$ of streptomycin (Sigma Aldrich, UK), 20 mM L-alanyl glutamine (Sigma Aldrich, UK), and 10% FCS (Biosera, UK). The remaining three scaffolds and three wells received an osteogenic medium containing α-MEM (Sigma Aldrich, UK) supplemented with 10 $units/ml$ of penicillin (Sigma Aldrich, UK) and 100 $\mu g/ml$ of streptomycin (Sigma Aldrich, UK), 20 mM L-alanyl glutamine (Sigma Aldrich, UK), 50 mg/ml ascorbic acid (Sigma Aldrich, UK), 10 mM β-glycerophosphate (Fluka Biochemika, UK), 10^{-8} M dexamethasone (Sigma Aldrich,

UK), and 10% FCS (Biosera, UK). The scaffolds and 2D controls were then cultured for 29 days, with media changes performed every 48-72 hours.

On the 29th day of culture, the cell cultures were fixed for analysis. The Alvetex® were washed in phosphate buffered saline (Sigma Aldrich, UK) twice, cut into quarters with a scalpel and each quarter was fixed in a different way to allow different analysis methods to be applied to the same scaffold. One quarter of each scaffold was fixed in methanol, cryopreserved in OCT, fixed for SEM in gluteraldehyde or fixed in 4% neutral buffered formalin. The 2D control cultures were fixed in methanol.

Conventional Analysis of Dynamically Seeded MSC Cultures on Coated Alvetex®

Fixation of a section from each scaffold as well as the 2D control cultures was performed using methanol (Fisher Scientific, UK) cooled to $-20°C$. Utilising the technique detailed in 4.1.2, 2D cultures were fixed and stained with alizarin red for calcium deposition and SIGMA FAST™ BCIP/NBT for alkaline phosphatase activity.

Methanol fixation of scaffold sections was performed by adding 2 ml of methanol (Fisher Scientific, UK) diluted to 70% in distilled water. The scaffold sections were firstly analysed by the p-nitrophenyl phosphate quantitative alkaline phosphatase assay. In the assay, p-nitrophenol phosphate is cleaved by the alkaline phosphatase enzyme to p-nitrophenol. This process can be detected by measuring absorption at 405 nm to determine p-nitrophenol concentration, which is related to the quantity of alkaline phosphatase present in the tested sample. For quantitative analysis, three scaffolds cultured with osteogenic medium, three scaffolds cultured with proliferation medium, and two non-cultured scaffolds, one with collagen coating and one without, were selected. Firstly, a standard concentration curve was developed via serial dilution of p-nitrophenol in a 50 mM glycine (Sigma Aldrich, UK) buffer containing 1 mM $ZnCl_2$ (Sigma Aldrich, UK), 1 mM $MgSO_4$ (Sigma Aldrich, UK), and 27.2 mM of NaOH (Sigma Aldrich, UK) at pH 9.6. The optical density of each known dilution was measured with a Tecan Infinite 200 PRO plate reader at 405 nm. In the experiment, 1 ml p-nitrophenol phosphatase was added to each well of a 12 well plate containing a segment of Alvetex® . After 13 minutes and 20 seconds of exposure to the substrate and 16 minutes of exposure under blackout, 200 μl of the p-nitrophenyl phosphate solution was removed from each well and placed in a 96 well plate with 50 μl of 1 M NaOH (Sigma Aldrich, UK) to stop the reaction. After collections at both time points, the optical density of each sample was measured at 405 nm and the concentration of p-nitrophenol produced in each case calculated.

During the measurement process, it became clear that the optical density values

for the smallest concentrations of p-nitrophenol were unreliable, as many of the measured optical densities were greater than for increased concentrations. Therefore, these values were omitted from the calculation of a standard curve. Finally, there was an error in the collection of the first sample of p-nitrophenol phosphatase acted on by alkaline phosphatase, as shown in the measured optical density value, and therefore, this reading was also omitted from the final results of the assay. In addition to measuring the optical density of the samples of produced p-nitrophenol, control measurements were taken from 8 wells of water, 8 wells of buffer and 8 wells of NaOH in the 96 well plate. The scaffold sections were then stained directly with alizain red or SIGMA FAST™ BCIP/NBT without sectioning. This step was taken because in the previous experiment (4.1.2) it was found that cells were mostly confined to the scaffold surface. Therefore, the easiest way to gain insight into what is happening on the scaffold surface is to simply stain the scaffold directly and image with light microscopy.

Preparation for SEM was performed on a section from each scaffold as described in Section 4.1.2.

Cryopreservation in OCT was also performed for a section of each scaffold as previously described in 4.1.2, stored at $-20°C$. Another section of each scaffold was fixed in 2 ml neutral buffered formalin at $4°C$ for 30 minutes, the formalin was then removed and the scaffolds were stored at $4°C$. However, sectioning and staining of these scaffold segments was not performed due to the results of the staining of the methanol fixed samples and captured SEM images.

The results produced from each analysis technique can be found in Chapter 5 Section 5.1.

4.2 The Background and Theory of the Development of the Raman Spectrometer

The key purpose of spectrometer development in this work is to create a system optimised for low irradiance operation, through the application of a low laser power and small focal point. Therefore, a method of detection enhancement will be required to be able to detect the small Raman signal over various forms of noise. Two forms of Raman spectroscopy which achieve signal amplification and background suppression by manipulating the physics of the Raman spectroscopy system are coherent anti-stokes Raman spectroscopy (CARS) and stimulated Raman spectroscopy (SRS) [248, 249]. CARS and SRS use two beams of laser light in the stimulation of Raman transitions in a pump-probe configuration, where a specific transition between energy levels is stimulated by the system. In a CARS set up, this leads to an increase

in the Raman signal generated and in SRS it leads to a measurable loss in the intensity of the scattered pump beam, known as stimulated Raman loss. Although both CARS and SRS have been shown to improve Raman spectral intensity, they can require complex optics set ups and use expensive equipment, making them less accessible for routine experimental use [248, 249]. One commonly used element of the CARS and SRS set up is the technique of lock-in amplification [248–250].

Lock-in amplification allows a signal with a periodic oscillation to be extracted from a noise background of the order of 10^3 times greater than the signal itself through phase sensitive detection [251] and is widely used to enable extraction of features hidden in a noisy background in many branches of optics and physics [252–254]. Lock-in amplifiers work by measuring a voltage that varies in time at a set reference frequency. In a noisy system, the input to a lock-in amplifier is given a signal we want to measure oscillating at the reference frequency plus an amount of noise. In cases where the signal level is of the same order as the noise, background subtraction can easily provide a pure result for the time varying signal we want to measure without a need to use a potentially expensive lock-in amplifier. However, when the noise signal is much greater than the signal level, background subtraction will be ineffective and the true signal will be hidden by noise [255]. Lock-in amplifiers make impressive noise removal possible by using phase sensitive detection schemes. As previously stated, the key thing for lock-in amplification is to have a signal modulated at a reference frequency. We define this reference frequency as a cosine wave of the form,

$$V_{ref} = A_{ref} cos\left(\omega_{ref} t + \phi_{ref}\right) [256], \tag{4.1}$$

where V_{ref} is the reference signal, A_{ref} is the amplitude of the reference signal, ω_{ref} is the frequency at which the reference oscillates, t is time and ϕ_{ref} is a phase factor. The signal that is to be measured, modulated by V_{ref} will have the form,

$$V_{sig} = A_{sig} cos\left(\omega_{ref} t + \phi_{sig}\right) + V_{noise} [256]. \tag{4.2}$$

V_{sig} is the overall signal, A_{sig} is the amplitude of the signal, ϕ_{sig} is a phase factor and V_{noise} is the noise affecting the signal. Theoretically, the noise signal could oscillate at any given frequency, or could be a DC component. Therefore, V_{noise} is given by the expression,

$$V_{noise} = \Sigma_{\omega_{noise}} A_{noise} cos\left(\omega_{noise} t + \phi_{noise}\right) [256]. \tag{4.3}$$

This equation sums over all noise frequencies present to give a summation of noise terms, characterised by A_{noise}, the amplitude of a noise component, ω_{noise} the frequency of a noise component and ϕ_{noise} the phase shift of a noise component. The

first step in lock-in amplification is to multiply V_{ref} by V_{sig} as given by,

$$\begin{aligned} V_{comp} =& A_{ref}A_{sig}cos\left(\omega_{ref}t+\phi_{ref}\right)cos\left(\omega_{ref}t+\phi_{sig}\right)+ \\ & A_{ref}cos\left(\omega_{ref}t+\phi_{ref}\right)\Sigma_{\omega_{noise}}A_{noise}cos\left(\omega_{noise}t+\phi_{noise}\right), \end{aligned} \tag{4.4}$$

where V_{comp} is the composite signal formed by the multiplication step. Using trigonometry, this expression can be simplified somewhat via the double angle formula (equation 2.11) to give,

$$\begin{aligned} V_{comp} =& \frac{1}{2}A_{ref}A_{sig}\left[cos\left(\omega_{ref}t-\omega_{ref}t+\phi_{ref}-\phi_{sig}\right)+cos\left(\omega_{ref}t+\omega_{ref}t+\phi_{sig}+\phi_{ref}\right)\right] \\ & +\Sigma_{\omega_{noise}}\frac{1}{2}A_{ref}A_{noise}cos\left(\omega_{ref}t+\omega_{noise}t+\phi_{ref}+\phi_{noise}\right)+ \\ & +\Sigma_{\omega_{noise}}\frac{1}{2}A_{ref}A_{noise}cos\left(\omega_{ref}t-\omega_{noise}t+\phi_{ref}-\phi_{noise}\right) \\ V_{comp} =& \frac{1}{2}A_{ref}A_{sig}\left[cos\left(\phi_{ref}-\phi_{sig}\right)+cos\left(2\omega_{ref}t+\phi_{sig}+\phi_{ref}\right)\right] \\ & +\Sigma_{\omega_{noise}}\frac{1}{2}A_{ref}A_{noise}cos\left((\omega_{ref}+\omega_{noise})t+\phi_{ref}+\phi_{noise}\right)+ \\ & +\Sigma_{\omega_{noise}}\frac{1}{2}A_{ref}A_{noise}cos\left((\omega_{ref}-\omega_{noise})t+\phi_{ref}-\phi_{noise}\right). \end{aligned} \tag{4.5}$$

After multiplication, V_{comp} is low-pass filtered. Low-pass filtering is a method to remove frequencies that oscillate above a certain cut off point [257]. In the lock-in the cut off frequency is set close to zero Hz. This is so that only the DC component of the multiplied signal is let through, which in turn means that only signals which oscillate at the reference frequency are detected [251]. The bandwidth of the low-pass filter is inversely proportional to the time constant applied to the filter and can be adjusted to suit the needs of the measurement being conducted [258]. After low-pass filtering, the following output will be obtained from the lock in amplifier

$$V_{PSD1} = A_{ref}A_{sig}cos(\phi_{ref}-\phi sig)+A_{ref}A_{noise}cos(\phi_{ref}-\phi_{noise})[256]. \tag{4.6}$$

Depending on the bandwidth of the low pass filter, there may also be some small noise signal which is not filtered out corresponding to noise with frequencies close to the reference frequency ($A_{ref}A_{noise}cos(\phi_{ref}-\phi_{noise})$). However, the better the low-pass filter and the smaller the bandwidth, the smaller this signal will be. Considering equation 4.6, the signal V_{PSD1} is dependent on the difference in phase between the signal and the reference, the signal will be maximal when the phase difference is 0° and minimal when it is 90°. Because of this, many lock-in amplifiers have phase tuning to allow the in phase signal component to be detected. However, if a signal is produced from the modulating signal that has both in and out of phase components, then some of the signal will be lost in this detection scheme. One method to avoid

this issue is to use a dual phase lock-in system. In dual phase lock-in amplification, the amplifier has two phase sensitive detectors formed of the multiplier and low-pass filter, in the first the signal and reference are multiplied as above. However, in the second phase sensitive detector, the signal is multiplied by the reference with an applied phase sift of 90°. When a cosine signal is phase shifted by 90° it becomes equivalent to a sine wave; therefore, in this case the phase shifted reference signal is

$$V_{ref2} = A_{ref} cos(\omega_{ref} t + \phi_{ref} - 90) \tag{4.7}$$

$$= sin(\omega_{ref} t + \phi_{ref})[251]. \tag{4.8}$$

In the multiplication step, this gives

$$\begin{aligned} V_{comp2} =& A_{ref} A_{sig} sin\left(\omega_{ref} t + \phi_{ref}\right) cos\left(\omega_{ref} t + \phi_{sig}\right) + \\ & A_{ref} sin\left(\omega_{ref} t + \phi_{ref}\right) \Sigma_{\omega_{noise}} A_{noise} cos\left(\omega_{noise} t + \phi_{noise}\right). \end{aligned} \tag{4.9}$$

In this case, a different trigonometric identity is used to simplify this expression,

$$sinAsinB = \frac{1}{2}\left[sin(A+B) + sin(A-B)\right], \tag{4.10}$$

where A and B are angles. Substituting equation 4.10 into 4.9 gives

$$\begin{aligned} V_{comp2} =& \frac{1}{2} A_{ref} A_{sig} \left[sin\left(\phi_{ref} - \phi_{sig}\right) + sin\left(2\omega_{ref} t + \phi_{sig} + \phi_{ref}\right)\right] \\ & + \Sigma_{\omega_{noise}} \frac{1}{2} A_{ref} A_{noise} sin\left((\omega_{ref} + \omega_{noise})t + \phi_{ref} + \phi_{noise}\right) + \\ & + \Sigma_{\omega_{noise}} \frac{1}{2} A_{ref} A_{noise} sin\left((\omega_{ref} - \omega_{noise})t + \phi_{ref} - \phi_{noise}\right), \end{aligned} \tag{4.11}$$

which, after low-pass filtering, becomes

$$V_{PSD2} = A_{ref} A_{sig} sin(\phi_{ref} - \phi sig) + A_{ref} A_{noise} sin(\phi_{ref} - \phi_{noise}). \tag{4.12}$$

V_{PSD2} is out of phase with V_{PSD1} and produces 1 when V_{PSD1} is zero and vis versa. V_{PSD1}, is known as the in-phase component, with V_{PSD2} known as the out of phase component of the signal. V_{PDS1} and V_{PSD2} can be rewritten as

$$V_{PSD1} \approx k_{ref} V_{sig} cos\Delta, \tag{4.13}$$

$$V_{PSD2} \approx k_{ref} V_{sig} sin\Delta[259], \tag{4.14}$$

where $k_{ref} = \dfrac{V_s ig}{2}$ and $\Delta = \phi_{ref} - \phi_{sig}$. In order to measure a phase independent

signal, the resultant of the two values is found,

$$R = \sqrt{V_{PSD1}^2 + V_{PSD2}^2}[251], \tag{4.15}$$

where a phase of θ is defined from the signal, relative to the lock in as,

$$\theta = tan^{-1}\left(\frac{V_{PSD2}}{V_{PSD1}}\right)[251]. \tag{4.16}$$

Although lock-in amplification is widely used in CARS and SRS [248–250], it is not widely employed in basic Raman spectroscopy. This could be a legacy from initial studies using lock-in amplified Raman spectroscopy. Research in 1968 demonstrated that methods such as noise-voltage and electron-pulse counting could generate greater signal to noise ratios than those obtained with a lock-in amplification set up [260]. However, since the 1960s lock-in amplification technology has been improved significantly. In particular, the switch from analogue lock-in amplification to digital lock-in amplification has improved the efficacy of the technique [251]. As a result, in recent years Cooper et al. demonstrated that lock-in amplification techniques can now be used to improve the output produced by a commercial Fourier transform Raman spectrometer [261]. More recently, several investigators have reported novel new spectrometer designs using lock-in amplification for signal enhancement [29, 30, 32, 248, 250]. These systems broadly fall into two categories, systems which modulate a laser and systems which modulate a sample.

Laser modulation has been successfully applied in Raman spectroscopy in a variety of ways. The simplest method for laser modulation is to periodically alter the amplitude of the excitation laser, which is commonly done via chopping. Chopping a laser is achieved by placing a rotating disc containing segments removed from an overall disc of laser blocking material to precise measurements. As the disc spins, the laser is blocked from the rest of the beam path with a periodic frequency as defined by the chopper motor. As the laser intensity varies, so does the Raman return and lock-in amplification can be applied to both the Raman and laser signal. This is the technique utilised by Cooper et al. in 1997 on a commercial spectrometer [261]. However, in this implementation, any background signal dependent on the laser, for example the spectrum of the air or laser sidebands, will not be removed from the spectrum. Therefore, chopping or any other form of amplitude modulation such as the application of an acousto-optic modulator or electro-optic modulator [248, 250] is sub-optimal as method of signal enhancement, background suppression, and noise removal in Raman spectroscopy. In this context, background refers to light components which do not arise from the Raman effect. These components can arise from the laser side bands, stray light from the environment, and Mie scattering which

produce a spectral background which can vary with wavelength. In addition, the Raman spectrum will also be overlayed with a contribution of electronic noise, with noise arising from the detection system such as a photodiode or charge-coupled device (CCD). Lock-in amplification has the capability to remove both these unwanted components which may obscure the signal of interest.

Another possible method of generating laser modulation for lock-in amplified Raman spectroscopy is wavelength modulation, which has been developed by the Dholakia group [30]. Inspired by the work of Rusciano et al. [29, 32] on lock-in amplified Raman spectroscopy and shifted excitation Raman difference spectroscopy (SERDS), De Luca et al. [30] developed a wavelength modulated Raman spectroscopy system in 2010. In SERDS, two Raman spectra are collected from a sample, each at a different wavelength. This means that the Raman components are shifted in wavelength. After spectral collection, one spectrum is subtracted from the other, this removes the constant background which is attributed to fluorescence in the original paper [262], but in actuality this will be due to Mie scattering [125], and producing a Raman difference spectrum [262]. Utilising the idea of the constant background and wavelength modulated Raman signal, De Luca et al. [30] applied a laser scanning over 60 GHz with a defined scan frequency and applied multichannel lock-in detection to enhance signal detection. This methodology produced differential spectra, free of background, with polystyrene captured as a proof of concept measurement, followed by an investigation of Chinese Hamster Ovary cells. In both cases, wavelength modulated Raman spectroscopy removed the background, producing clearer spectra than those collected using spontaneous Raman spectroscopy and SERDS [30]. After the initial spectrometer development, it was found that PCA could be used to create wavelength modulated spectra without the use of a lock-in amplifier [198]. Since this development, the spectrometer has been applied successfully to bone analysis [127], microfluidic biological analysis [263], cancer identification [264, 265] and in a proof of concept drug screening study [266]. Wavelength modulated Raman spectroscopy has been applied very effectively but, like with CARS and SRS, the laser needed for reliable frequency scanning is expensive. Additionally, the technique will amplify laser features and side bands by the same amount as the Raman signal. Therefore, there is value in pursuing alternate techniques for amplification of Raman spectra and suppression of background features and noise.

Sample modulation for lock-in amplification has been successfully explored using multiple methodologies. In 1978, Tzinis et al. [31] applied lock-in amplification to a Raman spectroscopy system by using a piezoelectric mount to apply a periodic stress to a sample under investigation. The periodic stress altered the vibrational and rotational energy level structure, generating a modulation in the frequency of

the Raman bands. Tzinis exploited this frequency modulation as the basis for lock-in amplification [31]. Rusciano et al. [29, 32] also applied the sample modulation to generate a signal for lock-in amplification. In their 2006 and 2007, works Rusicano et al. [29, 32] mounted molecules for Raman analysis in a set of optical tweezers and modulated the positions of individual molecules in an out of the Raman probe laser with a periodic oscillation. In this methodology, Raman scattering will occur with a periodic amplitude due to the motion of the molecule into and out of the exciting laser. This provides the modulation required for lock-in amplification and allows for separation of the Raman signal from the sample and the background as well as the Raman signal from the laser noise [29, 32]. Unfortunately, sample modulation is not a universally applicable method to generate a signal for lock-in amplification. It is not possible to apply an energy level modulation on a molecular scale to a gaseous or liquid sample through the use of the direct stress. Also, if a sample is inhomogeneous, with many different molecules present, the use of optical tweezers would not be possible. Finally, in a biological context, applying stresses to a sample could induce damage to a delicate construct or induce damage on a cellular level. In addition, applying stresses to a tissue engineered construct for a short period of time in an aseptic manner would be very challenging.

Two of the methods discussed above with strong background rejection involved the modulation of the sample itself to produce a signal suitable for lock-in amplification. Oscillating a biological sample in the ways described is sub-optimal. However, if the sample can be moved to produce a periodic variation of signal, why not simply move the focussing component of the optics? Moving the lens focussing the laser light onto a material under test changes the position of the focal point of the lens in the sample. This change should produce a modulation in Rayleigh scattered light and a larger change in the Raman scattered light, which can then be used to lock-in amplify. This is because as the laser focal spot moves into a sample, the area exposed to the laser, and therefore, the number of molecules able to undergo Raman transitions, increases. As elastic scattering from the surface dominates, it is hypothesised that the translation of the focal spot will have more impact on emitted intensity from the smaller proportion of Raman scattered photons than the overwhelming number of photons which undergo elastic scattering. Therefore, the small Raman signal can be extracted from a large background and facilitate the construction of a low irradiance spectrometer suitable for the interrogation of biological samples.

4.3 Preliminary Study

The initial step required to test whether focal point oscillation and lock-in amplification can work to produce a spectrometer is to test the effect of focal point depth in

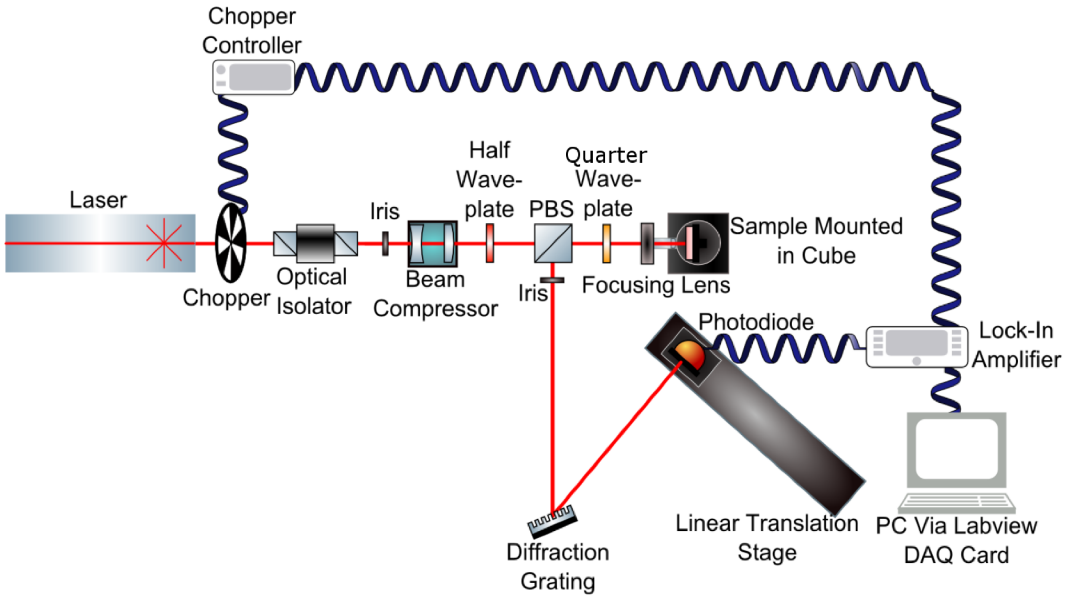

Fig. 4.1 Diagram of the initial basic Raman spectrometer in reflection mode.

a sample on Rayleigh and Raman scatter. Therefore, a basic Raman spectrometer in reflection mode was constructed as per Figure 4.1. In this setup, monochromatic light is produced by a Thorlabs Compact laser diode module (LDM785) at around 788 *nm*. This light has a linear polarisation in an arbitrary direction, which means the electric field of the produced light oscillates in a single plane (see Figure 4.2c). The laser light passes first through an optical isolator, which allows laser light to travel in a single direction, and preventing back reflections into the laser diode, which can cause damage to the diode or wavelength instabilities in the light emitted. This functionality is produced via the use of polarising plates to rotate the polarisation of the beam such that if it is reflected back towards the laser, it is prevented from re-entering the laser cavity. Upon exiting the laser the light has a random linear polarisation, it then enters the first part of the optical isolator, a polariser which transmits light with polarisation in a certain direction and reflects light with polarisation in the perpendicular direction. After passing through the polariser the light is rotated by 45° by a Faraday rotator, then passes through a matched output polariser designed to transmit the output of the Faraday rotator. If any light is reflected back towards the laser, components with a differing polarisation to the light initially output from the optical isolator is reflected, and any components with the same polarisation pass back through the output polariser and are rotated by a further 45° by the Faraday rotator. As a result, the reflected light has a polarisation perpendicular to that transmitted by the input polariser, so it is reflected and prevented from entering the laser [267]. Therefore, it is important to ensure that the optical isolator is tuned to accept the maximum amount of light from the laser [267]. The light is then passed into a beam compressor which shapes the beam into

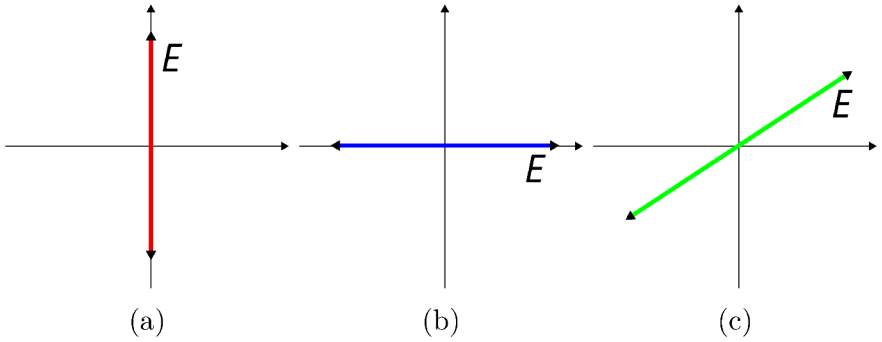

Fig. 4.2 The figures above illustrate the linear polarisation an EM wave. Each coloured line represents the direction in which the electric field oscillates in an EM wave as denoted by $\boldsymbol{E}$. Vertical polarisation is depicted in 4.2a, horizontal polarisation is depicted in 4.2b and 4.2c represents an EM wave linearly polarised in an arbitrary direction.

to a smaller and circular beam. Next the light passes through a half wave plate ($\lambda/2$) to prepare the polarisation for passage through the polarising beam splitter (PBS) .

A PBS transmits or reflects light based on its polarisation. If the light is vertically polarised it is transmitted, but if it is horizontally polarised it is reflected by the PBS (see Figure 4.2). As the laser light has an arbitrary polarisation, if the light was simply transmitted from the optical isolator straight into the PBS a large amount of light would be reflected and lost from the spectrometer. The half wave plate rotates the polarisation of the laser light so that a maximal amount is transmitted straight through the PBS, where the rotation of the axis of polarisation is equivalent to twice the angle between the direction of polarisation and the waveplate's principle axis [268]. The small amount of light reflected due to small imperfections in the optics is simply collected by an absorbing beam dump. After the PBS, the laser light passes through a quarter waveplate, which converts linearly polarised light to circularly polarised light and vice-versa. Circularly polarised light is formed from two linearly polarised EM waves of equal amplitude are superposed on top of each other, which have a 90° phase shift between them and have perpendicular polarisations, as shown diagrammatically in Figure 4.3. In a similar way, elliptical polarisation is formed from two EM waves are superposed waves with 90° phase shift between them, perpendicular polarisations and unequal amplitudes [269]. Circular polarisation is useful in Raman spectroscopy because Raman scattering is effected by the polarisation of the light exciting the Raman transition event [270, 271]. Therefore, the use of circularly polarised light could enable all Raman bands to be excited and examined at once, using a simple optical set-up.

The laser light is then focussed onto the surface of the sample under test by an aspheric lens with an 11 mm focal length and numerical aperture of 0.3. The sample

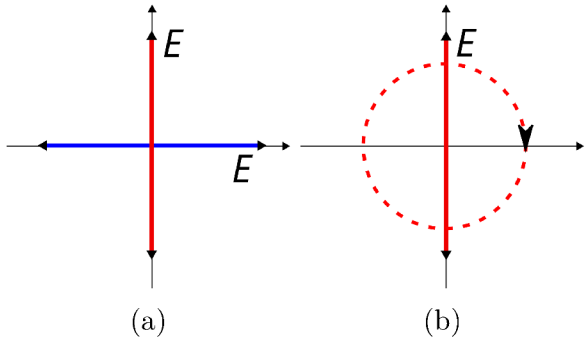

Fig. 4.3 The figures above illustrate the circular polarisation an EM wave. Figure 4.3a demonstrates the superposition of 2 EM waves, 90° out of phase and with perpendicular polarisation which together appear to produce a single EM wave where the direction of electric field oscillation appears to rotate as shown in Figure 4.3b.

is held in a z translation screw mount so it can be accurately translated into and out of the focal point of the lens. Both the Rayleigh and Raman scattered light are collected by the lens and are passed through the quarter waveplate once again to produce light with linear polarisation. The light is rotated from its original polarisation equivalent to the rotation produced if the light had simply passed through a half wave plate once, rather than a quarter waveplate twice [268]. In this case the quarter waveplate is angled to rotate the polarisation of linearly polarised light by 90° after scattering from the sample. Therefore, when the scattered light reaches the PBS again, it will be reflected rather than transmitted, allowing the light to be directed into the arm containing the diffraction grating. After reflection through the PBS, the light then travels through an iris to remove any stray reflections from the quarter waveplate before it reaches a 1200 line/mm reflective diffraction grating with a blaze angle of 750 nm. When light is incident on a grating, it hits a number of lines, causing the light to be diffracted by each of the lines. As each diffraction element has its own discrete position, the distance the light travels between each adjacent pair of lines on the grating differs by

$$P = d\,(sin\theta - sin\phi)\,[272], \tag{4.17}$$

where P is the path distance in meters, d is the distance between 2 lines, θ is the angle of diffraction and ϕ is the angle of incidence. After the waves of light hit the grating lines they are dispersed in every direction. However, due to interference phenomena, the waves of light are out of phase and thus destructively interfere for every value of θ other than the value which makes the path difference an integer number of wavelengths. This gives rise to the grating equation, which describes how

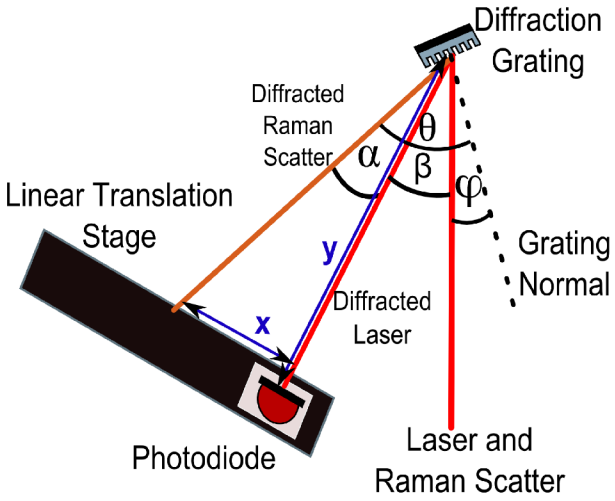

Fig. 4.4 The above diagram denotes the designations of the parameters used to calculate wavenumber values. ϕ is the angle of the incident laser and Raman light on the grating, θ is the angle at which the laser line is diffracted, α is the angle between the laser line and diffracted Raman line, x is the positional separation of the laser line and Raman line on the linear translation stage and y is the distance between the diffraction grating and detector.

different wavelengths of light are diffracted at different angles

$$n\lambda = a(sin(\theta) + sin(\phi))[272], \tag{4.18}$$

where λ is a wavelength, n is an integer, a is the spacing between lines on the grating, ϕ is the angle on incidence onto the grating, which was measured with an accuracy of $\pm 1°$, and θ is the angle of diffraction. After being dispersed, the scattered light is detected by photodiode on a Thorlabs 300 mm linear translation stage. This assembly includes a 50 μm slit mounted in front of it, in order to improve the resolution of the detector. As the grating equation tells us that if the angle between of diffraction is measured then it is possible to calculate the wavelength of light diffracted from the grating. In this set up, diffracted light is measured linearly and the angle of diffraction of each wavelength is not directly measured. However, it can be calculated using trigonometry as described in Figure 4.4. The angle of diffraction (θ) is defined as a sum of the angle at which the laser line is diffracted (β) and the angle between this line and the diffracted Raman light (α),

$$\theta = \alpha + \beta. \tag{4.19}$$

β can be trivially obtained by simply measuring the wavelength of the laser line with a wavemeter, and solving for the angle of diffraction in the grating equation. In order to obtain α, trigonometry is needed. As shown in Figure 4.4, the linear translation stage can produce a measurement of linear distance between the laser

line and the peak in the Raman spectra, x. By measuring the distance between the photodiode and diffraction grating at the laser line, y can be trivially obtained. Therefore, α can be calculated using the following trigonometric identity.

$$\alpha = tan^{-1}\left(\frac{x}{y}\right). \tag{4.20}$$

By finding this expression for α, the position of a feature on the linear translation stage relative to the laser line can be turned into an equation

$$\lambda = a\left(sin\left(\beta+\alpha\right)+sin\left(\phi\right)\right), \lambda \quad = a\left(sin\left(\beta + tan^{-1}\left(\frac{x}{y}\right)\right)+sin\left(\phi\right)\right). \tag{4.21}$$

As Raman spectra are commonly produced on a scale defining the wavenumber shift from the exciting laser line, the wavelength values of each position on the translation stage can be converted into wavenumber shifts using the equation,

$$\Delta\overline{\nu} = \left(\frac{1}{\lambda_l} - \frac{1}{\lambda}\right) \times 10^7 [116], \tag{4.22}$$

where $\Delta\overline{\nu}$ is the wavenumber shift in cm^{-1}, λ_l is the laser wavelength in nm and λ corresponds to a wavelength in nm associated with a point on the linear translation stage in mm. Using this set up with a grating-detector separation of (285 ± 1) mm, grating angle of $(17 \pm 1)^\circ$, and laser line at around 280 mm on the translation stage, gives a spectral resolution of around 2 cm^{-1} which is of the order of, or better than other Raman systems [15, 30, 32, 121]. However, resolution is position dependent and improves to 0.7 cm^{-1} at 2500 cm^{-1}. A tape measure was selected as an appropriate instrument for this measurement as the distance between the detector and grating was between 280 and 300 mm, far outside the range of measurement of vernier callipers. At this distance, the error in the measurement of ± 1 mm represents a measurement error of approximately 0.35%. The value of ϕ was determined by using a protractor. This measurement had a greater error in it. However, for use of the spectrometer as a proof of concept device, although the error of approximately $\pm 1^\circ$ is large, it will still enable an estimate in wavenumber value to be produced and will represent the largest error source outside of the approximations made in the wavelength calculation. By performing a systematic error analysis, the error in the calculation of wavenumbers using this method is of the other of 1.4%, suggesting that the calculation process is relatively accurate. However, this value only accounts for the error in the instruments used to calculate the wavenumber shift and does not account for the many other sources of error. The other sources of error which are not accounted for included, firstly, that the translation stage was unlikely to be exactly perpendicular to the diffracted laser line, as it was very difficult to confirm

the path of the laser compared to the translation stage. Also, the alignment of the laser to any Raman peaks, as regularly performed in the experiment to improve the SNR, was likely to further compromise this assumption. Secondly, the calculation it assumes that the angle α can be tracked to the photodiode exactly, which may not be the case due to the collimation of the light into the photodiode. Finally, the measurement of the grating angle was a relatively rough process using a protractor, and assumed ideal alignment between the laser light and the diffraction grating. Therefore, the wavenumbers shifts measures are likely to have a more significant error. Ideally, the accuracy of this set-up could be significantly improved by using precision motorised, computer controlled rotation stage with a fixed photodiode. However, this system does allow for a rough calculation of wavenumber shift to be performed and could be created without the requirement to purchase an expensive motorised rotation stage.

In order to be able to efficiently and accurately collect spectra, it was necessary to create data collection software using National Instruments' LabView development environment and data acquisition (DAQ) hardware. A program was produced to:

1. Define linear translation scan parameters.
2. Move the translation stage.
3. Trigger and digitise voltage measurements from the photodiode.
4. Write the scan data (photodiode voltage at each position on the stage) out into a file for analysis.

The program block diagram and front panel can be examined in Appendix 1.

The final elements of the preliminary spectrometer set up to be elucidated are the chopper and lock-in amplifier. A chopper is very simply a disc with alternate segments of opaque laser blocking material and open segments. When it is placed in the path of a laser and rotates the opaque blocks stop the laser travelling to the rest of the experiment, while the open segments allow the laser to pass through unimpeded. The chopper wheel is mounted on a highly precise rotary motor which allows the wheel to be spun at a controllable speed, meaning that the opaque areas block the laser at a constant rate, creating a square wave emission profile. When the chopper is added to a laser set up, the periodic switching on and off of the laser beam results in the signal at the detector changing between being the desired signal overlaid with background noise from the detector and external factors, and a signal which is purely due to detector and external noise. Via comparison of these components at the correct chopping frequency, the electronics of the lock-in amplifier suppress the noise, and amplify the voltage generated by laser interactions with the sample. In this experiment, a Thorlabs chopper wheel was placed in front of the laser

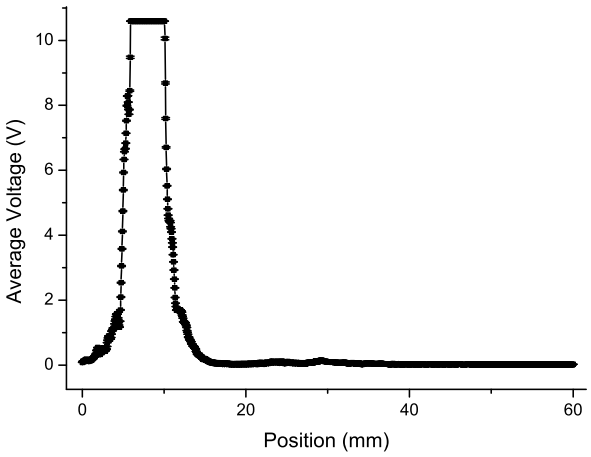

Fig. 4.5 Graph of silica spectrum captured via chopping the laser and lock-in amplification with a sensitivity of 5 mV and time constant of 100 ms, averaged over 50 measurements per point with error bars representing standard deviation.

and connected to a ThorLabs MC1000A control box which drives the chopper wheel at a speed which will result in a square wave laser profile at a particular frequency. The chopper driver is fed into a Signal Recovery 7265 lock-in amplifier along with the photodiode signal, so that the electronics can process the signals being driven at the chopper frequency, thus eliminating background noise and enhancing the Raman and laser signals.

With the spectrometer set up as described above, the next step was to test the hypothesis that focal point position will effect the signal received by the spectrometer. In order to conduct this study, the focal point was initially aligned to the back face of a piece of fused silica. This was found by maximising the laser and scattered power measured with a ThorLabs power meter at the diffraction grating. With the chopper running at approximately 200 Hz, the initial silica signal was captured and lock-in amplified at a sensitivity of 5 mV, with a time constant of 100 ms. As can be seen in Figure 4.5 that this produced a signal with two parts, a strong laser line and an apparent feature to its side at a longer wavelength, which is hypothetically the Raman signal. In the spectrum, position represents the position of the photodiode on the linear translation stage and the laser line saturates due to the signal being much greater than the potential spectral features. During the focal point depth study, the behaviour of the laser line and this feature was examined in order to ascertain the possible impact of lens-vibration lock-in amplification on the signals received from the laser and Raman light. Measurement of the displacement of the focal point was achieved using the screw gage on the sample translation mount, which marks out the distance moved by a turn of the screw (50 μm) in 10 μm steps. The focal point was translated from the silica back-face towards the centre of the silica

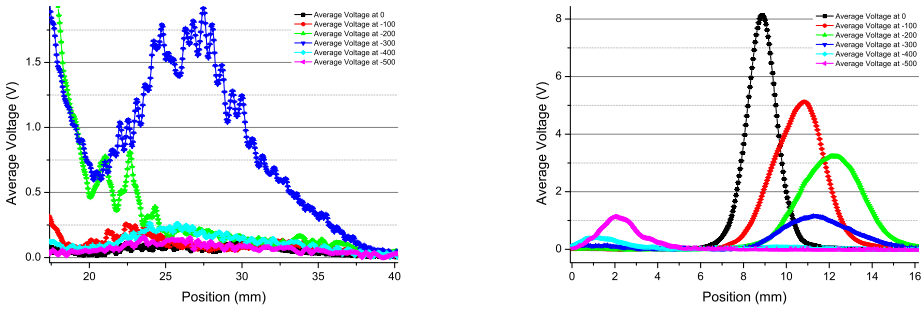

(a) (b)

Fig. 4.6 This graph presents the silica Raman signal (4.6a) and laser line signal (4.6b) at different displacements from the back face of silica. Raman data was collected at a lock-in sensitivity of 5 mV and time constant of 100 ms and the laser signal was collected at a lock-in sensitivity of 500 mV and time constant of 100 ms, with both data sets averaged over 50 measurements in each case and error bars representing standard deviation.

in 100 μm steps to produce a data set of spectra at six depths within the sample, tracking through the 2 mm sample. In this study, 500 mV lock-in sensitivity was used to examine the laser line and 5 mV was used to examine the Raman signal. As demonstrated in Figure 4.6, laser intensity declines, before recovering as the focal point approaches the front face of the silica, whereas the Raman intensity increases to the centre of the silica disc, before reducing towards the front face. To better visualise the trends in Figure 4.6, plots were constructed of the maximum intensity of the laser line and Raman feature with depth as shown in Figure 4.7. This figure shows that there is an inverse relationship between the Raman signal and laser line with distance from the face of the silica sample, where the amplitude of the reflected laser line decreases as the amplitude of the Raman signal increases.

The results gained in the preliminary silica depth study showed that a focal point modulation produces a changing Raman and laser signal with different characteristics in a translucent sample, suggesting that it is suitable for lock-in amplification. However, before proceeding, it was necessary to test whether the modulated effect could also be produced in a non-translucent substance. Therefore, the depth study was repeated with a sample of fused, synthetic hydroxyapatite, with the laser starting focused on the front face of the sample as given in Figure 4.8. As in the silica, the laser line and an area of presumed Raman emission could be seen, but with the Raman area having a slightly different form. Starting from the front face of the hydroxyapatite, found by adjusting the focus of the lens to give maximum power at the diffraction grating, the focal point was translated into the hydroxyapatite sample in 100 μm steps. As shown in Figure 4.8, this measurement demonstrated that Raman and laser line signals decrease with depth, meaning that lens-vibration

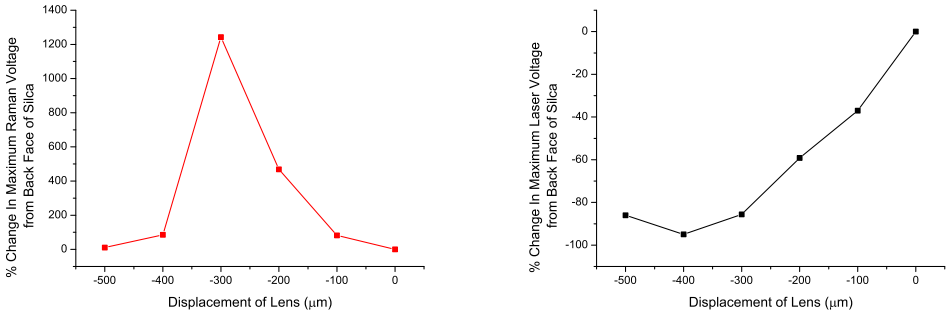

(a) (b)

Fig. 4.7 These graphs demonstrate the percentage change in maximum voltage in the Raman signal with displacement from the back face of silica at a lock-in sensitivity of 5 mV and time constant of 100 ms in 4.7a and the laser signal with the same displacement and lock-in sensitivity of 500 mV and time constant of 100 ms in 4.7b, averaged over 50 measurements in each case and error bars representing standard deviation.

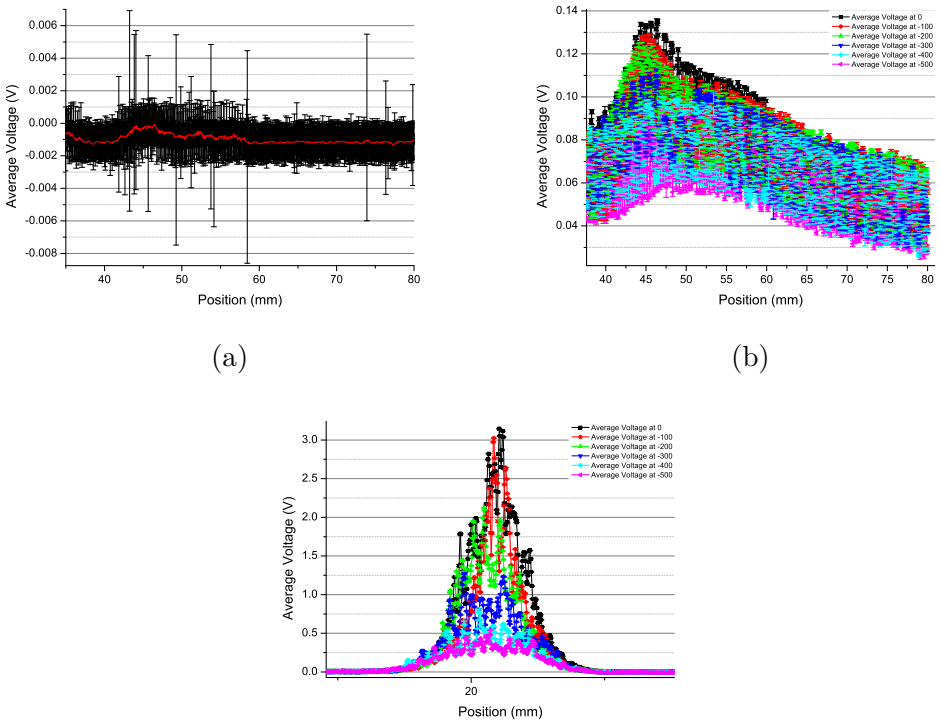

(a) (b)

(c)

Fig. 4.8 These graphs present the hydroxyapatite Raman signal (4.8b) and laser line signal (4.8c) at different displacements from the front face of a fused hydroxyapatite sample. Raman data was collected at a lock-in sensitivity of 5 mV and time constant of 100 ms and the laser signal was collected at a lock-in sensitivity of 500 mV and time constant of 100 ms, with both data sets averaged over 50 measurements in each case and error bars representing standard deviation.

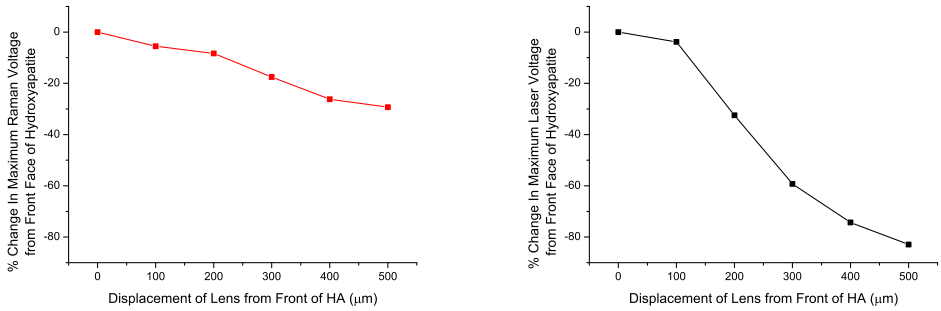

(a) (b)

Fig. 4.9 These graphs demonstrate the percentage change in maximum voltage in the Raman signal with displacement from the front face of fused hydroxyapatite at a lock-in sensitivity of 5 mV and time constant of 100 ms in 4.9a and the laser signal with the same displacement and lock-in sensitivity of 500 mV and time constant of 100 ms in 4.9b, averaged over 50 measurements in each case and error bars representing standard deviation.

will produce a signal suitable for lock-in amplification. To further characterise this behaviour, the percentage change in laser and Raman signal were plotted with focal point position as given in Figure 4.9, which shows that the laser line intensity reduced at a faster rate with depth than the Raman signal. Therefore, Raman signal and laser signals have independent responses with depth, meaning that it may be possible to selectively amplify the Raman signal, rather than just amplifying the laser and Raman signal equally.

The next logical step in developing the spectrometer was to test to see whether the vibration of the focusing lens will generate an amplitude modulation in the laser line. This was performed by applying a sine wave input of 186 Hz to the controller for the piezoelectric lens and measuring the variation in the diffracted laser line amplitude over time using an oscilloscope. The results of this test as given in Figure 4.10 using AC coupling, demonstrated that driving the lens created a clear sine wave response from the laser line. Therefore, lens vibration will provide a sufficient signal for lock-in amplification.

4.4 Spectrometer Design

After confirming that focal point depth has the properties required for lock-in amplification to isolate the laser interaction signal from background noise, along with the potential for discrimination between laser line and Raman spectra, the spectrometer was set up to use lens vibration as the driving modulation methodology.

Firstly, the the chopper was removed from the beam line; next the static lens mount was replaced with a lens containing a set of piezoelectric crystals. Piezoelec-

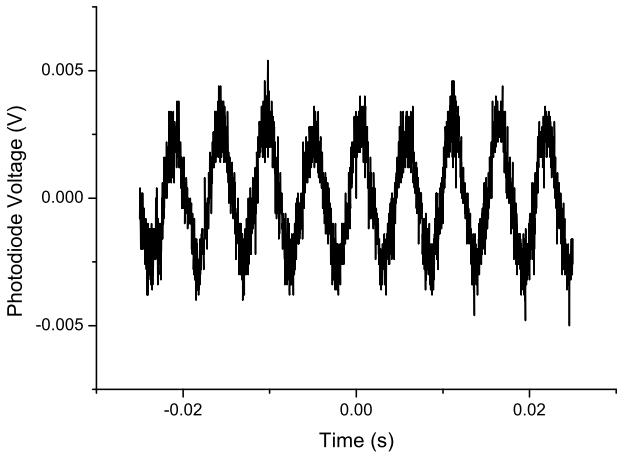

Fig. 4.10 Graph of diffracted laser voltage output from photodiode with lens vibrating with no amplification.

tric crystals exhibit the property of changing length when a voltage is applied across them. Therefore, in the mount they allow for a variable, well controlled position shift to be applied to the mount, the lens it contains and therefore the laser focal point. The lens controller which applies high voltages to the piezoelectric crystals to induce movement is provided with a TTi TG320 function generator, which is all supplied as the reference signal to the lock in amplifier. This set up is described in Figure 4.11, which is the same as used in the preliminary study, apart from the change from a chopper to the lens vibration element.

As in the preliminary experiment, silica was used for collecting pilot spectra with the spectrometer. The lens was vibrated at a frequency of 186 Hz (although the specific frequency is not of direct importance to the measurement) using a mean lens-driving voltage of approximately 60 V. The photodiode was aligned to the diffracted laser line for this measurement. Initially, silica spectra were collected at 5 mV sensitivity, 100 ms time constant and a single spectral measurement per point collected as soon as the photodiode reached each position on the translation stage. As shown in Figure 4.12, this spectrum appeared to demonstrate Raman silica features extracted from a noisy background. Next, improvements were made to the signal. Firstly, the spectrometer alignment was performed in order to increase the signal intensity in the Raman spectrum. Additionally, the LabView program was updated so that the data collection from the lock in amplifier was performed after one time constant had elapsed. Therefore, the data collected should be purely the lock-in amplified signal from the discrete position at which the photodiode is placed. This improvement should improve spectral quality and validity. Finally, lock-in amplification parameters were altered, sensitivity was increased to improve

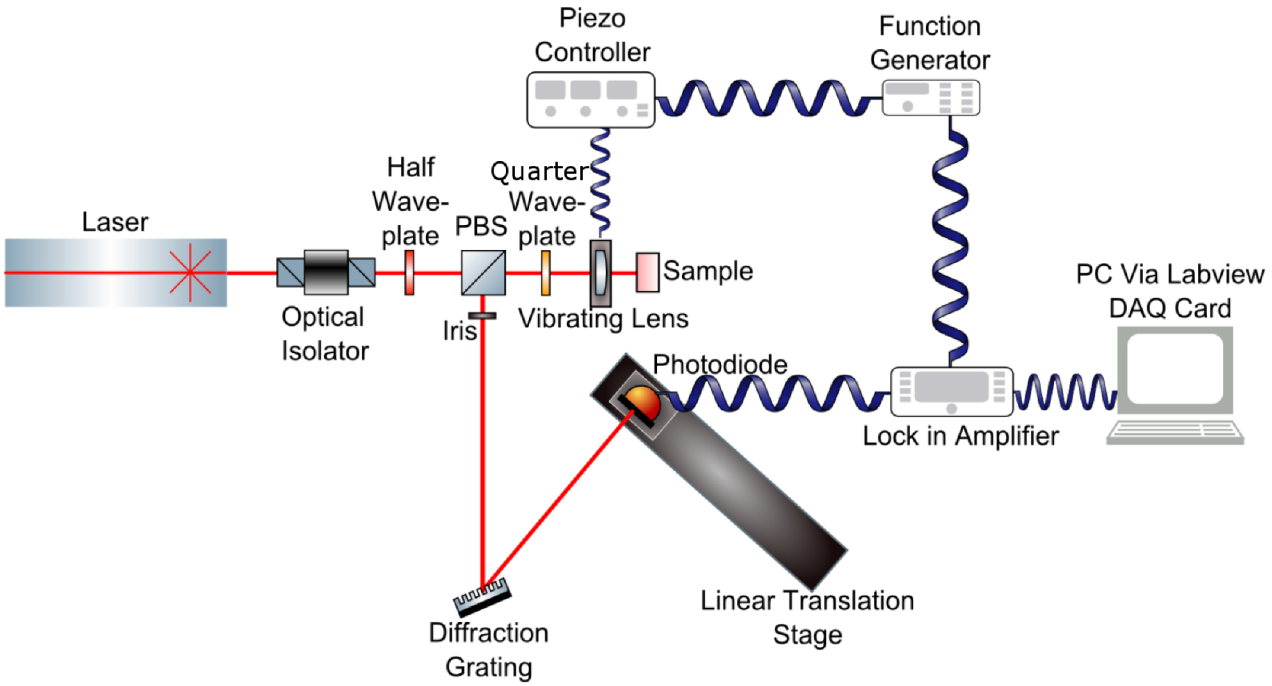

Fig. 4.11 Diagram of optics set up for the lens vibration lock-in amplified Raman spectrometer.

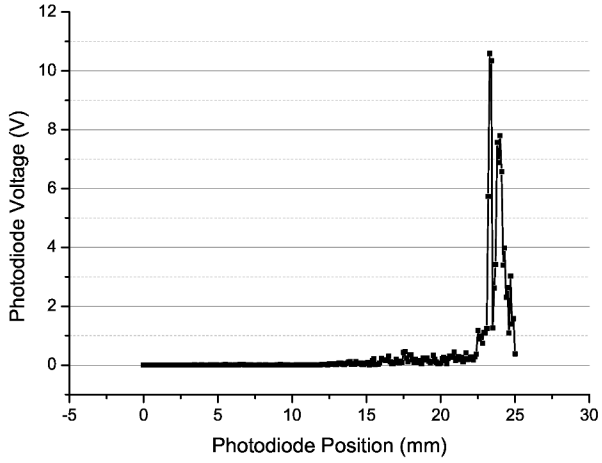

Fig. 4.12 First silica spectrum collected with the lens vibration lock-in amplified spectrometer. The spectrum was collected at 5 mV sensitivity and 100 ms time constant, with a single measurement made at each photodiode position.

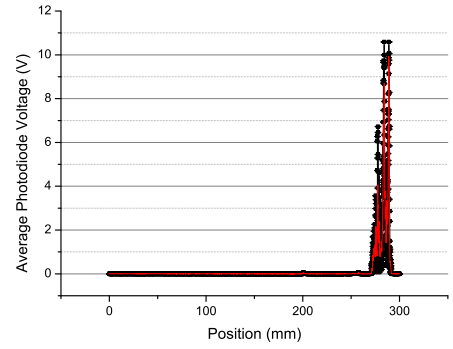

(a)

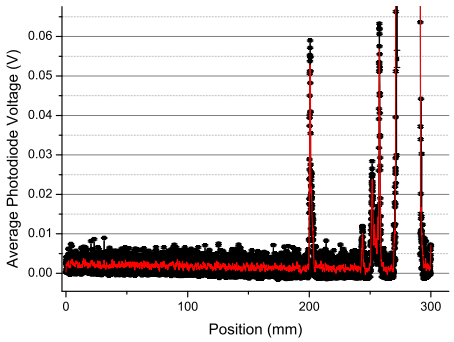

(b)

Fig. 4.13 The graphs show the Raman spectrum of silica collected at 50 measurements per point, 2 mV lock-in amplifier sensitivity and 200 ms lock-in amplifier time constant. The red line is an adjacent average with a window of 11 points, designed to produce a smoothed spectrum to allow spectral features to be easily identified. Figure 4.13a shows the full spectrum, with Figure 4.13b showing the same spectrum with over the range $0 - 0.0675$ V

the amplification of the Raman signal and the time constant was increased to improve the filtering effect provided by lock-in amplification. After these alterations, a new silica spectrum was collected at 50 measurements per point, 2 mV lock-in amplifier sensitivity and 200 ms lock-in amplifier time constant. The spectra collected, given in Figure 4.13 appeared to show a small Raman spectrum after the laser line. Therefore, the lock-in amplification process by lens vibration appeared to produce a Raman spectrum with low background interference. A key concern was that the generated spectrum was an artefact. Therefore, the first priority after this spectral collection was to confirm that this spectrum was not an artefact and was sample-dependent. This step was performed by collecting a glass spectrum from a glass microscope slide (Fisher Scientific, UK), as given in Figure 4.14. As expected, there were significant differences between the two spectra, indicating that the spectra generated are genuine.

In order to further confirm the validity of the spectrometer two further con-

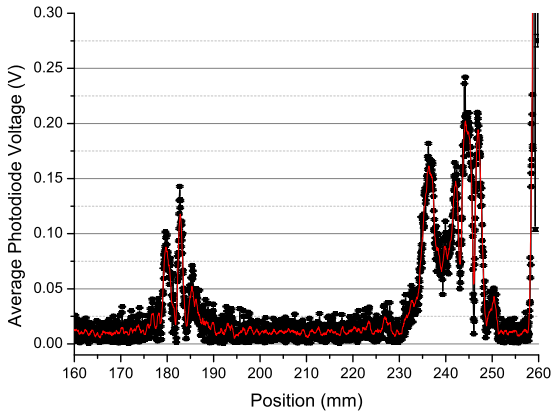

(a)

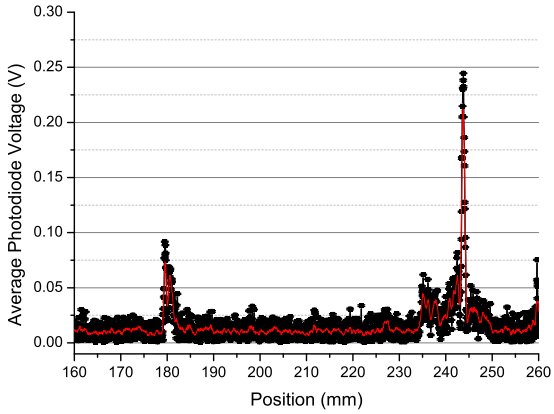

(b)

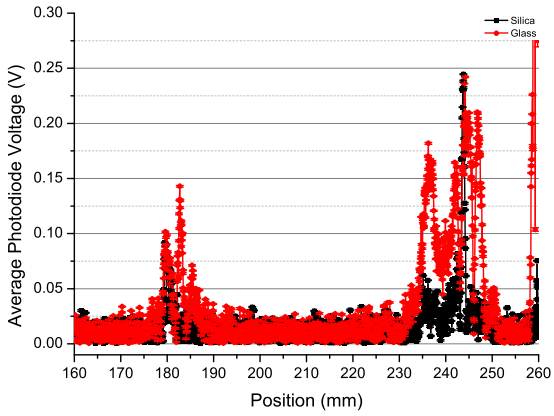

(c)

Fig. 4.14 The graphs show the Raman spectrum of silica and glass collected from separate time points at 20 measurements per point, 500 μV lock-in amplifier sensitivity and 200 ms lock-in amplifier time constant. The red line is an adjacent average with a window of 11 points, designed to produce a smoothed spectrum to allow spectral features to be easily identified. 4.14a shows a glass spectrum, 4.14b shows a silica spectrum and 4.14c shows the glass and silica spectra on the same axis for direct comparison.

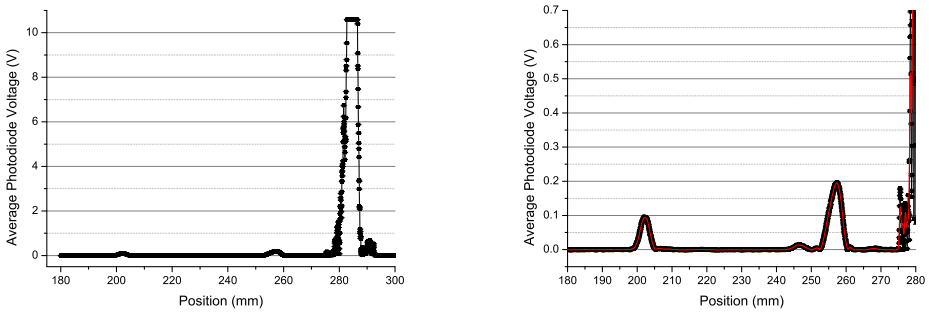

(a) (b)

Fig. 4.15 Spectrum of the ThorLabs LDM785 laser reflected straight from the PBS to the diffraction grating. The spectrum was captured with lock-in amplification to a chopped laser signal at 5 mV sensitivity and with a 200 ms time constant and is generated from an average of 20 measurements per spectral point. The red line in Figure 4.15b is an adjacent averaging smoothing function with a window of 11 points.

firmation spectra were collected. Firstly, the spectrum of the laser light diverted directly into the spectrometer through the PBS was collect. Doing this allowed for a spectrum of the laser light after passing through a minimal number components to be collected and examined using a chopping set up rather than lens vibration, using a lock-in sensitivity of 5 mV and 200 ms time constant. As Figure 4.15 shows, the spectrum of the laser line did not contain the same structure seen in the silica Raman signal. This indicated that the spectra collected from the silica is a Raman spectrum of the silica sample. Next, a spectrum was collected from the reflection of the laser with a mirror positioned in the z-translation mount. This measurement was performed to test if the observed spectral features were due to interactions with the optical components or the laser band structure. The spectrum from the mirror was collected using the lens vibration set up with the lock-in amplifier set to have a sensitivity of 5 mV and a time constant of 200 ms. As shown in Figure 4.16, this spectrum appeared to show similar elements to the silica spectrum. This suggests that either the optical components are strongly emitting a Raman signal (which could be due to the counter propagating beam pattern) or that the silica surface behind the aluminium mirror face is emitting a Raman signal. From the spectra collected from glass, laser, and reflection from a mirror, it becomes clear that the silica spectrum is not a product of the laser or the optics background. Therefore, it is possible to move forward with characterising key materials, confident that the spectrometer is producing valid data.

After the verification that the spectrometer was producing Raman spectra, the next step was to improve the accuracy of the wavenumber calculation, and therefore, the accuracy of the spectra. Firstly, the laser wavelength was measured by

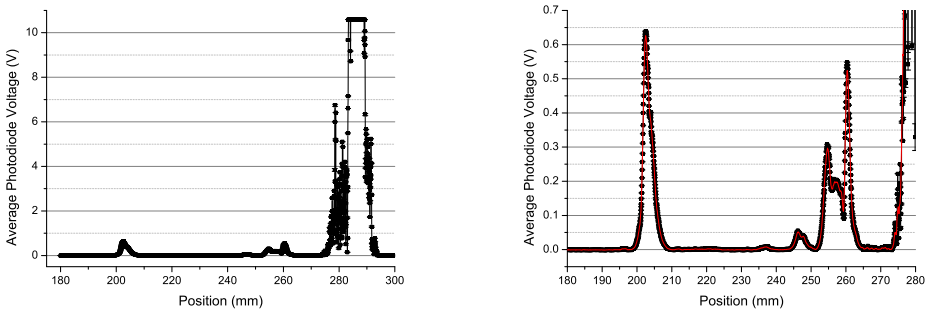

(a) (b)

Fig. 4.16 Spectrum of the ThorLabs LDM785 laser reflected from a mirror placed in the z translation sample mount. The spectrum was captured with lock-in amplification to the lens vibration signal at 5 mV sensitivity and with a 200 ms time constant and is generated from an average of 20 measurements per spectral point. The red line in Figure 4.16b is an adjacent averaging smoothing function with a window of 11 points.

simply tapping the initial small beam reflected at the PBS into a wavemeter for measurement. By doing this, a more accurate value for the wavelength than a manufacturer estimate can be found and used in calculating the wavelengths of the Raman shifted light. This is a vital step, as calculating accurate wavenumber shifts based on diffraction using the method outlined above is highly dependent on knowing the laser wavelength. The wavelength of the laser was measured using a Advantest (Munich, Germany) TQ8325 Digital Optical Wavelength Meter over 53 minutes and 20 s as shown in Figure 4.17. This measurement shows that the laser wavelength jumps twice during a warm up period, before settling after around 21 minutes. After the wavelength has stabilised, it was measured to be 788.8 nm, as shown in Figure 4.17. Secondly, improvements in alignment were performed as the signal is very dependent on the fine alignment of the system. An alignment protocol of aligning to the laser line, then the Raman signal iteratively was employed to maximise the Raman signal measured with the system. After this procedure, the grating angle was measured using a protractor to produce the ϕ in equations 4.18 and 4.21.

4.5 Spectral Collection Using Lock-In Amplification

4.5.1 Silica Raman Spectra

Silica spectra were collected from the Raman spectrometer using a piezoelectric modulation signal of approximately 60 V at 180 Hz to 200 Hz. To standardise

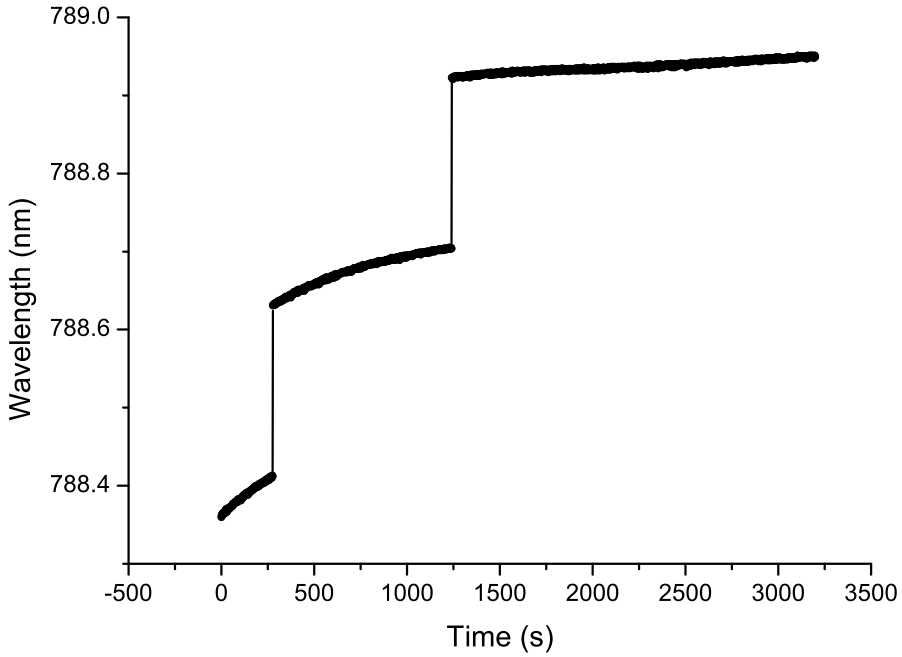

Fig. 4.17 Graph of the laser wavelength variation with time over 53 minutes immediately after initial laser start up.

measurements as much as possible the diffracted laser line was positioned to strike the detector at around 280 *mm* from the translation stage origin. The silica sample was set up in the spectrometer with the laser focused onto the front face of the sample for spectral collection. This positioning was determined by focussing the laser to the smallest possible beam width at the grating using a beam card, and ensuring that the beam travels in the center of the cage for the full travel distance out of the PBS. When the laser needed to directly strike a face of the silica, as well as alignment by sight, the focal point position was adjusted to maximise the power detected at the diffraction grating with a ThorLabs PM30 power meter. In order to generate the best quality silica spectra, the spectrometer was aligned so that the first component of the silica Raman spectrum was maximised. To do this, the spectrometer was aligned so that the diffracted laser entered the detector at approximately 280 *mm*, then a quick spectrum would be collected to confirm the position of the first clear silica spectral feature. After determination of the position of the spectral feature, the detector would be moved to this position and the diffraction grating rotated so that the diffracted laser line would illuminate the detector. The position of the detector in terms of the height, angle and input slit were then adjusted to maximise the signal from the laser. After this optimisation procedure was completed, the detector was moved to the position of the laser line in the previously collected spectrum and the diffraction grating rotated to produce the largest possible signal

at the detector. After this step, a high quality spectrum could be obtained. As the spectrometer was kept approximately consistent over the experimental procedure, standard Raman peak positions with respect to a diffracted laser position of 280 mm were identified. Therefore, the need to capture a new spectrum as part of the alignment process was not always necessary, except in trying to observe iterative improvement in collected spectra.

After spectral collection, the detector was moved to the position of the diffracted laser and the distance between the diffraction grating and front slit on the detector was measured with a tape measure. A tape measure was selected as an appropriate instrument for this measurement as the distance between the detector and grating was around 300 mm. The value of ϕ was then determined by using a protractor and was measured as $(17 \pm 1)^{\circ}$.

In the silica data collection step, lock-in amplifier settings have a strong influence on the spectrum collected by the instrument. Therefore, these settings should be carefully selected and should be chosen to be complementary to the lens vibration frequency. The lock-in amplifier time constant effects the low pass filtering and averaging effects of the lock-in amplifier and needs to cover multiple oscillations of the reference frequency. Considering an oscillation at 186 Hz, one complete oscillation of the lens is performed every 0.0054 s; therefore, the time constant needs to be much larger than this value. The larger the time constant, the better the low pass filter and the noise removal, but the longer the time taken to perform the measurement.

In biological systems, the laser exposure should be minimised not only to reduce the probability of laser damage to the sample, but also to reduce the time that the cell culture is exposed to a sub optimal environment, potentially outside of an incubator and in a non-feeding medium. Therefore, there is a trade off between signal quality and viability of the measurement process. In this experiment, a variety of time constants were tested. It was found that using a time constant of 200 ms was a good compromise between a short measurement interval and high spectral quality. In this experiment, R^2 was used as the lock-in amplifier output in order to minimise phase dependence and maximise signal recovery. Therefore, phase selection was relatively unimportant and was tuned by using the lock-in amplifier's auto-phase feature whilst the lock-in amplifier was receiving the laser line signal. The final key selection of lock-in amplifier parameter is the sensitivity of the measurement. Sensitivity determines the size of fluctuation the lock-in will consider significant. If this parameter is set to be too high, the output signal will be saturated. However, if it is too low, the small Raman features will not be extracted from the background. The initial selection of appropriate sensitivity was a process of trial and error. A starting point was selected to be of the order of mV, a factor of 10^3 less than

the laser line signal collected from the detector. This was selected as, although the Raman signal is of the order of 10^9 smaller than the laser irradiance, the laser line saturates the detector, and the fluctuations in Raman signal were seen to be significant through the chopping processes applied previously.

Firstly, spectra from silica with lock-in amplification parameters of 500 μV sensitivity and a time constant of 200 μs were collected, with a lens vibration of the order of 200 Hz used as the lens driving oscillation. The lock-in amplifier parameters are ultimately a compromise in terms of the selected sensitivity and time constant. The sensitivity should be selected as a compromise between signal intensity and noise, with the time constant selected as a compromise between speed and noise reduction. As discussed previously, the sensitivity parameter identifies the size of fluctuation that the lock-in amplifier identifies as signal. A sensitivity which is set to be too high will not isolate the required Raman signal, but if the sensitivity is too low, spurious background signals will be identified. The best fit parameters are found by trial and error in this case. Similarly, the time constant parameters were selected to give the best signal quality with the shortest required scan time. In order to be able to calculate the wavenumber shift scale for the Raman spectrum several parameters needed to be collected. Firstly, a Gaussian fit was applied to the collected non lock-in amplified spectrum to find the laser line position to enable the distance between the laser line and every other position on the translation stage (x in Figure 4.4) to be calculated. Next, the distance from the detector to the diffraction grating was measured with the detector set to the position of the laser line maximum intensity (y in Figure 4.4) and the angle of the diffraction grating was measured using a simple protractor (ϕ in Figure 4.4). These parameters were then substituted into equations 4.21 and 4.22 to calculate the wavenumber scale for the spectrum.

After collecting a satisfactory initial silica spectrum, the stability and reproducibility of spectra were investigated by measuring the variation in laser line, Raman peak and background signals over time and by comparing spectra collected over a period of many hours. To conduct stability measurements, a simple LabView script was created to read voltages in from the DAQ device at a specified rate for a defined length of time, then write the time and voltage data into a CSV file. The first stability measurement made was the laser line signal. A silica spectrum was collected and the position at which maximum voltage was measured from the laser was found. The translation stage was moved to this maximum voltage position and the non-amplified voltage signal from the photodiode was measured once per second every second for 90 minutes. The data was then processed and a linear fit was applied to fit the rate of change of the voltage. Next the reference spectrum was used to find the position of a Raman peak on the translation stage and the lock-in amplifier voltage (500 μV sensitivity, 200 ms time constant) was measured once a

second every second for 90 minutes and a line of best fit to this measurement found. Finally, the photodiode was positioned at 150 mm on the translation stage, a position with no detected Raman or laser signal, and the lock-in amplified voltage (500 μV sensitivity, 200 ms time constant) was measured as before, and the line of best fit to this data found. In order to examine spectral reproducibility, three spectra were collected at 0 hours, 44 hours 48 minutes, and 49 hours 58 minutes. The aim of this measurement was to examine the consistency of spectra over time and between operations of the spectrometer. Spectra were collected for this measurement with the lock-in amplifier operating with 500 μV sensitivity and a time constant of 200 ms, along with the corresponding raw photodiode voltages. The grating-angle and grating-detector separation were measured to be used to calculate the wavenumber scale when combined with the laser line position measurement. Throughout the experiment, the spectral alignment was kept constant so that position measurements as well as wavenumber measurements could be compared.

Next, a second depth study was conducted to examine how the Raman spectra of silica changes with depth when lens vibration lock-in amplification is used. In this experiment, Raman spectra were collected at 200 μm intervals starting with the laser focal point at the front face of the silica sample and moving through the sample bulk. The front face was found by maximising the power at the diffraction grating using the power meter. Spectra were collected with the lock-in amplifier operating at 500 μV sensitivity and with a time constant of 200 ms examining changes with focal point depth through 2 mm of sample thickness. The grating angle during this experiment was measured to be $(17 \pm 1)^\circ$ with a detector-grating separation of (285 ± 1) mm. The wavenumber scale was calculated individually for each step.

4.5.2 Hydroxyapatite Raman Spectra

Hydroxyapatite spectral collection was a key stage in the spectrometer development pathway. Firstly, it acted as a proof of concept step through moving away from translucent samples and proving that the lens vibration principle is a universally applicable method for lock-in amplification. Additionally, hydroxyapatite in substituted forms is the key mineral component in bone. Therefore, in studying mineralising cell cultures, a key aspect of interest is the detection and evolution of hydroxyapatite and other calcium phosphate compounds. Therefore, using hydroxyapatite as the non-translucent test sample also acts as a proof of concept for using the spectrometer to be able to detect a key material relevant to the biological process of interest in this work.

Three different forms of hydroxyapatite were analysed using Raman spectroscopy in this study. This step was performed as it allows a test of whether the spectrom-

eter can distinguish subtle differences between samples of what is classified as the same material in altered forms. A fused hydroxyapatite disc was the first sample to be examined, as it had a smooth polished surface to allow for easy alignment and would be uniform in composition through the vibration step, potentially producing the strongest signal and therefore, a convenient starting sample. The second hydroxyapatite test sample was a porous sample, in many ways this represents the trabecular nature of bone with a porous network of mineral and so acts as a simulation of biology. Additionally, it is a similar structure to those being postulated for use in bone tissue engineering so allows a rough test of whether Raman spectroscopy could analyse constructs of this form. The final hydroxyapatite sample was a powdered form. This allowed for a rough simulation of the small crystals which will be the initial form of hydroxyapatite in cell culture, testing whether the lens vibration technique is suitable for a non-bulk sample.

Fused hydroxyapatite (Plasma Biotal, UK) was initially tested as it allowed for the application of roughly the same alignment process as used for glass and silica, making the alignment procedure a more straight-forward task for an initial analysis. The laser return from the sample was much reduced in comparison to the silica signal, so the sensitivity and time constants used with the lock-in amplifier were increased in comparison to those used for silica spectral collection. An initial hydroxyapatite spectrum was collected with 500 μV sensitivity and 200 ms time constant with a grating angle of $(19 \pm 1)^{\circ}$ and a photodiode-grating separation at maximum laser line intensity of (285 ± 1) mm. Next, without changing the alignment so that the wavenumber scale would be constant, a spectrum was captured just over the Raman signal at an increased sensitivity of 200 μV and an increased time constant of 2 s, and then at 50 μV and 5 s to see if spectral quality was improved.

After refining the fused hydroxyapatite spectra, the porous hydroxyapatite sample (Plasma Biotal, UK) was interrogated with the spectrometer. Porous hydroxyapatite spectra were initially collected at a sensitivity of 100 μV over a full spectrum. These parameters were chosen to allow for a representative initial spectrum to be collected based on the parameters used for fused hydroxyapatite. After producing this initial spectrum, the distance between the detector and grating at maximum laser intensity was found to be (285.0 ± 1) mm and the grating angle was measured at $(19 \pm 1)^{\circ}$ and a wavenumber scale was calculated. The spectrum collection was then repeated over the Raman region for an increased sensitivity and time constant of 50 μV and 2 s to produce a strong and clear spectrum for the porous sample of hydroxyapatite. This repeat was required as the previous parameters did not fully capture a Raman spectra. Therefore, increasing the sensitivity was required to increase the amplification provided and increasing the time constant was required to improve the averaging.

Finally, the more challenging powdered hydroxyapatite (Plasma Biotal, UK) sample was analysed with the spectrometer. In order to mount the powder for analysis, a back piece of plastic was prepared and coated by a standard optics adhesive; the hydroxyapatite powder was applied onto the adhesive surface and left to set. In the application process, enough powder was applied to create a layer, with no exposed adhesive. After the setting process was complete, the sample was loaded into the spectrometer, with alignment performed in terms of maximum power at the grating and to the diffracted laser line only. The laser spot returned from the hydroxyapatite to the diffraction grating was stronger than for the porous sample, so initial spectral collection parameters of 200 μV sensitivity and 0.5 s time constant were selected. The full spectrum was collected with a detector-grating separation of (285 ± 1) mm at a grating angle of $(19 \pm 1)^\circ$ and the wavenumber scale calculated. These collection parameters were found to generate a clear spectral signal from the sample and so no further spectra were collected.

4.5.3 SEM Prepared MSC Culture Raman Spectra

The first organic sample to be analysed with the Raman spectrometer was a sample of MSCs cultured under osteogenic conditions fixed and prepared for SEM. This sample was selected as a test case because SEM prepared samples are coated with gold, so are stable at standard conditions and can withstand continued exposure to air without the need for a liquid medium. Therefore, for the initial spectrometer development working with a stable cell culture, whilst not fully reflective of the exact biology of a living system, will allow for a consistent sample to be analysed whilst the spectrometer is adjusted to suit the requirements of biological analysis. Additionally, although the cell cultures in this form are not living, the cells and ECM deposited during growth should be preserved. Therefore, using this form of cell culture it should be possible to ascertain whether the spectrometer is powerful enough to distinguish between mineralised and non-mineralised MSC cultures, a key requirement for the instrument.

In order to analyse the SEM prepared cultures, the prepared samples were attached to lens mounts and inserted into the spectrometer optical set up. The sample was focused to produce the clearest spot at the diffraction grating and initial spectra were collected from an osteogenic sample at settings of 10 measurements per point, 50 mV sensitivity and 2 s time constant, analogous to optimal spectral collection conditions for porous hydroxyapatite spectrum. Spectra were then obtained at 200 mV sensitivity and 200 ms time constant to see if a faster acquisition could generate an acceptable spectrum. Spectra were then obtained from the gold coated carbon sticker and the gold coated Alvetex® to identify whether the cellular Raman

spectrum is being detected, rather than the background. These spectra were both collected using the initial spectral collection parameters for the osteogenic sample, to provide an equivalent point of comparison between signal and potential confounding noise features. Spectra were then obtained from a non-mineralised cell culture, again using the same spectral collection parameters, to try to ensure a high quality spectrum was generated. Next, the depth dependent behaviour of the Raman spectrum in the osteogenic cell culture was investigated to see if the laser could penetrate through the cell surface. The spectra were collected at five 10 μm increments, 10 measurements per point, 50 μV sensitivity, and a 200 ms time constant for speed of analysis.

Initial spectral analysis found an exceptionally strong Raman return from the SEM prepared samples. This could be due to the layer of gold coating acting in a similar way to a surface enhanced Raman experiment and enhancing the Raman signal from the samples. During this portion of the work it was found that removing the beam compressor improved the transmission through to the sample, leading to a reduction in required lock-in amplification parameters. Optimum spectral collection parameters for the SEM prepared cell cultures were found to be 10 measurements per point, 500 mV, and 200 ms time constant.

4.5.4 Scanning System Design

After achieving positive results with the spectrometer for inorganic and cellular samples, a sample scanning system was developed for the spectrometer. This was developed so that Raman mapping might be applied to cellular samples, either by collecting full spectra at multiple points over an area of a sample to allow examination of changes in the whole spectrum or by examining how a single Raman signal alters over a sample area. By mapping changes in a spectrum over a defined area, it will be possible to produce images of the location of molecules or molecular groups indicated by the spectral component over a sample.

The scanning system was constructed from 2 Thorlabs 300 mm translation stages bolted together at right angles to produce two dimensional movement of a sample horizontally and vertically in front of the lens, as shown in Figure 4.18. These stages have the ability to scan with a maximal scan resolution of 5μm in both dimensions. The next step was to set up a LabView program to control the system and to trigger the collection of the relevant spectral data at a series of points over a sample. The first program developed was designed to collect data in the simplest case where a single spectral point is tracked over a 2D scan of a sample. This system initialised the photodiode to the correct position, then selected the start point of the scan, and consequently collected a number of values of the spectral component for every

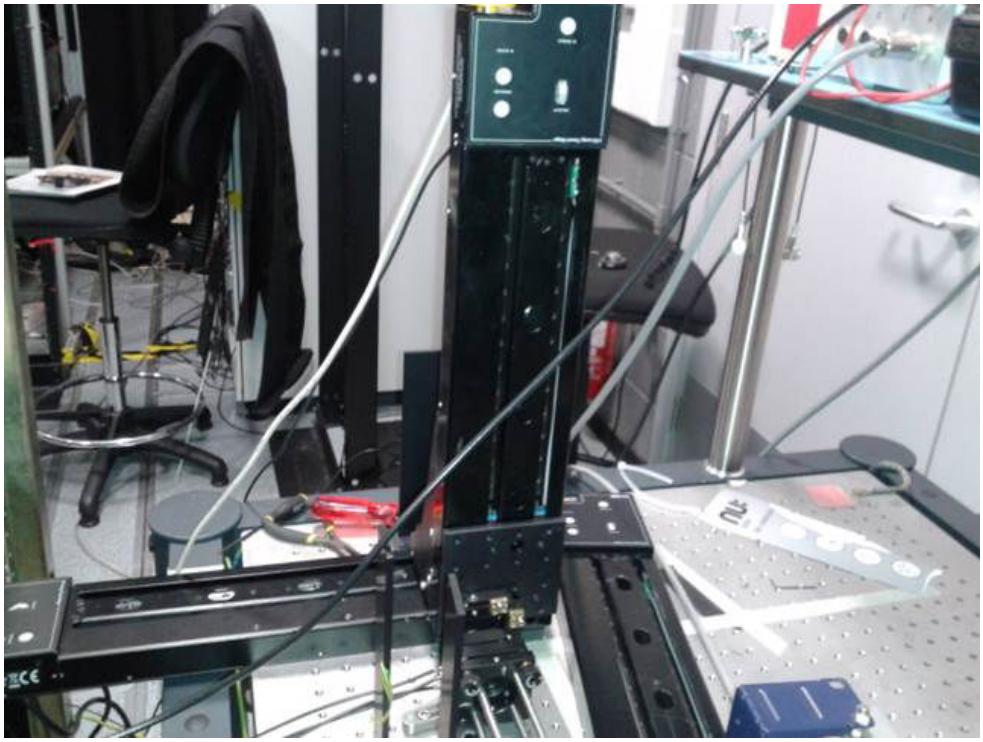

Fig. 4.18 Photograph of the translation stage set up used to translate the cell cultures and acquire Raman signals from across their surfaces.

position required in the scan. The second program collected full spectra over a 2D scan of the sample and could be manipulated to allow single spectral point data to be quickly mapped.

To define the scanning parameters, firstly, the spectral position of interest or full spectrum start and end points (in mm) were determined and entered into the scanning program control. Next, the starting position of the sample was found by manipulating the position of the translation stage to set the laser spot on the required spot on the sample, and the number of movements and step size in each direction entered into the program. Once these parameters had been defined, the scanning program was started, repeated measurements were collected as in for previous spectra, and the voltages measured from the lock-in amplifier written into comma delimited files.

Mapping Data Analysis

Using a scanning system creates a large data set for manipulation, particularly when full spectra are being collected. Therefore, data processing must be automated rather than manual, otherwise a great deal of time would be required to produce a passable analysis. As a result, a program must be written in order to process the data and plot it into a graphical form for interpretation. In this work, analytical processing was done using python scripting augmented by the matplotlib library

[273]. For full spectra collected at each position, data acquired at each photodiode position needed to be averaged, then condensed into a spectrum for plotting. The series of spectra can be presented as a density or waterfall plot to represent the material composition over a defined line of the material. From this representation, it is then possible to extract values from individual spectral positions and plot how they vary across the material in the form of a wire mesh plot or density map, in a simulated 3D space. In a density map the numerical intensity values measured at a specific spectral point at each position are represented by a colour value.

Raman Mapping SEM Prepared MSC Cultures

Raman mapping of SEM prepared cell cultures was a straightforward process after the creation of the scanning system software as it is simply an extension of the previous technique for scanning. The sample to be scanned was mounted on a lens mount and screwed into an 1" optics component mount bolted to the translation stages. At the start of the scan, the resolution, and length in each dimension were defined, then the starting position selected through the user moving the stage to line the laser and sample up as required. The initially defined position is read directly from the stages by the program and used to calculate the required positions for spectral collection. Finally, the stages are translated to the required positions and data collection executed in a fully automated process.

Mapping was performed initially in 1D, with full spectra collected along a line of the culture using automated translation of the cell culture. Initially, data was captured for an osteogenic cell culture along a 5 mm line with spectra captured at every 0.25 mm using a sensitivity of 200 mV, time constant of 200 ms, and 10 measurements per spectral point. This process showed that there are spectral changes which can be mapped across the surface of the cell culture as detailed in Chapter 5 Figure 5.62. Therefore, to try to map the variation of certain spectral points along the line, data was stripped from the full spectra collected along the 1D line for estimated wavenumbers of: 703.86 cm^{-1} (277.25 mm), 970.79 cm^{-1} (268.35 mm), 1210.2 cm^{-1} (259.40 mm), and 2149.1 cm^{-1} (215.00 mm) as calculated by averaging the wavenumbers for data collected at a single spatial collection point across all points on the sample. Next, automated collection of spectral data at a single spectral point was performed along a 1 cm line, with the detector fixed at 215 mm and 260 mm relative to the translation stage, which approximately corresponded to a wavenumber shifts of 2149.1 cm^{-1} and 1194.6 cm^{-1}. The 1D intensity maps were collected with a resolution of 10 μm for both spectral positions, 200 μV sensitivity, and 200 ms time constant. Next, the benefit of increasing resolution was tested by repeating the map at 2149.1 cm^{-1} at a resolution of 1 μm.

After validating that the spectral collection program worked in the 1D case, spec-

tra were then collected in 2D. The map was collected at an estimated wavenumber shift of 2149.1 cm^{-1} over the osteogenic sample. The spectral map was acquired over a 2x5 mm area using a 10 μm resolution, using the lock-in amplifier with 200 μV sensitivity and 200 ms time constant.

4.6 Development of a CCD Lens Vibration Raman Spectrometer

After the prototype spectrometer had been developed and tested, the next stage in the process was to translate the effect into a more conventional spectrometer set up. The use of photodiode and translation stage is excellent in providing a proof of concept spectrometer as lock-in amplification can be applied point by point to the spectrum. Therefore, it allows for fast verification of the augmentation to Raman spectroscopy. However, as a working analysis tool, this system has several drawbacks. Firstly, there is a reliance on a large number of assumptions to calculate the Raman shift wavenumbers, which will add a level of uncertainty and error into the measurements. This is due to the use of the protractor to measure the grating angle, the assumption that the stage is perpendicular to the laser line, and due to the fact that the dispersion of the Raman spectral feature will trace out an arc, not a line. Of these, the biggest source of error is due to the fact that the spectral features trace out an arc, meaning that trigonometric approximation introduces the greatest error. Secondly, There is a long associated time with performing the step-measurement method. Each full Raman spectrum takes 20 minutes to collect, which is much longer than a commercial system.

To attempt to provide a proof of concept that the lens vibration system can be used with commercial systems, the step scan method of spectral collection was changed to a charge-coupled device (CCD) array. To provide a CCD array a Thorlabs CCS175/M compact spectrometer was purchased and placed in the spectrometer set up, replacing the diffraction grating, photodiode and linear translation stage. The compact spectrometer comes pre-calibrated and can measure wavelengths in the range of $500 - 1000$ nm with a resolution of 0.167 nm, which represents a large advantage over the prototype system as the wavelengths of the Raman light can be accurately measured by the instrument without the need of approximations. The compact spectrometer contains a fixed diffraction grating with 830 lines/mm to disperse the light into its constituent wavelengths and a CCD of 3648 pixels to detect the light. Each CCD pixel has a fixed position with respect to the diffraction grating. Therefore, the initial calibration of the device by the manufacturer will produce consistent, accurate wavelength measurements which can easily be converted into

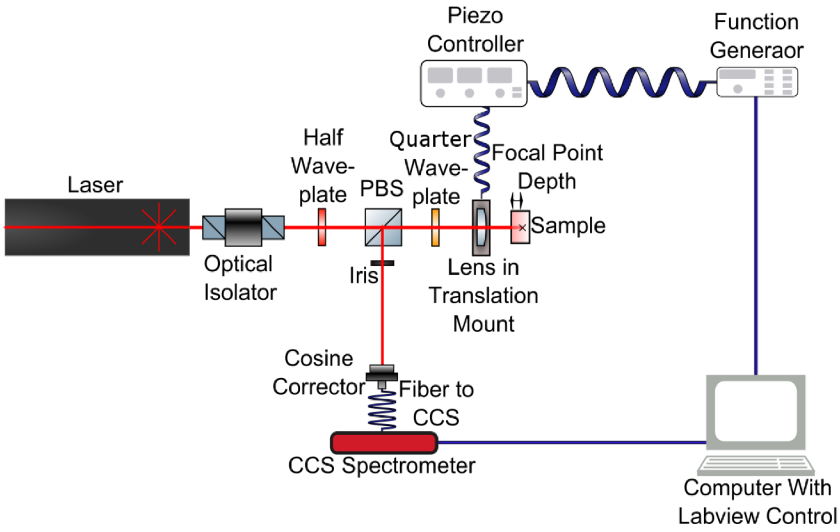

Fig. 4.19 Diagram of final spectrometer build with Thorlabs CCS compact spectrometer.

wavenumbers. A schematic is detailed in Figure 4.19, demonstrating the incorporation of the spectrometer into the existing optics set up. As can be seen in the diagram, the diffraction grating and previous light collection apparatus are replaced by a cosine corrector (Thorlabs LTD, UK), which launches the Rayleigh and Raman scattered light, even that which is not tightly collimated, into the spectrometer.

The main problem which needed to be tackled in this design was how to lock-in amplify the signal from the CCD. The CCD collects a full spectrum in one go, so in order to lock-in amplify in real time a multichannel lock-in system would be required. Using multi-channel lock-in amplification would be extremely expensive. Therefore, an alternative could be to use a simulated lock-in amplifier. However, this would be very difficult without a large amount of computing power and would be inferior to using a physical device. As a result, the optimal solution is to perform lock-in amplification on a reconstructed signal generated from the data collected from the CCD. In previous experiments, the lens was been driven with a sine wave. Consequently, the intuitive way to perform spectral collection with the compact spectrometer would be to drive the lens with a defined sine wave, and sample the spectrum at a frequency greater than the Nyquist limit [274]. Unfortunately, this is not a feasible option, because the CCD would need to sample at 360 Hz, i.e. once every 2.78 ms, which is beyond the capability of the system. Also, even if the spectrometer could collect spectra quickly enough, the short integration time would result in the collected spectra being smothered by noise. Therefore, the input lock-in amplified signal cannot be collected at a native rate. As a result, the signal for lock-in amplification must be artificially constructed. The most convenient signal a lock-in amplifier can process is a square wave, in which a signal simply passes from one value to another at a set frequency, as demonstrated in Figure 4.20.

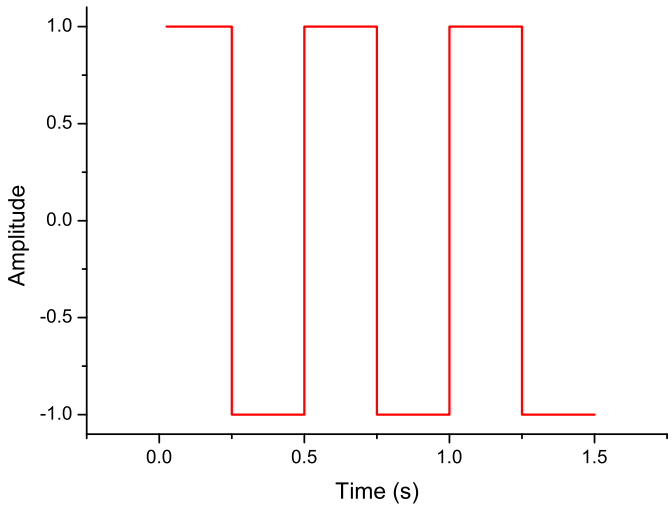

Fig. 4.20 Example of a square wave with a frequency of 2 Hz.

If a simulation of the signal for a chopper was desired, the procedure required would be to collect a set of spectra with the laser on, collect a set of spectra with the laser off, reconstruct these sets into a square wave signal, create a reference signal based on the properties of the constructed square wave, feed the simulated input and reference into a lock-in amplifier at a well defined rate, and collect the output. Similarly, the same process can be performed for the lens at two different positions as set by passing the piezoelectric mount a set voltage, aligning the lens to the front face of the sample, collecting a set of spectra, then applying a second voltage to the piezoelectric mount. From these two spectral sets a simulated square wave based on lens modulation can be generated and fed into a lock-in amplifier for analysis. Although this method seems complex on first glance, it is relatively simple to use once the required program design has been completed. Firstly a LabView program was developed in order to collect multiple spectra at a certain integration time collated into a single comma delimited file. A second LabView program was then developed to take two data files, process them together to form a square wave alternating between each data set and a corresponding reference signal. After generating the data stream and reference, the program output the two data sets at a defined frequency, creating a signal and reference oscillating at the same frequency to be inputted into the lock-in amplifier. The program reads in the lock-in output and saves it to a file. To allow for flexibility in data collection the overall output time of each pixel was set to be 2 s, a waveform 'size' of 20 samples per wavelength was deemed to be appropriate, a constructed wave frequency of 180 Hz was used and therefore an in/output rate of 3600 samples per second was selected.

Initially, a lock-in amplification based on a simulated chopped signal was per-

formed. To form the signal square wave, 10 background and silica spectra were acquired using a 50 s integration time. Next, each set of spectra were averaged together and interleaved to form a square wave to input into the lock-in amplifier. The data was processed at 10 mV sensitivity 200 ms time constant with the first 10 data points after one time constant had elapsed averaged together to form the final spectrum. It is worth noting that amplitude modulation is not able to remove the Raman background from silica in the optical set up. Therefore, this step was performed as a proof of concept to demonstrate that simulating an output could be successfully processed by the lock-in amplifier.

Next, lens vibration lock-in amplification was simulated. This was achieved by collecting spectra with the piezoelectric actuator on the lens mount displaced by two different voltages, then combining the data for both voltages at each spectral point, as for the chopped signal, to produce a waveform which is fed to the lock-in amplifier. In this case, the spectra were collected with 45 V and 75 V applied to the lens actuator, using five spectra at each voltage collected over an integration time of 50 s and averaged together. An output waveform was then constructed of 20 samples per wavelength (10 from each data set, made by duplicating all with five spectra), with the generated signal being output at a frequency of 180 Hz, and lock-in amplification applied with a sensitivity of $10mV$ and 200 ms time constant. The final spectrum was constructed by averaging the first 10 data points after one time constant at each spectra point.

To attempt to improve the final spectrum acquired after simulated lens vibration lock-in amplification, a dual-phase process was used. Firstly, the spectra at each lens position were individually lock-in amplified through a simulated chop to remove environmental noise. Next, the two lock-in amplified chopped spectra are output together as a square wave so as to produce a simulated pre-chopped, lens vibrated spectrum. In this case, 50 spectra were collected with a 10 s integration time for the background, 10 V piezoelectric displacement, and 90 V piezoelectric displacement. The spectra under each condition were averaged, generating one average spectrum from each set of 50. Initially, the spectra at each voltage were output as a square wave and lock-in amplified with the background data in a simulated chopped signal, with the lock-in amplifier set at 20 mV sensitivity, 200 ms time constant. Next, the lock-in amplified 'chopped' spectral data was normalised to a maximum voltage of 10 V (to prevent overloading the lock-in amplifier on the second pass) and the first 10 values for each spectral point after one time constant used to form the waveform for simulated lens vibration. Finally, the new simulated waveform was output and lock-in amplified at 500 mV sensitivity and 200 ms time constant to produce a final spectrum.

Chapter 5

Results

5.1 Conventional Analysis of MSC Cultures

5.1.1 Analysis of Statically Seeded MSC Cultures on Uncoated Scaffolds

Statically seeded MSC cultures on uncoated Alvetex® were analysed via staining of 2D MSC cultures along with wax embedded histological processing with staining, μ-CT, cryopreservation processing with staining, and SEM imaging.

Staining of 2D MSC Cultures

In order to examine the results of 2D culture, the cells were fixed in methanol and then imaged with light microscopy. Firstly, two wells containing mineralised cells and two wells containing non-mineralised cells were imaged with a microscope, as can be seen in Figure 5.1.

Next, staining for alkaline phosphatase activity with SIGMA FAST™BCIP/NBT (5-Bromo-4-chloro-3-indolyl phosphate/Nitro blue tetrazolium) was conducted as detailed in Section 4.1.2 and imaged with light microscopy as detailed in Figure 5.2.

Finally, the alizarin red stain was applied as detailed in Section 4.1.2 and microscope images collected within 10 minutes of stain removal to prevent leaching of the stain causing image artefacts. A selection of images of the alizarin red stained MSCs in 2D wells are given in Figure 5.3.

Histology of Wax Embedded Scaffold Samples

Scaffolds were wax embedded using standard histological techniques, sectioned at a thickness of 5 μm, mounted on slides and stained with haematoxylin and eosin as described in Section 4.1.2. Haematoxylin and eosin staining was performed on one sample cultured in proliferation medium, and one sample cultured in osteogenic

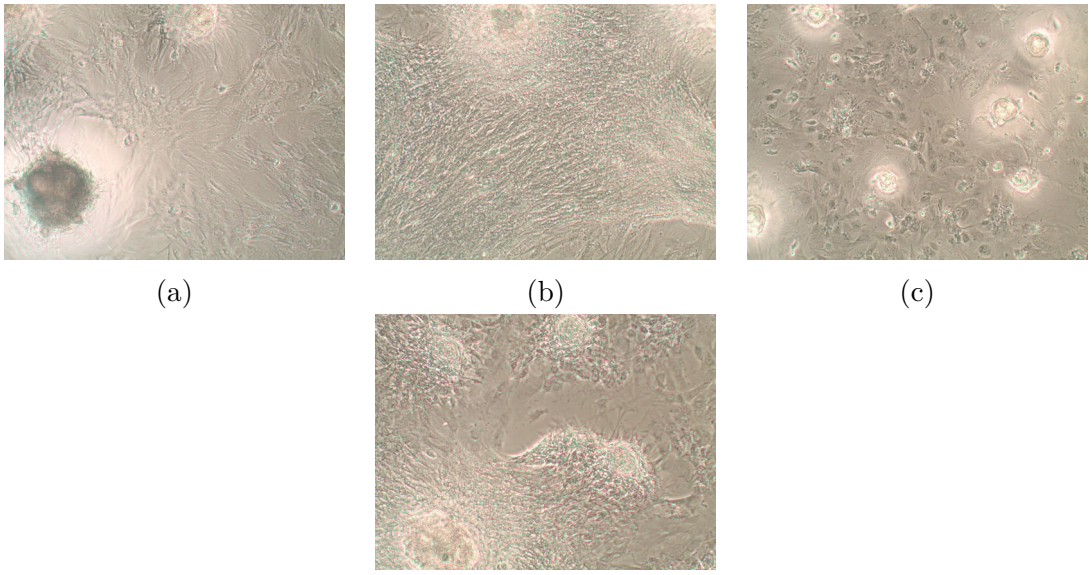

(a) (b) (c)

(d)

Fig. 5.1 Microscopy images of cells with no staining in 2D well cultures of MSCs. Cells cultured with proliferation medium at 5.1a 20× magnification and 5.1b 10× magnification. Images of cells in wells cultured with osteogenic medium at 5.1c 20× magnification and 5.1d 10× magnification.

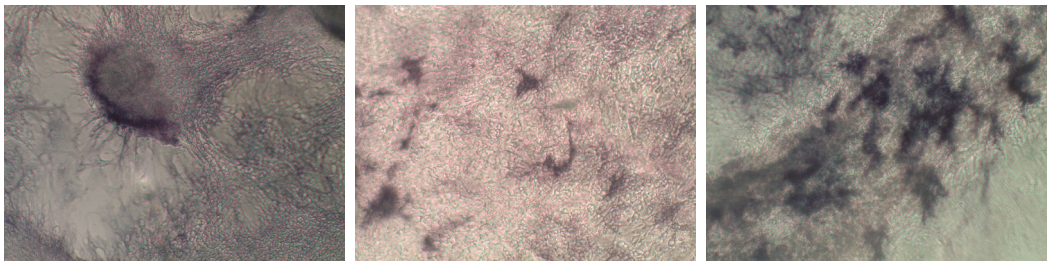

(a) (b) (c)

Fig. 5.2 Microscopy images of alkaline phosphatase staining in 2D well cultures of MSCs. 5.2a alkaline phosphatase staining in wells cultured with proliferation medium at 10× magnification. 5.2b & 5.2c Alkaline phosphatase staining of MSCs cultured in osteogenic medium at 5 × magnification.

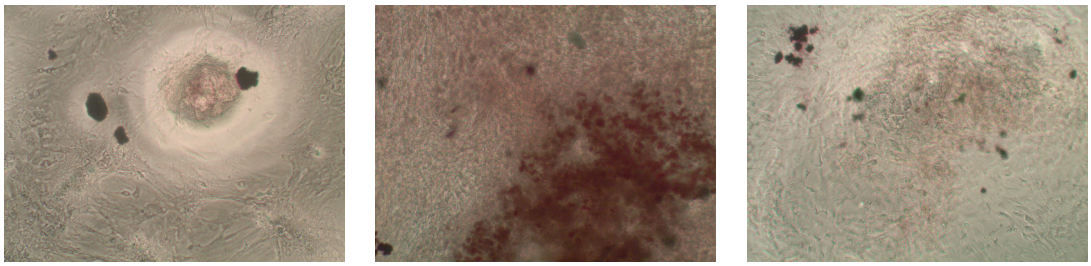

(a) (b) (c)

Fig. 5.3 Microscopy images of cells with alizarin red staining in 2D well cultures of MSCs. 5.3a Alizarin red staining of MSCs cultured with proliferation medium at 10× magnification and 5.3b 5× magnification. 5.3c alizarin red staining of MSCs cultured with osteogenic medium at 10× magnification.

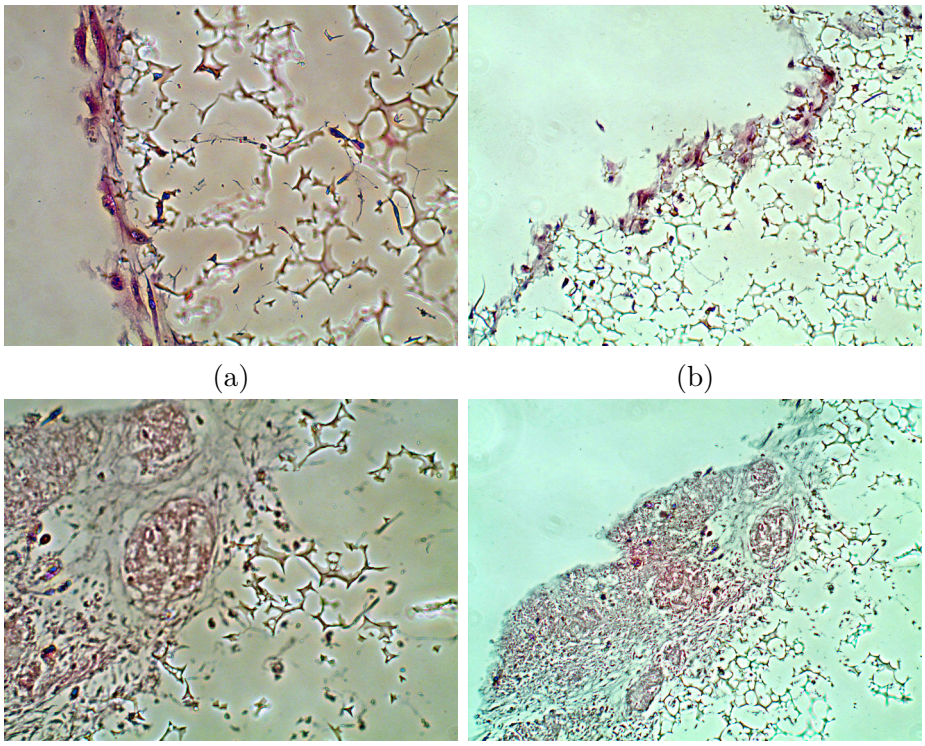

(a) (b)

(c) (d)

Fig. 5.4 Microscopy images of the first slice of a scaffold cultured in proliferation medium 5.4a & 5.4c 20× magnification and 5.4b & 5.4d at 10× magnification.

medium in order to see if any cell populations could be identified within the sections collected. The slides stained for imaging were the first and last of a selection of 10 5 μm sections. This methodology was selected in order to see what was present on the scaffold surface and what was present 50 μm under the scaffold surface. These slides were then imaged with light microscopy. Images of haematoxylin and eosin staining from scaffolds cultured in proliferation medium are displayed in Figure 5.4 for the scaffold surface and 5.5 for 50 μm under the scaffold surface. Images of haematoxylin and eosin staining from scaffolds grown in osteogenic medium are given in Figure 5.6 for the scaffold surface and 5.7 for 50 μm under the scaffold surface.

All images of haematoxylin and eosin staining of wax embedded sections were processed in GNU Image Manipulation Program 2 to improve image contrast. As can be seen in Figures 5.4, 5.5, 5.6, and 5.7, on the whole the scaffolds contain very little cellular materials, with mainly hematoxylin staining for nuclei present. Additionally, it can be seen that the majority of the staining was confined to the edges of the sections. In this sectioning procedure, a full cross section through the entire scaffold was not achieved. Therefore, there is some difficulty in determining where the edges seen in the sections correspond to in terms of the overall geometry of the full scaffold.

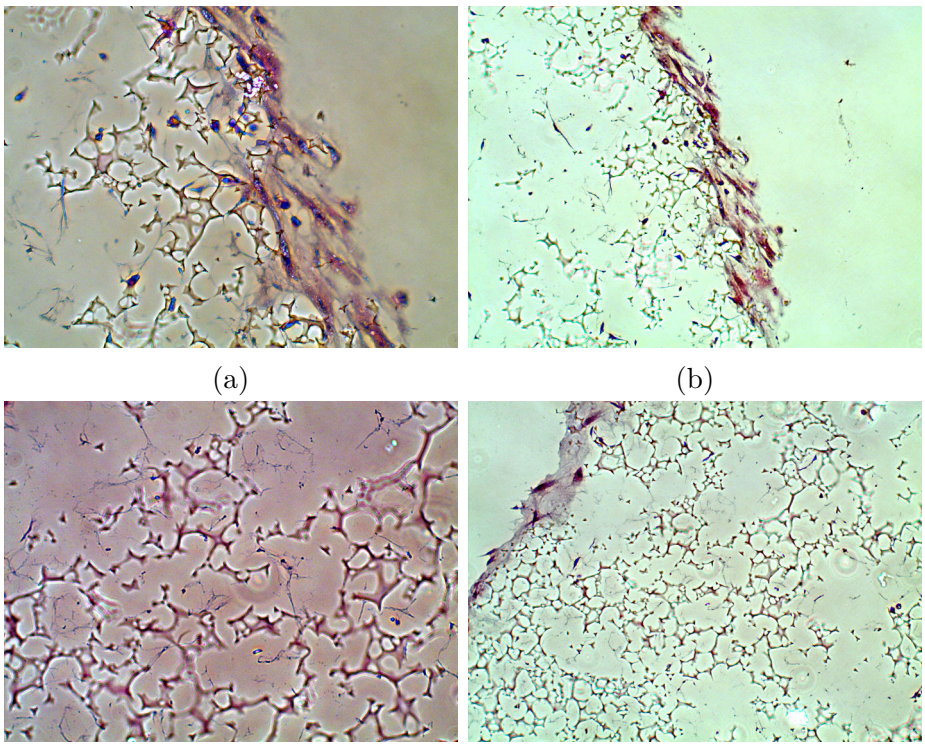

(a) (b)

(c) (d)

Fig. 5.5 Microscopy images of a slice 50 μm into a scaffold cultured in proliferation medium at 5.5a & 5.5c 20× magnification and 5.5b & 5.5d 10× magnification.

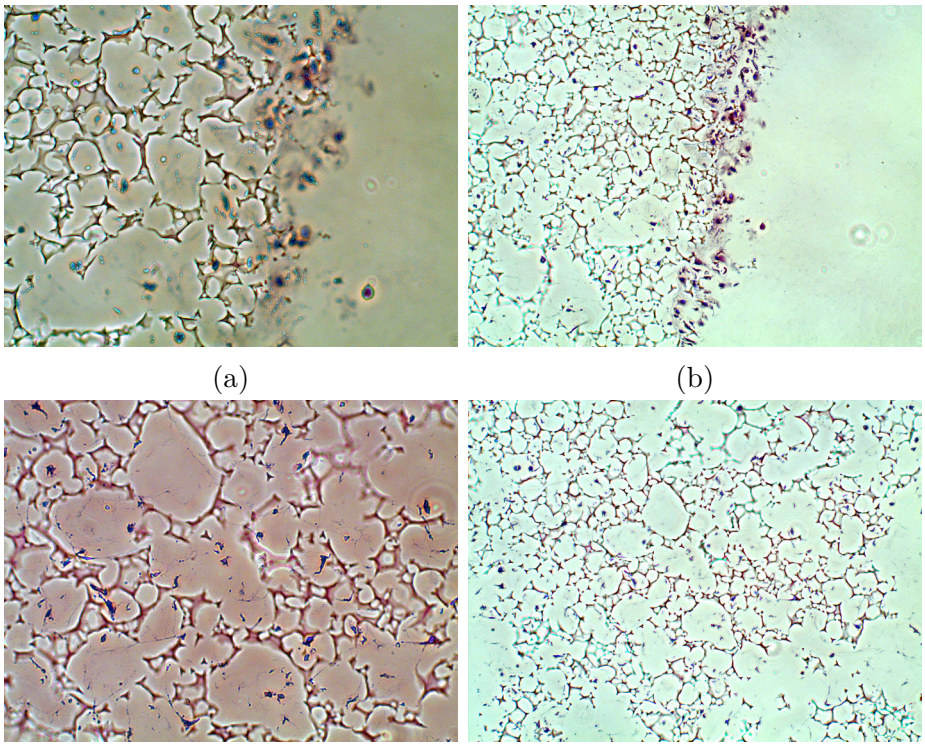

(a) (b)

(c) (d)

Fig. 5.6 Microscopy images of the first slice of a scaffold cultured in osteogenic medium 5.6a & 5.6c 20× magnification and 5.6b & 5.6d at 10× magnification.

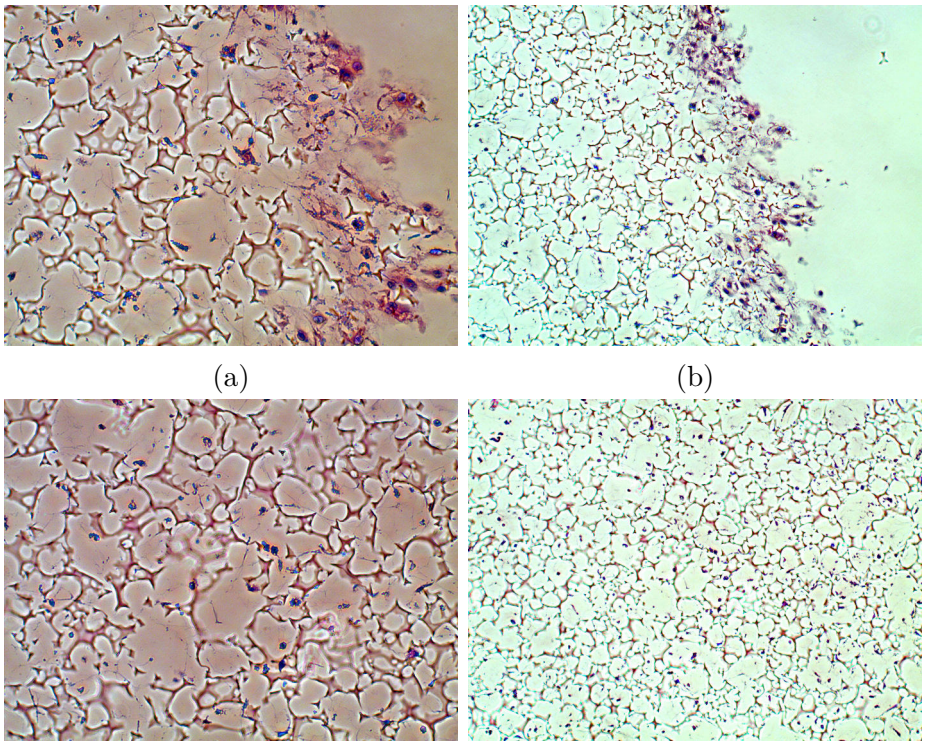

(a) (b)

(c) (d)

Fig. 5.7 Microscopy images of a slice 50 μm into a scaffold cultured in osteogenic medium at 5.7a & 5.7c 20× magnification and 5.7b & 5.7d 10× magnification.

μ-CT of Scaffold Sample

The first method of analysis used on the reconstructed slices was the production of a maximum projection image. In order to do this, the slices are stacked, and the maximum pixel value from the set of slices at each is used to create the image. In order to enhance the contrast between the areas of strong and weak absorption, the original greys of the image were replaced with the ImageJ fire look up table. The results of this process can be seen in Figure 5.8.

In order to give a frame of reference for mineral distribution in the plane of the cryosectioned scaffolds, the CT data was reconstructed into this cross-sectional plane. Example slices from the cross-section for each scaffold are given in Figure 5.9. These images clearly demonstrate that the position of the scaffold moves in the vertical plane, as it did not lie completely flat in the polystyrene mount. Therefore, this demonstrates that the data from the maximum z projection will spread out slightly over the image. To attempt to identify the mineral in the CT images, a threshold was applied to the maximum z projections. The value was chosen to reject the scaffold and background and focus only on the high intensity sections. In order to do this, the threshold selected was a pixel value of 195. This value was selected for thresholding by examining the pixel histogram and selecting out the high intensity pixel component. The thresholded images, along with the threshold

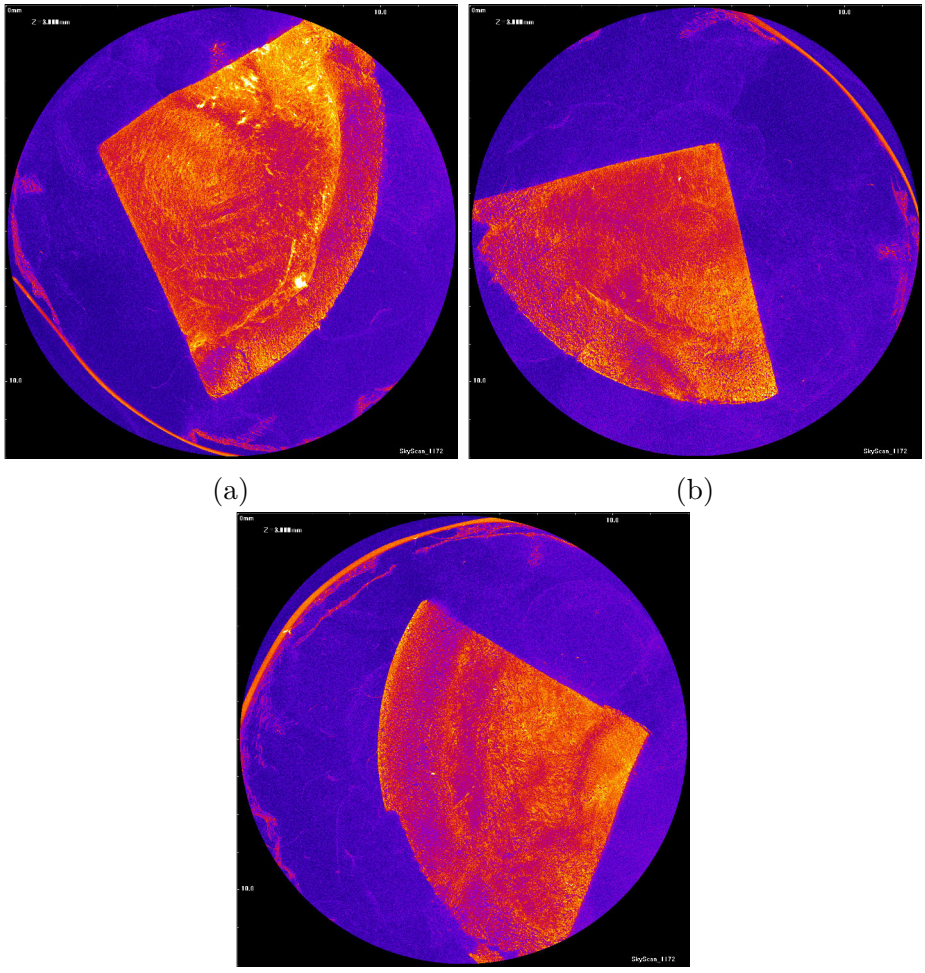

(a) (b)

(c)

Fig. 5.8 μ-CT maximum z projection data from the three successfully imaged scaffolds. 5.8a Shows the maximum z projection from a scaffold grown in osteogenic medium, with 5.8b and 5.8c showing the maximum z projection of 2 different scaffolds grown in proliferation medium.

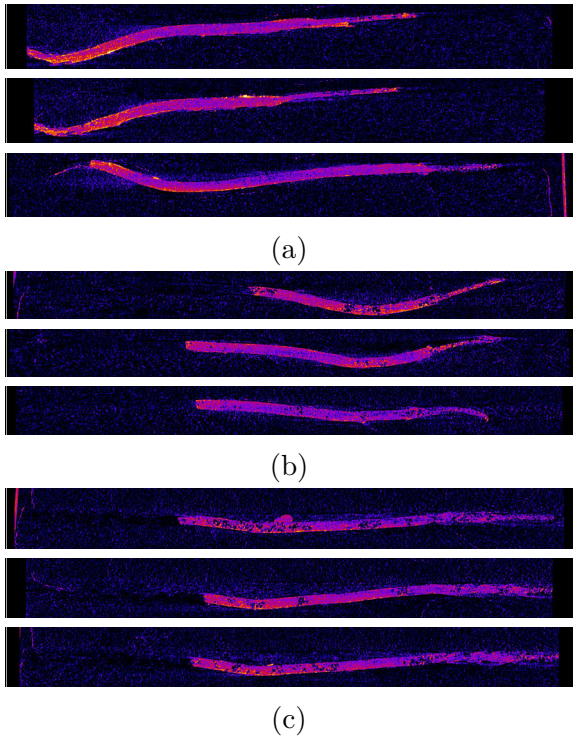

Fig. 5.9 Example cross sectional CT slices through the imaged scaffolds. 5.9a Shows cross sections through a scaffold cultured in osteogenic medium with 5.9b and 5.9c showing cross sections through 2 different scaffolds cultured in proliferation medium.

data overlaid on the maximum projections are given in Figure 5.10.

Histology of Cryosectioned Scaffold Samples

Images depicting alizarin red staining in the Alvetex® scaffold from MSCs cultured in both osteogenic and proliferative medium were collected with light microscopy at 10 and 20× magnification. The resulting images are given in Figure 5.11. Images of alkaline phosphatase staining of the scaffolds at 10 and 20× magnification are presented in Figure 5.12. Haematoxylin and eosin stained scaffold images at 10 and 20× magnification for MSCs cultured in proliferation and osteogenic medium are given in Figure 5.13. Finally, scaffolds stained with toluidine blue are imaged at 10 and 20× magnifications for scaffolds cultured in both osteogenic and proliferative medium are given in Figure 5.14. Although commonly used to stain cartilage samples for glycosaminoglycans, it works as an alternate stain for DNA and RNA in this context [247].

SEM of Scaffold Samples

The scaffolds were analysed with SEM in order to image the scaffolds, cells and extracellular matrix in high resolution. An overview of a scaffold of MSCs cultured in proliferation medium was captured, as shown in Figure 5.15. After generating a

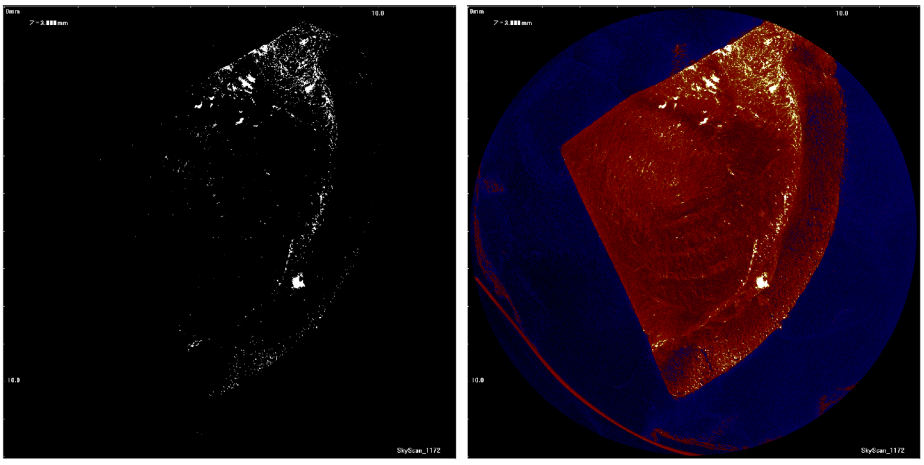

(a)

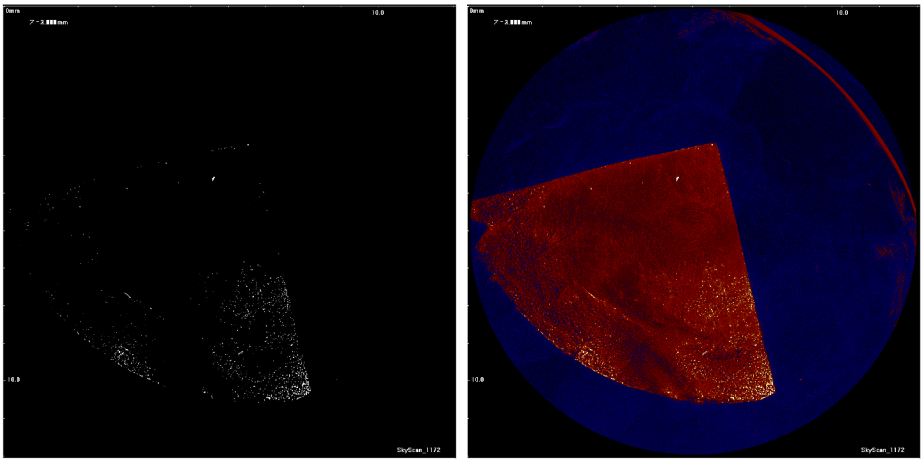

(b)

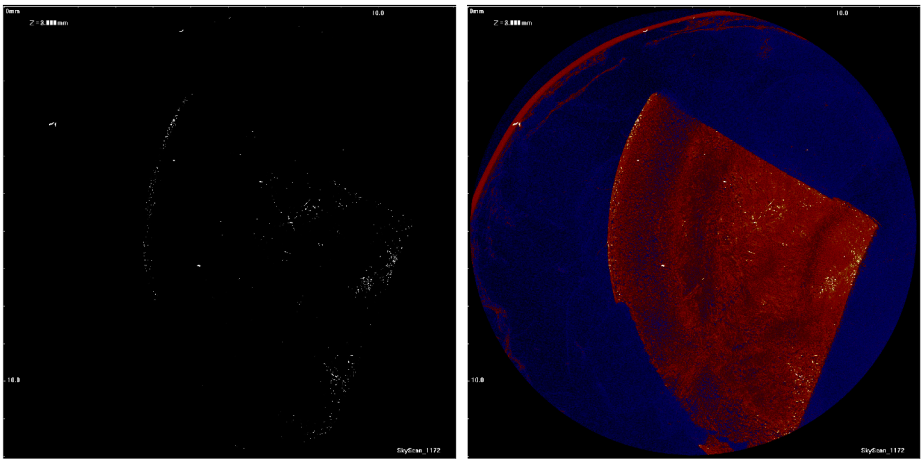

(c)

Fig. 5.10 CT images with a threshold of 195 applied to isolate mineral candidates for each scaffold, along with this threshold image applied to the maximum z projection images so that the yellow and white areas mark areas with pixel values greater than 195. 5.10a Shows the threshold applied to a scaffold cultured in osteogenic medium with 5.10b and 5.10c showing the threshold applied to two different scaffolds cultured in proliferation medium.

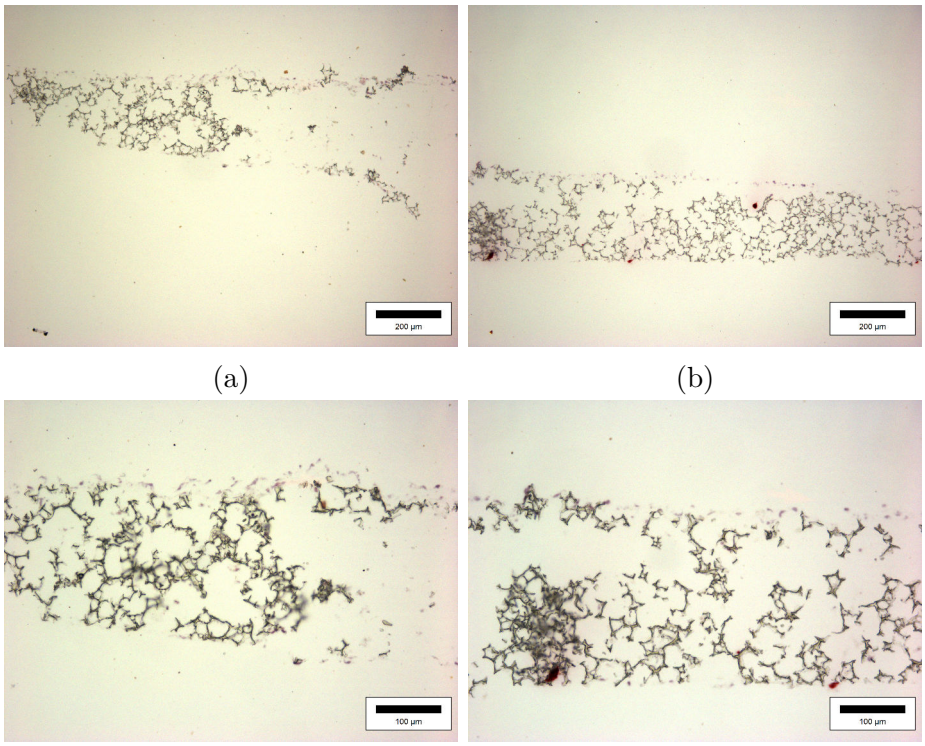

(a) (b)

(c) (d)

Fig. 5.11 Microscopy images of MSCs in Alvetex® scaffolds stained with alizarin red. MSC cells in Alvetex® at 10× magnification cultured with 5.11a proliferation medium and 5.11b osteogenic medium. MSC cells in Alvetex® at 20× magnification cultured with 5.11c proliferation medium and 5.11d osteogenic medium.

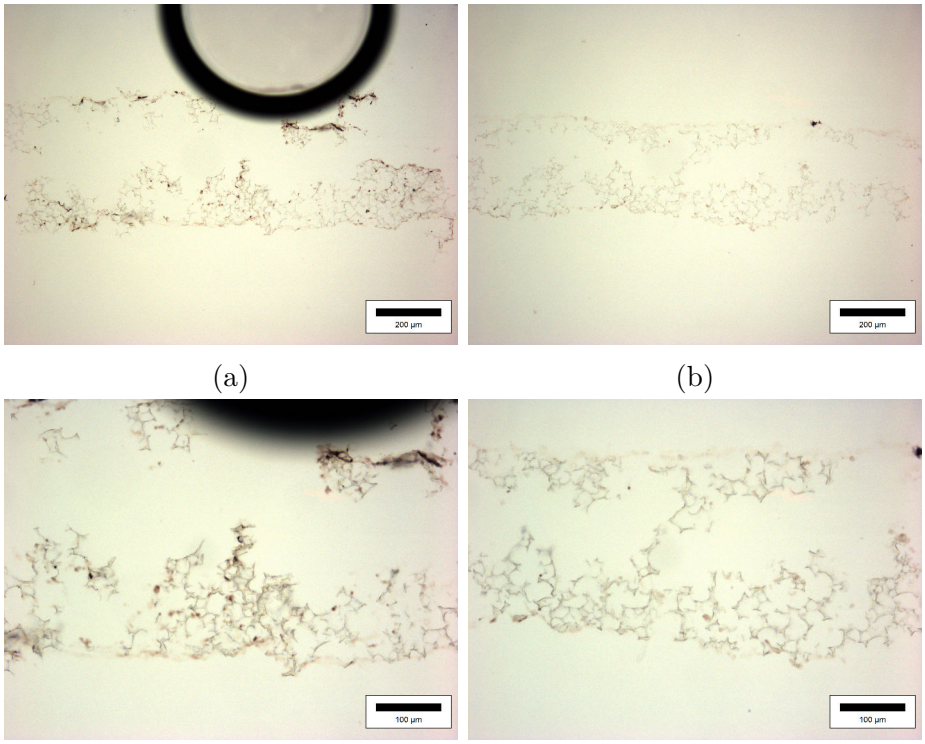

(a) (b)

(c) (d)

Fig. 5.12 Microscopy images of MSCs in Alvetex® scaffolds stained with alkaline phosphatase. MSC cells in Alvetex® at 10× magnification cultured in 5.12a proliferation medium and 5.12b osteogenic medium. MSC cells in Alvetex® at 20× magnification and of cells in a scaffold cultured in 5.12c proliferation medium and 5.12d osteogenic medium.

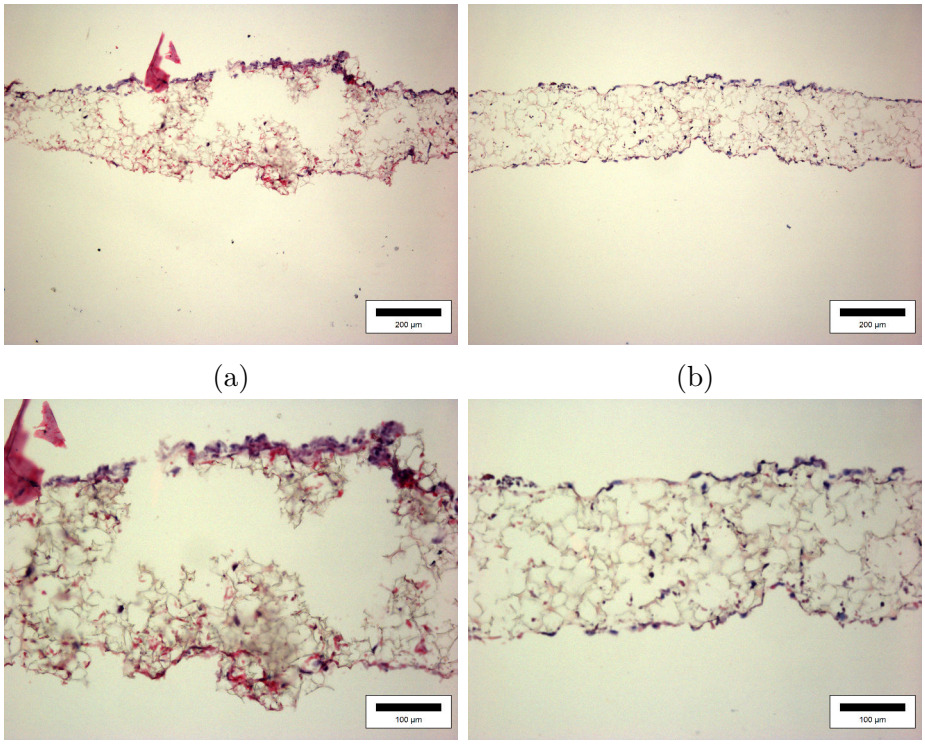

(a) (b)

(c) (d)

Fig. 5.13 Microscopy images of MSCs in Alvetex® scaffolds stained with haematoxylin and eosin. MSC cells in Alvetex® at 10× magnification cultured in 5.13a proliferation medium and 5.13b osteogenic medium. MSC cells in Alvetex® at 20× magnification and of cells in a scaffold cultured in 5.13c proliferation medium and 5.13d osteogenic medium.

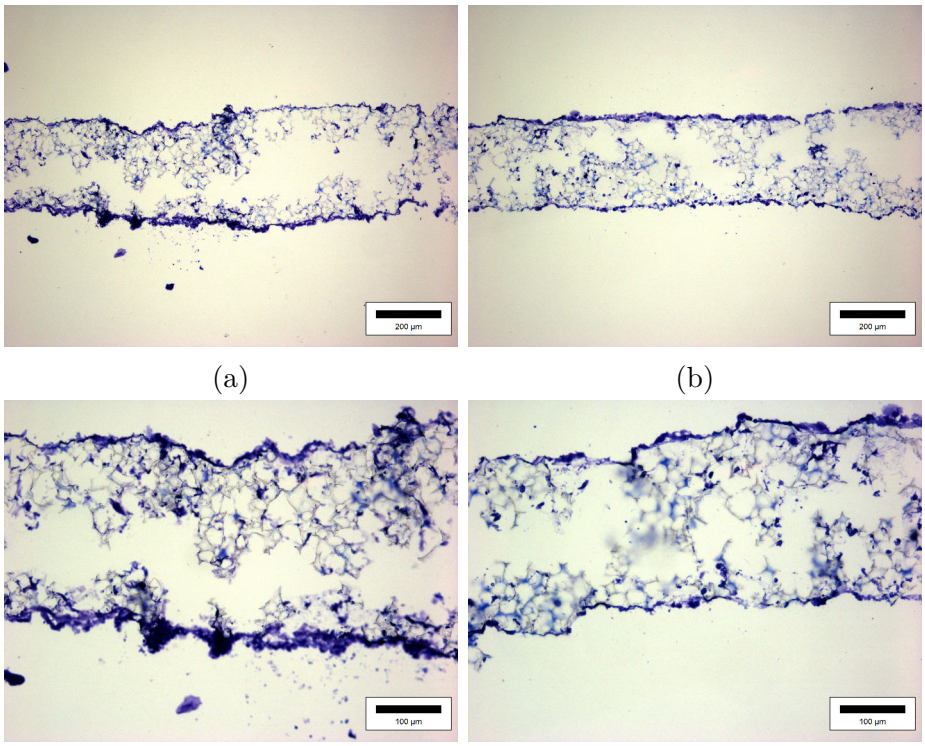

(a) (b)

(c) (d)

Fig. 5.14 Microscopy images of MSCs in Alvetex® scaffolds stained with toluidine blue. Images of MSCs in Alvetex® at 10× magnification cultured in 5.14a proliferation medium and 5.14b osteogenic medium. Images of MSCs in Alvetex® at 20× magnification cultured in 5.14c proliferation medium and 5.14d osteogenic medium.

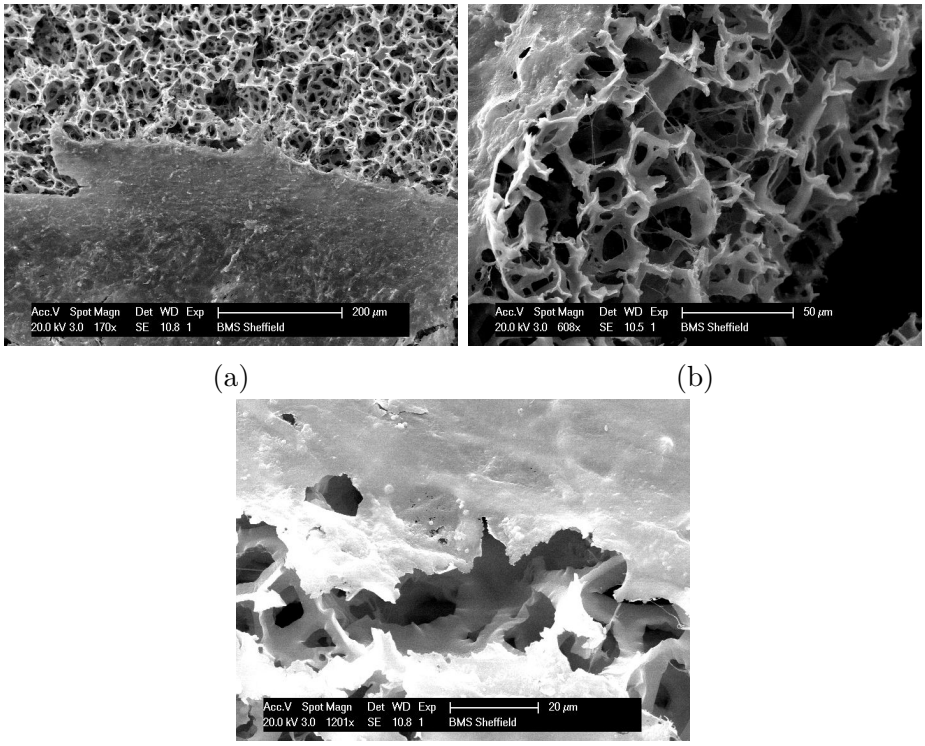

Fig. 5.15 SEM images of MSCs in Alvetex® scaffolds cultured in proliferation medium at 5.15a 170× magnification, 5.15b 608x magnification and 5.15c 1201x magnification.

data set over larger areas to capture the general form of the cells on the scaffold, further images were captured at higher magnifications to visualise the cell sheet in more detail and the scaffold interior in more detail as displayed in Figure 5.16. Next, images capturing an overview of a scaffold of MSCs cultured in osteogenic medium were collected, as displayed in Figure 5.17. This was followed by the collection of more in depth higher magnification images over the scaffold of MSCs cultured in osteogenic medium as displayed in Figure 5.18.

5.1.2 Analysis of Dynamically Seeded MSC Cultures on Collagen Coated Scaffolds

Staining of 2D MSC Cultures

The 2D control cultures were stained with the SIGMA FAST™ BCIP/NBT (5-Bromo-4-chloro-3-indolyl phosphate/Nitro blue tetrazolium) and the alizarin red stain, then imaged with light microscopy. Figures 5.19 and 5.20 show 2D microscopy images for MSCs cultured in both osteogenic and proliferation medium stained for alkaline phosphatase activity and alizarin red respectively.

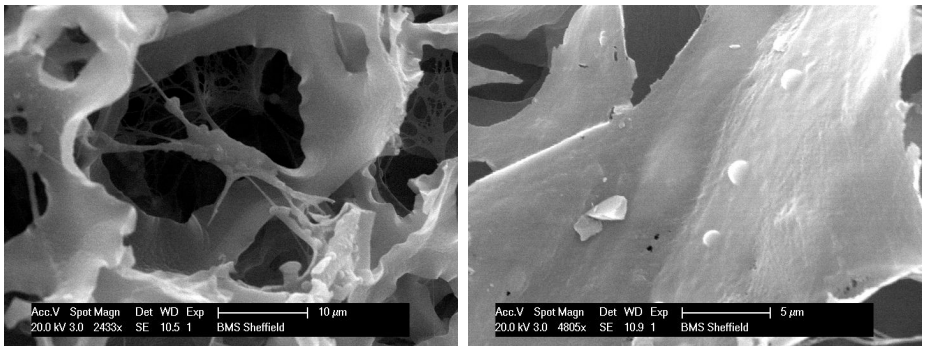

(a) (b)

Fig. 5.16 Higher magnification SEM images of MSCs in Alvetex® scaffolds cultured in proliferation medium at 5.16a 2433× magnification and 5.16b 4805× magnification.

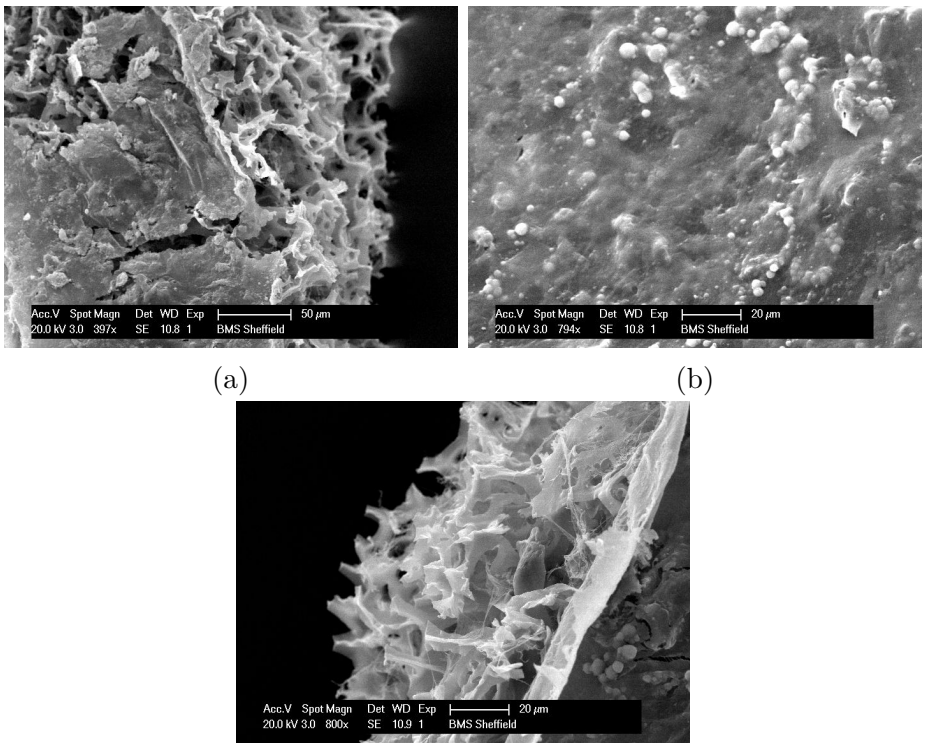

(a) (b)

(c)

Fig. 5.17 SEM images of MSCs in Alvetex® scaffolds cultured in osteogenic medium at 5.17a 397x magnification, 5.15b 794× magnification and 5.17c 800× magnification.

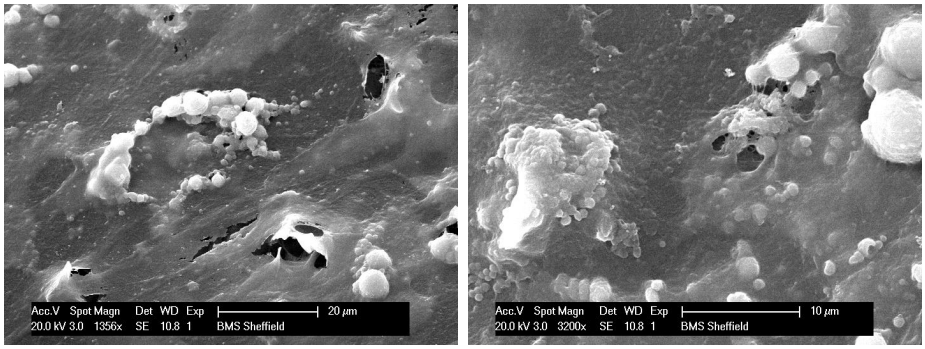

(a) (b)

Fig. 5.18 Higher magnification SEM images of MSCs in Alvetex® scaffolds cultured in proliferation medium at 5.18a 1356× magnification and 5.18b 3200× magnification.

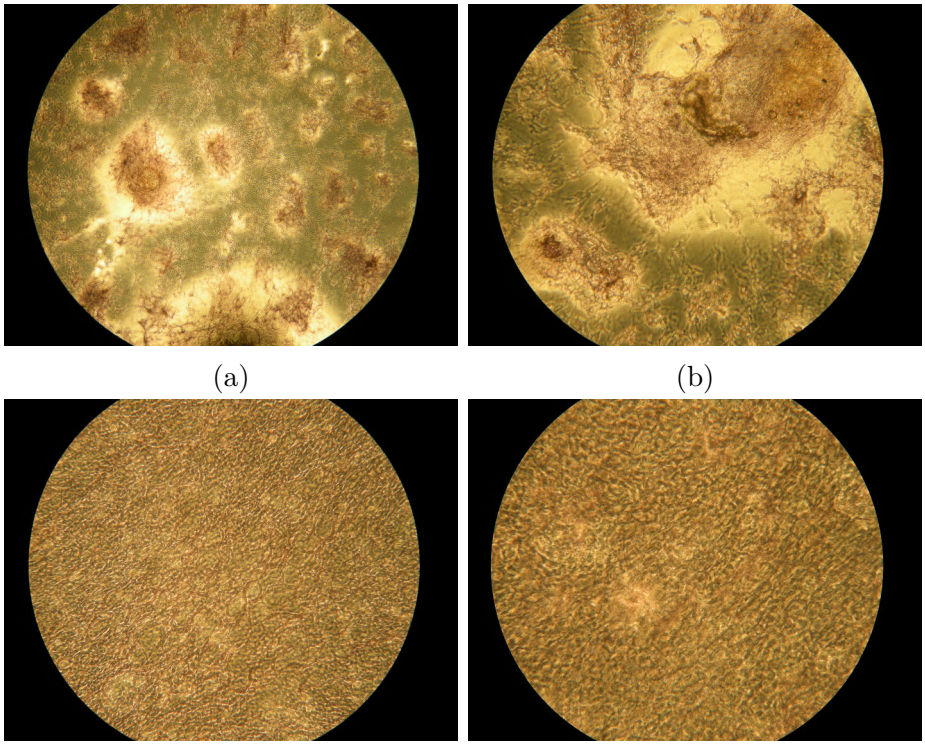

(a) (b)

(c) (d)

Fig. 5.19 Standard light microscopy images of MSCs stained for alkaline phosphatase cultured in 2D with osteogenic medium (5.19a and 5.19b) and proliferation medium (5.19c and 5.19d) at 10× magnification (5.19a and 5.19c) and 20× magnification (5.19b and 5.19d) as a control for dynamic scaffold seeing.

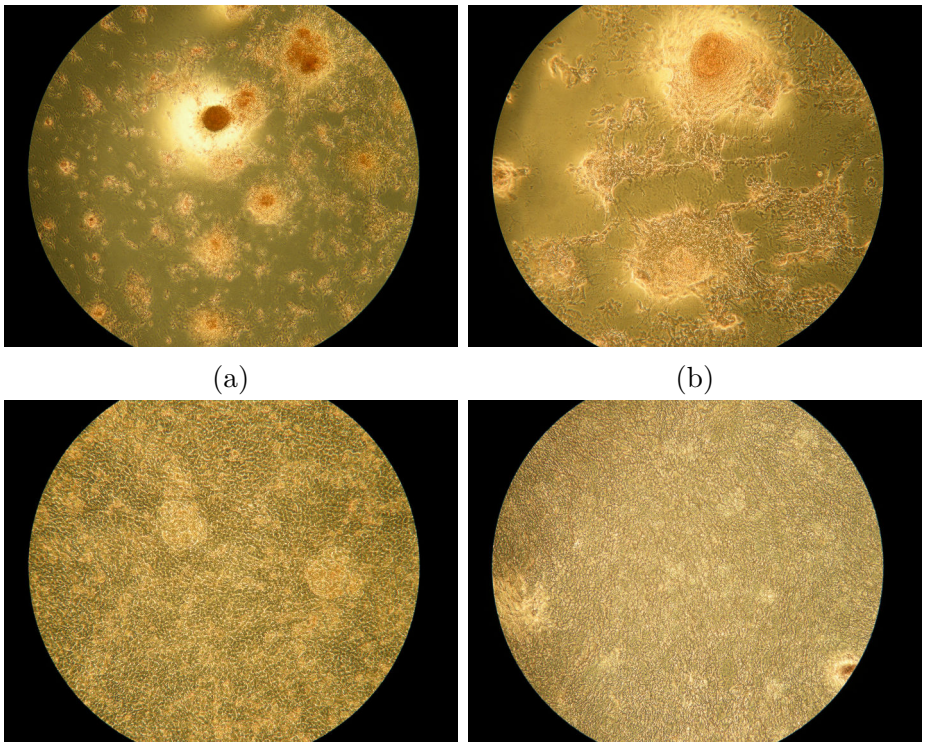

(a) (b)

(c) (d)

Fig. 5.20 Standard light microscopy images of MSCs stained for alkaline phosphatase cultured in 2D with osteogenic medium (5.20a and 5.20b) and proliferation medium (5.20c and 5.20d) at 10× magnification (5.20a and 5.20c) and 20× magnification (5.20b and 5.20d) as a control for dynamic scaffold seeing.

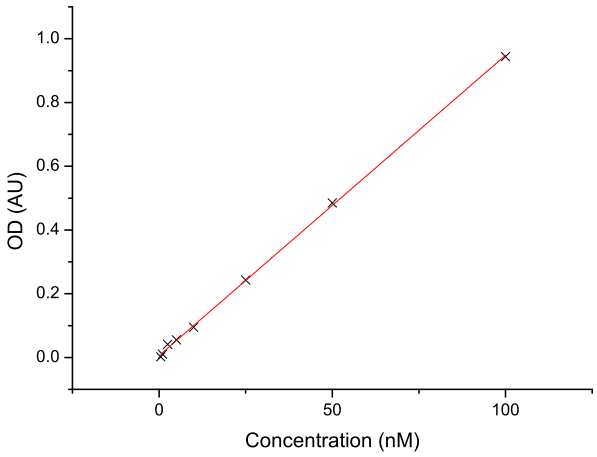

Fig. 5.21 Graph of the standard concentration curve for p-nitrophenol at 405 nm, with the calculated line of best fit given in red.

Quantitative Alkaline Phosphatase Assay

After collecting optical density (OD) measurements, the first calculation made was to find a value for the average contribution of water and the buffer to the OD measurement. The average OD value for water at 405 nm was 0.0457 ± 0.0002, the average OD for the buffer including water was 0.163 ± 0.002, the OD of the buffer alone (found by subtracting the OD of water) was 0.117 ± 0.002, the OD of NaOH was found to be 0.0490 ± 0.0004 with a contribution of water and 0.0034 ± 0.0004 without water.

The average values of water and buffer OD were subtracted from each of the OD readings for the prepared, known concentrations of p-nitrophenol. These values were then plotted as shown in Figure 5.21 and the function relating OD to concentration was found by fitting a straight line.

In this case, it was found that

$$OD = 0.00942C + 0.0059, \tag{5.1}$$

where OD is the measured optical density in arbitrary units and C is the concentration of p-nitrophenol in nM, which can be rearranged to find concentration of p-nitrophenol in nM given a known optical density as

$$C = \frac{OD - 0.0059}{0.00942}. \tag{5.2}$$

Next, the OD values for water, buffer only and NaOH only were subtracted from the OD data from the scaffolds with MSCs cultured in proliferation medium, osteogenic medium, collagen scaffold without cells and scaffold without cells or coat-

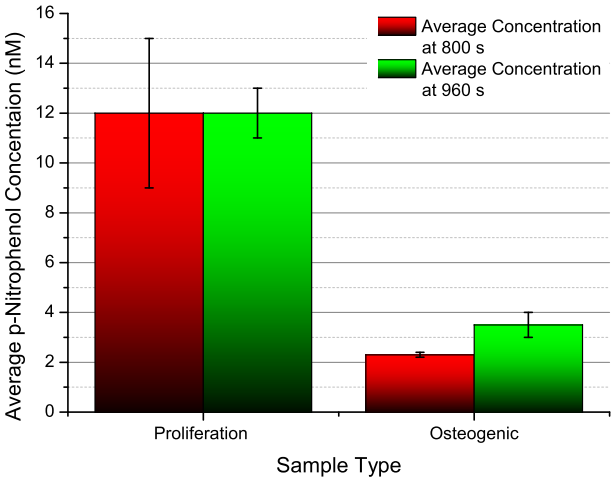

Fig. 5.22 Graph of average concentration of p-nitrophenol produced from alkaline phosphatase activity at 405 nm from MSCs on Alvetex® scaffolds cultured in osteogenic and proliferative medium 800 s and 960 s of exposure with errorbars from the calculated standard error.

ing. The next step was to apply equation 5.2 to the OD values found and calculate the concentration of p-nitrophenol for each scaffold sample at each time point, then the average p-nitrophenol concentration for each cell population was calculated. These values are given in Figure 5.22 with error bars representing the standard error. As the figure demonstrates, the cells cultured in osteogenic medium have a lower concentration of alkaline phosphatase than those cultured in proliferative medium. This could be due to a number of factors, which are more thoroughly discussed in 6.1.2.

Direct Staining of Methanol Fixed Scaffolds of MSC Cultures

After performing the quantitative alkaline phosphatase assay, the scaffolds were stained directly with SIGMA FAST™ BCIP/NBT (5-Bromo-4-chloro-3-indolyl phosphate/Nitro blue tetrazolium) and alizarin red without sectioning. This method was chosen in order to allow direct visualisation of cells and ECM produced on the scaffold surface. In addition to the scaffolds with MSCs cultured on them, two control samples were also stained. The first control was an unused Alvetex® scaffold, the second being an Alvetex® scaffold with a collagen coating, but no cells present. These controls were selected as they would demonstrate the level of background non-specific staining present. In order to visualise the overall staining of the scaffolds, photographs were taken after staining was applied. Figure 5.23 shows coated Alvetex® cultured with MSCs in proliferation medium on the left hand side and osteogenic medium on the right hand side stained for calcium deposition on the top row

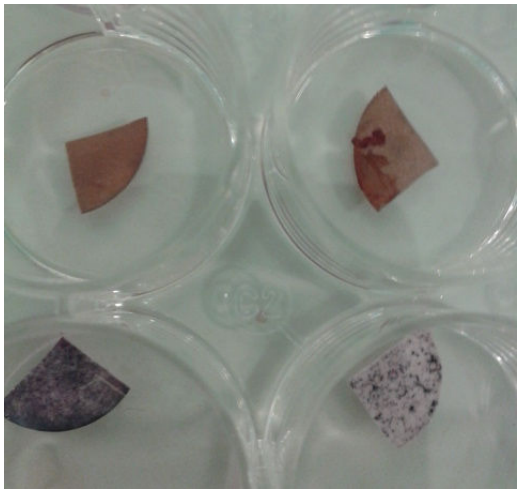

Fig. 5.23 Photograph of calcium staining with alizarin red (top row) and alkaline phosphatase staining with with SIGMA FAST™ BCIP/NBT (5-Bromo-4-chloro-3-indolyl phosphate/Nitro blue tetrazolium) (bottom row) of MSCs cultured on dynamically seeded, collagen coated Alvtex® . Scaffolds on the left hand side were cultured in proliferation medium and scaffolds on the right hand side were cultured in osteogenic medium.

and alkaline phosphatase on the bottom row. Photographs of staining with alizarin red and SIGMA FAST™ BCIP/NBT (5-Bromo-4-chloro-3-indolyl phosphate/Nitro blue tetrazolium) of coated and uncoated unseeded Alvetex® were also taken to act as a reference for the amount of non-specific staining present and are presented in Figure 5.24.

Images from light microscopy were also collected in order to show the staining of cellular material and, in the case of the unseeded scaffolds, non-specific staining in more detail. Figure 5.25 shows microscopy images from unseeded scaffolds with and without the collagen coating. Light microscopy images from seeded scaffold surfaces were then collected for samples cultured in osteogenic and proliferation medium, with alizarin red staining and SIGMA FAST™ BCIP/NBT (5-Bromo-4-chloro-3-indolyl phosphate/Nitro blue tetrazolium) staining applied. Figures 5.26 and 5.27 present images captured from scaffolds cultured in osteogenic (5.26) and proliferative (5.27) medium stained for calcium deposition with alizarin red. Figures 5.28 and 5.29 present images captured from scaffolds cultured in osteogenic (5.28) and proliferative (5.29) medium stained for alkaline phosphatase activity with SIGMA FAST™ BCIP/NBT (5-Bromo-4-chloro-3-indolyl phosphate/Nitro blue tetrazolium).

SEM of Scaffold Samples

SEM of the dynamically seeded scaffolds was performed in order to produce more information about the properties of the cells on the scaffold surface and to see if any cells could be found infiltrated into the top layers of the scaffold. SEM images with

(a) (b)

Fig. 5.24 Photographs of 5.24a alizarin red and 5.24b SIGMA FAST™ BCIP/NBT (5-Bromo-4-chloro-3-indolyl phosphate/Nitro blue tetrazolium) non-specific staining on unseeded Alvetex® (top row) and collagen coated unseeded Alvtex® (bottom row).

a 20 keV beam were captured for the unseeded Alvetex® scaffolds, both with and without collagen coating and for the Alvetex® scaffolds dynamically seeded with MSCs and cultured in osteogenic and proliferation medium. Figure 5.30 presents images of an unseeded, uncoated Alvetex® scaffold, with Figure 5.31 presenting images of an unseeded collagen coated Alvetex® scaffold. Dynamically seeded cultures with images focused on the outer scaffold edge are presented in Figure 5.32 for MSCs cultured in proliferation medium and 5.33 for MSCs cultured in osteogenic medium.

After focussing on the scaffold edge, the bulk of the scaffolds seeded with MSCs were examined, to see if any significant cellular penetration had occurred. SEM images of the bulk of the collagen coated Alvetex seeded with MSCs cultured in proliferation medium are presented in Figure 5.34 and SEM images of cells cultured in osteogenic medium are presented in Figure 5.35.

In samples cultured in proliferation medium, in addition to the presence of a fragmented cell layer, some scaffolds contained a rolled up cell sheet. An example of this is given in Figure 5.36. The assertion that this is a rolled up cell sheet is backed up by the fact that similar features were shown on light microscopy images as in Figure 5.27.

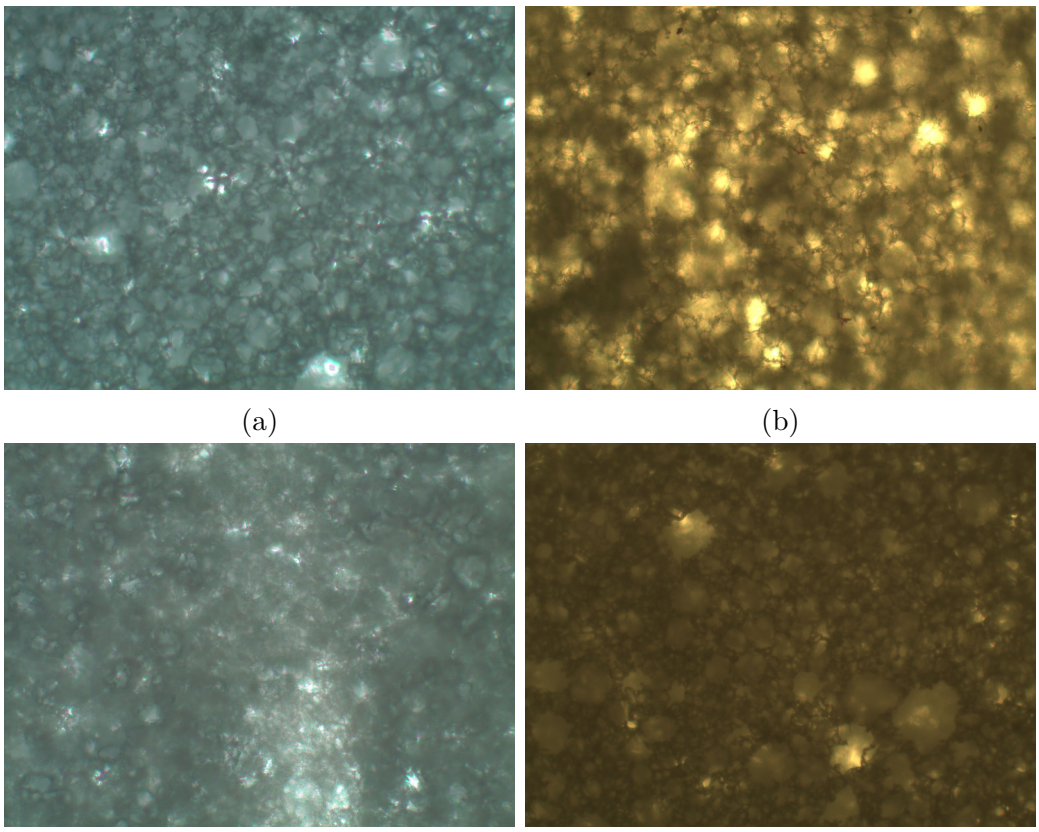

(a) (b)

(c) (d)

Fig. 5.25 Microscopy images of alizarin red (5.25a and 5.25c) and SIGMA FAST™ BCIP/NBT (5-Bromo-4-chloro-3-indolyl phosphate/Nitro blue tetrazolium) (5.25b and 5.25d) non-specific staining on unseeded Alvetex® (top row) and collagen coated unseeded Alvtex® (bottom row) at 10× magnification.

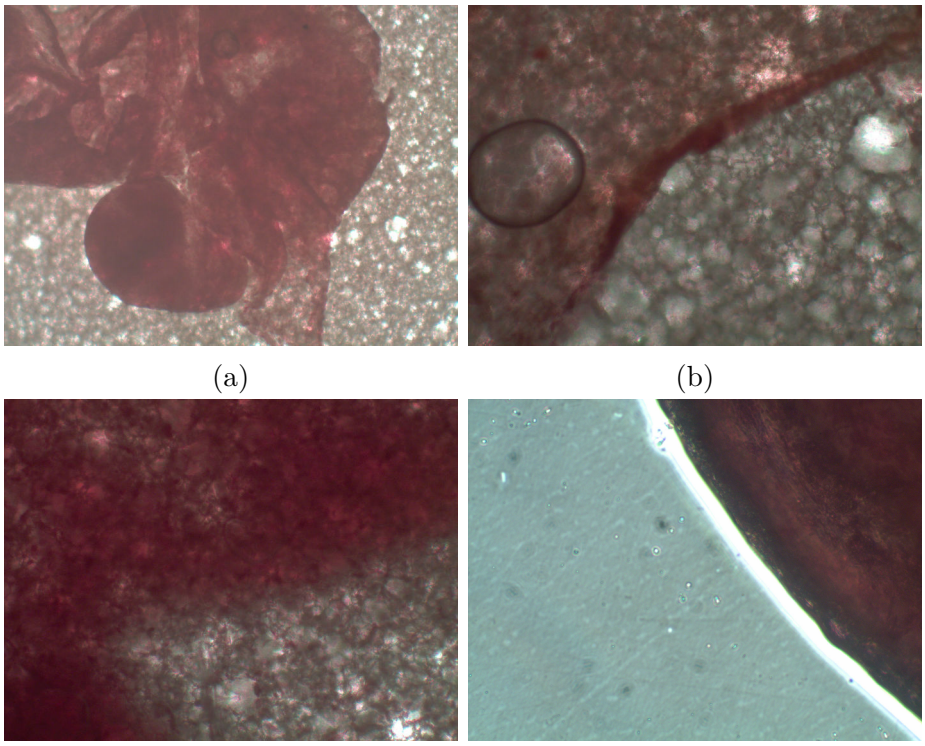

(a) (b)

(c) (d)

Fig. 5.26 Microscopy images of calcium staining on collagen coated Alvetex® dynamically seeded with MSCs and cultured in osteogenic medium at 4x magnification (5.26a and 5.26b) and 20× magnification (5.26c and 5.26d)

5.2 Raman Spectrum of Silica

After initial spectra were generated from the fused silica sample, the alignment and collection parameters were gradually improved, leading to the collection of improved spectra with more detail present, as presented in Figures 4.5 to 4.17.

Initial Raman spectra were captured with 500 μV sensitivity and 200 ms time constant settings with the lock-in amplifier. A silica Raman spectrum captured with these parameters is given in Figure 5.37. In order to transform this data set into wavenumber data, using the procedure outlined in Section 4.3, the laser line position was found by applying a Gaussian fit to the non-amplified data (as in Figure 5.38). The grating angle was also measured to give a value of ϕ and these two values were used to compute a silica spectrum in terms of wavenumbers. In the case of the data given in Figure 5.37, the laser line position was found to be (282.179 ± 0.003) mm through performing a Gaussian peak fitting in OriginPro 8.6 graphing software, the grating angle was measured as $(19 \pm 1)^{\circ}$, the distance between the grating and detector was measured as 285 ± 1 mm and the laser wavelength of 778.8 nm was used to calculate the wavenumbers. The resulting spectrum after calculating wavenumber values is given in Figure 5.39.

After generating a strong Raman signal from the silica sample, the stability of the

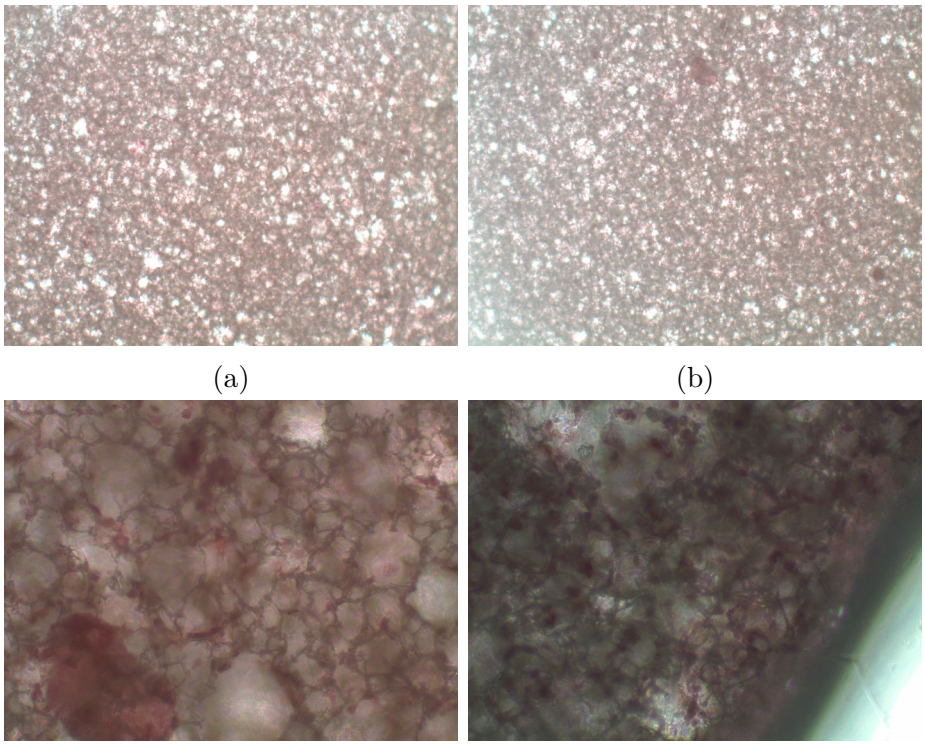

(a) (b)

(c) (d)

Fig. 5.27 Microscopy images of calcium staining on collagen coated Alvetex® dynamically seeded with MSCs and cultured in osteogenic medium at 4x magnification (5.27a and 5.27b) and 20× magnification (5.27c and 5.27d)

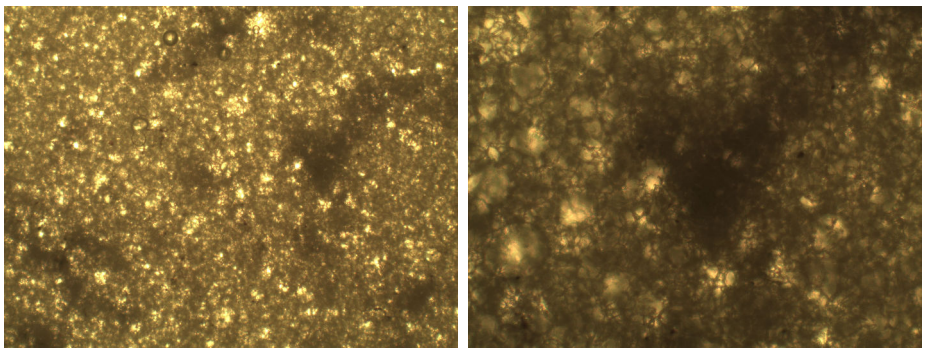

(a) (b)

Fig. 5.28 Microscopy images of alkaline phosphatase staining on collagen coated Alvetex® dynamically seeded with MSCs and cultured in osteogenic medium at 4x magnification (5.28a) and 10× magnification (5.28b)

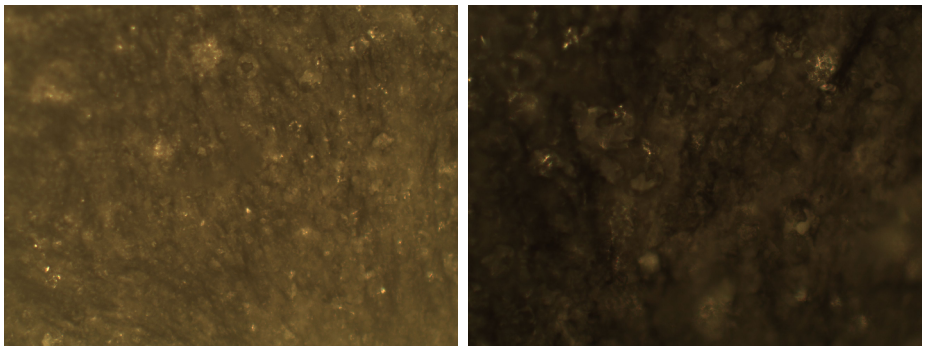

(a) (b)

Fig. 5.29 Microscopy images of calcium staining on collagen coated Alvetex® dynamically seeded with MSCs and cultured in proliferative medium at 4x magnification (5.29a) and 10× magnification (5.29b)

signal was investigated. Firstly, a Raman spectrum was collected and the position of the strongest Raman peak was identified, as shown in Figure 5.40 at 789.87 cm^{-1} wavenumber shift from the laser line which corresponds to 258.45 mm on the linear translation stage. The photodiode was positioned at the required point and the lock-in amplified photodiode voltage was measured once a second, every second for 90 minutes, with the lock-in amplifier operating at a sensitivity of 500 μV with a time constant of 200 ms. The results of this measurement are given in Figure 5.41, the red line representing the linear fit to the stability data with an equation of,

$$V_{LIA} = (-8.07 \times 10^{-6})T_S + 0.782, \tag{5.3}$$

where V_{LIA} is the voltage output of the lock-in amplifier operating with 500 μV sensitivity and 200 ms time constant at 789.87 cm^{-1} of wavenumber shift and T_S is the time elapsed in the stability measurement. Over the measurement period, the average voltage at 789.87 cm^{-1} after lock-in amplification was found to be 0.760 V with a standard deviation over 90 minutes of 0.0160 V.

In addition to the stability of a Raman feature, the stability of the laser signal without lock-in amplification and the background signal with lock-in amplification at 500 μV sensitivity and 200 ms time constant were also measured over a 90 minute period. The laser signal measurement was made at 282 mm on the translation stage, the position of maximum laser line signal, as found from a collected silica spectrum taken just before the stability measurement was made, as shown in Figure 5.42. The results of the laser line stability measurement are shown in Figure 5.43. The environmental background signal over time was measured at 150 mm, an area on the silica spectrum where no signal was present, with the result given in Figure 5.44. A linear fit was applied to each measurement, given by the red line. The equation

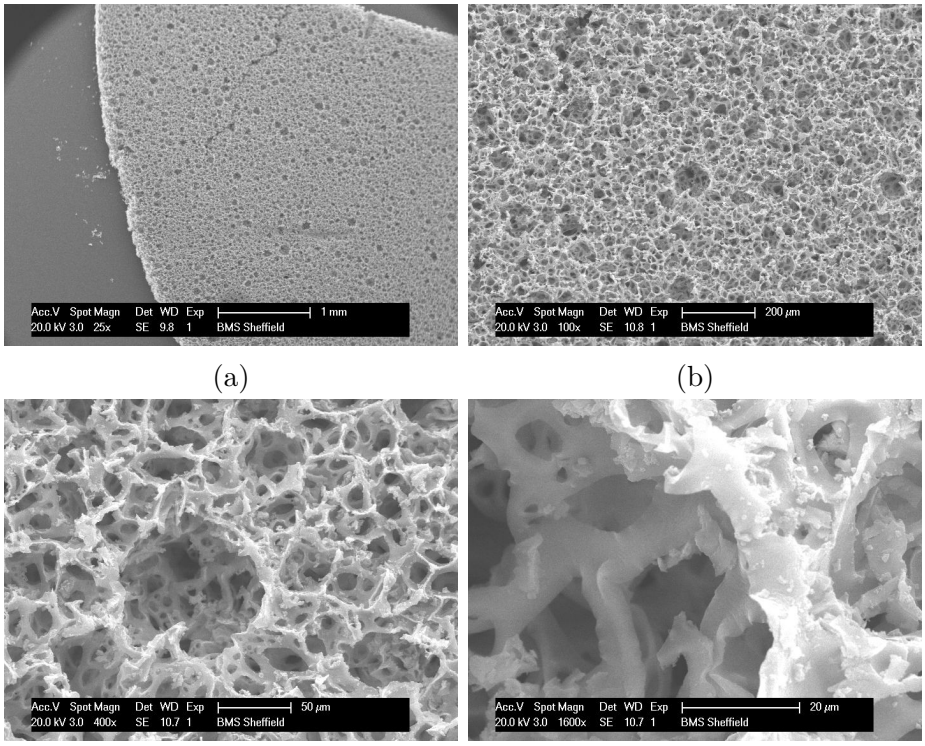

Fig. 5.30 SEM images of Alvetex® scaffold at 25× (5.30a), 100× (5.30b), 400× (5.30c) and 1600× (5.30d) magnification.

corresponding to this fit for the laser line is given by,

$$V_L = (-3.3 \times 10^{-6})T_S + 3.988, \tag{5.4}$$

where V_L is the photodiode output voltage from the laser. Over the measurement period, the average photodiode voltage from the laser line was found to be 3.98 V with a standard deviation over 90 minutes of 0.0917 V. The linear fit to the background voltage output from the lock-in amplifier with sensitivity 500 μV and time constant 200 ms and is described by the equation,

$$V_{BG} = (2 \times 10^{-8})T_S + 0.0101, \tag{5.5}$$

where V_{BG} is the lock-in amplified background voltage. Over the measurement period the average background voltage after lock-in amplification was found to be 0.0101 V with a standard deviation over 90 minutes of 0.00667 V.

To further examine the stability of the spectrometer, silica spectra were collected over an extended period. Silica spectra were collected with 500 μV sensitivity and 200 ms time constant, with collection occurring at at 0 hours, 44 hours, 47 minutes and 44 seconds separation hours and 49 hours 57 minutes and 12 seconds. The resulting spectra are shown in Figure 5.45 for the non-lock-in amplified spectra and

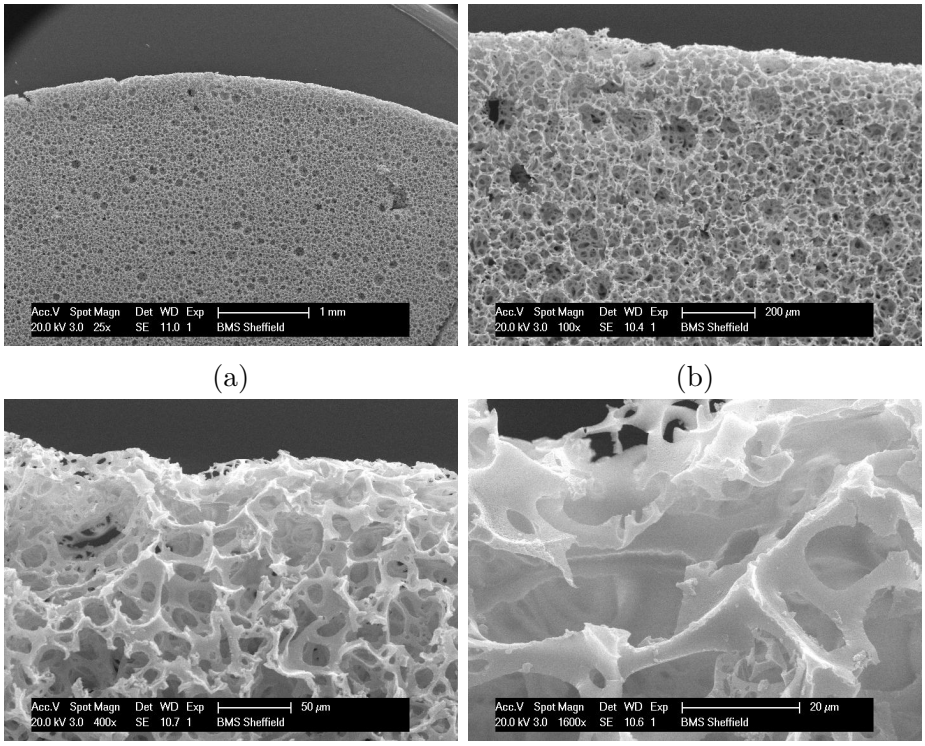

Fig. 5.31 SEM images of collagen coated Alvetex® scaffold at 25× (5.31a), 100× (5.31b), 400× (5.31c) and 1600× (5.31d) magnification.

5.46 for the amplified spectra.

Next, the spectral characteristics with changing focal point depth were investigated in the lens vibration lock-in amplification regime. Spectra were collected at 500 μV sensitivity and 200 ms time constant as before, with each spectra collected in 200 μm steps through 1.4 mm of the silica target. The results of this study are given in Figure 5.47. The spectra are plotted in a waterfall plot on the same axis to allow for easier determination of the spectral differences between focal point positions. This is useful data to collect as it helps to illustrate the source of spectral amplification. When the laser is crossing through the surface of the sample the laser line is moving from an area of no Raman signal to Raman signal. Whereas, when the laser is already in the sample the modulation is only slightly changing the volume irradiated. As a result, if lock-in amplification is occurring due to the lens vibration, it would be expected that the output from the lock-in amplifier is maximum at an interface, where there will be the greatest change in Raman signal during the modulation of lens position and minimal during modulation in the center of a sample, where there is minimal change in Raman signal. Figure 5.47 demonstrates that the lock-in amplified signal is maximal near the front face and reduces the further focal point moves into the sample, before increasing as it increases the back face. Therefore, this suggests that the lock-in amplification is dependent on

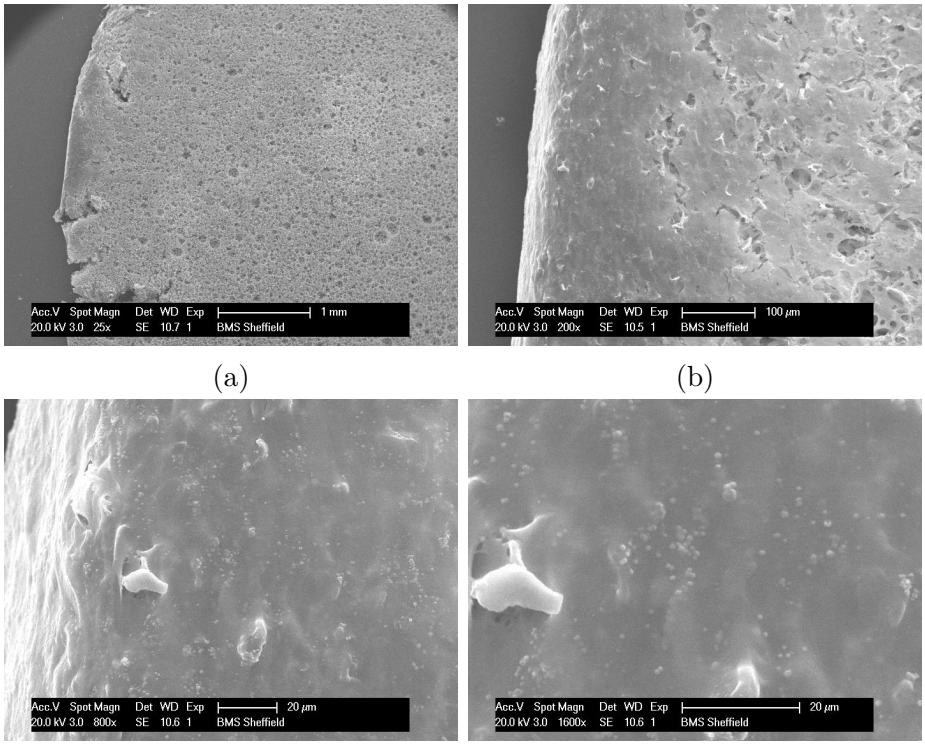

Fig. 5.32 SEM images of the outer edge of collagen coated Alvetex® scaffolds cultured with MSCs in proliferation at 25× (5.32a), 200× (5.32b), 800× (5.32c) and 1600× (5.32d) magnification.

lens vibration and the spectrometer is acting as hypothesised.

5.3 Raman Spectrum of Hydroxyapatite

Hydroxyapatite is a key component of bone and is a key molecule of interest in examining the growth of mineralising bone cell cultures. Hydroxyapatite has a defined molecular structure of $Ca_{10}(PO_4)_6(OH)_2$ and therefore, it can be manufactured with known properties. As artificial hydroxyapatites are well defined, they should produce clear, well defined Raman spectra and as a result were a good starting point for testing the Raman spectrometer design [275].

A fused hydroxyapatite (Biotol, UK) was used as the initial test sample, with collected spectra from this target shown in Figures 5.48, 5.49 and 5.50. Data collected at 500 μV with a time constant of 200 ms as shown in Figure 5.48 was used to generate the wavelength scale for the further fused hydroxyapatite spectra as there was no change in alignment between spectra and all spectra were taken on the same day. This meant that the longer time constant data could be collected quicker by removing the need to scan over the laser line. Further scans were collected at 200 μV with a 2 s time constant and 50 μV with a 5 s. Collecting the spectrum at a

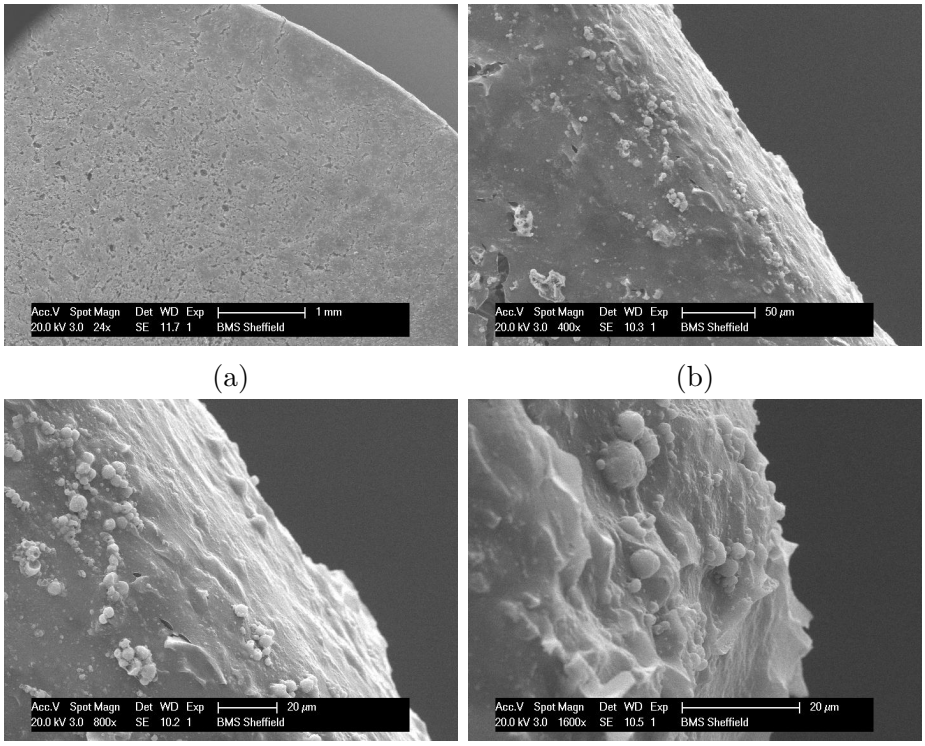

Fig. 5.33 SEM images of the outer edge of collagen coated Alvetex® scaffolds MSCs and cultured with osteogenic medium at 24× (5.33a), 400× (5.33b), 800× (5.33c) and 1600× (5.33d) magnification.

higher sensitivity and longer time constant improved the spectral quality.

Next, different hydroxyapatites were analysed in order to hopefully discriminate between different mineral forms and to demonstrate that as well as being able to identify spectra of samples in bulk, the spectrometer can produce spectra from porous and powdered hydroxyapatite samples. The samples of hydroxyapatite used have the same basic molecular structure, but the porous and fused samples have undergone further processing to alter their states from a base powder. This processing will alter the chemical environment of the hydroxyapatite, through formation of lattice structures which could impact on the generated Raman signal. In addition, the hydroxyapatite samples had different optical properties which could be seen visually. Firstly, the fused and porous samples are pale blue in colour, whereas the powdered hydroxyapatite is white. Secondly, the fused sample was more reflective, than the porous and powdered samples. Therefore, this suggests that a chemical change may take place in the formation of these structures which may be identifiable using Raman spectroscopy. A porous hydroxyapatite sample (Biotol, UK) was the next sample analysed with the spectrometer as the procedure would be relatively similar to that used for the fused hydroxyapatite, with the previously collected data sets used to inform the initial lock-in amplifier collection parameters for spectral

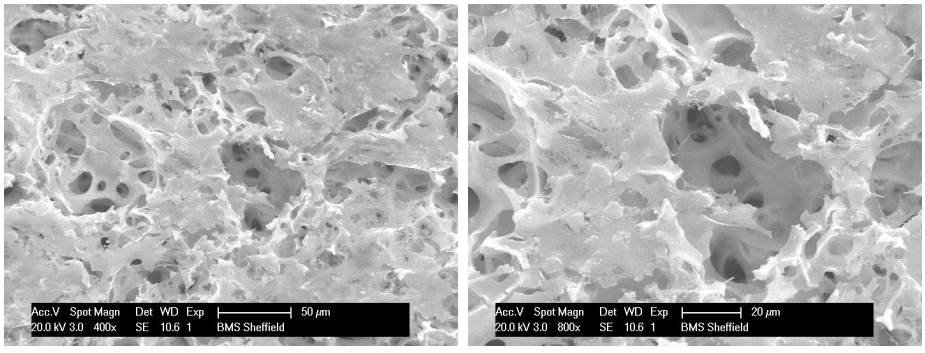

(a) (b)

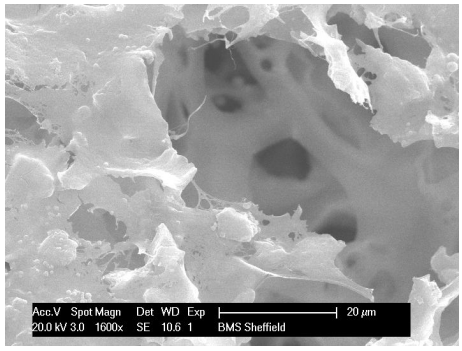

(c)

Fig. 5.34 SEM images of collagen coated Alvetex® scaffold cultured with MSCs in proliferation at 400× (5.34a), 800× (5.34b) and 1600× (5.34c) magnification focusing on the bulk of the scaffold.

processing. Initially, a porous hydroxyapatite spectrum was collected at 100 μV sensitivity with a time constant of 1 s over the entire Raman spectrum and laser line. A Gaussian fit was applied to the laser line signal in the non lock-in amplified data set, finding the laser line position to be at (282.02 ± 0.2) mm as shown in Figure 5.51. This measurement, along with the measured grating-detector separation of 285 mm and grating angle of 19°, allowed a wavenumber scale to be definite for every point on the translation stage. This allowed the spectrum to be represented in terms of wavenumbers as can be seen in Figure 5.52. Next, without changing the alignment, the porous hydroxyapatite spectra was captured with a sensitivity of 50 μV and 2 s time constant over the Raman region only, in order to improve the spectral quality, as shown in Figure 5.53a with the non lock-in amplified spectrum collected during at the same time shown in Figure 5.53b.

Finally, the Raman spectrum of a powdered hydroxyapatite sample was collected. The initial spectrum collection lock-in amplification parameters used were 200 μV sensitivity and 0.5 s time constant. As before, a Gaussian fit was applied to the non lock-in amplified Raman spectrum to find the laser line peak position. The laser line peak was found to be located at (281.74 ± 0.01) mm using this method as shown in Figure 5.54, and this value was used along with the detector grating separation

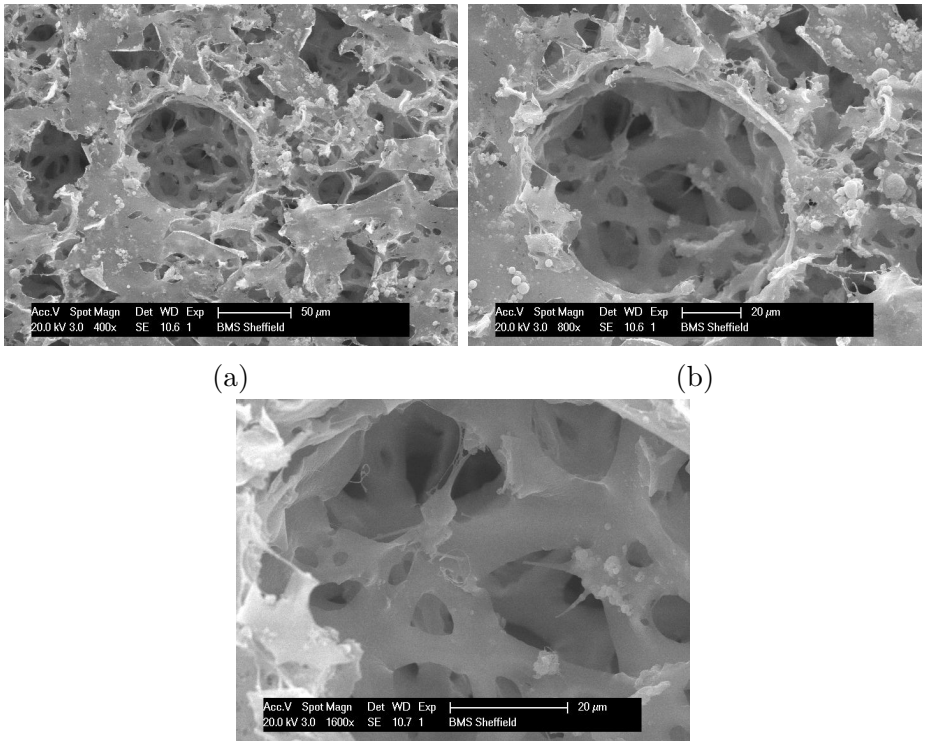

Fig. 5.35 SEM images of collagen coated Alvetex® scaffold MSCs and cultured with osteogenic medium at 400× (5.35a), 800× (5.35b) and 1600× (5.35c) magnification focusing on the bulk of the scaffold.

of (285 ± 1) and grating angle of $(19 \pm 1)^\circ$ to generate the wavenumber scale for the spectral data. The full lock-in amplified spectrum, the lock-in amplified Raman region and non lock-in amplified spectrum in the Raman region, with respect to the wavenumber scale, are given in Figure 5.55.

5.4 Raman Spectra of SEM Prepared MSC Cell Cultures

Raman spectra of cell culture samples were initially performed using standard methods of simply aligning the sample in the translation mount to the laser beam and collecting a spectrum through the lock-in amplifier. Initially, single spectra were collected for samples cultured in osteogenic medium and samples cultured in proliferative medium. Initial lock-in amplification parameters were selected from previously successful hydroxyapatite parameters and were chosen as 50 μV sensitivity and 2 s time constant in line with the optimal porous hydroxyapatite spectrum. During this scan the grating angle was measured as $(17 \pm 1)^\circ$. The results of this pilot measurement are given in Figure 5.56. Next, the scan was repeated with 200 μV and 200 ms to see if a quicker scan would be acceptable, with the same grating

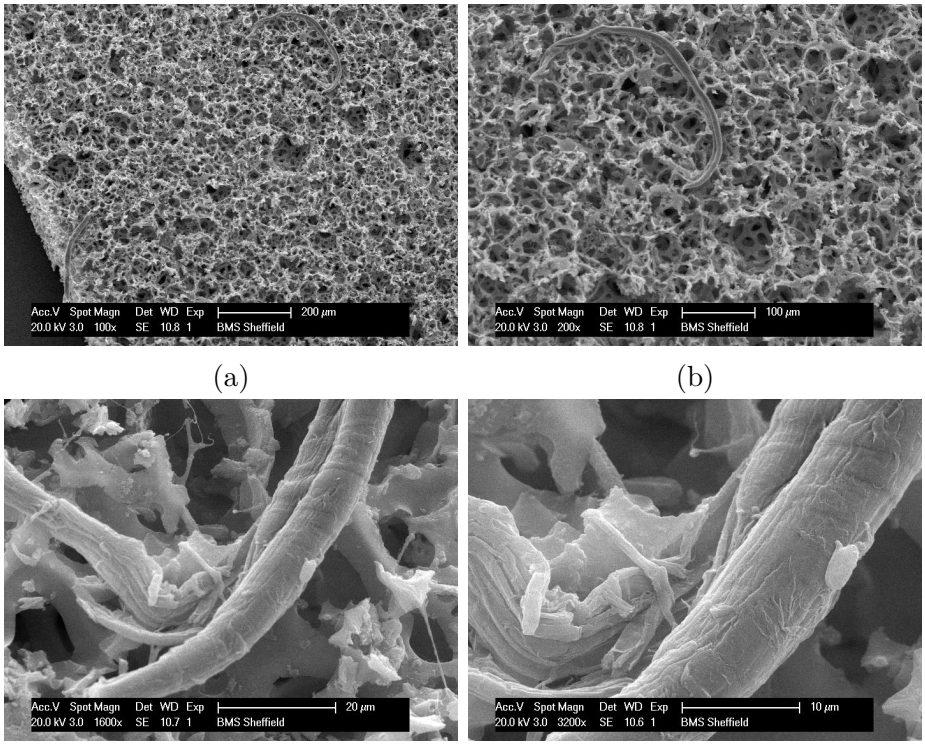

Fig. 5.36 SEM images of the rolled up cell layer produced on collagen coated Alvetex® scaffold cultured with MSCs in proliferation at 100× (5.36a), 200× (5.36b), 1600× (5.36c) and 3200× (5.36d) magnification.

condition, as shown in Figure 5.57. A clear improvement in resolution and amplitude is achieved using the higher sensitivity settings, however the faster scan does create an acceptable spectrum if speed is required.

After collecting cell spectra the next stage was to collect a spectral measurement from the gold coated carbon sticker which the scaffold was mounted on, and the gold coated Alvetex® alone. This will confirm that the source of difference in the measured spectra was due to the cells, not just scaffold or sticker being observed, which is potentially feasible as the scaffold is only 200 μm thick. As Figure 5.58 demonstrates, the gold coated carbon sticker and Alvetex® do not account for the full spectra. Therefore, the spectrometer is able to allow for analysis of cell cultures after SEM processing, which is an advantage for spectrometer development as SEM prepared samples are highly stable and do not require hydration. Additionally, it indicates that it could be possible to gain multiple forms of information regarding chemical composition and microscopic morphology with one fixation technique. With this confirmation that the spectrometer is working in this application an initial spectrum was collected from a proliferative control in two positions, demonstrating a different signal from different areas of the cell culture. This was done to determine whether the tool is sensitive enough to not just differentiate between cell popula-

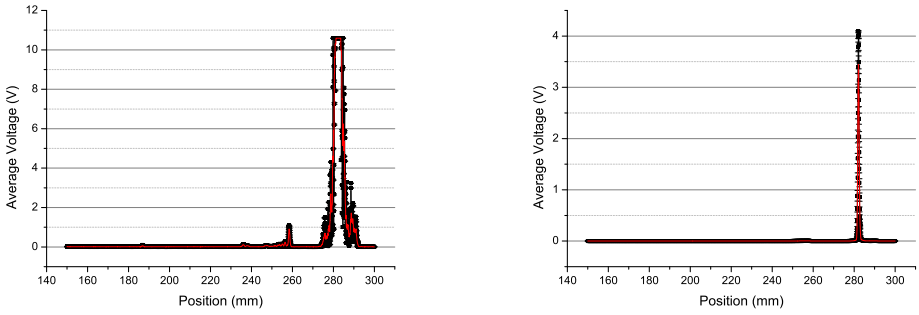

(a) (b)

Fig. 5.37 Initially collected lens vibration Raman spectra from silica in terms of photodiode position. Figures 5.37a was collected with the lock-in amplifier at 500 μV sensitivity and 200 ms time constant, with Figure 5.37b showing the non-amplified data set. Each spectrum is an average of 10 measurements per point with error bars as standard deviation, the red line is the smoothed spectrum produced by adjacent averaging over a window of 11 points.

tions, but to also differentiate different molecular compositions within a population. If this differentiation is achieved Raman mapping and image generation is a viable prospect using the spectrometer.

As 5.59 demonstrates, the spectra are different to the spectra from cells cultured in osteogenic medium, and as can be seen in Figures 5.59a and 5.59c, the spectra collected from different positions on the scaffold have different spectral features. Therefore, the spectrometer has potential applications in monitoring the generation of extracellular matrix and cell differentiation processes.

As with silica, the depth dependent behaviour was investigated for an osteogenic cell culture. This was performed to demonstrate whether the spectrometer could penetrate the surface level of the cells. As can be seen in Figure 5.60, the signal generated changes with depth and dose more than simply exhibiting a decrease of signal with depth. Therefore, this suggests that penetration below the surface layers is possible with this instrument.

After the initial measurements the spectrometer was modified to remove the beam compressor and improve the irradiance at the sample and therefore increase the Raman signal. Spectra collected with this altered set up are given in Figure 5.61s. Removal of the beam compressor improved the delivery of light to the lens, therefore increasing the potential Raman return to the sample. As a result, it was decided that all further measurements would be performed without the compressor in place.

As can be seen in the spectra collected from the MSC cultures, there is clear evidence that the use of lock-in amplification improves the Raman spectra generated, that the spectrometer is sensitive enough to differentiate between different cell populations, and can penetrate below the surface of the cell cultures. Therefore, after

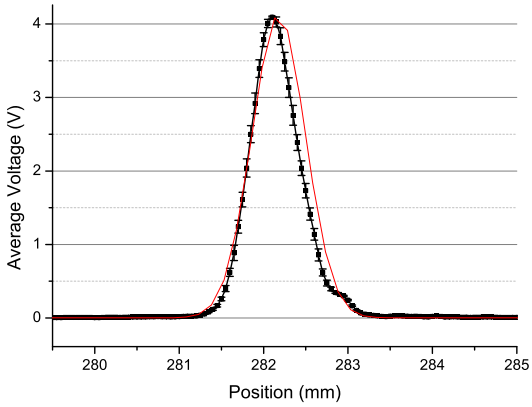

Fig. 5.38 Graph of Gaussian fit to the raw reflected silica laser line, used to find the laser line position to calculate the wavenumber scale for the silica spectrum given in Figure 5.37

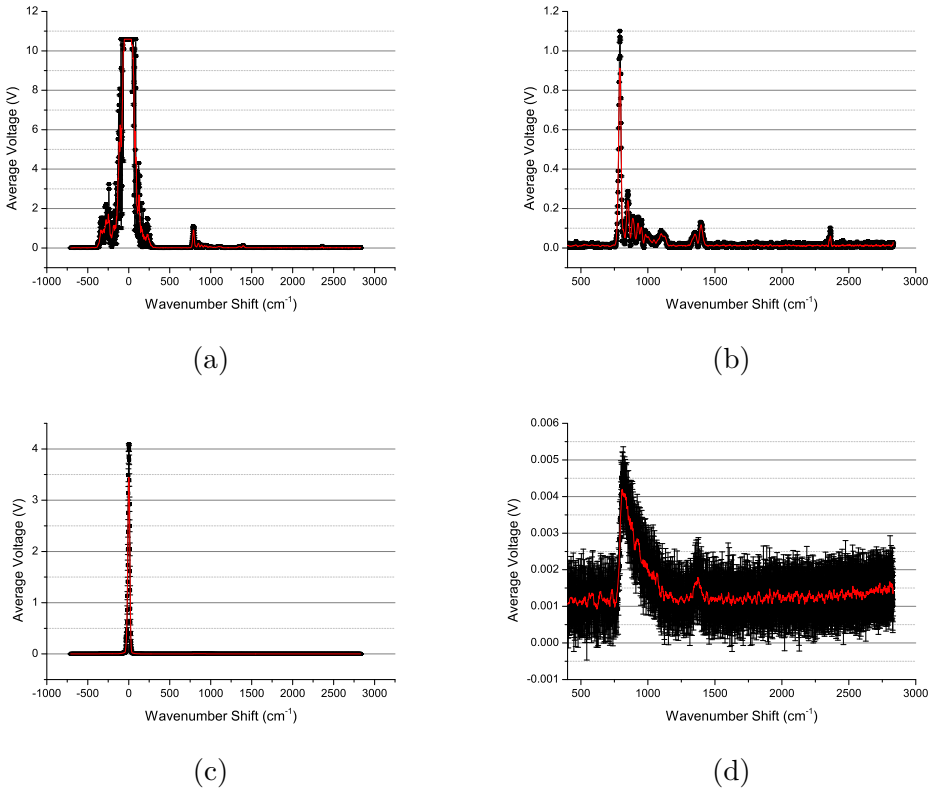

Fig. 5.39 Initially collected lens vibration Raman spectra from silica in terms of wavenumbers. Figures 5.39a and 5.39b were collected with the lock-in amplifier at 500 μV sensitivity and 200 ms time constant, with Figures 5.39c and 5.39d showing the non-amplified data set. Figures 5.39a and 5.39c display the fully collected spectrum with Figures 5.39b and 5.39d presenting the same data focussed on the Raman region. Each spectrum is an average of 10 measurements per point with error bars as standard deviation, the red line is the smoothed spectrum produced by adjacent averaging over a window of 11 points.

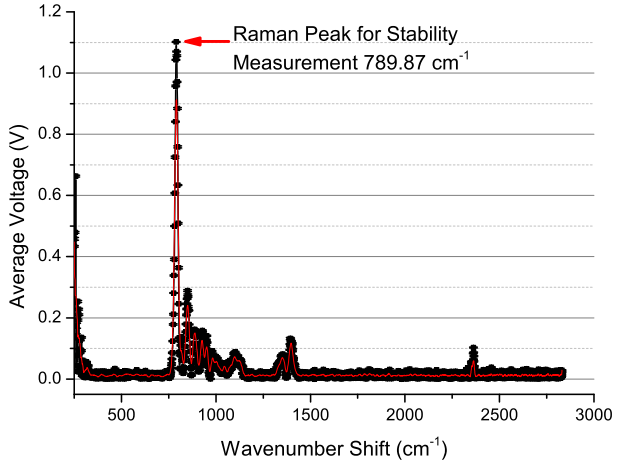

Fig. 5.40 Silica spectrum collected through lock-in amplification at 500 μV, with a 200 ms time constant with the Raman peak to be measured for stability indicated. The spectrum is an average of 10 spectral measurements per point with the error bars representing the measurement standard deviation.

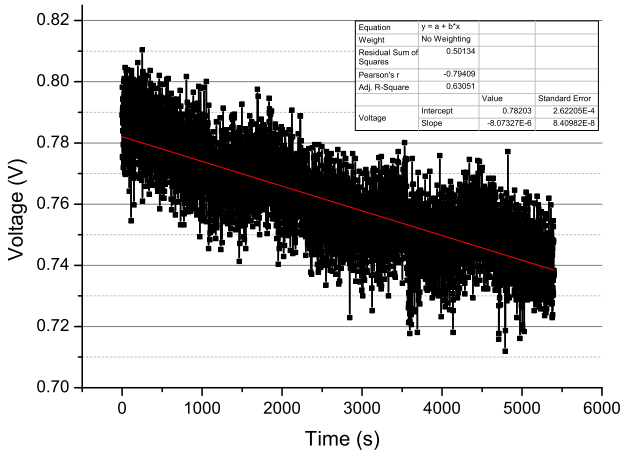

Fig. 5.41 Graph of the stability of the lock-in amplified Raman signal at 789.87 cm^{-1} wavenumber shift over 90 minutes with measurements made at a rate of 1 s^{-1}. The red line denotes the linear fit to the data.

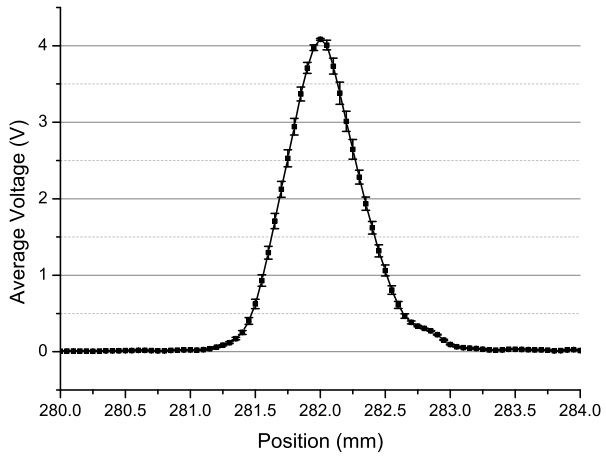

Fig. 5.42 Graph displaying the location of maximum measured voltage from the laser used to determine the required photodiode position for stability measurement of the laser line.

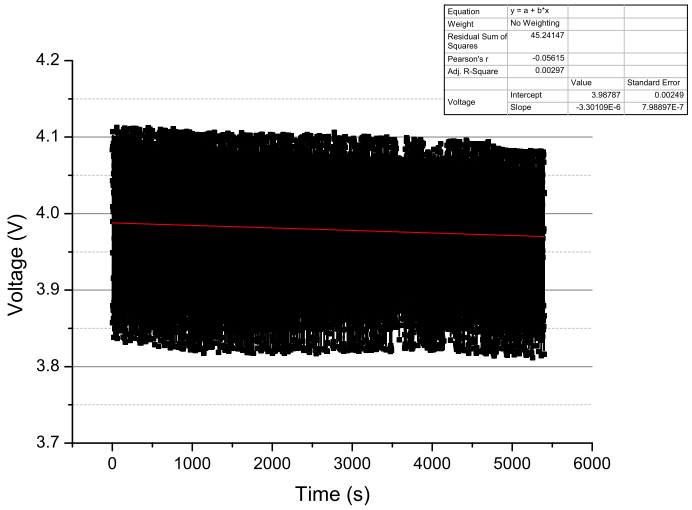

Fig. 5.43 Graph displaying the raw photodiode output voltage at the position of maximum laser signal over time. The red line denotes a linear fit to the data, as calculated by OrignPro 8.6.

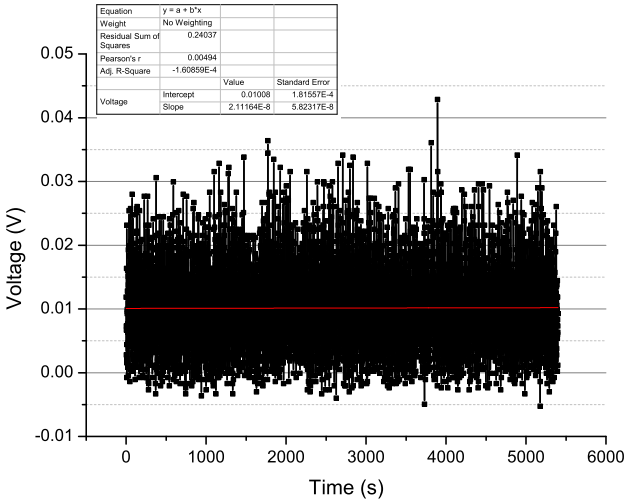

Fig. 5.44 Graph displaying the lock-in amplified output voltage of the environmental background processed at 500 μV sensitivity and 200 ms time constant. The red line denotes a linear fit to the data, as calculated by OrignPro 8.6.

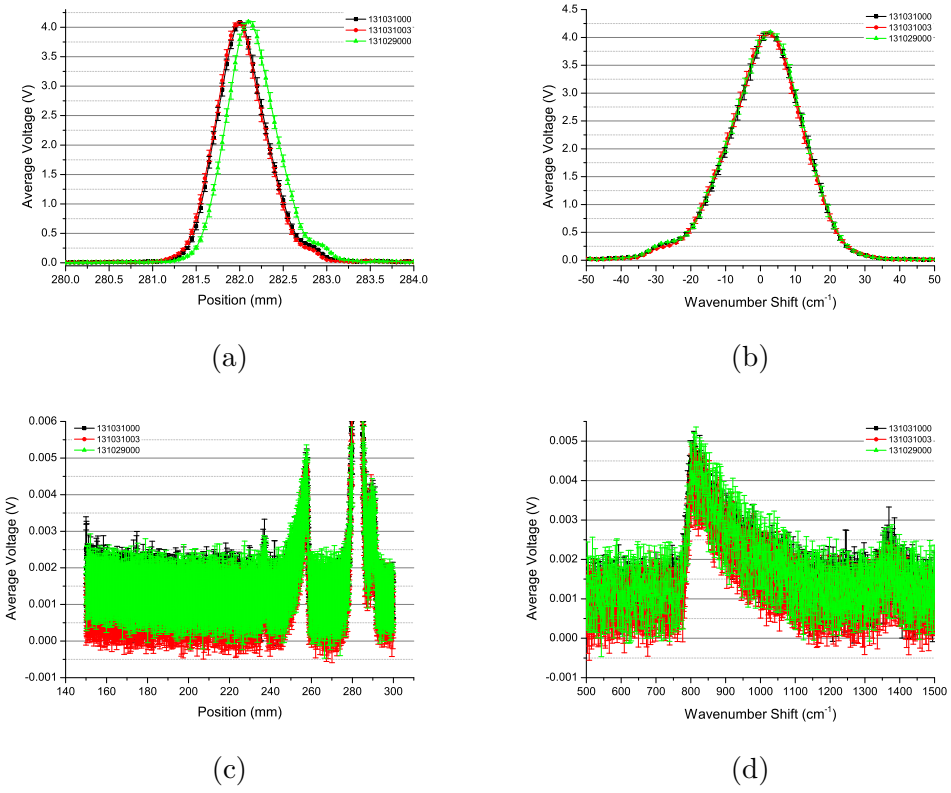

(a) (b)

(c) (d)

Fig. 5.45 Spectra of silica over time to assess spectrometer stability in terms of absolute position data and wavenumber. Spectra 5.45a and 5.45b show the raw laser line data for silica, with 5.45a given in terms of absolute position and 5.45b given in terms of wavenumber. Spectra 5.45c and 5.45d show the raw Raman data for silica, with 5.45c given in terms of absolute position and 5.45d given in terms of wavenumber. All spectra were constructed from the average of 10 measurements per position with error bars representing the measurement standard deviation.

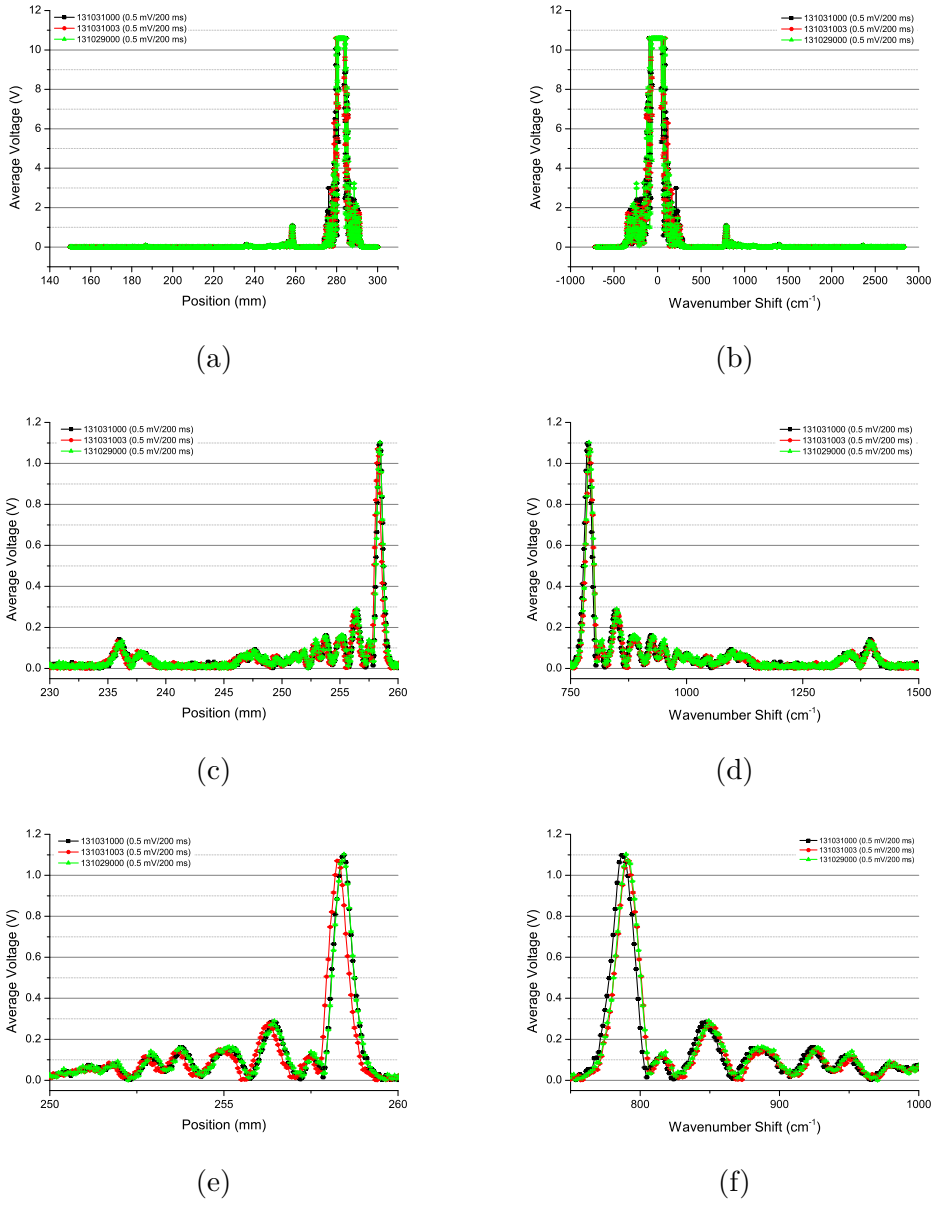

Fig. 5.46 Spectra of silica over time to assess spectrometer stability in terms of absolute position data and wavenumber. Spectra 5.46a and 5.46b display the lock-in amplified silica laser line variation over time in terms of absolute position for 5.46a and wavenumber for 5.46b. Spectra 5.46c and 5.46d display the variation in the lock-in amplified silica Raman spectra over time in terms of absolute position for 5.46c and wavenumber for 5.46d. Spectra 5.46e and 5.46f display the variation in the inital lock-in amplified silica Raman features over time in terms of absolute position for 5.46e and wavenumber for 5.46f. All spectra were collected at 500 μm sensitivity with a 200 ms time constant, with spectra constructed from the average 10 measurements per detector position with error bars representing the measurement standard deviation.

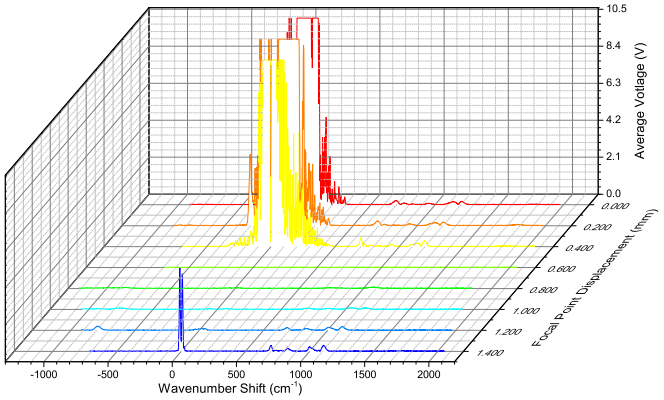

(a)

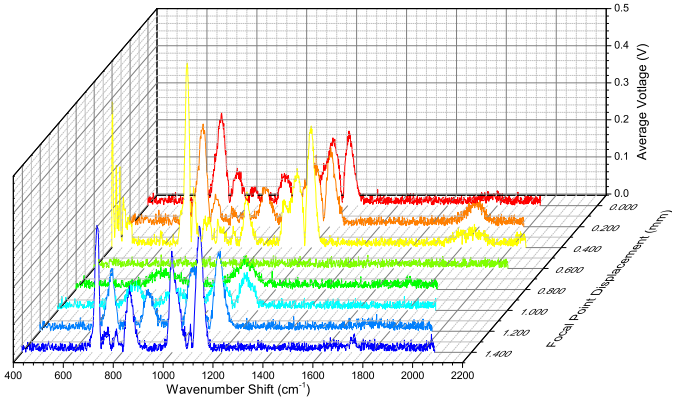

(b)

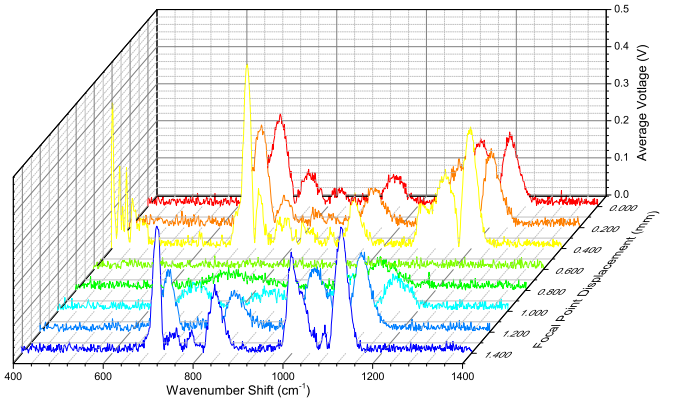

(c)

Fig. 5.47 Silica spectra collected with the focal point at varying depth positions using lens vibration lock-in amplification. The spectra were collected with a sensitivity of 500 μV and time constant of 200 ms. Figure 5.47a shows the entire spectrum, including the laser line, Figure 5.47b shows the Raman region of the spectrum, from 400 cm^{-1} of shift onwards and Figure 5.47c displays a smaller segment of the Raman spectrum to allow for more detail to be seen.

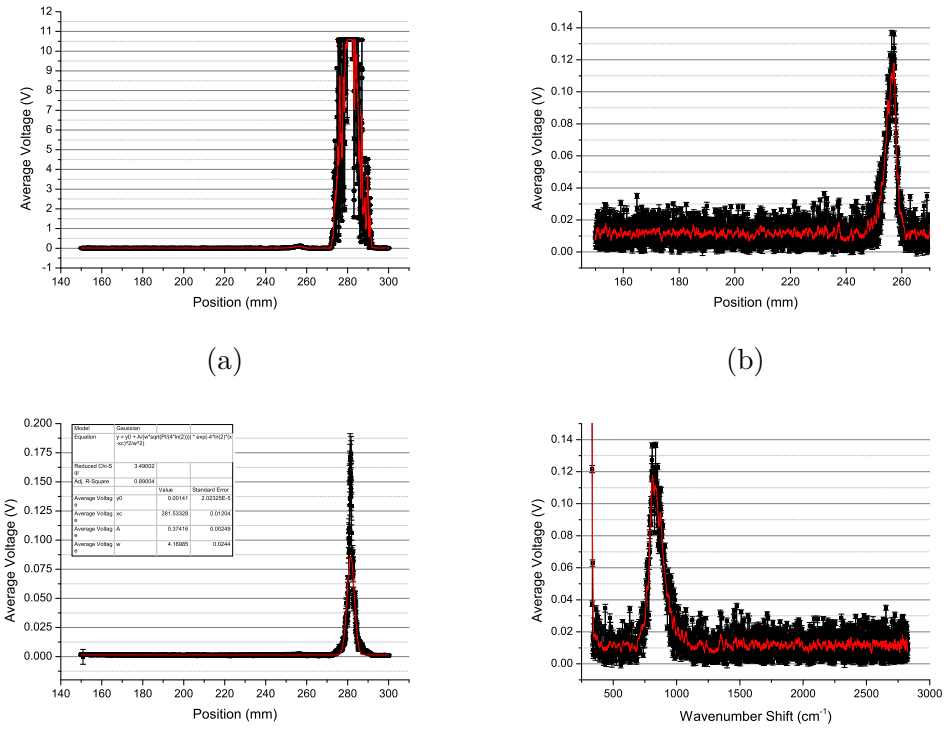

Fig. 5.48 Initial fused hydroxyapatite Raman spectra displayed in terms of detector position on the translation stage in Figures 5.48a, 5.48b and 5.48c and in terms of wavenumber in Figure 5.48d. Figures 5.48a, 5.48b and 5.48d show the fused hydroxyapatite spectra collected with the lock-in amplifier set to 500 μV sensitivity and a time constant of 200 ms. Each spectra is formed of the average of 10 measurements per point with error bars representing the standard deviation and the red line displaying a smoothed spectrum from applying an adjacent average function with a window of 11 points. Figure 5.48c shows the unamplified spectrum generated from 10 measurements averaged together, with the red line showing a Gaussian fit applied to the laser peak to enable the wavenumber scale to be calculated.

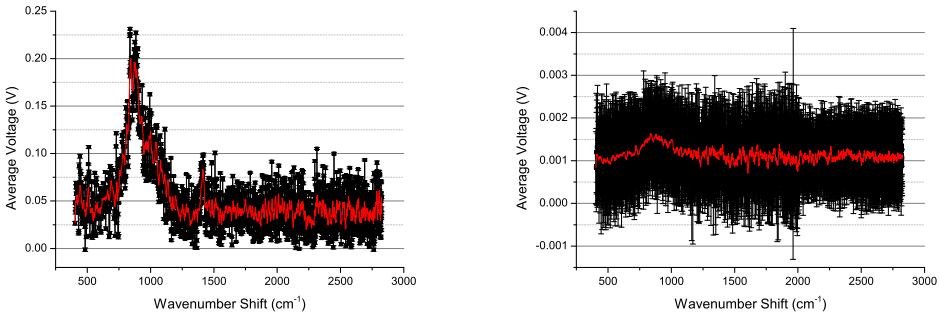

(a) (b)

Fig. 5.49 Fused hydroxyapatite spectra with 5.49a collected with lock-in amplifier set to 200 μV sensitivity and a 2 s time constant and 5.49b being the same spectrum collected with no LIA. The spectra are generated from an average of 10 measurements per point, with error bars representing the measurement standard deviation and the red line representing the smoothed spectra created by adjacent averaging over a window of 11 points.

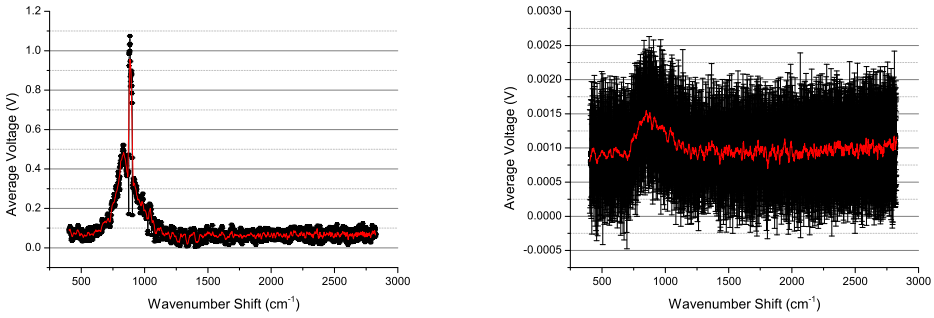

(a) (b)

Fig. 5.50 Fused hydroxyapatite spectra with 5.50a collected with lock-in amplifier set to 50 μV sensitivity and a 5 s time constant and 5.50b being the same spectrum collected with no LIA. The spectra are generated from an average of 10 measurements per point, with error bars representing the measurement standard deviation and the red line representing the smoothed spectra created by adjacent averaging over a window of 11 points.

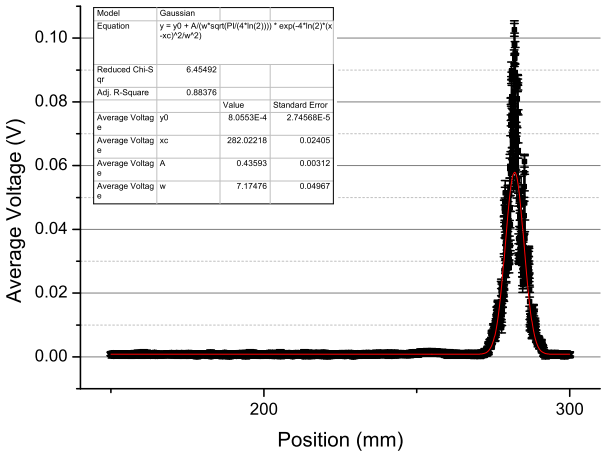

Fig. 5.51 Graph of the non-lock-in amplified porous hydroxyapatite spectrum, with the red line representing the Gaussian fit to the data set.

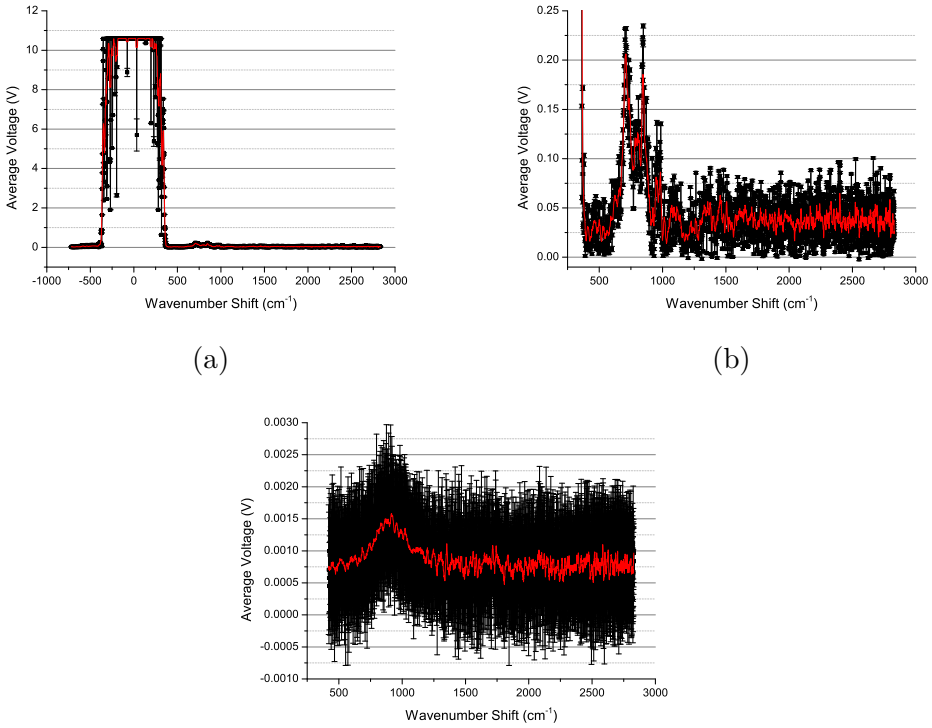

Fig. 5.52 Porous hydroxyapatite spectra with 5.52a and 5.52b collected with lock-in amplifier set to 100 μV sensitivity and a 1 s time constant and 5.52c being the same spectrum collected with no lock-in amplification. The spectra are generated from an average of 10 measurements per point, with error bars representing the measurement standard deviation and the red line representing the smoothed spectra created by adjacent averaging over a window of 11 points.

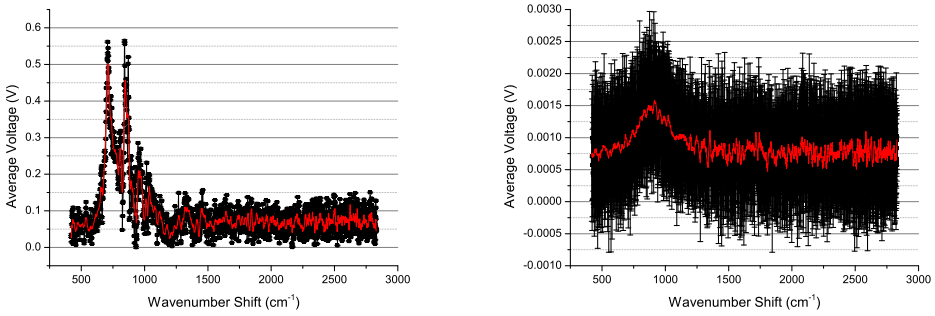

(a) (b)

Fig. 5.53 Porous hydroxyapatite spectrum collected with 5.53a the lock-in amplifier at 50 μV sensitivity and 2 s time constant and without the lock-in amplifier 5.53b. The spectra are generated from an average of 10 measurements per point, with error bars representing the measurement standard deviation and the red line representing the smoothed spectra created by adjacent averaging over a window of 11 points.

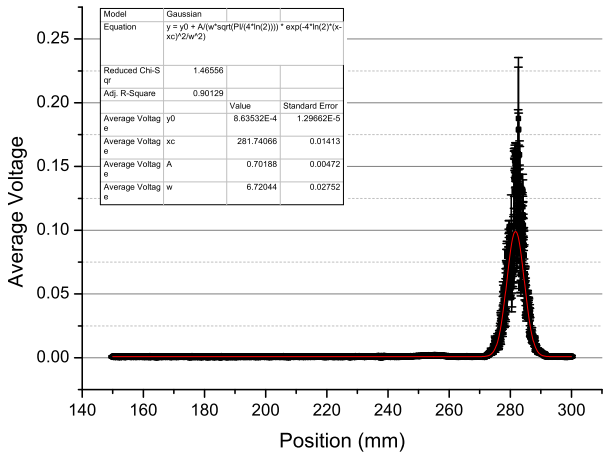

Fig. 5.54 Powdered hydroxyapatite spectrum without lock-in amplification, with respect to detector position. The red line is the Gaussian fit to the laser line used to calculate the wavenumber scale. The spectrum was generated from an average of 10 measurements per point, with error bars representing the measurement standard deviation.

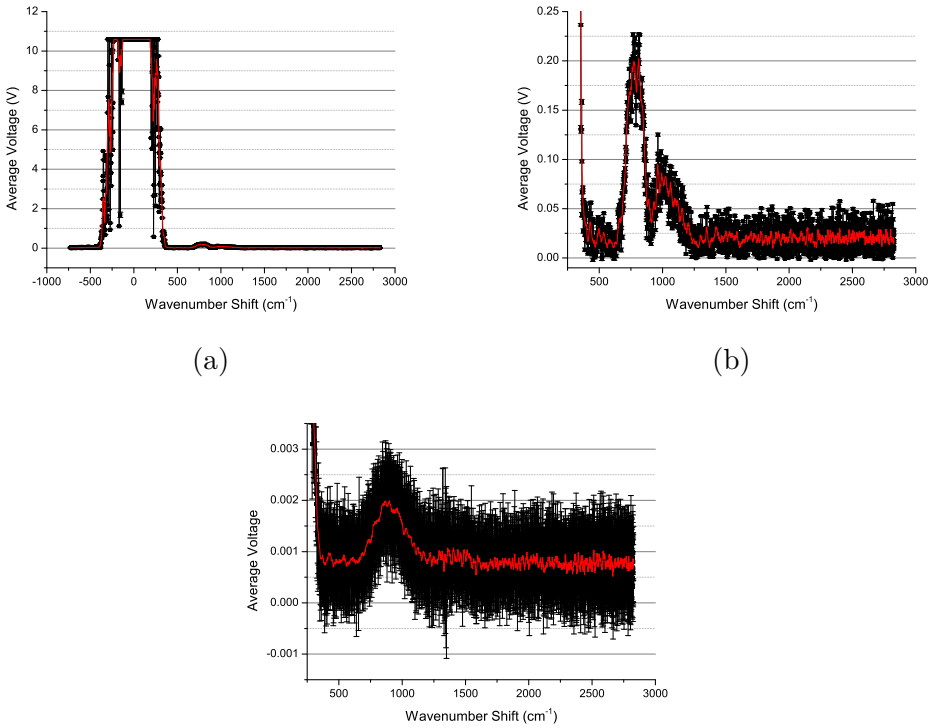

(a) (b)

(c)

Fig. 5.55 Spectra collected from powdered hydroxyapatite collected with (5.55a, 5.55b) and without (5.55c) lock-in amplification at 200 μV sensitivity with a 0.5 s time constant. The spectra are generated from an average of 10 measurements per point, with error bars representing the measurement standard deviation and the red line representing the smoothed spectra created by adjacent averaging over a window of 11 points.

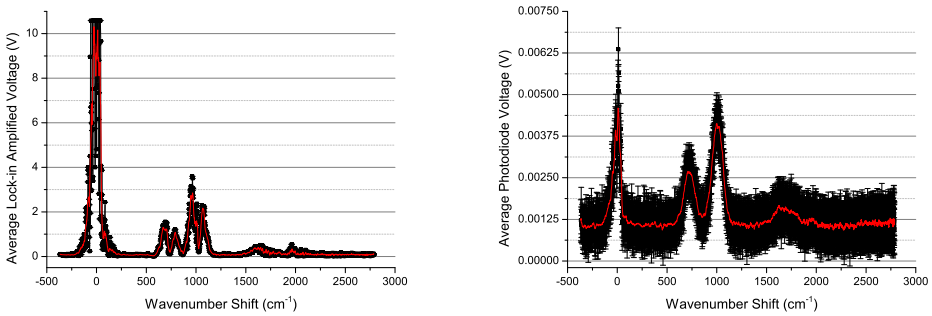

(a) (b)

Fig. 5.56 Spectra collected from an osteogenically differentiated cell culture prepared for SEM analysis. Figure 5.56a displays data collected with lock-in amplification at 50 μV sensitivity with a 2 s time constant, with Figure 5.56b collected without lock-in amplification. The spectra are generated from an average of 10 measurements per point, with error bars representing the measurement standard deviation and the red line representing the smoothed spectra created by adjacent averaging over a window of 11 points.

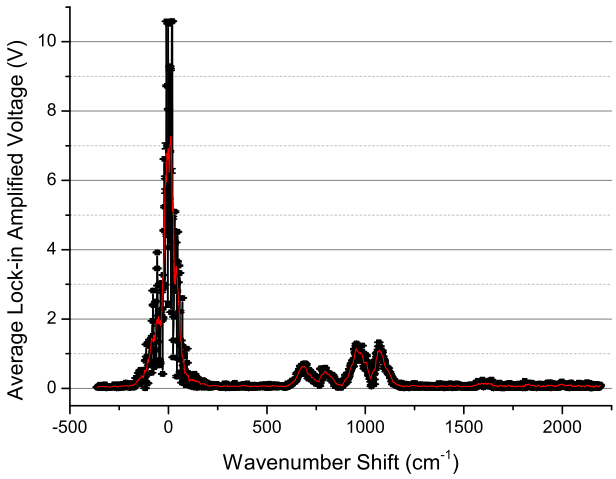

(a)

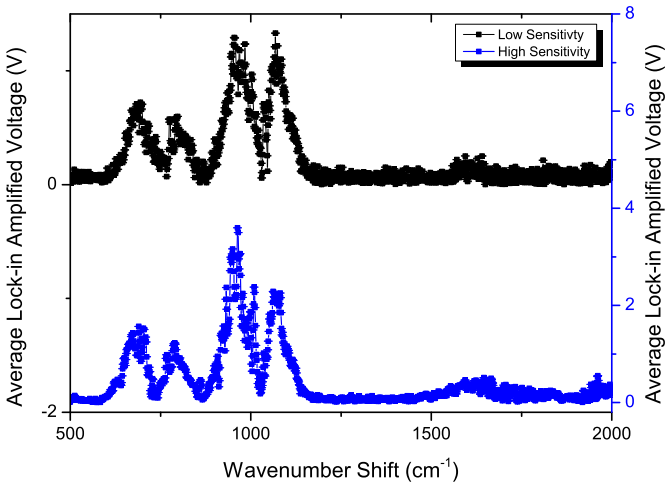

(b)

Fig. 5.57 Spectra collected from an osteogenically differentiated cell culture prepared for SEM analysis. Figure 5.57a displays data collected with lock-in amplification at 200 μV sensitivity with a 200 ms time constant, with Figure 5.57b comparing the high sensitivity data presented in Figure 5.56a with 50 μV sensitivity with a 2 s time constant to the low sensitivity, high speed data of Figure 5.57a. The spectra are generated from an average of 10 measurements per point, with error bars representing the measurement standard deviation and the red line representing the smoothed spectra created by adjacent averaging over a window of 11 points.

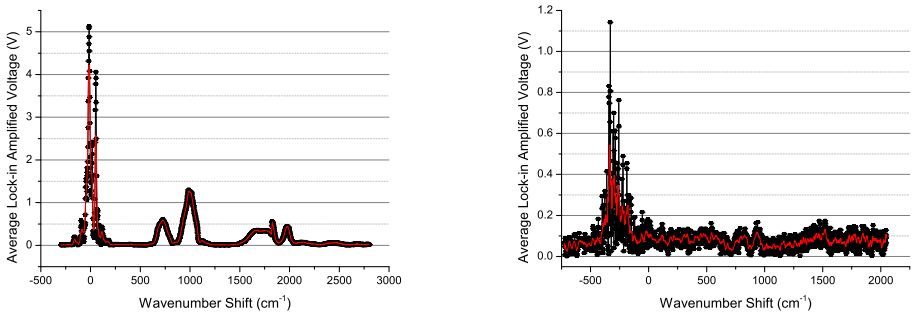

(a) (b)

Fig. 5.58 The spectrum collected from the gold coated mounting sticker was collected as shown in Figure 5.58a. The spectrum was collected at 200 μV sensitivity, with 2 s time constant, and the grating at $(17 \pm 1)°$, with wavenumbers set based on a laser line at 291.95 cm. Figure 5.58b is the spectrum of the gold sputter coated Alvetex® with no cells. The spectrum was collected at 50 μV sensitivity and 2 s time constant, and the grating at 17°. Wavenumbers were set based on a laser line at 281.17 cm. The spectra are generated from an average of 10 measurements per point, with error bars representing the measurement standard deviation and the red line representing the smoothed spectra created by adjacent averaging over a window of 11 points.

this successful generation of Raman spectra at individual points across cell cultures, the next stage was to begin to produce data sets of spectra in 1 and 2 dimensions and to attempt Raman mapping.

5.5 Raman Mapping of SEM Prepared MSC Cell Cultures

Individual spectral measurements provide a sample of the chemical composition in one position of the scaffold. As highlighted above, cell cultures are heterogeneous which means that single measurements are insufficient for full characterisation. As a result, the spectrometer was modified as discussed in Section 4.5.4 to allow for Raman mapping in 1 and 2D. Initially, spectra were collected translated over a line of specimen in order to quickly validate that compositional changes over the spectrum can be captured by the spectrometer using this method. Additionally, the process of collecting full spectra across a line of the cell culture was able to allow for identification of preliminary mapping markers for Raman imaging applications.

1D data sets were initially captured as sets of full spectra collected along a line of the culture using automated translation of the cell culture. Initially data was captured for an osteogenic cell culture along a 5 mm line with spectra captured at every 0.25 mm. The generation of spectra as given in Figure 5.62 demonstrates that

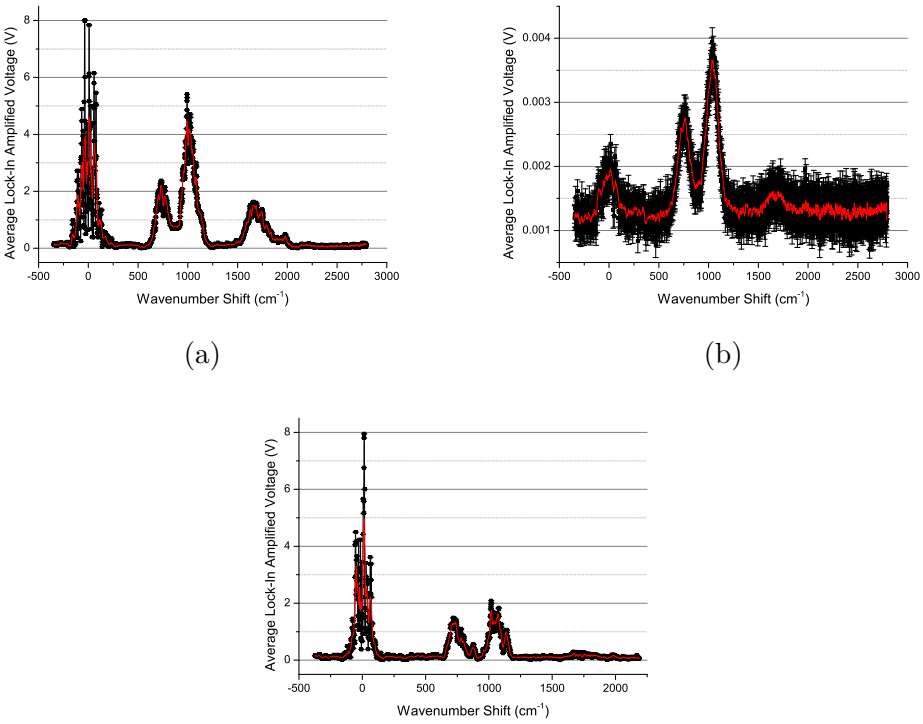

Fig. 5.59 Spectra collected from a proliferation control cell culture prepared for SEM analysis. Figure 5.59a displays data collected with lock-in amplification at 50 μV sensitivity with a 2 s time constant, with Figure 5.59b collected without lock-in amplification for demonstration. Figure 5.59c displays data collected with lock-in amplification at 50 μV sensitivity with a 2 s time constant at a different position on the scaffold. The spectra are generated from an average of 10 measurements per point, with error bars representing the measurement standard deviation and the red line representing the smoothed spectra created by adjacent averaging over a window of 11 points.

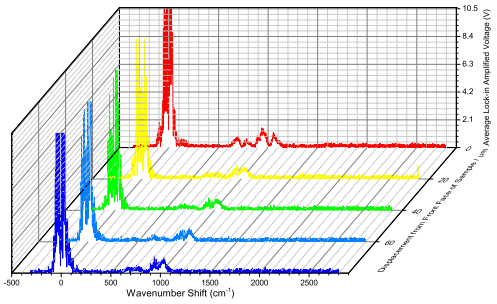

Fig. 5.60 Spectra collected from an osteogenic cell culture with depth of focal spot collected with lock-in amplification at 50 μV sensitivity with a 200 ms time constant at 20 μm intervals. The spectra are generated from an average of 10 measurements per point.

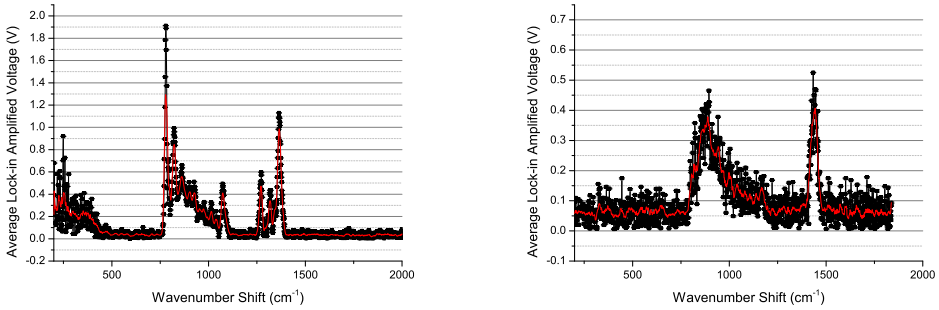

(a)

(b)

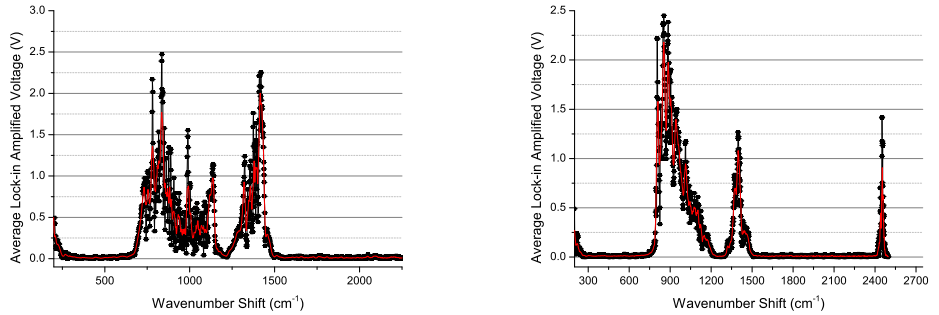

(c)

(d)

Fig. 5.61 Spectra collected from 5.61a silica, 5.61b gold and carbon sticker area, 5.61c cell culture of MSCs grown in proliferation medium and 5.61d cell culture of MSCs grown in osteogenic medium. The spectra are generated from an average of 10 measurements per point, with error bars representing the measurement standard deviation and the red line representing the smoothed spectra created by adjacent averaging over a window of 11 points.

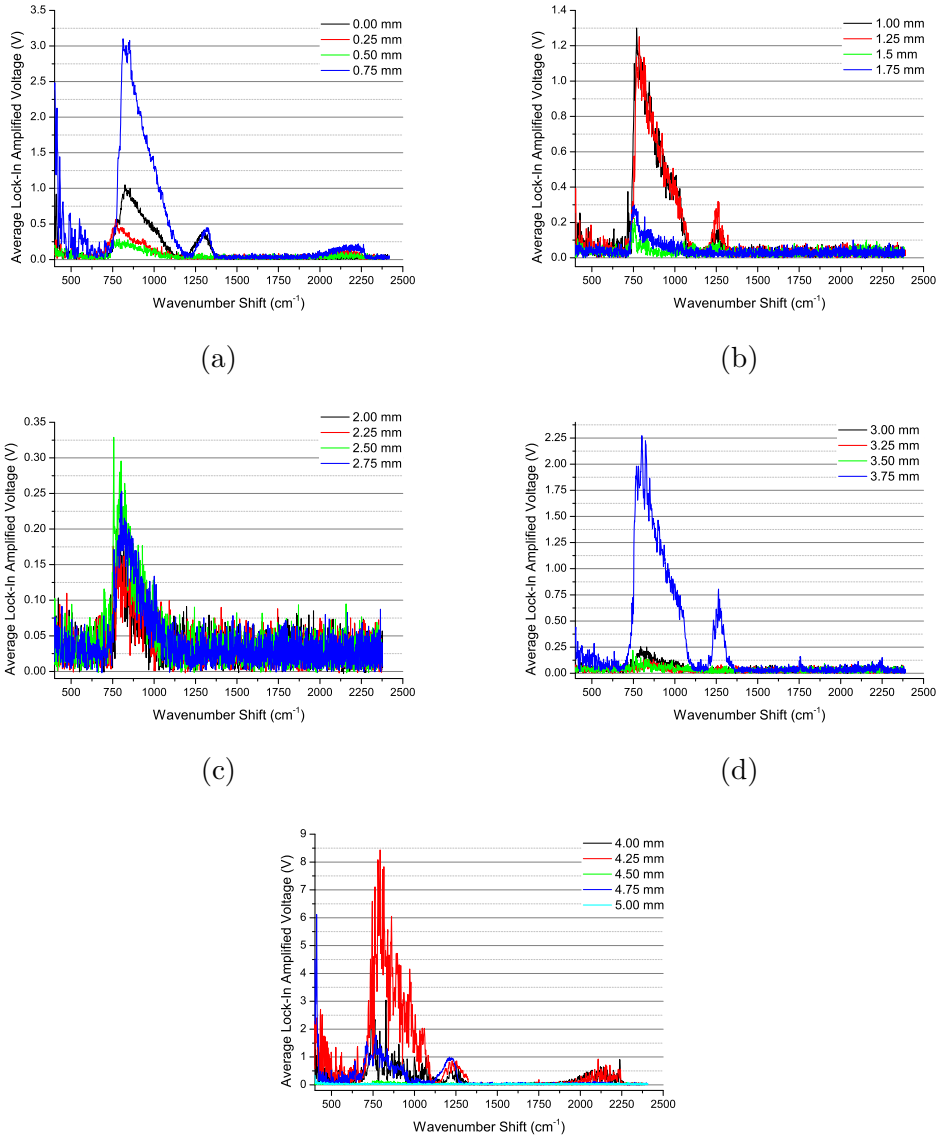

Fig. 5.62 Spectra collected from an SEM prepared cell culture grown in osteogenic medium, sampled along a line of scaffold of 5 *mm* length in 0.25 *mm* steps. The spectra are generated from an average of 10 measurements per point and demonstrate that the spectrometer can detect changes in cell culture composition.

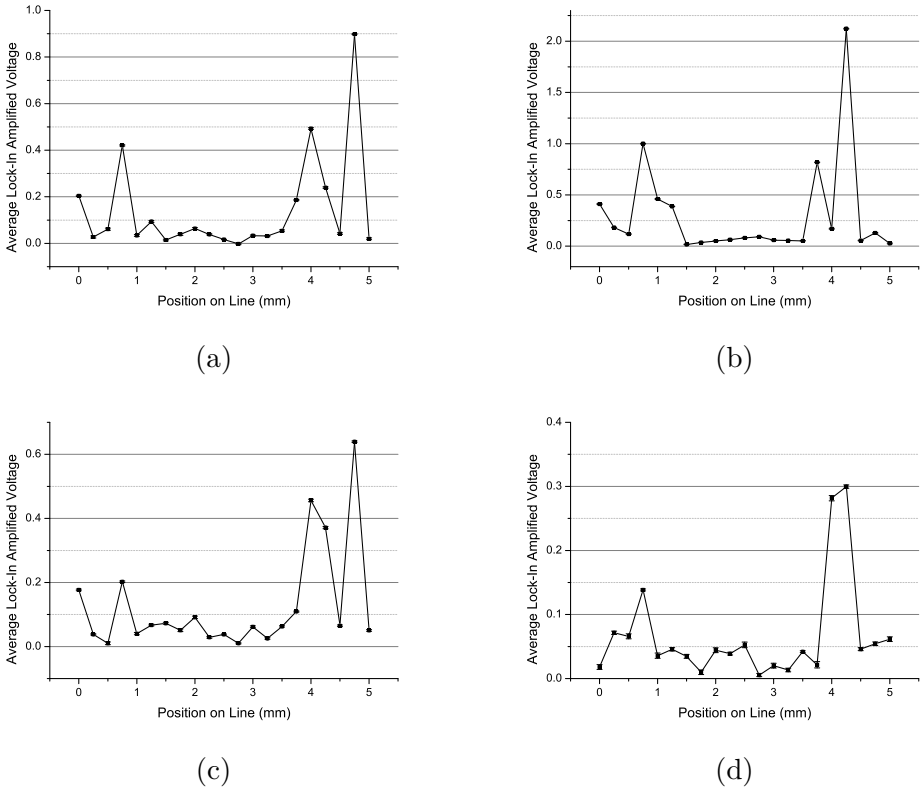

Fig. 5.63 Intensity line profiles collected from an SEM prepared cell culture grown in osteogenic medium along a line of scaffold of 5 mm length in 0.25 mm steps at (5.63a) 703.86 cm^{-1}, (5.63b) 970.79 cm^{-1}, (5.63c) 1210.2 cm^{-1} and (5.63d) 2149.1 cm^{-1}. The spectra are generated from an average of 10 measurements per point. This demonstrates that the spectrometer can produce maps of the changes across a cell population.

there are spectral changes which can be mapped across the surface of the cell culture. This is a proof of concept that the spectrometer can provide mapping functionality. Therefore, the next logical progression is to map the presence of specific spectral features across a line. The difficulty in this process is that the laser line position moves slightly during the process. Therefore, the spectral position can only be estimated based on a pre-evaluated laser line position. As a result, any laser line drift will not be accounted for. An initial mapping methodology used was to strip data from the 1D line spectra already generated and plot intensity for a certain estimated wavenumber across the line of previous data collection. Therefore, 1D spectral maps were plotted at approximately 703.86 cm^{-1} (277.25 mm), 970.79 cm^{-1} (268.35 mm), 1210.2 cm^{-1} (259.40 mm) and 2149.1 cm^{-1} (215.00 mm) as calculated by averaging the wavenumbers for data collected at a single spatial collection point across all points on the sample. Line profiles across the sample at each of these spectral points are given in Figure 5.63.

The next stage in moving towards 2D mapping was to set up a 1D mapping

system at a single spectral position and map the intensity across a longer, higher resolution line. In order to do this in an acceptable amount of time, the collection of a full spectrum is avoided. Instead, as in Figure 5.63, data is collected from a single spectral point and the sample simply moved through the laser line. In this case, considering the areas of change depicted in Figures 5.62 and 5.63, and previously collected spectra, the detector was fixed at a position relative to the translation stage of 215 mm which approximately corresponds to a wavenumber shift of 2149.1 cm^{-1}, then 260 mm which approximately corresponds to a wavenumber shift of 1194.6 cm^{-1}. Initially, spectra were collected with a resolution of 10 μm over 1 cm, then the scan at 2149.1 cm^{-1} was repeated at a resolution of 1 μm over a 1 cm area as shown in Figure 5.64. The figure charts the transition from the the gold coated SEM mount to the cells (at 2343 μm) and Alvetex® , back onto the SEM mount (at 8422 μm) then onto the optics mount at (9372 μm). These transitions can be visualised in the figure with the highest intensity areas over the cells, but demonstrating a spatial variation, indicating the heterogeneous nature of the cell culture.

The spectra given in Figure 5.64 map from the carbon sticker to the scaffold with cells, to the scaffold alone, back onto the carbon sticker. After this 1D mapping pilot, a transition was made to a 2D mapping system. As a natural extension of the 1D mapping, 2D mapping was repeated at 2149.1 cm^{-1} for the osteogenic sample, both with and without lock-in amplification as given in Figure 5.65, which may be a spectral band representing water content [276, 277]. In the case of the lock-in amplified data as given in Figure 5.65b, the sudden changes in amplitude result from changes in overall light level in the laboratory during the experiment, however this is removed by the action of the lock-in amplifier. In addition, three clear regions can be identified in the Raman maps; the carbon sticker at the top of the map, the band of Alvetex® with no cells, and the area of Alvetex®where cells and ECM have been cultured. After initial data collection and processing the data was normalised to the maximum signal in both the lock-in amplified and non-amplified cases to allow for a more direct comparison of the data, as given in Figure 5.66.

Figure 5.66 demonstrates that the lock-in amplification increases the differentiation between the regions on the structure, the spectrometer achieving a suitable level of Raman imaging of the sample. This acts as a strong proof of concept that this is a useful tool. As a consequence, rather than continually mapping more samples, the focus of the project shifted to try to take the base innovation in the Raman system of lens vibration lock-in amplification and build it into a commercialisable spectrometer set up.

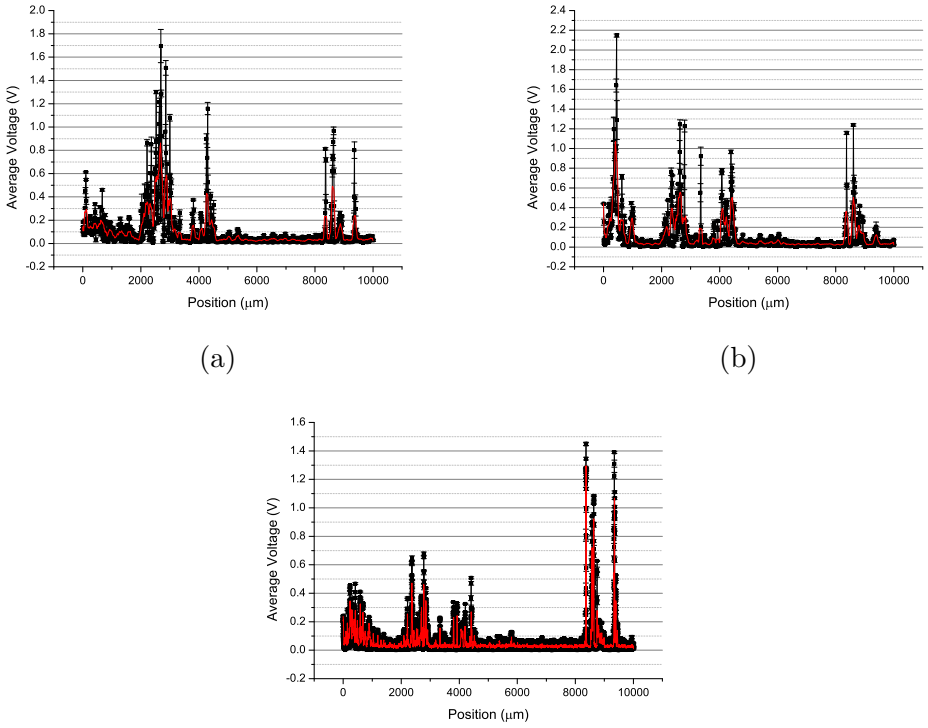

Fig. 5.64 Intensity line profiles collected from an SEM prepared cell culture grown in osteogenic medium to test the system's automatic 1D spectral collection capabilities. 1D profiles were acquired along a line of scaffold of 10 mm at (5.64a) 2149.1 cm^{-1} with a resolution of 10 μm (5.64b) 1194.6 cm^{-1} with a resolution of 10 μm and (5.64c) 2149.1 cm^{-1} with a resolution of 1 μm. The spectra are generated from an average of 100 measurements per point with the lock-in amplifier at 200 μV and 200 ms.

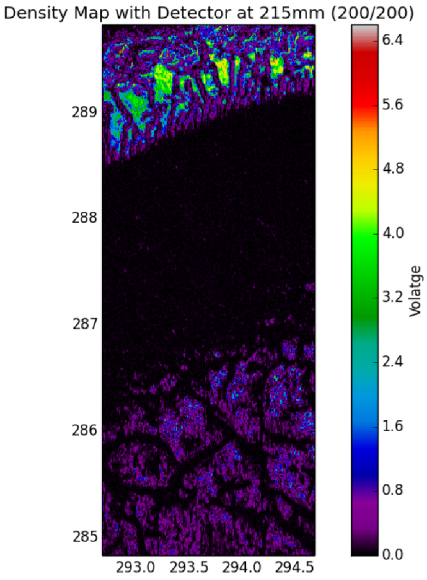

(a)

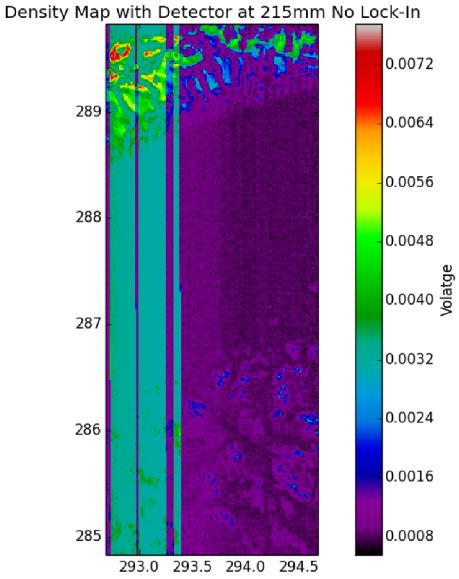

(b)

Fig. 5.65 2D Raman intensity map over a 2x5 mm area at 2149.1 cm^{-1} with a resolution of 10 μm (5.65a) presents the data with lock-in amplification at 200 μV and 200 ms and (5.65a) presents the non lock-in amplified data. All data represented is derived from the average of 100 measurements.

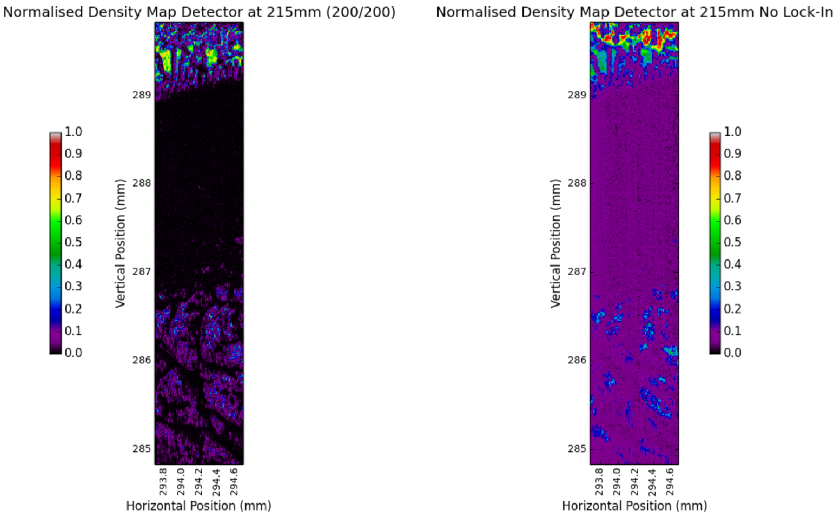

(a)

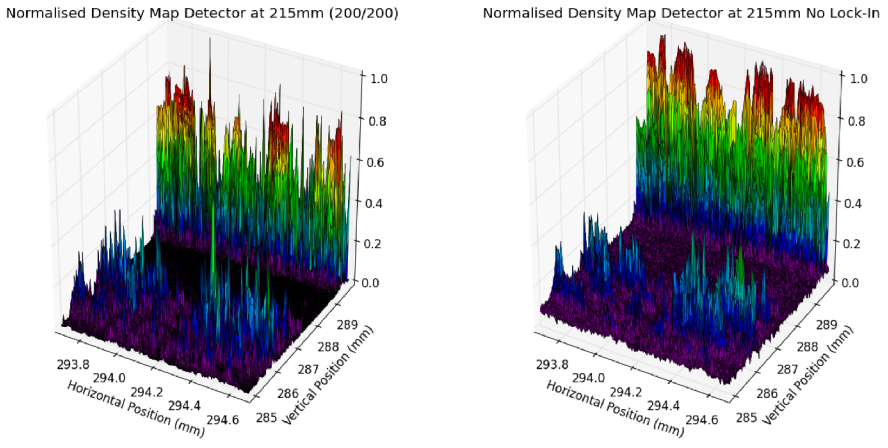

(b)

Fig. 5.66 2D Raman intensity map over a 2x5 mm area at 2149.1 cm^{-1} with a resolution of 10 μm (5.66a) presents the normalised data with and without lock-in amplification as a 2D map and (5.66b) presents the data as a 3D surface plot. All data represented is derived from the average of 100 measurements, with lock-in amplified data collected at 200 μV and 200 ms.

5.6 Raman Spectra Collected with the Compact CCD Spectrometer

To be able to introduce this method of Raman spectroscopy as a viable laboratory analytical tool for use outside the laser laboratory and improve the suitability for live cell analysis, the photodiode, grating, and translation stage were replaced with a compact CCD spectrometer. Initially Raman spectra were collected from a silica sample using the CCD spectrometer and its own processing functionality. As can be seen in 5.67, the spectrometer cannot extract a silica spectrum at this power level without background subtraction. As a result there is a clear need to develop lock-in amplification methods to use with this spectrometer in order to improve the ability of the spectrometer to work at low incident powers. It is notable when background subtraction is performed there are striking similarities between the spectra given in Figure 5.67b and the raw spectra given in Figure 5.39d. It can be seen in the figures that the best case spectra appear similar to the non-amplified spectra previously collected.

Using the strategies for lock-in amplification described in Section 4.6 of Chapter 4, silica spectra were collected using a chopped lock-in amplified signal. In this case the average spectra of 10 constituent background and silica spectra, collected with an integration time 50 s, were used form the square wave for lock-in amplification. The lock-in amplified spectrum was produced by lock-in amplifying at 10 mV sensitivity and 200 ms time constant, averaging the first 10 data points after one time constant together to form the final spectrum, as plotted in Figure 5.68a. For comparison, the spectrum without lock-in amplification (average silica spectrum minus average background spectrum) is plotted in the same Figure 5.68b. As expected from results with the original spectrometer, chopping improves the spectrum collected, but does not full provide all the detail from the spectrum. Additionally, it is worth noting that amplitude modulation is not able to remove the Raman background from silica in the optics train.

Next, data was collected from a simulation of lens vibration. This used a waveform constructed of five spectra, with an integration time of 50 s, collected with 45 V and 75 V applied to the lens actuator. When a constant voltage is applied to the piezoelectric crystal the shape of the crystal changes thickness in proportion to the voltage applied [278]. Figure 5.69 shows the average spectra collected at each voltage and the difference spectrum formed by subtracting the data at each voltage. Using this data, an output waveform was constructed and lock-in amplification applied with a sensitivity of $10mV$ and 200 ms time constant. The final spectrum was constructed by averaging the first 10 data points after one time constant at each spectra point.

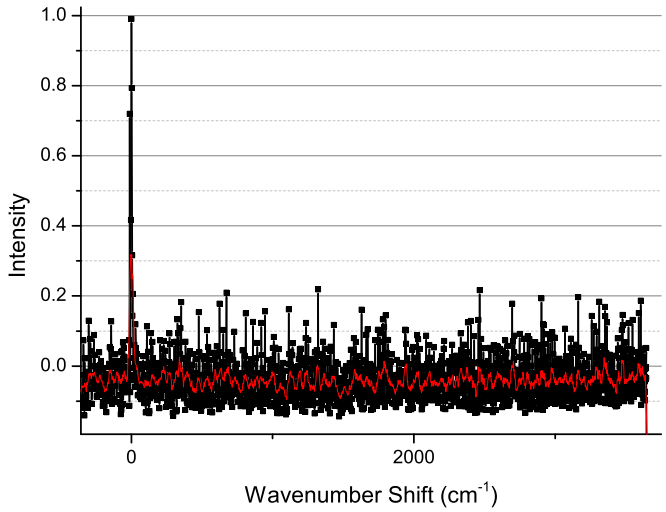

(a)

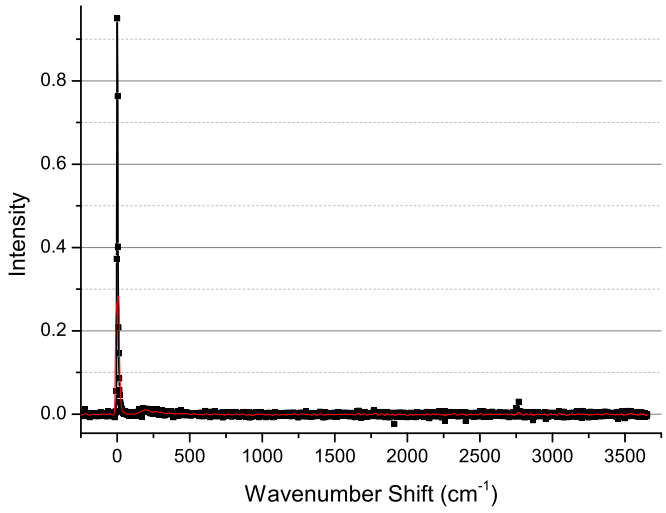

(b)

Fig. 5.67 Silica spectra collected with the CCD spectrometer with an integration time of 30 *s*. Figure 5.67a gives the silica spectrum and Figure 5.67b gives the silica spectrum minus the background spectrum.

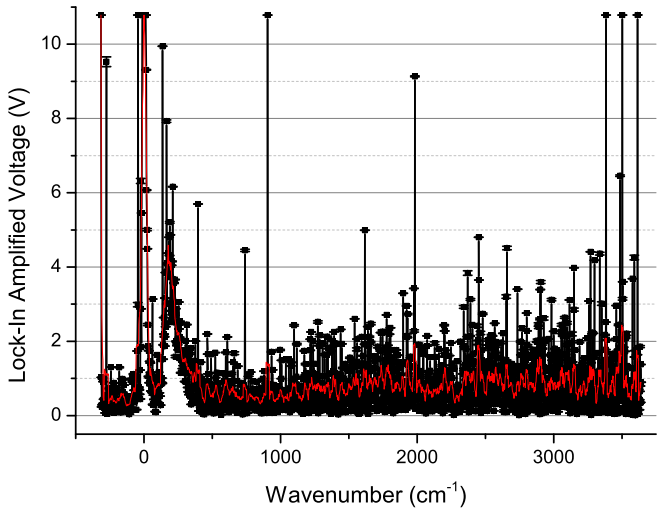

(a)

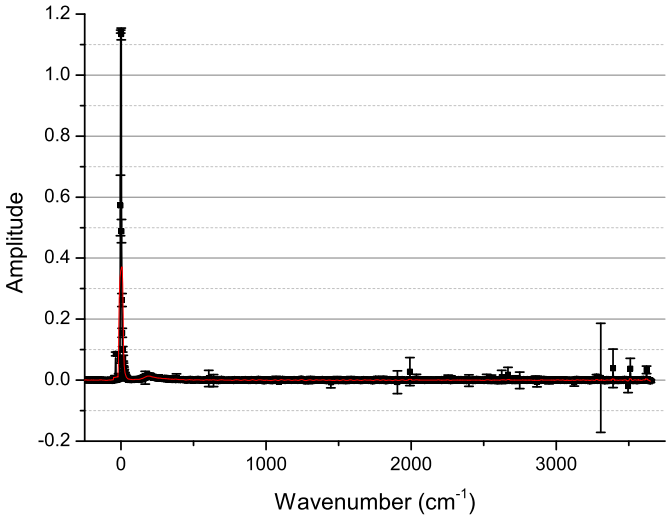

(b)

Fig. 5.68 Silica spectra collected with the CCD spectrometer using a 50 s integration time, averaged over 10 measurements for the laser on and off. This was sequenced to simulate a chopper and processed using lock-in amplification at 10 mV sensitivity, 200 ms time constant, and the final spectra constructed from the first 10 measurements after one time constant had elapsed, the error bars represent one standard deviation. Figure 5.68a gives the lock-in amplified silica spectrum and Figure 5.68b gives the corresponding average silica spectrum minus the background spectrum.

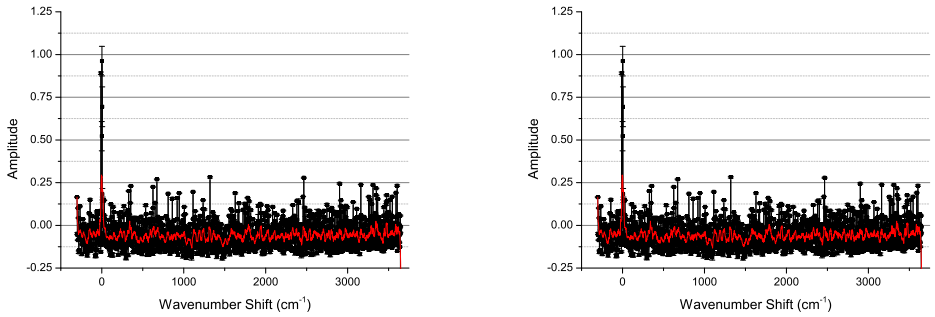

(a)

(b)

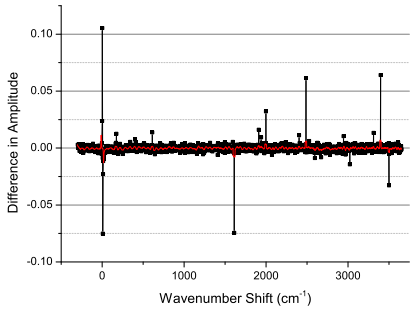

(c)

Fig. 5.69 Silica spectra collected with the CCD spectrometer with the lens displaced by applying a constant 45 V (5.69a) and 75 V (5.69b) across the piezoelectric crystal, and the difference spectrum (5.69c). The spectra are formed from an average of 5 spectra collected at 50 s integration time, with the red line showing adjacent averaging over a window of 11 points. The difference spectrum has some identifiable features suggesting that lock-in amplification may be possible using this signal.

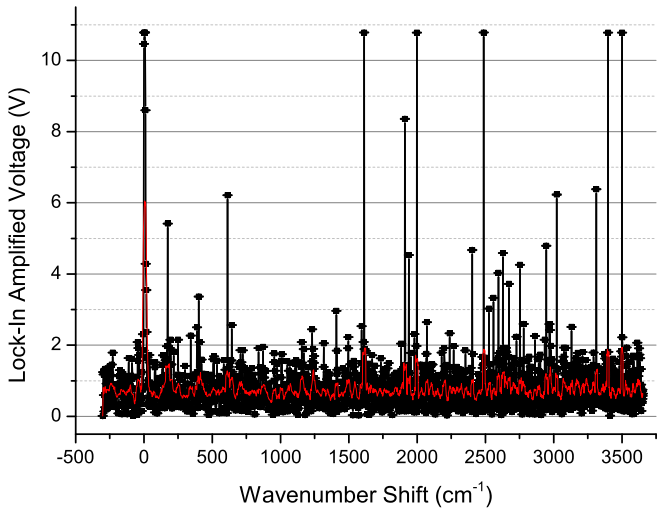

Fig. 5.70 Lock-in amplified silica spectrum with simulated lens vibration. The spectrum was generated from spectra collected with the lens displaced by applying a constant voltage 45 and 75 V using the piezoelectric lens as described above, to produce a constant different displacement in each case. Lock-in amplification was applied at 10 mV sensitivity, 200 ms time constant, and averaging the first 10 measurements collected after one time constant. The red line shows adjacent averaging over a window of 11 points

Figure 5.70 shows that this methodology doesn't instantly provide the improvement an actual vibration does. This may indicate that the effect of the transit of the focal spot through the front face is instrumental in producing the signal the lock-in amplifier extracts. Subsequently, other methods were applied to try to improve the spectrum based upon the simple square wave output method. It was determined that a likely avenue for improvement was the use of simulated dual phase lock-in amplification. 50 spectra were collected with a 10 s integration time for the background, 10 V piezoelectric displacement and 90 V piezoelectric displacement and averaged together. In the first pass, the average spectra were formed into a simulated chopped signal and lock-in amplified at 20 mV sensitivity and 200 ms time constant. The lock-in amplified spectra were normalised to 10 V, and the new simulated waveform was output and lock-in amplified, at 500 mV sensitivity and 200 ms time constant, to produce a final dual phase lock-in amplified spectrum. The chopped spectrum and final dual phase lock-in amplified spectrum are given in Figure 5.71, and appears to present a more detailed spectrum, closer to that produced with full lens vibration and light collection via a photodiode. Therefore, it appears that with further refinement lens vibration lock-in amplification could be used as an adjunct to commercial spectroscopy systems to allow for low power high resolution spectroscopy of biological constructs.

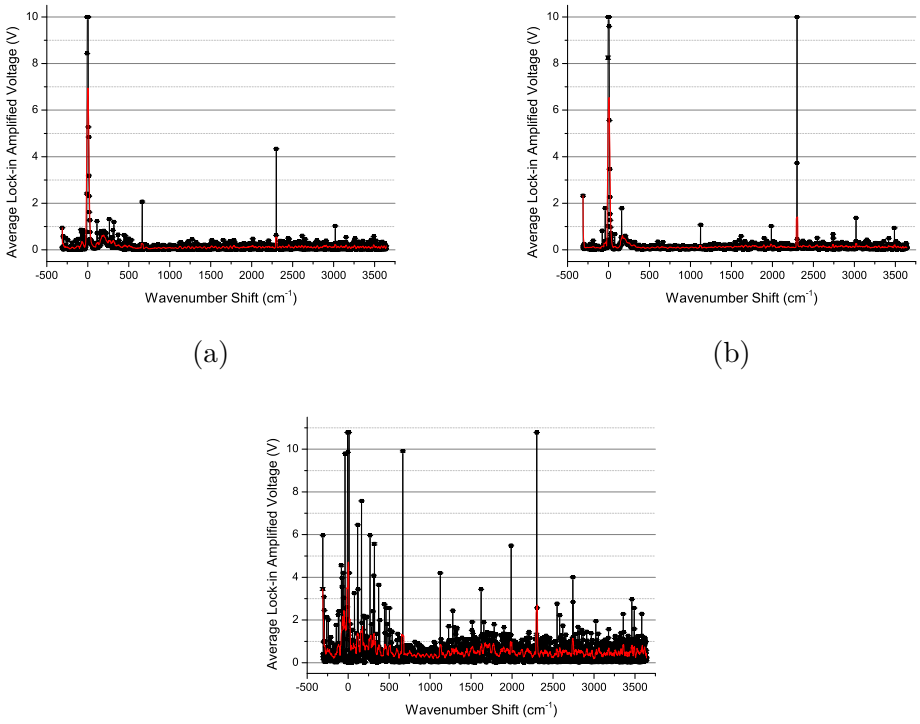

Fig. 5.71 Spectra lock-in amplified to a simulated chop for the lens displaced by 10 V (5.71a) and 90 V (5.71b) through piezoelectric electric mount with 20 mV and 200 ms. The data presented is the average of the first 10 data points collected after 1 time constant. This data was then constructed into a waveform to simulate lens vibration and lock-in amplified to create a dual phase lock-in amplified spectrum (5.71c) at lock-in amplified at 500 mV sensitivity and 200 ms time constant. In each case the error bars represent one standard deviation and the red line showing adjacent averaging over a window of 11 points.

Chapter 6

Discussion

6.1 Conventional Analysis of MSC cultures

6.1.1 Analysis of Alvetex® Scaffolds Statically Seeded with MSCs

Staining of MSC Cell Cultures

The staining performed for the initial 2D cell cultures in both osteogenic and proliferative medium were very encouraging. The cell cultures had proliferated well, with bone forming nodules exhibited in both the proliferative and osteogenic medium conditions. In addition, alkaline phosphatase and alizarin red staining suggests that the cells had successfully mineralised, along with the proliferative control. Due to the nature of the endpoint staining used, there was no analytical way to quantify the degree of mineralisation of the different samples, other than by observing the vibrancy of staining.

Figure 6.1 depicts the stained 2D cultures and appears to suggest that overall the cultures grown in proliferation medium had greater expression of mineralisation markers over the whole well. However, the cultures sustained with osteogenic medium have small regions where the expression of mineralisation markers is very strong. The proliferative control is likely to have mineralised due to the large cell density present in these wells driving the formation of mineralisation nodules. However, in the lower cell density areas of the cells cultured with osteogenic medium, mineralisation still occurs, indicating that the medium is driving the mineralisation process.

From the results of these 2D cultures, it is possible to assert that the cells used in the experiment have the capacity to mineralise and that the medium applied to the cells did not have an adverse effect on the cultures. Therefore, any problems in the 3D Alvetex® cultures is down to the nature of the 3D system itself rather than

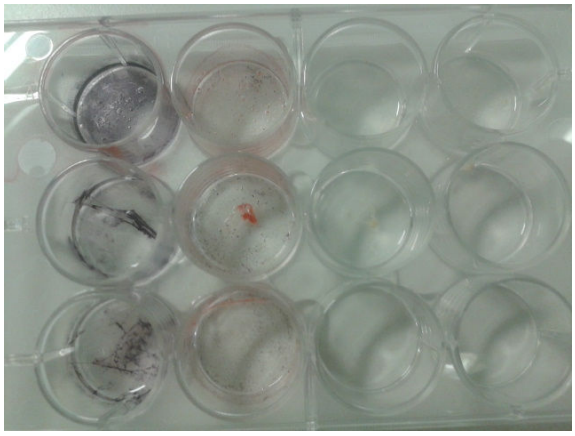

Fig. 6.1 Photograph of the 2D control cultures at experiment termination. The top row was cultured with proliferation medium, with the second and third rows cultured with osteogenic medium. The first column is stained with alkaline phosphatase and the second column is stained with alizarin red. The final two columns do not contain any cells.

a problem with the medium or a problem directly stemming from an abnormality in the cells used in the experiment.

Looking at the histological results from haematoxylin and eosin staining in both the cryosectioned and wax embedded constructs for the 3D Alvetex® cultures (Figures 5.4 to 5.13), there is a clear problem with proliferation into the centre of the scaffold. The results of the staining suggest that the ultimate cell density was not high enough, which was reinforced by the observation that a large population of cells was lost from the scaffold either through migration or by being washed out during media changes. Therefore, there may also be a problem with the quality of the attachment to the scaffold. The haematoxylin and eosin staining also suggests that the cells are mostly confined to the outer surfaces of the scaffold, with very little migration into the bulk of the scaffold. This could have been a result of the cell density being too low, or because the scaffold was not conducive to supporting 3D bone cell cultures. Another noticeable feature, is that there was only small about of eosin staining present in the sections. This is suggestive that there is a high cell density present, but with relatively little extracellular matrix produced [244]. Staining for toluidine blue, which stains acidic cellular components in blue (Figure 5.14), also provides similar results to those obtained from haematoxylin and eosin staining. The scaffold cultured in proliferation has a greater level of staining. Therefore, it has more DNA, RNA and other acidic tissue components present than the scaffold cultured in osteogenic medium. This provides further evidence that, unsurprisingly, there was more cellular material present in the scaffold cultured in proliferation medium.

Staining for osteogenic markers using alizarin red and alkaline phosphatase (Fig-

ures 5.11 and 5.12) on cryosectioned Alvetex® suggests that the scaffolds cultured in proliferation medium have a larger number of mineralising colonies than the scaffolds cultured in osteogenic medium. For the scaffold in proliferation medium, the greatest staining for alkaline phosphatase is on the surface of the scaffold. This is to be expected, as the haematoxylin and eosin stains show that the surface of the scaffold has the greatest concentration of cells and as a result is more likely to produce mineralising nodules. However, there is also evidence of staining for alkaline phosphatase in the center of the scaffold as well, suggesting that some cells have proliferated into the scaffold and have begun to form a small number of mineralising nodules inside the scaffold. In comparison, the alizarin red staining for the same scaffold is relatively poor and confined to the scaffold surface. Alkaline phosphatase is an early marker of bone formation. Therefore, the low level of alizarin red staining combined with the strong level of alkaline phosphatase staining (compared to culture in osteogenic medium) suggests that the cells have not fully differentiated [279]. In many ways, this is not unexpected as these cells have not received any supplements to enhance osteogenic differentiation. Sections from the scaffold cultured in osteogenic medium have a very limited amount of alkaline phosphatase staining present in the scaffold. The little stain that is present is highly concentrated in a few small areas close to the scaffold surface. The alizarin red staining for this scaffold also shows a few small areas of strong staining close to the surface of the scaffold, with a larger amount of strong alizarin red spots present compared to the number of alkaline phosphatase spots present. This data suggests primarily that the cells were unevenly spread over the scaffold and didn't have a high enough cell density to form mineralising nodules. However, in the few areas where nodules did form, the MSCs cultured in osteogenic medium have differentiated more than the MSCs cultured in proliferation medium. This can be inferred as there are more areas of mineralisation than of alkaline phosphatase activity and the areas where mineralisation has occurred have stained strongly, indicating a significant deposit is present.

μ-CT of Scaffold Sample

As in all CT processes, μ-CT works by collecting 2D X-ray absorption projections at many angles through the sample. X-rays are a form of electromagnetic radiation, which interact with the materials they pass through by absorption or scattering processes. As a result the X-ray intensity is reduced according to Beer's law when it passes through a material.

$$I(x) = I_0 e^{-\mu(x)} [280], \tag{6.1}$$

where $I(x)$ is the X-ray intensity after interaction, I_0 is the X-ray intensity before interaction and μ is the linear attenuation coefficient describing the fraction of X-ray intensity lost for every centimetre travelled in the interaction. As different materials have different linear attenuation coefficients, they absorb X-rays to different extents, which leads to contrast in an X-ray image, whereby denser materials exhibit larger values of linear attenuation coefficient and so are more strongly absorbing of X-rays. In μ-CT, X-ray projections are collected in a ring around the imaged object. These projections are then reconstructed into slice-wise data through the application of the filtered back projection algorithm [110]. When projections are obtained for all levels within an object, it is then possible to produce a slice by slice reconstruction of the object as a map of X-ray absorbency in different areas of the object. In the scaffolds there should be approximately three different attenuation coefficients present, one for the Alvetex® scaffold, one for the hydroxyapatite mineral, and one for the cells and the proteins they create. Alvetex® is made of polystyrene, which has a linear attenuation coefficient of 0.19822 cm^{-1} [281] at 60 keV, typical hydroxyapatite has a linear attenuation coefficient of 1.28205 cm^{-1} [282] at 60 keV, and finally soft tissues have a linear attenuation coefficient of 0.26288 cm^{-1} [281] at 60 keV. Therefore, the strongest signal will be obtained from any hydroxyapatite particles present in the scaffolds, followed by the cellular component with the Alvetex® producing the lowest absorption of X-rays.

Examining the CT results, the maximum z projections and thresholded images (Figures 5.8 to 5.9), there are more areas with high pixel values and therefore, high linear attenuation coefficients in the osteogenic samples. Therefore, it is clear that the scaffold cultured in osteogenic medium has a greater amount of mineralisation than the two scaffolds cultured in proliferation medium. The CT images also show that the mineral deposition is not uniform, which in turn indicates a non-uniform distribution of mineralising nodules and cells. If only the histology results are considered, it appears that the scaffolds cultured in proliferation medium exhibited more widespread of mineralisation. However, histological slides examine thin sections of the scaffold and due to the non-uniform mineral deposition it appears that the slices used for examination of calcium deposition were not representative of the full scaffold sample. Nevertheless, the cross sectional views of the scaffolds confirm that the majority of higher density areas are on the scaffold surfaces, rather than in the centre.

SEM of Scaffold Samples

SEM analysis of the scaffold samples yielded similar results to those obtained with μ-CT, but it also enabled more detailed visualisation of the scaffold's surface (Figures 5.15 to 5.18). The SEM images clearly show that the cells have formed a layer

over the top of the Alvetex® without fully penetrating into the scaffold. Additionally, when comparing the samples cultured in osteogenic medium to those cultured in proliferative medium, those cultured in osteogenic medium appear to have a higher number of visible mineralising nodules present on the surface of the scaffold.

Implications of the Analysis of Alvetex® Scaffolds Statically Seeded with MSCs

Considering the analysis data as a whole, it can be concluded that the initial differentiation and mineralisation of MSC cells was successful using the cell culture technique. However, there were potential areas for improvement of the 3D cultures on Alvetex®, with a clear need to try to improve cell density, attachment and migration into the scaffold. Therefore, a second attempt at culturing the MSCs on the scaffold was conducted, where a biological coating and dynamic seeding were used to try and improve the outcome of the cell culture process, the method for which is described in Section 4.1.2.

6.1.2 Analysis of Collagen Coated Alvetex® Scaffolds Dynamically Seeded with MSCs

Quantitative Alkaline Phosphatase Assay

In this experiment, alkaline phosphatase content was quantitatively analysed for all scaffolds (Figures 5.21 to 5.22). In the assay, alkaline phosphatase enzyme activity is measured by examining the concentration of p-nitrophenol at two time points via optical density. The assay demonstrates no alkaline phosphatase activity is present on the scaffolds without cells, as these scaffolds produced negative optical density and concentration values, which are likely due to statistical fluctuations in the plate reader. This measurement means that any concentration of p-nitrophenol measured is likely due to the activity of alkaline phosphatase and not due to the scaffolds releasing a substrate in the p-nitrophenol phosphate solution. Therefore, the assay clearly demonstrates that there is more alkaline phosphatase activity in the scaffolds cultured in proliferative medium than the scaffolds cultured in osteogenic medium. There are a variety of potential reasons for this observed increase. Firstly, alkaline phosphatase is an early bone marker. Therefore, it would be expected that more mature cultures of differentiating MSCs have a lower concentration of alkaline phosphatase than immature cultures. As a result, the MSCs cultured in osteogenic medium would be expected to have a lower concentration than those cultured in proliferation medium [283]. Secondly, the higher the number of cells, the higher the concentration of alkaline phosphatase which will be produced. Cells cultured in

differentiation medium should not proliferate, meaning that it could be possible for the proliferating cells to be producing more alkaline phosphatase due to their large number, rather than purely due to their differentiation state alone. In order to fully interpret the source of the higher concentration of increased alkaline phosphatase concentration in the cells cultured in proliferation medium, the number of cells in each scaffold would need to be known as measured by the CytoTox96 assay [129] or a viability assay such as the MTT assay [284]. However, in this case the aim was to quantify that there is distinct difference between the cell populations, despite being initially treated in the same way. Therefore, the results of the alkaline phosphatase assay demonstrating a higher concentration in cells cultured in proliferation medium is enough to suggest that the cells cultured in osteogenic medium have behaved differently to those in proliferation medium, and have likely differentiated based on his result and the results of the other cell assays.

Staining of Dynamically Seeded MSC Cultures

Culture and analysis of 2D samples was undertaken once again to act as a control for the experiment. The osteogenic and proliferative cultures were stained with alkaline phosphatase and alizarin red to analyse the differentiation and mineralisation of the two cell populations (Figures 5.19 and 5.20). In this case, the cells cultured in osteogenic medium formed nodules which can be seen to exhibit strong alkaline phosphatase and alizarin red staining. In comparison, the cells cultured in proliferative medium stayed as a bulk cell sheet and stained mildly for alkaline phosphatase and alizarin red. This meant that, as expected, the proliferative cells were much less differentiated and mineralised than those grown in osteogenic medium. Therefore, the control test demonstrated that the cells and culture methodology is working as expected.

In this experiment, it was decided that bulk staining would be applied to the scaffolds, as previous histology had shown that the sections selected for staining may not be fully representative of the whole sample. Therefore, a segment of the scaffolds cultured in both types of media was stained with alizarin red and for alkaline phosphatase, along with 2 samples of uncultured Alvetex®, one coated with collagen and one prepared as directed by the manufacturer to identify any background staining (Figures 5.23 to 5.29). Considering the unseeded scaffolds, there is very little non-specific staining, except for a weak background of alizarin red on the collagen coated scaffold. This suggests that a small component of any alizarin red stain on the cultured scaffolds will be a background due to the collagen coating, but any staining from alkaline phosphatase will be due to cellular activity. Considering staining for alkaline phosphatase, as before, samples coated in proliferative medium appear to have a stronger alkaline phosphatase content, suggesting that

they are more immature than the cells grown in osteogenic medium. This is further confirmed by the results of alizarin red staining which demonstrate that, while both scaffolds stain for calcium, the osteogenic sample stains more strongly than the proliferative sample, meaning that the staining is more likely to represent mineralisation in the osteogenic case. Therefore, the bulk staining method verified that the cells successfully grew, differentiated and mineralised on the dynamically seeded, collagen coated Alvetex® scaffolds.

In addition to verifying cellular differentiation and mineralisation, bulk staining and microscopy also indicated where the cells grew in and on the scaffolds. As the microscopy images show, the cells seem to have formed clusters on the outside edge of the scaffold and cell sheets on top of the scaffold, as evidenced by the apparent rolled up sheet in Figures 5.26a and 5.26b. In addition, the bulk of the scaffold appears to be translucent, indicating that the cells did not penetrate well into the scaffold.

SEM of Dynamically Seeded Cell Cultures

SEM was performed on all scaffold samples including those without cells cultured on them (Figures 5.30 to 5.36). In this case, coating the scaffold with collagen potentially appears to smooth the scaffold slightly, however, very little difference can be seen between the uncoated and coated scaffolds under SEM. Considering the seeded scaffolds, the cultures grown in osteogenic medium once again exhibit more nodules than the cultures grown in proliferative medium, indicating, as expected, that the cultures grown in osteogenic medium are more mature and have mineralised.

In addition to examining the scaffolds for nodules, the SEM images also give information about the distribution of cells in the scaffolds. Examining the images, the cells appear to have failed to fully infiltrate the scaffold, as was observed in the static seeding case. In this experiment, the cells seem to have colonised the edge of the scaffold and infiltrated towards the centre where necessary in a fragmented layer. By examining the high magnification images it becomes clear that the cells are still only populating the outside of the scaffold, with the exception of a few individual cells near the surface of the scaffolds, despite the application of collagen and dynamic seeding. In addition, in some of the scaffolds the cell layers have rolled up, suggesting that the collagen coating has not improved adherence to the scaffold. As a result the SEM data suggests, like the microscopy data, that the cells are, where possible, adhering to each other, rather than to the scaffold, and are still only populating the outside of the scaffold.

Implications of the Analysis of Collagen Coated Alvetex® Scaffolds Dynamically Seeded with MSCs

Considering the full data sets describing the outcome of the cell culture, the protocol for expanding, differentiating and mineralising the cells was successful. However, once again the cells failed to form a fully 3D culture in the Alvetex® scaffold. In addition, the cells appeared to prefer to adhere to each other, rather than to the scaffold, so they formed a thick ring around the outside of the scaffolds. Therefore, this experiment, and the previous experiment with static culture, suggest that Alevetex® is a suboptimal scaffold for the 3D culture of MSCs.

6.2 Raman Analysis of Synthetic Materials with Lens Vibration Lock-In Amplified Raman Spectroscopy

The initial spectra collected with the spectrometer are clear, have high resolution (between 0.7 and 2 cm^{-1}), and appear to have a high SNR ratio signal. There is a wide range of signal quality metrics which can be calculated to analyse and compare different spectra. The applicable metrics in this work are SNR, differential signal to noise ratio ($\mathrm{SNR_{Diff}}$) and contrast (C). SNR and $\mathrm{SNR_{Diff}}$ are different ways of defining how well the desired signal can be differentiated from the background and noise [285]. Contrast is a way to express the relative height of a peak to the background signal level and is calculated as,

$$\mathrm{C} = \frac{S_p - \overline{S_{BG}}}{\overline{S_{BG}}}[286], \tag{6.2}$$

where S_p is the voltage of the Raman or laser peak, and $\overline{S_{BG}}$ is the average voltage of the background and noise signal. SNR is a measure of the peak voltage relative to the variation present in the background. SNR is calculated as,

$$\mathrm{SNR} = \frac{S_p}{\sigma_{BG}}[286], \tag{6.3}$$

where σ_{BG} is the standard deviation of the background and noise signal. Finally, the $\mathrm{SNR_{Diff}}$ is a measure of the peak voltage over the background, relative to the variation in the background signal. $\mathrm{SNR_{Diff}}$ is calculated as,

$$\mathrm{SNR_{Diff}} = \frac{S_p - \overline{S_{BG}}}{\sigma_{BG}}[286]. \tag{6.4}$$

Each of the three quality metrics were calculated for each lock-in amplified and raw spectra so that the efficacy of the amplification step could be quantitatively assessed.

As well as calculating metrics for image quality, rough peak assignment was performed for silica and the samples of hydroxyapatite. However, due to the inaccuracies in calculating wavenumbers in the initial method, the peak positions and therefore, the molecular groups assigned to the peaks are presented as a guide, rather than definitive peak assignments. Ideally, exact peak assignments would be made. However, the scope of this project was to develop a potentially new spectroscopy system rather than catalogue Raman spectra. Therefore, rough peak assignments are sufficient within this context.

Considering the collected spectra of hydroxyapatite and silica as a whole, there appears to be a consistent ramp feature upon which both the hydroxyapatite and silica spectra are positioned. This is likely due to light emission from the optical components forming a background feature. In the case of the silica spectrum, the background feature and silica spectrum align, and the ramp is visible on the non-lock-in amplified spectrum. This is because the optical components are all silica and, as a result, the spectrum acquired is mostly from the sample, with a small contribution from the optics. In the case of the hydroxyapatite spectra, a background ramp feature is present in a similar position to that of the silica feature, but additionally peaks are overlaid with different features than those seen in the silica spectrum. As a result, even though there is a conserved feature in the spectra, this does not diminish the prototype spectrometer's ability to distinguish between different substances of different molecular compositions.

6.2.1 Analysis of Silica Spectra

SNR was calculated for the silica spectrum with and without lock-in amplification for various features using the spectra given in Figure 6.2 below. The average and standard deviation of the background amplitude was measured in the regions 300-700 cm^{-1} and 1500-2250 cm^{-1}. Initially, to allow for comparison, the values of SNR and contrast were calculated for the main peak positions in the spectrum with no lock-in amplification and the similar peaks in the spectrum with lock-in amplification as marked on Figure 6.2. Next, further values of SNR and contrast were calculated; these are given in Table 6.1. The metrics show that there are improvements in SNR and contrast in comparison to non-lock-in amplified data.

It also worth noting that the quality of the signal generated by this spectrometer is affected by the alignment. In another spectrum collected as shown in Figure 6.3, the feature around 1100 cm^{-1} has an SNR of 54.1, SNR_{Diff} of 52.5 and contrast

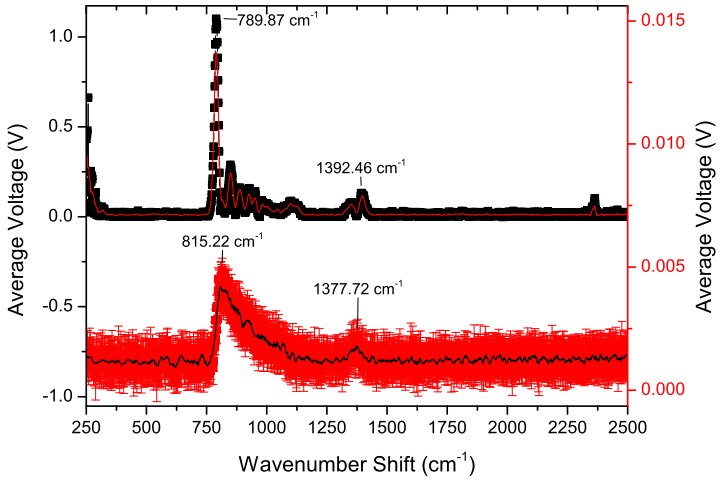

Fig. 6.2 Silica spectrum used for SNR and contrast calculations. The spectrum in black denotes the lock-in amplified spectrum, with the red trend line representing adjacent averaging with a window of 11 points. The red spectrum denotes the raw spectrum, with the black trend line representing adjacent averaging with a window of 11 points. The lock-in amplified spectrum was processed with a sensitivity of 500 μV and a time constant of 200 ms.

Lock-In Amplified				Non-Lock-In Amplified			
Wavenumber Shift / cm^{-1}	SNR	SNR_{Diff}	Contrast	Wavenumber Shift / cm^{-1}	SNR	SNR_{Diff}	Contrast
789.9	151.3	149.6	87.9	789.9	12.5	8.0	1.8
849.2	39.7	38.0	22.3	849.2	12.9	8.4	1.9
884.3	22.1	20.4	12.0	884.3	13.3	8.8	2.0
926.2	21.4	20.4	11.5	926.2	10.1	5.6	1.2
1096.8	11.7	10.0	5.9	1096.8	2.7	-1.8	-0.4
1392.5	18.2	16.5	9.7	1392.5	6.2	1.7	0.4
				815.2*	18.1	13.6	3.0
				1377.7*	8.1	3.6	0.8

Table 6.1 SNR, SNR_{Diff} and contrast data for all peaks with and without lock-in amplification for a spectrum of silica. The positions marked * are the the locations of the peaks in the non-lock-in amplified spectrum.

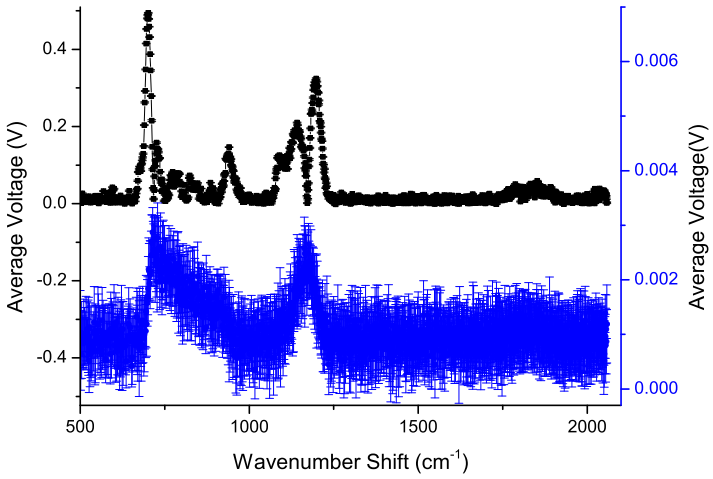

Fig. 6.3 Silica spectrum with a different alignment The lock-in amplified spectrum was processed with a sensitivity of 200 μV and a time constant of 200 ms.

of 33.0 in the lock-in amplified case and SNR of 0.4, SNR_{Diff} of -1.2 and contrast of -0.7 in the non-lock-in amplified case. Additionally, considering these spectra, it is clear that there are differences between the lock-in amplified and non-lock-in amplified spectra. Therefore, this also provides evidence that the action of the spectrometer provides a background suppressive and signal enhancing effect.

Figure 6.4 shows a silica spectrum generated with the spectrometer, labelled with peak assignments, as given in Figure 6.4a, and a reference silica spectra collected by Logunov and Kuchinsky in 2005, as given in Figure 6.4b, collected at 633 nm using a custom built spectrometer [287]. The reference spectra shown agrees with previous works such as those by Bates et al. [271], Shibata et al. [288] and Sharma et al. [289] which reported resolving silica peaks at 793-800 cm^{-1}, 830-835 cm^{-1}, 1060 cm^{-1}, 1200 cm^{-1}, which have some agreement with the peak assignments found in this work. The lack of a feature in the area of 490 cm^{-1} found in this work could be due to the fact that this band has been shown to be very sensitive to polarisation of laser light [271], and the use of circularly polarised light in this experiment potentially suppresses this feature. Considering the generated spectrum, it is clear that the spectrum contains more peaks than those in previously collected silica spectra. This suggests that the spectrometer is able to resolve the continuum features by its action.

In order to demonstrate that the background feature in the non-lock-in amplified spectrum was removed by lock-in amplification, both spectra were normalised to the voltages at 815.2 cm^{-1}, which is the peak of the feature in the non-lock-in amplified spectrum. After normalisation, the non-lock-in amplified spectrum was subtracted from the lock-in amplified spectrum, removing any background contribution, as

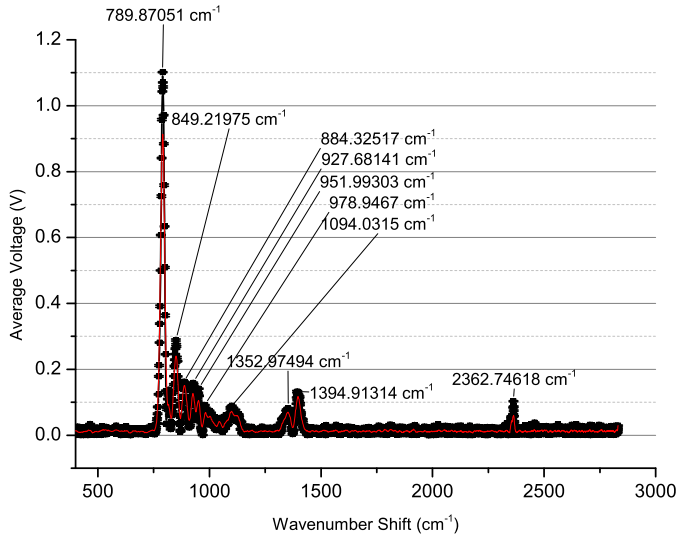

(a)

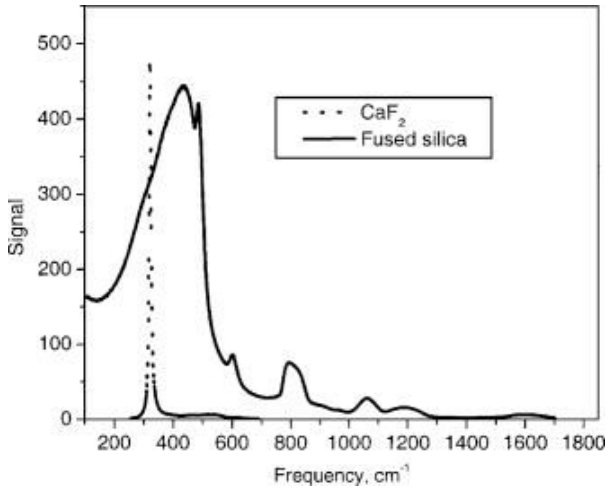

(b)

Fig. 6.4 (a) Silica spectrum labelled with approximate wavenumber assignments, collected with the lock-in amplifier at 500 μV sensitivity and 200 ms time constant with an average of 10 spectral measurements per point as previously shown in figure 5.40.(b) Reference spectrum of silica produced by Logunov and Kuchinsky using a custom spectrometer with excitation at 633 nm [287], reprinted from *S. Logunov and S. Kuchinsky, "Experimental and theoretical study of bulk light scattering in CaF2 monocrystals", Journal of Applied Physics, vol. 98, no. 5, pp.053501, 2005* with the permission of AIP Publishing.

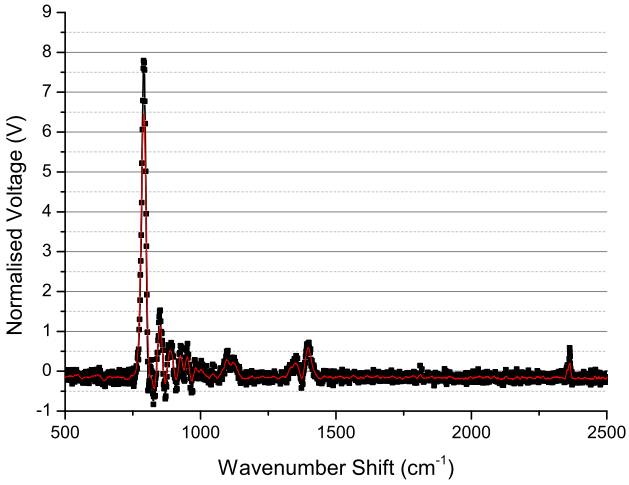

Fig. 6.5 Normalised lock-in amplified silica spectrum with normalised non-lock-in amplified spectrum subtracted.

shown in Figure 6.5. The figure demonstrates that the spectral features are likely overlaid on a suppressed background [290], although the peaks are independent of any structure within the non-lock-in amplified spectrum. The subtraction spectrum fluctuates beneath zero, which is likely due to the high level of fluctuations in the non-lock-in amplified spectrum and the fact that the feature is suppressed by lock-in amplification.

6.2.2 Analysis of Hydroxyapatite Spectra

As for the silica spectra, hydroxyapatite spectra were analysed in terms of SNR, SNR_{Diff} and contrast for a variety of spectral features with and without lock-in amplification. In the case of the fused hydroxyapatite spectrum, the background was taken to be from 1400-2824 cm^{-1} (the end of the spectrum) and spectral quality metrics were calculated for the spectrum collected with 50 μV sensitivity and 5 s time constant. The lock-in amplified and raw fused hydroxyapatite spectra are given in Figure 6.6. The values for SNR, SNR_{Diff} and contrast metrics are given in Table 6.2. As can be seen in the Figure 6.6 and Table 6.2, the spectral quality metrics are improved for a lock-in amplified spectral feature, when compared to a raw spectral feature at a similar position. Once again, the positions of spectral features after lock-in amplification, compared to their positions in the raw spectrum, are slightly different. This suggests that the lock-in amplification allows for spectral features to be amplified over the background.

Next, spectral quality was assessed for a porous sample of hydroxyapatite. The lock-in amplified spectrum was collected using a sensitivity of 50 μV and 2 s time

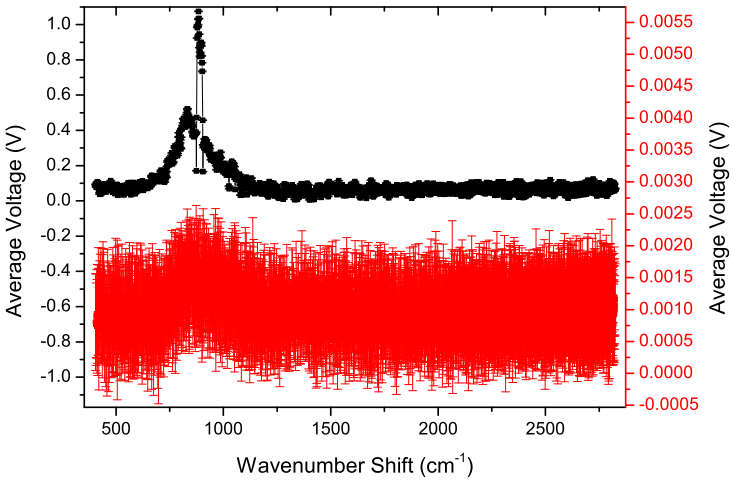

Fig. 6.6 Fused hydroxyapatite spectrum used for SNR, SNR_{Diff} and contrast with and without lock-in amplification, using a sensitivity of 50 μV and a time constant of 5 s.

Lock-In Amplified				Non-Lock-In Amplified			
Wavenumber Shift / cm^{-1}	SNR	SNR_{Diff}	Contrast	Wavenumber Shift / cm^{-1}	SNR	SNR_{Diff}	Contrast
833.0	28.6	25.0	6.9	833.0	8	3	0.6
884.4	58.9	55.2	15.2	884.4	8	4	0.8
896.0	49.3	45.7	12.6	896.0	6	2	0.3
986.0	15.1	11.5	3.2	986.0	6	1	0.2
1039.1	12.3	8.7	2.4	1039.1	6	1	0.2
				872.7*	8.9	4.0	0.8

Table 6.2 SNR, SNR_{Diff} and contrast data for all peaks with and without lock-in amplification for a spectrum of fused HA. Wavenumber marked with a * represents the peak in the non-lock-in amplified spectrum.

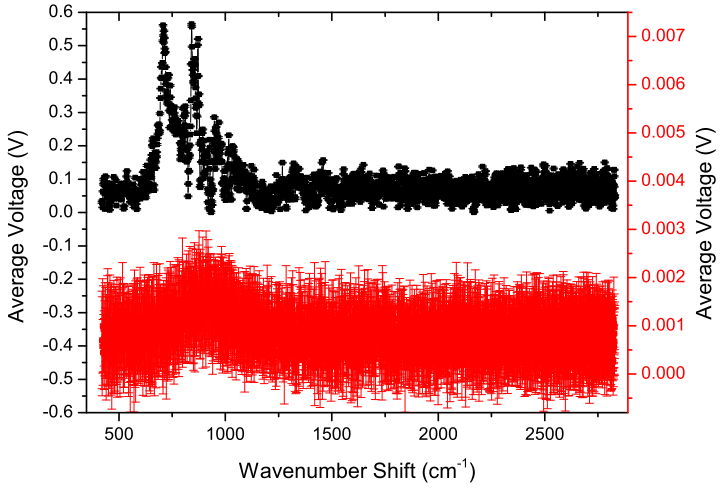

Fig. 6.7 Porous hydroxyapatite spectrum used for SNR, SNR_{Diff} and contrast with and without lock-in amplification, using a sensitivity of 50 μV and a time constant of 2 s.

constant as given in Figure 6.7, with the SNR and contrast metrics detailed in Table 6.3. Once again, comparing features at similar wavenumber shifts demonstrates a superior signal is generated after lock-in amplification. This is further evidenced by the lock-in amplification allowing several spectral features that are not visible in the raw spectrum to be distinguished.

Finally, spectral signal metrics were calculated for powdered hydroxyapatite in the same way as using the same methodology as previously, with the results given in Table 6.4 with reference to the spectra given in Figure 6.8. As shown the values of SNR and contrast are higher in the lock-in amplified case. Additionally there is a difference seen again in the position of spectral features between the lock-in amplified and raw spectra.

Rough peak assignments were applied to the lock-in amplified spectra for hydroxyapatite, as given in Figure 6.9 for fused HA, 6.10 for porous hydroxyapatite and 6.11 for powdered HA. Hydroxyapatite spectra have been documented by many researchers over the years. The work of Penel et al. [123] in 1998 and Koutsopoulos [28] in 2002 document Raman shifts observed at 433, 448, 580, 591, 607, 614, 964, 1029, 1034, 1041, 1048, 1057, 1064, 1077 and 3575 cm^{-1} [28][123]. A reference hydroxyapatite spectra collected by Koutsopoulos from hydroxyapatites synthesised in 3 different ways, using a FRA 106/S FT-Raman, Bruker spectrometer with an excitation wavelength of 1064 nm [28] are provided in figure 6.12 to help with comparison between previous results and those found here. In these previous works the main spectral feature is the peak at 964 cm^{-1} which represents the phosphate ν_1 vibrational mode. Considering the data collected here, the Raman spectra appear

Lock-In Amplified				Non-Lock-In Amplified			
Wavenumber Shift / cm^{-1}	SNR	SNR_{Diff}	Contrast	Wavenumber Shift / cm^{-1}	SNR	SNR_{Diff}	Contrast
707.2	20.7	18.1	6.9	707.2	1.9	-0.5	-0.2
811.4	11.8	9.2	3.5	811.4	4.1	1.6	0.7
841.0	20.9	18.3	7.0	841.0	4.2	1.7	0.7
871.8	19.2	16.6	6.4	871.8	5.0	2.5	1.0
893.7	9.2	6.6	2.5	893.7	4.7	2.2	0.9
948.3	10.5	7.9	3.1	948.3	4.7	2.2	0.9
1016.0	8.6	6.0	2.3	1016.0	4.8	2.3	0.9
1034.1	7.37	4.7	1.8	1034.1	3.4	1.0	0.4
				909.6*	6.8	4.4	1.8

Table 6.3 SNR, SNR_{Diff} and contrast data for all peaks with and without lock-in amplification for a spectrum of porous HA. Wavenumber marked with a * represents the peak in the non-lock-in amplified spectrum.

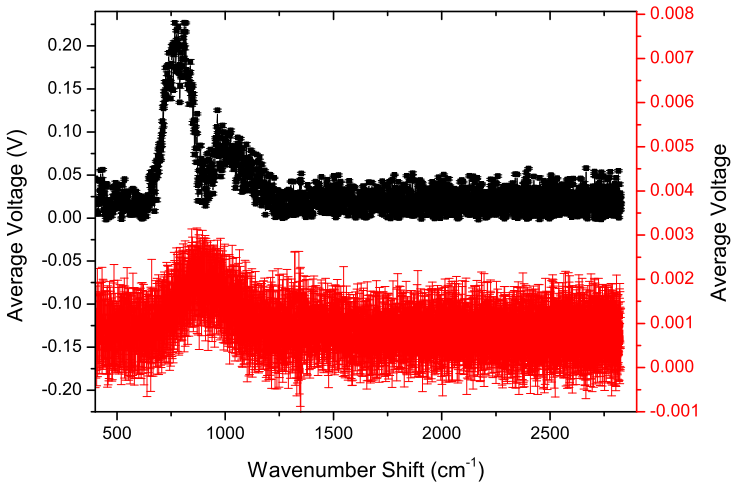

Fig. 6.8 Powdered hydroxyapatite spectrum used for SNR, SNR_{Diff} and contrast with and without lock-in amplification, using a sensitivity of 200 μV and a time constant of 0.5 s.

Lock-In Amplified				Non-Lock-In Amplified			
Wavenumber Shift / cm^{-1}	SNR	SNR_{Diff}	Contrast	Wavenumber Shift / cm^{-1}	SNR	SNR_{Diff}	Contrast
767.7	20.2	18.4	10.2	767.7	4.8	2.0	0.7
811.1	20.2	18.4	10.2	811.1	4.2	1.5	0.5
963.7	11.2	9.4	5.2	963.7	7.1	4.4	1.6
				868.6*	8.1	5.4	2.0

Table 6.4 SNR, SNR_{Diff} and contrast data for all peaks with and without lock-in amplification for a spectrum of powdered HA. Wavenumber marked with a * represents the peak in the non-lock-in amplified spectrum.

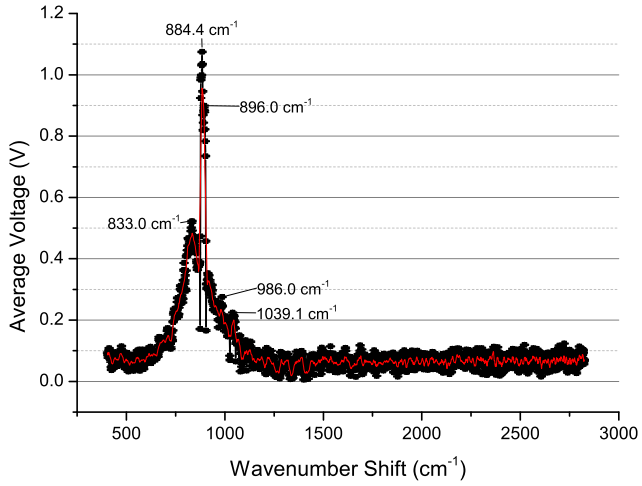

Fig. 6.9 Fused hydroxyapatite spectrum labelled with approximate wavenumber assignments.

to have major bands at around 800 cm^{-1}. This discrepancy may be attributable to inaccuracies in the calculations of wavenumber shifts, which have a number of underlying assumptions and simplifications as described previously. These are likely to be more clearly visualised in the case of hydroxyapatite as its Raman bands are more sharply defined than silica's.

The lock-in amplification process appears to enable a spectral enhancement to occur for hydroxyapatite. However, this spectra does not relate very well to previous results, especially in comparison to the match of some of the wavenumber assignments for silica. This could be due to inaccuracies in the wavenumber calculation process. As well as the calculation having an inherent systematic error of 0.35%, it also introduces an unknown error through the assumptions made about the geometry of the spectral collection system. Therefore, it is possible that this could lead to the spectral features being mislabelled. This aspect could be further accentuated in hydroxyapatite spectra, rather than silica spectra due to the reduction in the laser line reflection. The reflected laser line is vital to the alignment of the spectrometer and as this was harder to visualise for the hydroxyapatite samples, it is more likely that errors in the alignment can be magnified. Due to these difficulties the fused sample was used to optimised the alignment of the spectrometer, and was simply replaced with the porous sample and powdered sample whilst maintaining the pre-defined geometry. Therefore, these spectra are most likely to be subject to compounded errors. As a possibly methodology to improve the result, it is possible to adjust the scale applied to the fused hydroxyapatite spectrum, assuming that the maximum peak position is at 964 cm^{-1}. In order to achieve this, a grating angle of 25.1° or a laser line position of 284.3 cm could be used producing results as shown

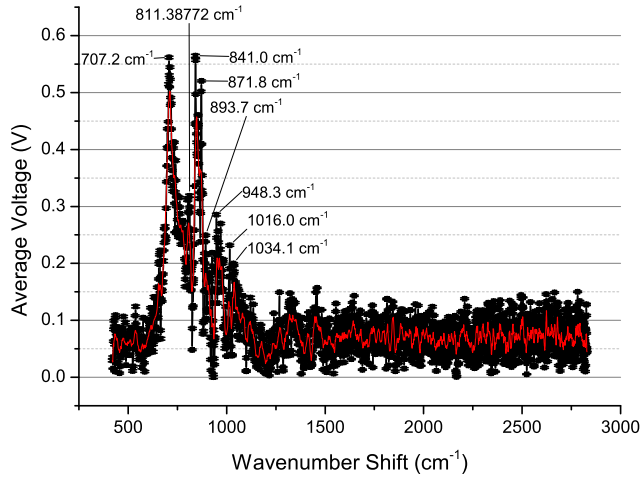

Fig. 6.10 Porous hydroxyapatite spectrum labelled with approximate wavenumber assignments.

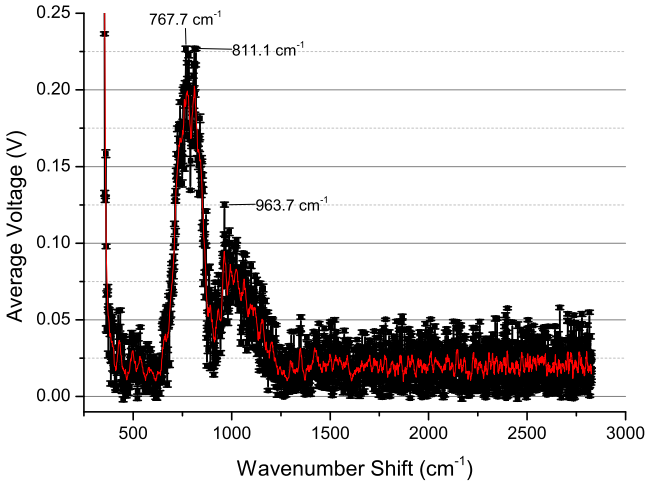

Fig. 6.11 Powdered hydroxyapatite spectrum labelled with approximate wavenumber assignments.

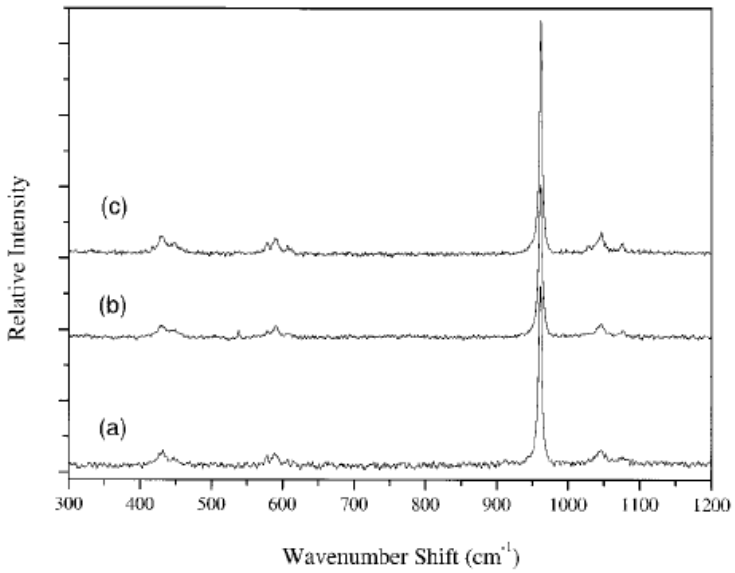

Fig. 6.12 Reference raman spectra of hydroxyapatites produce via 3 different synthesis routes by collected by Koutsopoulos using an FRA 106/S FT-Raman, Bruker spectrometer operating at 1064 *nm* [28]. Reprinted from *S Koutsopoulos,"Synthesis and characterization of hydroxyapatite crystals: A review study on the analytical methods", Journal of Biomedical Materials Research Part A, vol. 62, no. 4, pp. 600-612, 2002* with permission from Wiley Periodicals, Inc. Copyright © 2002 Wiley Periodicals, Inc.

in Figure 6.13. Although this accounts for the some of the discrepancies, it does not account for all of them, which suggests that a combination of laser line position and grating angle errors were responsible for the discrepancy. Therefore, it is likely that this is not a fundamental failing of the spectrometer, but that it is more likely due to errors in the wavenumber approximation process.

As with silica, the hydroxyapatite sample spectra with and without lock-in amplification were normalised to the position of the peak in the non-lock-in amplified spectrum and the non-lock-in amplified spectrum subtracted. The results of this process are given in Figure 6.14, and demonstrate that the spectral features in the lock-in amplified spectra are independent of the features on the non-lock-in amplified spectrum. Therefore, this shows that the lock-in amplification process subtracts the background and draws the sample's Raman spectrum out of the background.

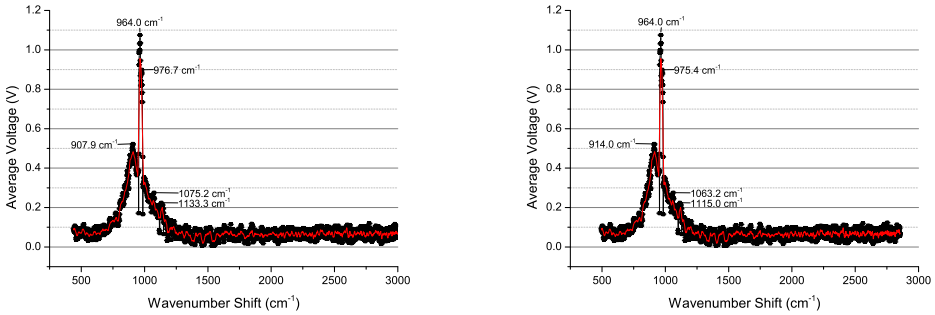

(a) (b)

Fig. 6.13 Spectra of fused hydroxyapatite shifted so that the highest voltage peak is at 964 cm^{-1}, this was achieved by shifting the grating line by (6.13a) changing the grating angle to 25.1° or by (6.13b) changing the laser line position to 284.3 cm.

6.3 Raman Analysis of Fixed MSC Cultures with Lens Vibration Lock-In Amplified Raman Spectroscopy

As previously, SNR and contrast values were computed for the spectra and peak assignments attempted with the consideration of possible errors in estimated wavenumber analysis.

Table 6.5 gives the SNR and contrast values for the sample cultured in proliferation medium and Table 6.6 gives the SNR and contrast values for the sample cultured in the osteogenic medium. In both cases, comparable peaks in the lock-in amplified and non-lock-in amplified spectra demonstrate that lock-in amplification significantly improves these spectral quality metrics. In addition, there are offsets between the peaks in both the lock-in amplified and non-lock-in amplified spectra, suggesting that the spectrometer is able to correctly distinguish between the different cell populations as well as providing amplification for the cell cultures.

After calculating the spectral quality metrics for a variety of of peaks, a more complete set of peak assignments was defined for both spectra, as given in Figure 6.15 and 6.16. These peak assignments, as all others derived in this work, will have a degree of error and uncertainty in them due to the calculation method. However, they can still be compared to previously captured spectra in the literature to give an impression of whether the spectra collected here have good agreement with previous works. McManus et al. [122] characterised the differentiation of human MSCs on a silica substrate in 2011, allowing for a good point of comparison between the differentiation of rat MSCs performed here. The spectral features identified by this group are detailed in Table 6.7.

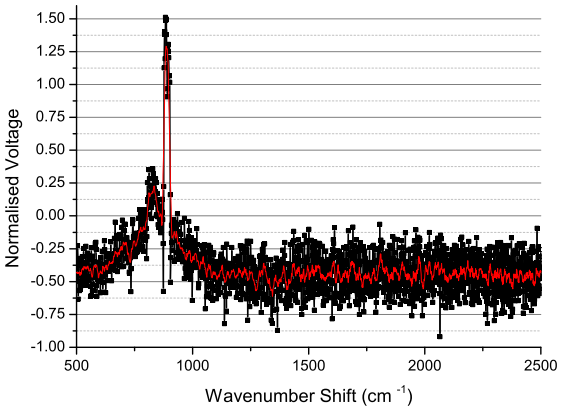

(a)

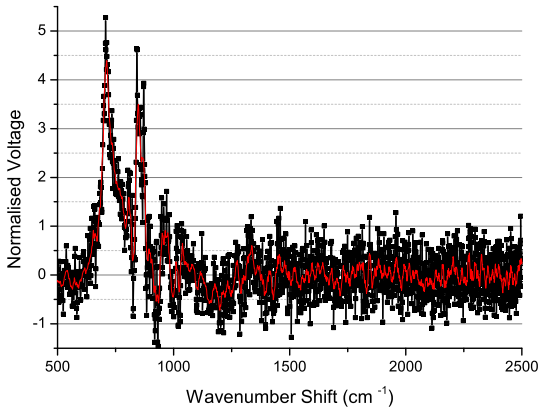

(b)

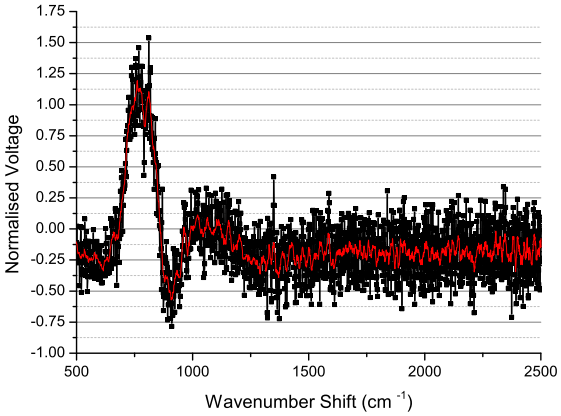

(c)

Fig. 6.14 Spectra of hydroxyapatite, normalised to the peak of the non-lock-in amplified feature and with the non-lock-in amplified spectra subtracted from the lock-in amplified spectra for (6.14a) fused HA, (6.14b) porous HA, and (6.14c) powdered HA.

Lock-In Amplified				Non-Lock-In Amplified			
Wavenumber Shift / cm^{-1}	SNR	SNR_{Diff}	Contrast	Wavenumber Shift / cm^{-1}	SNR	SNR_{Diff}	Contrast
706.7	60.2	57.8	23.8	764.8	18.4	10.3	1.3
734.4	70.3	67.9	27.9	1031.0	23.9	15.8	1.9
770.6	63.4	61.0	25.1	1671.8	11.1	3.0	0.4
960	85.4	83.0	34.1				
992.5	159.9	157.4	64.8				
1025.8	139.3	139.6	56.3				
1084.7	88.9	86.5	35.6				
1627.5	43.6	41.2	16.9				
1661.6	47.5	45.1	18.6				
1745.0	40.7	38.3	15.8				
1979.6	14.1	11.6	4.8				

Table 6.5 SNR, SNR_{Diff} and contrast data for all peaks with and without lock-in amplification for a spectrum from MSCs cultured in proliferation medium.

Lock-In Amplified				Non-Lock-In Amplified			
Wavenumber Shift / cm^{-1}	SNR	SNR_{Diff}	Contrast	Wavenumber Shift / cm^{-1}	SNR	SNR_{Diff}	Contrast
673.4	47.2	44.4	16.3	721.9	18.7	11.3	1.5
689.6	51.5	48.8	17.9	994.4	29.3	21.8	2.9
766.8	32.4	29.7	10.9	1677.3	12.0	4.6	0.6
786.9	39.8	37.1	13.6				
860.5	15.3	12.6	4.6				
932.2	77.9	75.1	27.6				
950.0	103.9	101.2	37.1				
964.9	115.0	112.3	41.3				
1009.1	78.2	75.4	27.7				
1593.0	11.3	8.6	3.1				
1645.6	16.9	14.2	12.1				
1706.7	12.1	9.4	3.5				
1836.9	7.8	5.1	1.9				
1960.7	17.6	14.9	5.5				

Table 6.6 SNR, SNR_{Diff} and contrast data for all peaks with and without lock-in amplification for a spectrum from MSCs cultured in osteogenic medium.

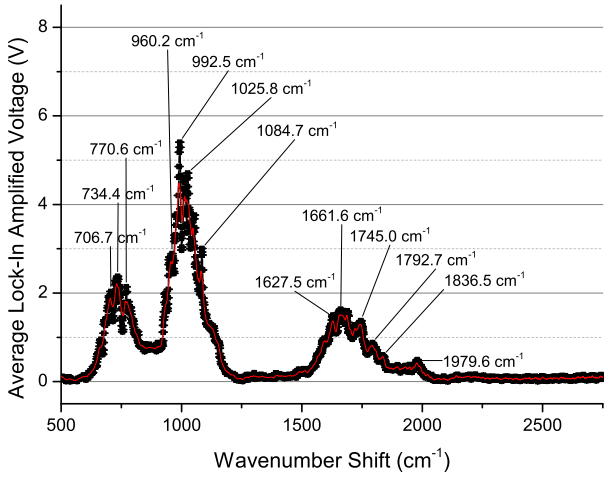

Fig. 6.15 Spectrum of gold coated MSCs on Alvetex® cultured in proliferative medium labelled with approximate wavenumber assignments.

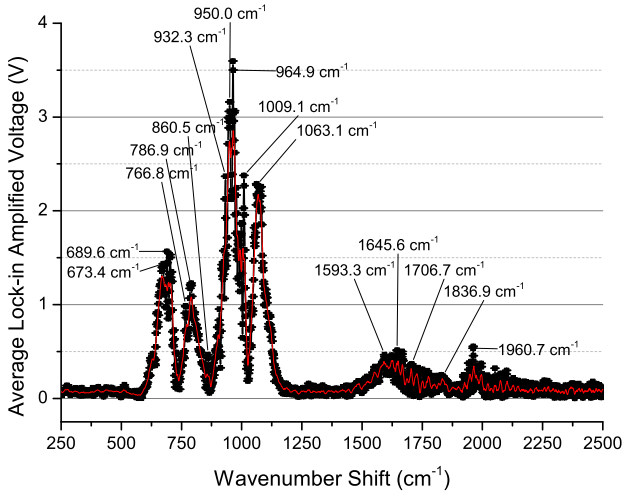

Fig. 6.16 Spectrum of gold coated MSCs on Alvetex® cultured in osteogenic medium labelled with approximate wavenumber assignments.

Wavenumber Shift Per McManus 2011 [122] / cm^{-1}	Assignment
1659	Amide I
1665	Amide I
936	Skeletal C-C Vibration
1284	Amide III Vibration
1246	Amide III Stretches
1269	Amide III Stretches
1245-1270	Amide III
786	Lipid
1095	Lipid
1575	Lipid
1065	Phospholipids
1127	Phospholipids
1301	Phospholipids
950	Hydroxyproline
921	Proline
1445	CH_2 Wag
945-950	Amorphous Apatite Lattice
955	B-Type Carbonate-Substituted Apatite
960	Hydroxyapatite
962-964	Crystalline Non-Substituted Apatite
1070	Carbonate Substituted Hydroxyapatite
1030-1100	Phosphate

Table 6.7 Raman features observed during the culture of human MSCs by McManus et al. [122].

The characterisation of MSCs by McManus et al. [122] in table 6.7 can be compared to the spectral features found in the proliferative spectra collected in this work. Therefore, the spectrum of proliferative MSCs has peaks indicative of lipid content at around 770.0 cm^{-1}, a small amount of hydroxyapatite potentially at 960.0 cm^{-1}, phospholipid content at 1025.8 cm^{-1}, phosphate potentially at 1084.7 cm^{-1}, and amide I at 1661.6 cm^{-1}. Considering the sample cultured in osteogenic medium, there appears to be lipid content at 786.9 cm^{-1}, some amorphous apatite at 950.0 cm^{-1}, a large crystalline non-substituted apatite peak at 964.0 cm^{-1}, potential carbonate substituted apatite at 1063.1 cm^{-1} on a potential phosphate background and amide I content at 1645.6 cm^{-1} [122]. Therefore, the spectrum collected from the MSCs cultured in proliferative medium is indicative of an immature culture of MSCs and the spectrum from the MSCs cultured in osteogenic medium is indicative of a more mature culture of MSCs. The proliferative Raman spectrum appears to demonstrate some immature hydroxyapatite, which matches the histological analysis produced for samples prepared in the same way. In order to help identify additional peaks present in the spectra further literature was considered, namely the work by Azrad et al. [192] in 2006 using MSCs and Notingher et al. [187] in 2004 on human osteoblasts, with approximate peak assignments using these sources given in Table 6.8. In the table, the associated wavenumber value for each Raman band given in the referenced literature is given in brackets for reference. After applying these peak assignments, there are very few unexplained peaks. Therefore, this suggests that the Raman spectra are being collected in an expected manner. Interestingly, this also suggests that there is very little interference from the scaffold, gold coating and SEM preparation. Therefore, it could be that a surface enhancement effect from the gold coating could be coming into play. This hypothesis arose from the fact that the hydroxyapatite spectrum had a much lower signal intensity, compared to that from the gold coated cell cultures. As a result, this work may suggest that cell cultures prepared for SEM analysis may also have the potential to be probed by Raman spectroscopy. Consequently, this suggests that SEM prepared samples could be used to provide morphological information via traditional SEM and chemical information via Raman spectroscopic investigation, a very interesting and promising finding.

Considering the peak assignments detailed in table 6.8 and the comparison with the work of McManus' et al. there are some differences between the peak assignments derived in this work and those detailed in the literature. Unfortunately, this difference is not constant and ranges from -16 cm^{-1} to 6.4 cm^{-1}. Therefore, applying

Wavenumber Shift For Differentiated Culture / cm^{-1}	Assignment
673.4	Thymine [187] (667) [192] (670)
689.9	Guanine [192] (684)
766	Thymine, Tryptophan [187] (760 - Tryptophan)[192] (755 - Thymine)
786.9	O-P-O Stretch in DNA [187] (788)
860	Tyrosine [187] (854)
932	C-C stretch in an α helix or C-C-N symmetric stretch or C-O-C glycos [187] (937)
1009.1	Phenol Symmetric Ring Breathing [187] (1005)
Wavenumber Shift for Undifferentiated Culture / cm^{-1}	Assignment
706.7	Cholesterol [192] (702)
734.4	Adenine [192] (729) [187] (729)
1745.0	Ester C=O bond [187] (1736)

Table 6.8 Tentative wavenumber assignments for additional spectral features in the spectra of differentiated and undifferentiated MSCs.

a simple wavelength correction factor would not adjust the spectrum to completely match those detailed in the literature.

As the samples had been fixed with glutaraldehyde and had an application of osmium tetroxide applied, the key peaks of these compounds were also found in the literature and compared to the peaks exhibited in the Raman spectra of the fixed cells. When cells are fixed with glutaraldehyde, amine groups are converted to imines and osmium tetroxide reacts with unsaturated lipids to form cyclic esters, resulting in fixed cells which retain much of their structure. However, this has previously been found to be acceptable in terms of analysing structures with infrared spectroscopy [291]. Furthermore, there are indications that fixation with glutaraldhyde for less than 2 hours generates an acceptable Raman spectrum in studies of pericardium tissue [292] and glutaraldehyde fixtion has been noted to preserve the Raman spectrum in K 562 cells [293]. Considering the fixatives themselves, osmium tetroxide has been found to exhibit peaks at 322.7 cm^{-1}, 331.1 cm^{-1}, 954 cm^{-1}, 964.2 cm^{-1} [294]. Therefore, there could be a small contribution from unbound osmium tetroixde in the differentiated sample's spectrum at 964.9 cm^{-1}, but as there is no such feature present in the undifferentiated cells' spectra, it is unlikely that the contribution is significant. As a result, although the fixation process may have changed the form of the lipid content and converted amide groups into imines, it is unlikely that the full spectra are artefacts of the fixation process.

To characterise the action of the spectrometer, the process of calculating values

	Lock-In Amplified			Non-Lock-In Amplified		
Position / μm	SNR	SNR_{Diff}	Contrast	SNR	SNR_{Diff}	Contrast
450.01	111.5	109.9	67.8	44.4	21.9	1.0
960.022	23.2	21.6	13.6	27.3	4.8	0.2
2329.956	39.7	38.1	23.5	25.3	2.8	0.1
2630.005	64.6	63.0	38.9	28.0	5.5	0.2
3350.006	47.9	46.2	28.6	25.0	2.5	0.1
4079.956	40.5	38.8	24.0	27.1	4.6	0.2
4390.015	50.2	48.6	30.0	32.0	9.5	0.4
8369.995	60.1	58.5	36.1	40.8	18.3	0.8
8609.985	64.3	62.7	38.7	69.2	46.7	2.1
9390.015	10.8	9.2	5.7	26.8	4.4	0.2

Table 6.9 Spectral quality metrics over the line profile of an osteogenic sample at approximately 1194.6 cm^{-1} wavenumber shift with 10 μm resolution, lock-in amplified at 200 μV sensitivity and 200 ms time constant, averaged over 100 measurements per point.

of SNR and contrast were performed for spectral mapping processes in 1D for the osteogenic cell cultures and for the final line of the 2D Raman spectral map of the proliferative cell culture. Tables 6.9, 6.10 and 6.11 demonstrate Raman mapping using lock-in amplification greatly increases the SNR, SNR_{Diff} and contrast in all the line profiles considered. To further demonstrate this, the maximum spectral quality metrics for the final line of the 2D scan over the scaffold body were calculated for both the lock-in amplified and raw results. For the lock-in amplified spectrum, the maximum SNR was measured to be 131.7, maximum SNR_{Diff} was measured to be 129.8 and the maximum contrast was measured to be 67.1. For the raw spectrum the maximum SNR was measured to be 37.8, the maximum SNR_{Diff} was measured to be 25.9 and the maximum contrast was measured to be 2.2.

A final point to consider for the Raman maps is the area of increased signal amplitude in the area corresponding to the carbon sticker. This was unexpected as the lock-in amplified Raman signal at 2149.1 cm^{-1} for the carbon sticker is 0.0597 V at 200 μV sensitivity and 2 s time constant. The key difference between the scans is the time constant, which was 10 times shorter during the mapping process. Therefore, the increased signal could be due to the time constant used for mapping not being high enough to eliminate noise generated over this high return area.

The peak assignments made for the spectra captured in this work match quite well with those in the literature. However, this contrasts strongly with the differences between the spectra from the hydroxyapatite samples where there are significant differences between the potential peak assignments and the literature. The SEM prepared samples had a strong reflected laser line signal, which made alignment

	Lock-In Amplified			Non-Lock-In Amplified		
Position / μm	SNR	SNR_{Diff}	Contrast	SNR	SNR_{Diff}	Contrast
418.03	30.9	29.1	15.7	16.4	0	0
2369.995	42.8	41.0	22.2	43.4	4.6	0.1
2776.001	44.8	43.0	23.3	41.8	2.9	0.1
3334.045	14.5	12.7	6.9	40.7	1.9	0.0
3802.002	22.3	20.5	11.1	45.8	6.9	0.2
3925.995	21.7	19.9	10.8	42.0	3.1	0.1
4210.022	21.5	19.7	10.6	38.3	0	0.0
4407.989	33.6	31.8	17.2	41.1	2.2	0.1
5799.975	8.6	6.7	3.6	40.0	1.1	0.0
8361.004	53.4	51.5	27.9	50.5	11.6	0.3
8635.986	71.6	69.8	37.8	45.2	6.4	0.2
9343.994	91.8	90.0	48.7	42.4	3.5	0.1

Table 6.10 Spectral quality metrics over the line profile of an osteogenic sample at approximately 2149.1 cm^{-1} wavenumber shift with 1 μm resolution, lock-in amplified at 200 μV sensitivity and 200 ms time constant, averaged over 100 measurements per point. Values of exactly zero represent a negative calculated value.

	Lock-In Amplified			Non-Lock-In Amplified		
Position / mm	SNR	SNR_{Diff}	Contrast	SNR	SNR_{Diff}	Contrast
285.40	55.5	53.6	27.7	15.6	3.6	0.3
285.84	101.5	99.6	51.5	17.0	5.1	0.4
286.01	131.7	34.9	67.1	34.9	23.0	1.9
286.67	53.4	51.4	26.6	14.2	2.2	0.9
286.71	63.9	62.0	32.1	12.9	1.0	0.1
278.40	40.2	38.3	19.8	11.1	-0.9	-0.1

Table 6.11 SNR, SNR_{Diff} and contrast data for major peaks with and without lock-in amplification for the spectral map of MSCs cultured in proliferative medium at 2149.1 cm^{-1} using lock-in amplification at 200 μV sensitivity and 200 ms time constant.

relatively easy, whereas the low reflectivity of the hydroxyapatite samples made alignment more difficult. Therefore, this discrepancy in differences between spectral peaks in this work and in the literature could be due to additional alignment errors in the hydroxyapatite case. Considering the spectra collected for silica, although there is some agreement between the wavenumber shifts observed in this work and in the literature, there are clear differences in the general form of the spectra from those seen in the literature. Considering this along with the discrepancies seen in the hydroxyapatite spectra, it is possible that the spectra generated here may not be explicitly arising from the standard Raman effect.

6.4 Raman Optical Activity

After reflecting upon the differences in the spectra produced here and in the literature, and discussion with Prof. Hugh J. Byrne and Dr Frederik Claeyssens, it was hypothesised that the spectra collected in this work may arise from Raman optical activity (ROA), rather than the Raman effect. Unfortunately, it was not possible to fully explore this possibility experimentally, but an initial literature search was performed to ascertain its feasibility.

ROA is a phenomena which occurs when chiral molecules are excited with laser light. When circularly polarised light is used to excite a chiral molecule, differences in the spectral intensity can be identified [295]. When circularly polarised light excites a Raman transition in a chiral molecule, the light scattered by the Raman effect will have a spectrum which depends on whether the incident light is right handedly or left handedly circularly polarised light [295–297]. The spectra collected with the application of left and right handed circularly polarised light are then added and subtracted to produce the classic ROA spectrum for a chiral molecule [296]. Therefore, in this experiment it is possible that half of the ROA spectral signal is being collected though the application of circularly polarised light rotating one 1 direction only [295].

As ROA as a phenomena only occurs in chiral molecules, the first stage in verifying if the phenomena may be happening in this case is is verifying whether the samples being analysed contain chiral molecules. Silica, particularly in the natural form of quartz, is chiral [298], and there has also been some investigation into the ROA of quartz, although this has mostly centred around the 132 cm^{-1} band alone [299, 300]. There is also evidence to suggest that hydroxyapatite is a chiral molecule [301, 302]. However, hydroxyapatite or bone are yet to be characterised with ROA techniques Therefore, it may be that rather than capturing the pure Raman spectra, this work is measuring the ROA spectrum.

The cell spectra may be closer to those in the literature, possibly as a result of the

surface enhancement effect. If this is the case, the spectral features observed may be due to conventional Raman scattering, which would mean that the spectral feature observed and mapped at 2150 cm^{-1} may simply arise due to water content [276, 277]. However, ROA of biomolecules have been investigated in more detail than that of hydroxyapatite or silica so further comparisons between this work and the literature can be made. Comparing ROA spectral features reported in the literature to those found in this work suggests that both the proliferative and osteogenic samples could have an amide I feature in the 1630 to 1700 cm^{-1}, potentially from a C=O stretch [296], and the feature at 992.5 cm^{-1} may be an RNA feature [296, 303]. Based on the work of Synytsya et al. [304] the following peak asignment may be feasible for the osteogenic sample, with spectra collected in this work matching those reported by Syntsya within ± 3 cm^{-1}; the feature at 932.3 cm^{-1} may be due to C-C and C-N bonds in an α-helix, the feature at 1009.1 cm^{-1} may be due to phenol ring C-H bond, the feature at 1063.1 cm^{-1} may also be due to C-C and C-N bonds, and the feature at 1645.6 cm^{-1} may be due to an unordered amide I β-sheet[304]. For the proliferative sample, the following peak assignments may be appropriate with the spectral features measured in this work matching those reported in the literature within ± 5 cm^{-1}; the feature at 960.2 cm^{-1} may be due to C-C and C-N bonds, and the feature at 1661.6 cm^{-1} may be due to amide I in an α-helix [304]. However, complete analysis of the potential origins of the cellular spectra is difficult as cells as a whole have not yet been analysed using ROA [296]. Unfortunately, there is has been little work to capture ROA spectra of biomolecules at wavenumbers greater than 2000 cm^{-1} [296, 297, 305–307]. Therefore, it is not possible to say if the feature at 2150 cm^{-1} charts anything more interesting than water content. In addition, although ROA peaks have been observed between 400 and 900, there are many which have not been directly linked to a molecular signature [304].

Due to limited work on ROA spectra for the samples tested in this work, it is not possible to categorically state that the signal detected is due to ROA. However, it is an interesting avenue which requires further investigation.

6.5 Potential Surfaced Enhanced Raman Spectroscopy via SEM Preparation

The strong spectral signal produced from the SEM prepared cell culture samples suggests that the gold coating may be producing a surface enhancement of the Raman spectra. It is well known than gold nanolayers generate a surface enhanced Raman effect [192, 308]. Therefore, it is perhaps not unexpected that SEM prepared samples also demonstrate this same effect as to enable SEM to be performed

samples must be coated with a thin layer of gold, which may provide surface enhancement. Unfortunately, no definitive data was collected in this study to demonstrably indicate that the Raman spectra were surface enhanced. The main evidence which supports the hypothesis that surface enhancement is occurring, is that the spectra from the porous and powdered hydroxyapatite required high sensitivities and long time constants to develop a high quality spectrum, but the cell cultures required much shorter time constants and generated a Raman signal of greater amplitude than in hydroxyapatite. In addition, there will be a heterogeneous mixture of molecules excited by the laser in the cell cultures compared to a single molecular species for the hydroxyapatite and silica samples. As a result, one would expect the Raman return from the homogeneous sample to be of a greater amplitude as there are more molecules scattering light by the same amount. Therefore, the comparably strong signal from the heterogeneous population in the cell cultures is suggestive of a surface enhancement effect.

If a surface enhancement was occurring it would be from the molecules close to the gold sputter coating as SRS enhancement has a $r-12$ dependence on distance, with molecules required to be $<$ 10s nm from the enhancing surface [308]. Considering the biological samples produced in this work, conventional analysis methods demonstrated that a cell sheet was produced on top of the scaffold's surface. Therefore, cells and secreted ECM will be in closest to the gold coating, meaning that if surface enhancement is occurring, the enhanced signal is likely to originate from the cellular materials on the top of the scaffold. As observed in the SEM images presented in Figures 5.15 to 5.18, and corroborated by scaffold staining, mineralising nodules appear to be present on the surface of the cell cultures. Therefore, this means that the Raman signal from hydroxyapatite can undergo surface enhancement, as well as that from the cells themselves. As a result, it is plausible that all the spectral features observed in the Raman spectra collected from the two cell populations have undergone surface enhancement due to the presence of the gold sputter coating used for SEM.

6.6 Use of the CCD Spectrometer and Lock-in Amplification

Considering the spectra collected with the CCD spectrometer, it appears that the action of the simulated lock-in amplification is not having the same effect as the full translation of the lens through the front face of a substrate. However, there is a consistent ramp feature present in the spectra collected at around 136 cm^{-1} as can be seen in Figure 5.68a. This means that the feature is at a significantly

lower wavenumber shift that any identified in the Raman spectra, which suggests this may be a side band which becomes incorporated into the laser line area or suppressed during lock-in amplification with the photodiode based spectrometer. In the spectrum collected using dual phase lock-in amplification, as in Figure 5.71, there appears to be weak spectral features present at 1125 cm^{-1} and 667 cm^{-1}, which are a more likely to map to the features seen in the lock-in amplified spectra. However, considering the wavenumber shifts of these potential features and the previously described ramp, neither correlate well with spectra described previously in the literature [271] [288] [289]. Therefore, this suggests that there is a need to improve the CCD spectrometer set-up to allow for unambiguous detection of a Raman spectrum. In order to improve spectral collection, steps that may be taken include:

1. Improving light coupling into the spectrometer by optimisation of the optical set up.

2. Insertion of an edge pass filter to remove the laser line. An edge pass filter was not needed in the photodiode spectrometer as the distance for dispersion and use of the laser line for calibration did not overwhelm the spectrometer. However, in this case, it may improve spectral performance.

However, it may be that the difficulty in replicating the results of the photodiode based spectrometer could be due to the change in the collection method of the raw spectral data. In the photodiode spectrometer the data was collected and processed during the sinusoidal vibration of the lens, whereas only two points were used to collect the data in the case of the CCD spectrometer pilot experiment. It could be that the inclusion of further points in a static collection system to simulate a sinusoid rather than a square wave may improve the lock-in amplification step as it may be the slope which holds the key information which can be lock-in amplified. Alternatively, dynamic data collection while the lens is vibrating may be required to capture the key element of the signal which is extracted during lock-in amplification.

As a result, although it is unfortunate that the CCD spectrometer has not replicated the results of the photodiode spectrometer at this stage, there are many avenues to explore to help develop a more commercially viable version of the lens-vibration lock-in amplification spectrometer.

Chapter 7

Conclusions

In this work a strong body of research has been conducted into new methods for Raman spectroscopy in biological research. Although Raman spectroscopy is a promising technique for biological analysis and in real-time *in situ, in vivo* live analysis, current Raman systems are not fully optimised for biological spectroscopy, particularly in the analysis of tissue engineered constructs. Therefore, research such as work performed here is important, despite the maturity of Raman spectroscopy, to optimise the technique for biological systems.

In this work a novel Raman spectrometer was designed and built for use in biological systems, with a focus on the tissue engineering applications. Initial work indicated that the lens position in both translucent and opaque samples demonstrated changing signal amplitude from the laser signal and possible Raman signal with focal point depth in the sample. Therefore, it was shown that lens position can provide a signal suitable for lock-in amplification. Furthermore, the characteristic behaviours of the laser and possible Raman signal with focal point depth in both materials suggested that it could be possible to disentangle the laser and possible Raman signals through a phase selective lock-in amplification process. Following this preliminary experiment, the proposed spectrometer was designed with the key feature of a piezoelectric controlled lens to provide automated motion of the focal point. Verification of the key principal of operation was completed by successfully demonstrating that providing a periodic oscillation to the lens, through application of a periodic oscillation in voltage, produced a clear oscillation in the laser line. Next, the ability of the system to produce spectra with a high level of noise extraction using a low laser power was determined by collecting spectra for silica and numerous forms of hydroxyapatite. In these spectra it was revealed that the lock-in amplification process increased the SNR and contrast compared to the raw signal, and that the technique possibly allowed for clearer spectral resolution of previously observed spectral continuum. Therefore, this work has clearly shown that lens vibration is a viable mode of operation for Raman spectrometry and a novel spectrometer with

universal applicability has been designed and demonstrated in this thesis.

Moreover, as well as enhancing spectral quality metrics, the spectrometer was able to distinguish between very chemically similar samples. This was achieved through acquiring spectra from fused, porous and powdered hydroxyapatites. These spectra indicated clear differences between the different samples, with each sample producing distinct spectra. Therefore, this finding indicated that the spectrometer is able to distinguish between chemically similar samples. This is an extremely important property, particularly in the analysis of mineralising cell cultures, where there are a mix of different calcium phosphates acting as precursors to hydroxyapatite formation.

The potential of the spectrometer was further established in this work through analysis of mineralised and non-mineralised MSC cultures. Most importantly, the spectrometer could distinguish between the different cell cultures with ease; with a strong signal improvement through lock-in amplification. Additionally, the utility of the spectrometer to perform spectral mapping over a sample was demonstrated by producing a Raman image of a culture of MSCs grown in proliferation medium. Analysing line profiles for signal quality metrics demonstrated that the use of lens vibration lock-in amplified spectroscopy was also advantageous in this application and improved the information gathered. Therefore, the spectrometer proved that it could be useful in performing chemical analysis and mapping for tissue engineered constructs and research applications.

Upon comparison with the literature, it was found that the spectrometer was potentially detecting a spectra as a result of ROA, rather than pure Raman spectra. Although this was not the original intention of this work, it is a potentially promising finding as no complete ROA spectra of the samples analysed in this work have previously been captured.

The mineralised and non-mineralised MSC cultures analysed in this work had been fixed and prepared for SEM analysis, prior to their investigation with the spectrometer. The potential Raman return from the samples appeared to be very strong, particularly in comparison to the spectral return of homogeneous bulk samples. Therefore, as an adjunct to the main aims of the work, this research appears to demonstrate that SEM preparation may indeed provide a suitable substrate for surface enhanced Raman spectroscopy. This finding could potentially be very useful in allowing researchers to gain both morphological and detailed chemical information from SEM prepared cell cultures, allowing for the generation of multi-modal data sets from a single set of cell culture repeats. However, studying methods for surface enhanced Raman spectroscopy along with its utility was not the main goal of this work, therefore, it was not investigated in detail. Moreover, the spectra generated here showed that there is a research opportunity in the further investigation of this

finding.

Finally, lens vibration lock-in amplified spectroscopy was developed to compliment existing standard Raman technologies. Proof of concept data was collected from compact CCD spectrometer, with post spectral collection lock-in amplification applied. The pilot work in this area used a dual phase lock-in amplification based on a simulated lens vibration system, which demonstrated some enhancement which was not as conclusive as in the photodiode based system. The initial methods applied were not quite as successful as had been hoped for in replicating the results achieved with the photodiode based spectrometer. However, the results obtained suggested that with further work and improvements in the collection and reconstruction of the signals to be lock-in amplified, it may be be possible to use lens vibration lock-in amplified Raman or ROA spectroscopy with or in a commercial Raman system. Furthermore, it may be possible for those who use compact spectrometer optics to modify their optics set up and collection software to benefit from the potential signal improvements by lens vibration lock-in amplified Raman or, potentially, ROA spectroscopy.

In summary, the key finding of this work are as follows:

- Lens-vibration provided a suitable signal for lock-in amplification in Raman, or potentially ROA, spectroscopy.
- The application of lens vibration lock-in amplification to the spectra collected by a photodiode-translation monochromator improved spectral quality.
- Lens vibration lock-in amplification was used to differentiate between chemically similar samples of different forms using fused, porous and powdered hydroxyapatite.
- The developed spectrometer was be used to enhance the spectra collected from cultures of MSCs.
- The spectrometer differentiated between mineralised and non-mineralised cell cultures of MSCs.
- The spectrometer demonstrated spectral differences at different points the same population of cells.
- Lens vibration lock-in amplification improved the quality of spectral mapping.
- SEM preparation may enable SERS of cell cultures.
- The spectrometer may have captured complete ROA spectra for the first time from silica, hydroxyapatite, and MSCs.

- With further work lens vibration lock-in amplified Raman, or potentially ROA, spectroscopy could be adapted for and applied to existing custom built Raman spectrometers using CCD spectrometers or into complete commercial Raman systems.

Therefore, this work has successfully developed a new technique for Raman or ROA spectroscopy which has the potential to provide a more optimum technique for Raman analysis of cell cultures.

Therefore, it may be possible that with further work on integrating the technology into commercial "off the shelf" and custom built spectrometers, lens vibration Raman, or ROA, spectroscopy could be implemented within tissue engineering in order to improve the quality of Raman spectroscopy and reduce irradiance. As a result Raman and ROA spectroscopy could become viable quality assurance and research aids, reducing costs and improving outcomes.

Chapter 8

Future Work

This thesis documented the early development of a new spectroscopic tool. Although this investigation was successful, development of the system and adapting it to work with optimal modern technologies was a substantial body of work. Therefore, the full potential of the system is yet to be explored and this work hopefully represents an opportunity for further development in optimising Raman spectroscopy for biological cultures.

A key area for future research with the spectrometer, is the further testing of the potential spectra arising from ROA phenomena. This can be approached in two ways. Firstly, spectra should be collected with the direction of rotation of the circularly polarised light reversed. This can be achieved through simply changing the angle of the quarter waveplate, and will demonstrate that the spectrometer is detecting ROA spectra if there is a difference found between spectra collected with circularly polarised light rotating in opposite directions. Secondly, the optical set up should be modified so that the light exciting the sample has a linear polarisation. This could simply be achieved by adding a second quarter waveplate between the polarising beam splitter, and tuning the angle of each plate to produce maximum reflection of the laser light towards the diffraction grating by the polarising beam splitter after the light has been scattered by the sample. As a result of these experiments, it will be possible to identify whether the spectrometer is operating as a ROA spectrometer and, if so, allow the utility of the instrument as a pure Raman spectrometer to be better explored. In addition, if it appears that ROA signal is being detected, then a sample which has been well characterised in the ROA literature, such as egg white[304].

Two other important areas in which future research into the use of this Raman system include analysing live cell cultures and examination of the mineralisation pathway of the rat MSC model. Firstly, as the spectrometer design using the photodiode is more developed, further work should be conducted in the analysis of fixed and live cell cultures using the lens vibration lock-in amplified Raman spectrome-

ter. Due to the developmental nature of this work, fixed MSC cell cultures were examined as part of this thesis as they are very stable and allowed for repeat and prolonged analysis periods and the spectrometer successfully demonstrated the ability to distinguish between different cell populations. Although this is very useful in the development of a new technology, it does not fully demonstrate the ideal final purpose of the spectrometer in the online analysis of *in vitro* cell cultures. Therefore, future work using the system should focus on the application of the spectrometer to live cell cultures. This could open up avenues in rigorously examining the mineralisation pathway and nature of the mineral formed in the rat MSC mineralisation model in comparison to mature bone and a human cell models. In addition the spectrometer should be used on further cell models to characterise more biological species.

A useful avenue for investigation with the photodiode based spectrometer is the Raman mapping of a fixed SEM prepared osteogenic cell culture in the region of 2149.1 cm^{-1}, which was identified as an area of change in the spectra collected along a line of the cell culture detailed in Figure 5.62, then used to generate the Raman maps of the proliferative cell cultures. This is because it allowed for changes within the proliferative cell culture to be visualised. Next, further Raman mapping should be performed at a variety of wavenumber shifts across the SEM fixed cell culture samples. Some key areas which could be investigated include at 964 cm^{-1} to compare the distribution of potentially more mature hydroxyapatite, and at around 950 cm^{-1} to compare the distribution of potentially less mature apatite. Therefore, further comparisons between the differentiated and non-differentiated cell cultures could be made. In addition, other peaks representing general ECM and cellular components could be compared across the two cell cultures.

It could be useful to work on better optimising the lens vibration protocol and settings used with the lock-in amplifier. After these examinations and optimisations, a natural next step would be to attempt to use the spectrometer to analyse cell culture samples which have been fixed, but not sputter-coated for SEM. This would investigate how well the spectrometer can be used to analyse cell cultures which do not potentially undergo spectral enhancement. The key steps in analysis of these cultures would be to initially capture full spectra and optimise the lock-in amplification settings, then perform Raman mapping over the cell cultures. As performed for the cultures analysed here, signal quality metrics should be analysed to show whether the lock-in amplifier provides selective spectral amplification. After verifying the ability of the spectrometer to analyse fixed cell cultures the next step could be to see if the spectrometer can still resolve the spectrum of a fixed sample in cell culture medium. This would allow for testing to see if the spectrometer would work in an on-line *in vitro* situation without having to overcome other technical

difficulties. As the focal spot transitions from the culture medium into the cells there is a potential that cell spectra can be enhanced selectively, instead of the medium, if the phase selection on the lock-in amplifier is chosen correctly. To work towards this goal it may be appropriate to make a simple simulation by placing a sample of fused hydroxyapatite in a well of cell culture medium. Therefore, optimisation can be performed using a more stable system which may be easier to work with over a more extended period of time.

Evidently, the ultimate aim of the work described above would be to use the system for online analysis of 3D cell cultures. As a result, after successfully performing the analysis of fixed cultures in tissue culture medium, the next stage would be to develop a system for the spectrometer to perform live analysis. Initially, crude live analysis could be performed on a culture exposed to the air as an endpoint type study, but then efforts could be made to use tissue culture plates with optically clear windows or in bioreactors during the culture processes.

Secondly, further work in the development of the more commercially applicable CCD spectrometer should be conducted. The photodiode based spectrometer is effective, but it is not ideal for use in many biology laboratories due to the need for many items of specialist optics equipment and specialist knowledge to assemble them. Additionally, there would be a cost implication due to the need to buy a suitable lock-in amplifier and custom spectral collection control systems. Therefore, the adaptation of existing systems to include lens vibration lock-in amplification or the development of new commercially viable spectrometers based on the design would be highly desirable. Initial attempts at applying lens-vibration Raman spectroscopy using a commercial compact CCD spectrometer suggested that it is possible to adapt the technology to a spectrometer of this form. However, there are further developments required in the data collection and post processing with lock-in amplification. CCD spectrometers often collect the spectrum as a whole, without access to individual spectral components with configurable data collection procedures. As a result, all of the data will need to be collected prior to lock-in amplification and the optimal data collection methodologies need to be determined. This is likely either to be using spectral collection at several static points with different voltages, and therefore displacements, applied to to the lens, or by vibrating the lens and performing gated acquisition of data throughout the lens operation. As a result new software for the construction of the signal for lock-in amplification and for collecting the spectral data would need to be developed.

Another area of interest to investigate could be that, in general, normal tissue culture substrates are incompatible with Raman spectroscopy. This is a key failing of many current spectroscopy systems. During this project this difficultly was encountered through an attempt at the Raman analysis of cell monolayers cultured on

tissue culture plastic designed for microscopy using a Raman microscope at another institution. Interestingly, initial findings from the examination of SEM prepared cell cultures on a tissue culture plastic substrate suggest that this is not a problem for the lens vibration system. However, the non-interference of tissue culture plastic in the absence of the SEM coating is needed to confirm this conclusion. Therefore, the program of work described above in working towards live cell culture analysis would help to demonstrate that this spectrometer overcomes this issue. Furthermore, additional work should also be performed using the Raman spectrometer to analyse cells cultured on normal tissue culture plastic plates and other common cell culture substrates. If initial studies are not favourable, it could be that tuning the phase of the lock-in amplifier could help to better isolate the cell spectra.

Considering the potential findings of surface enhanced Raman spectroscopy from cell cultures prepared for SEM present other avenues for future work. Initially, a comparison between the spectra acquired with this spectrometer from cells fixed and stained for SEM, but not sputter-coated, and cells fully prepared for SEM should be undertaken using the same parameters. As a result, this would allow for the direct comparison of spectra with and without potential surface enhanced effects occurring, allowing for verification that an enhancement effect is occurring. In the event that this work demonstrated an enhancement it would be useful to test to see if gold sputter-coating reliably produces surface enhancement, or whether there is an inherent variability in the coating process which modulates the success of the coating for producing a SERS effect. The natural follow up to work of this nature would be to try to optimise the sputter-coating process for Raman spectroscopy and to test to see if this still allowed for SEM images of a useful quality to be obtained from the same sample. The next stage could be to compare SERS spectra acquired with a sample prepared for SEM to SERS spectra acquired using current SERS techniques using nano-particles and gold cell culture substrates.

As shown above, there are many potential areas for further investigation and improvement of the lens vibration lock-in amplified spectrometer. There are many different avenues for investigation which have the potential for improving the spectrometer and helping to improve Raman spectroscopy for use in biological applications.

References

[1] A. Villasante and G. Vunjak-Novakovic, "Tissue-engineered models of human tumors for cancer research," *Expert Opinion on Drug Discovery*, vol. 10, no. 3, pp. 257–268, 2015.

[2] M. Ravi, V. Paramesh, S. Kaviya, E. Anuradha, and F. P. Solomon, "3d cell culture systems: Advantages and applications," *Journal of Cellular Physiology*, vol. 230, no. 1, pp. 16–26, 2015.

[3] A. Akhtar, "The flaws and human harms of animal experimentation," *Cambridge Quarterly of Healthcare Ethics*, vol. 24, no. 04, pp. 407–419, 09 2015.

[4] H. Government, "The animals (scientific procedures) act 1986 (no. 3039)," London, UK, 2012.

[5] G. de la Roza. (2016, 04) Histology of bone: Background, gross structure of long bone, nerves and vasculature of bone. [Online]. Available: http://emedicine.medscape.com/article/1254517-overview

[6] R. Buckley. (2016, 01) General principles of fracture care: Background, pathophysiology, etiology. [Online]. Available: http://emedicine.medscape.com/article/1270717-overview#a4

[7] A. Ilyas and S. Rehman, *Contemporary surgical management of fractures and complications: Volume II*, 1st ed. New Delhi, India: Jaypee Brothers Medical Publishers, 2013.

[8] C. do Nascimento, J. P. M. Issa, R. R. de Oliveira, M. M. Iyomasa, S. Siéssere, and S. C. H. Regalo, "Biomaterials applied to the bone healing process," *International Journal of Morphology*, vol. 25, no. 4, pp. 839–846, 2007.

[9] F. Matassi, L. Nistri, D. C. Paez, and M. Innocenti, "New biomaterials for bone regeneration," *Clinical Cases in Mineral and Bone Metabolism*, vol. 8, no. 1, pp. 21–24, 2011.

[10] C. R. M. Black, V. Goriainov, D. Gibbs, J. Kanczler, R. S. Tare, and R. O. C. Oreffo, "Bone tissue engineering," *Current Molecular Biology Reports*, vol. 1, no. 3, pp. 132–140, 2015.

[11] K. A. Athanasiou, M. Detamore, and A. Almarzar, *Tissue Engineering of Temporomandibular Joint Cartilage*. Williston, USA: Morgan & Claypool, 2009.

[12] J. Frese, A. Morgenroth, M. E. Mertens, S. Koch, L. Rongen, A. T. Vogg, A. T. Vogg, B. Neumaier, V. N. Gesche, T. Lammers, T. Schmitz-Rode, P. Mela, S. Jockenhoevel, F. M. Mottaghy, and F. Kiessling, "Nondestructive monitoring of tissue-engineered constructs," *Biomedical Engineering / Biomedizinische Technik*, vol. 59, no. 2, pp. 165–175, 2014.

[13] R. Edmondson, J. J. Broglie, A. F. Adcock, and L. Yang, "Three-dimensional cell culture systems and their applications in drug discovery and cell-based biosensors." *Assay and drug development technologies*, vol. 12, no. 4, pp. 207–218, 2014. [Online]. Available: http://www.ncbi.nlm.nih.gov/pubmed/24831787{%}5Cnhttp://www.pubmedcentral.nih.gov/articlerender.fcgi?artid=PMC4026212

[14] L. Kimlin, J. Kassis, and V. Virador, "3d in vitro tissue models and their potential for drug screening," *Expert Opinion on Drug Discovery*, vol. 8, no. 12, pp. 1455–1466, 2013.

[15] E. B. Hanlon, R. Manoharan, T.-W. Koo, K. E. Shafer, J. T. Motz, M. Fitzmaurice, J. R. Kramer, I. Itzkan, R. R. Dasari, and M. S. Feld, "Prospects for in vitro Raman spectroscopy," *Physics in Medicine and Biology*, vol. 45, no. 2, pp. R1–R59, 2000.

[16] M. M. Jawad, S. T. A. Qade, A. Zaidan, B. Zaidan, A. Naji, and I. T. A. Qade, "An overview of laser principle, laser-tissue interaction mechanisms and laser safety precautions for medical laser users," *International Journal of Pharmacology*, vol. 7, no. 2, pp. 149–160, 02 2011.

[17] M. S. Foltz, N. A. Whitlock, L. E. Estlack, M. A. Figueroa, R. J. Thomas, B. A. Rockwell, and M. L. Denton, "Photochemical damage from chronic 458-nm laser exposures in an artificially pigmented htert-rpe1 cell line," *Proc. SPIE*, vol. 6084, pp. 608 415–608 415–12, 2006. [Online]. Available: http://dx.doi.org/10.1117/12.644690

[18] F. Cammarata, "Medical lasers and laser–tissue interactions," *Physics Education*, vol. 34, no. 3, pp. 156–161, 05 1999.

[19] F. Yildiz, M. Gulsoy, and I. Cilesiz, "An experimental study on photothermal damage to tissue: The role of irradiance and wavelength," *Laser Physics*, vol. 26, no. 9, p. 095601, 07 2016.

[20] E. Yousif and R. Haddad, "Photodegradation and photostabilization of polymers, especially polystyrene: Review," *SpringerPlus*, vol. 2, no. 1, p. 398, 2013.

[21] B. R. Hammond, B. A. Johnson, and E. R. George, "Oxidative photodegradation of ocular tissues: Beneficial effects of filtering and exogenous antioxidants," *Experimental Eye Research*, vol. 129, pp. 135 – 150, 2014. [Online]. Available: //www.sciencedirect.com/science/article/pii/S0014483514002504

[22] A. S. K. Mohanty, A. Rapp, S. Monajembashi, P. K. Gupta, and K. O. Greulich, "Comet Assay Measurements of DNA Damage in Cells by Laser Microbeams and Trapping Beams with Wavelengths Spanning a Range of 308 nm to 1064 nm," *Radiation Research*, vol. 157, no. 4, pp. 378–385, 2002.

[23] D. Long, *The Raman Effect: A Unified Treatment of the Theory of Raman Scattering by Molecules*. Chichester, West Sussex: John Wiley & Sons Ltd, 2002.

[24] Y.-H. Chiang, S. H. Wu, Y.-C. Kuo, H.-F. Chen, A. Chiou, and O. K. Lee, "Raman spectroscopy for grading of live osteosarcoma cells," *Stem Cell Research & Therapy*, vol. 6, no. 1, p. 81, 2015.

[25] S. Takanezawa, S.-i. Morita, Y. Ozaki, and Y. Sako, "Raman Spectral Dynamics of Single Cells in the Early Stages of Growth Factor Stimulation," *Biophysical Journal*, vol. 108, no. 9, pp. 2148–2157, 2015.

[26] C. a. Owen, J. Selvakumaran, I. Notingher, G. Jell, L. L. Hench, and M. M. Stevens, "In vitro toxicology evaluation of pharmaceuticals using Raman micro-spectroscopy," *Journal of Cellular Biochemistry*, vol. 99, no. 1, pp. 178–186, 2006.

[27] T. Ichimura, L. D. Chiu, K. Fujita, S. Kawata, T. M. Watanabe, T. Yanagida, and H. Fujita, "Visualizing cell state transition using raman spectroscopy," *PLoS ONE*, vol. 9, no. 1, 2014.

[28] S. Koutsopoulos, "Synthesis and characterization of hydroxyapatite crystals: A review study on the analytical methods," *Journal of Biomedical Materials Research Part A*, vol. 62, no. 4, pp. 600–612, 2002.

[29] G. Rusciano, A. C. De Luca, and A. Sasso, "Enhancing Raman Tweezers by Phase-Sensitive Detection," *Analytical Chemistry*, vol. 79, no. 10, pp. 3708–3715, 2007.

[30] A. C. De Luca, M. Mazilu, A. Riches, C. S. Herrington, and K. Dholakia, "Online fluorescence suppression in modulated Raman spectroscopy," *Analytical Chemistry*, vol. 82, no. 2, pp. 738–745, 2010.

[31] C. Tzinis, S. K. Bahl, P. Davidson, W. M. Risen, and R. H. Baughman, "Sample modulated Raman spectroscopy and frequency modulated visible light—resonance Raman spectrum of a polydiacetylene fiber," *Review of Scientific Instruments*, vol. 49, no. 12, pp. 1725–1728, 1978.

[32] G. Rusciano, A. C. De Luca, A. Sasso, and G. Pesce, "Phase-sensitive detection in Raman tweezers," *Applied Physics Letters*, vol. 89, no. 26, p. 261116, 2006.

[33] D. B. Burr and M. R. Allen, *Basic and Applied Bone Biology*. Academic Press - Elsevier, 2013.

[34] A. S. Brydone, D. Meek, and S. Maclaine, "Bone grafting, orthopaedic biomaterials, and the clinical need for bone engineering." *Proceedings of the Institution of Mechanical Engineers. Part H, Journal of engineering in medicine*, vol. 224, no. 12, pp. 1329–1343, 2010.

[35] V. Campana, G. Milano, E. Pagano, M. Barba, C. Cicione, G. Salonna, W. Lattanzi, and G. Logroscino, "Bone substitutes in orthopaedic surgery: from basic science to clinical practice," *Journal of Materials Science: Materials in Medicine*, vol. 25, pp. 2445–2461, 2014.

[36] T. T. Roberts and A. J. Rosenbaum, "Bone grafts, bone substitutes and orthobiologics: the bridge between basic science and clinical advancements in fracture healing." *Organogenesis*, vol. 8, no. 4, pp. 114–124, 2012.

[37] C. G. Finkemeier, "Bone-Grafting and Bone-Graft Substitutes," *The Journal of Bone and Joint Surgery*, vol. 84A, no. 3, pp. 454–463, 2002.

[38] R. Lomas, A. Chandrasekar, and T. N. Board, "Bone allograft in the UK: Perceptions and realities," *HIP International*, vol. 23, no. 5, pp. 427–433, 2013.

[39] American Academy of Orthopaedic Surgeons, A. S. Greenwald, S. D. Boden, R. L. Barrak, M. P. Bostrom, V. M. Goldberg, M. J. Yaszemski, and C. S. Heim, "The Evolving Role of Bone-Graft Sunbsitiutes," in *American Academy of Orthopaedic Surgeons 77th Annual Meeting*, New Orleans, USA, 2010.

[40] R. Langer and J. P. Vacanti, "Tissue Engineering," *Science*, vol. 260, pp. 920–926, 1993.

[41] A. J. Salgado, O. P. Coutinho, and R. L. Reis, "Bone tissue engineering: State of the art and future trends," *Macromolecular Bioscience*, vol. 4, no. 8, pp. 743–765, 2004.

[42] U. A. Stock and J. P. Vacanti, "Tissue Engineering : Current State and Prospects," *Annual Review of Medicine*, vol. 52, pp. 443–451, 2001.

[43] NHS Blood and Transplant, "Organ Donation and Transplantation Activity Data: Unitied Kingdom [Date Accessed: 11.06.2015]," 2015. [Online]. Available: https://nhsbtmediaservices.blob.core.windows.net/organ-donation-assets/pdfs/united_kingdom.pdf

[44] NHS Blood and Transplant, "Transplants Save Lives Fact Sheets [Date Accessed: 11.06.2015]," 2014. [Online]. Available: http://www.organdonation.nhs.uk/newsroom/fact_sheets/transplants_save_lives.asp

[45] G. Vunjak-Novakovic, N. Tandon, A. Godier, R. Maidhof, A. Marsano, T. P. Martens, and M. Radisic, "Challenges in cardiac tissue engineering." *Tissue engineering. Part B, Reviews*, vol. 16, no. 2, pp. 169–187, 2010.

[46] F. R. A. J. Rose and R. O. C. Oreffo, "Bone tissue engineering: hope vs hype." *Biochemical and biophysical research communications*, vol. 292, no. 1, pp. 1–7, 2002.

[47] M. Cnop, N. Welsh, J.-C. Jonas, A. Jo, and S. Lenzen, "Mechanisms of Pancreatic beta-Cell Death in Type 1 and Type 2 Diabetes: Many Differences, Few Similarities," *Diabetes*, vol. 54, no. suppl 2, pp. S97–S107, 2014.

[48] Diabetes UK, "The Cost of Diabetes Report [Date Accessed 11.06.2015]," Tech. Rep., 2014. [Online]. Available: https://www.diabetes.org.uk/Documents/DiabetesUKCostofDiabetesReport.pdf

[49] K. Y. Ching, O. G. Andriotis, S. Li, P. Basnett, B. Su, I. Roy, R. S. Tare, B. G. Sengers, and M. Stolz, "Nanofibrous poly(3-hydroxybutyrate)/poly(3-hydroxyoctanoate) scaffolds provide a functional microenvironment for cartilage repair," *Journal of Biomaterials Applications*, vol. 31, no. 1, pp. 77–91, 2016.

[50] S. J. Hollister and W. L. Murphy, "Scaffold Translation: Barriers Between Concept and Clinic," *Tissue Engineering Part B: Reviews*, vol. 17, no. 6, pp. 459–474, 2011.

[51] J. Mitra, G. Tripathi, A. Sharma, and B. Basu, "Scaffolds for bone tissue engineering: role of surface patterning on osteoblast response," *RSC Advances*, vol. 3, no. 28, p. 11073, 2013.

[52] V. Karageorgiou and D. Kaplan, "Porosity of 3D biomaterial scaffolds and osteogenesis," *Biomaterials*, vol. 26, no. 27, pp. 5474–5491, 2005.

[53] A. R. Amini, C. T. Laurencin, and S. P. Nukavarapu, "Bone tissue engineering: recent advances and challenges." *Critical reviews in biomedical engineering*, vol. 40, no. 5, pp. 363–408, 2012.

[54] A. Ratcliffe, "The Translation of Product Concept to Bone Products: A Partnership of Therapeutic Effectiveness and Commercialization," *Tissue Engineering Part B: Reviews*, vol. 17, no. 6, pp. 443–447, 2011.

[55] U.S. Food and Drug Administration, "FDA Medical Device Approvals: InFUSE™ Bone Graft/LT-CAGE™ Lumbar Tapered Fusion Device - P000058 [Date Accessed: 11.06.2015]," 2002. [Online]. Available: http://www.accessdata.fda.gov/cdrh_docs/pdf/P000058a.pdf

[56] E. C. Novosel, C. Kleinhans, and P. J. Kluger, "Vascularization is the key challenge in tissue engineering," *Advanced Drug Delivery Reviews*, vol. 63, no. 4, pp. 300–311, 2011.

[57] C. E. P. Aronin, K. W. Sadik, A. L. Lay, D. B. Rion, S. S. Tholpady, R. C. Ogle, and E. A. Botchwey, "Comparative effects of scaffold pore size, pore volume, and total void volume on cranial bone healing patterns using microsphere-based scaffolds," *Journal of Biomedical Materials Research A*, vol. 89, no. 3, pp. 632–341, 2009.

[58] Y. Ikada, "Challenges in tissue engineering." *Journal of the Royal Society, Interface / the Royal Society*, vol. 3, no. 10, pp. 589–601, 2006.

[59] Y. Ikada, *Tissue Engineering: Fundamentals and Applications*, 1st ed. Oxford, UK: Academic Press - Elsevier, 2006.

[60] D. Howard, L. D. Buttery, K. M. Shakesheff, and S. J. Roberts, "Tissue engineering: Strategies, stem cells and scaffolds," *Journal of Anatomy*, vol. 213, no. 1, pp. 66–72, 2008.

[61] A. A. Palakkan, D. C. Hay, A. K. PR, K. TV, and J. A. Ross, "Liver tissue engineering and cell sources: Issues and challenges," *Liver International*, vol. 33, no. 5, pp. 666–676, 2013.

[62] J. M. Polak, *Advances in Tissue Engineering*, 1st ed., Polak Julia M, S. Mantalaris, and S. Harding, Eds. London, UK: Imperial College Press, 2008.

[63] C. A. Herberts, M. S. G. Kwa, and H. P. H. Hermsen, "Risk factors in the development of stem cell therapy." *Journal of Translational Medicine*, vol. 9, no. 1, p. 29, 2011.

[64] U. Ben-David and N. Benvenisty, "The tumorigenicity of human embryonic and induced pluripotent stem cells." *Nature Reviews. Cancer*, vol. 11, no. 4, pp. 268–277, 2011.

[65] P. S. Knoepfler, "Deconstructing stem cell tumorigenicity: A roadmap to safe regenerative medicine," *Stem Cells*, vol. 27, no. 5, pp. 1050–1056, 2009.

[66] R. M. L. Winston, "Does government regulation inhibit embryonic stem cell research and can it be effective?" *Cell Stem Cell*, vol. 1, no. 1, pp. 27–34, 2007.

[67] R. S. Tuan, G. Boland, and R. Tuli, "Adult mesenchymal stem cells and cell-based tissue engineering." *Arthritis research & therapy*, vol. 5, no. 1, pp. 32–45, 2003.

[68] A. C. White and W. E. Lowry, "Refining the role for adult stem cells as cancer cells of origin," *Trends in Cell Biology*, vol. 25, no. 1, pp. 11–20, 2015.

[69] C. B. Cohen, *Renewing the Stuff of Life : Stem Cells, Ethics, and Public Policy*. New York, USA: Oxford University Press, 2007.

[70] C. E. Gargett, "Adult stem cells in the human endometrium," in *Stem Cells in Human Reproduction: Basic Science and Therapeutic Potential*, 2nd ed., C. Simon and A. Pellicier, Eds. CRC Press, 2007, ch. 9, pp. 105–120.

[71] D. G. Zacharias, T. J. Nelson, P. S. Mueller, and C. C. Hook, "The science and ethics of induced pluripotency: what will become of embryonic stem cells?" *Mayo Clinic Proceedings*, vol. 86, no. 7, pp. 634–640, 2011.

[72] S. V. Liu, "iPS cells: a more critical review." *Stem cells and development*, vol. 17, no. 3, pp. 391–397, 2008.

[73] F. J. O'Brien, "Biomaterials & scaffolds for tissue engineering," *Materials Today*, vol. 14, no. 3, pp. 88–95, 2011.

[74] J. D. Boer, C. V. Blitterswijk, P. Thomsen, J. Hubbell, R. Cancedda, J. de Bruijn, A. Lindahl, J. Sohier, and D. F. Williams, *Tissue Engineering*, 1st ed., C. V. Blitterswijk, Ed. London, UK: Academic Press - Elsevier, 2008.

[75] X. Wang, J. S. Nyman, and M. Reyes, *Fundamental Biomechanics in Bone Tissue Engineering*. Morgan and Claypool Publishers, 2010.

[76] P. M. Dohmen and W. Konertz, "Tissue-engineered heart valve scaffolds," *Annals of Thoracic and Cardiovascular Surgery*, vol. 15, no. 6, pp. 362–367, 2009.

[77] D. Williams, "Benefit and risk in tissue engineering," *Materials Today*, vol. 7, no. 5, pp. 24–29, 2004.

[78] T. Gourlay and R. A. Black, *Biomaterials and Devices for the Circulatory System*. Cambridge, UK: Woodhead Publishing, 2010.

[79] A. Anthony, *Methods of Tissue Engineering*, 1st ed., A. Atala and R. P. Lanza, Eds. San Diego CA, USA: Academic Press - Elsevier, 2002.

[80] R. S. Voronov, S. B. VanGordon, R. L. Shambaugh, D. V. Papavassiliou, and V. I. Sikavitsas, "3D tissue engineered construct analysis via conventional high resolution microCT without x-ray contrast," *Tissue Engineering Part C: Methods*, vol. 19, no. 5, pp. 327–335, 2013.

[81] L. G. Griffith and M. A. Swartz, "Capturing complex 3D tissue physiology in vitro." *Nature reviews. Molecular cell biology*, vol. 7, no. 3, pp. 211–224, 2006.

[82] F. Pampaloni, E. G. Reynaud, and E. H. K. Stelzer, "Most of the cell-based data-harvesting efforts that drive the integration of cell biology," *Nature reviews. Molecular cell biology*, vol. 8, no. 10, pp. 839–845, 2007.

[83] K. M. Yamada and E. Cukierman, "Modeling Tissue Morphogenesis and Cancer in 3D," *Cell*, vol. 130, no. 4, pp. 601–610, 2007.

[84] S. K. Doke and S. C. Dhawale, "Alternatives to animal testing: A review." *Saudi Pharmaceutical Journal*, vol. 23, no. 3, pp. 223–229, 2015. [Online]. Available: http://www.sciencedirect.com/science/article/pii/S1319016413001096

[85] J. E. Davies, "In Vitro modeling of the bone/mplant Interface," *The Anatomical Record*, vol. 245, pp. 426–445, 1996.

[86] K.-h. Nam, A. S. T. Smith, S. Lone, S. Kwon, and D.-H. Kim, "Biomimetic three-dimensional tissue models for advanced high-throughput drug screening," *Journal of Laboratory Automation*, vol. 20, no. 3, pp. 201–215, 2015.

[87] S. Bersini, J. S. Jeon, G. Dubini, C. Arrigoni, S. Chung, J. L. Charest, M. Moretti, and R. D. Kamm, "A Microfluidic 3D In Vitro Model for Specificity of Breast Cancer Metastasis to Bone," *Biomaterials*, vol. 35, no. 8, pp. 2454–2561, 2014.

[88] Y.-s. Torisawa, C. S. Spina, T. Mammoto, A. Mammoto, J. C. Weaver, T. Tat, J. J. Collins, and D. E. Ingber, "Bone marrow–on–a–chip replicates hematopoietic niche physiology in vitro," *Nature Methods*, vol. 11, no. 6, pp. 663–669, 2014.

[89] E. W. Esch, A. Bahinski, and D. Huh, "Organs-on-chips at the frontiers of drug discovery." *Nature reviews. Drug discovery*, vol. 14, no. 4, pp. 248–260, 2015. [Online]. Available: http://www.scopus.com/inward/record.url?eid=2-s2.0-84926408953{&}partnerID=tZOtx3y1

[90] J. Leighton, "A Sponge Matrix Method For Tissue Culture. Formation Of Organized Aggregates Of Cells In Vitro," *Journal of the National Cancer Institute*, vol. 12, no. 3, pp. 545–561, 1951.

[91] J. Leighton, "Studies on Human Cancer Using Sponge-Matrix Tissue Culture. I. The growth patterns of a malignant melanoma, adenocarcinoma of the parotid gland, papillary adenocarcinoma of the thyroid gland, adenocarcinoma of the pancreas, and epidermoid carcinom," *Texas Reports on Biology and Medicine*, vol. 12, no. 4, pp. 847–864, 1954.

[92] J. Leighton, R. L. Kalla, I. Kline, and M. Belkin, "Pathogenesis of Tumor Invasion I. Interaction between Normal Tissues and "Transformed" Cells in Tissue Culture," *Cancer research*, vol. 19, no. 1, pp. 23–27, 1959.

[93] J. Leighton, R. L. Kalla, J. M. Turner Jr., and R. H. Fennell Jr., "Pathogenesis of Tumor Invasion: II. Aggregate Replication," *Cancer research*, vol. 20, no. 5, pp. 575–586, 1960.

[94] J. Leighton and I. Klein, "Studies on Human Cancer Using Sponge-Matrix Tissue Culture. II. Inavsion of Connective Tissue by Carcinoma (Strain HeLa)," *Texas Reports on Biology and Medicine*, vol. 12, no. 4, pp. 865–873, 1954.

[95] J. Leighton, I. Kline, M. Belkin, and Z. Tetenbaum, "Studies on human cancer using sponge-matrix tissue culture. III. The invasive properties of a carcinoma (strain HeLa) as influenced by temperature variations, by conditioned media, and in contact with rapidly growing chick embryonic tissue." *Journal of the National Cancer Institute*, vol. 16, no. 6, pp. 1353–1373, 1956.

[96] J. Lee, M. J. Cuddihy, and N. A. Kotov, "Three-dimensional cell culture matrices: state of the art." *Tissue engineering. Part B, Reviews*, vol. 14, no. 1, pp. 61–86, 2008.

[97] B. M. Baker and C. S. Chen, "Deconstructing the third dimension - how 3D culture microenvironments alter cellular cues," *Journal of Cell Science*, vol. 125, no. 13, pp. 3015–3024, 2012.

[98] D. Antoni, H. Burckel, E. Josset, and G. Noel, "Three-dimensional cell culture: A breakthrough in vivo," *International Journal of Molecular Sciences*, vol. 16, no. 3, pp. 5517–5527, 2015.

[99] Y. Kim and P. Rajagopalan, "3D hepatic cultures simultaneously maintain primary hepatocyte and liver sinusoidal endothelial cell phenotypes," *PLoS ONE*, vol. 5, no. 11, p. e15456, 2010.

[100] N. Altman and M. Krzywinski, "Points of significance: Sources of variation," *Nature Methods*, vol. 12, no. 1, pp. 5–6, 2015.

[101] C. H. Lee, J. J. Flint, B. Hansen, and S. J. Blackband, "Investigation of the subcellular architecture of L7 neurons of Aplysia californica using magnetic resonance microscopy (MRM) at 7.8 microns," *Scientific Reports*, vol. 5, p. 11147, 2015.

[102] S. C. Bushong, *Magnetic Resonance Imaging: Physical and Biological Principles*, 3rd ed. St. Louis, USA: Mosby, 2003.

[103] Y.-B. Jiang, J. Jacobson, H. K. Genant, and J. Zhao, "Application of Micro-CT and MRI in Clinical and Preclinical Studies of Osteoporosis and Related Disorders," in *Advanced Bioimaging Technologies in Assessment of the Quality of Bone and Scaffold Materials*, L. Qin, H. K. Genant, J. F. Griffith, and K. S. Leung, Eds. Springer-Verlag Berlin Heidelberg, 2007, pp. 399–415.

[104] J. Sharpe, "Optical Projection Tomography," *Annual Review of Biomedical Engineering*, vol. 6, no. 1, pp. 209–228, 2004.

[105] J. B. Aguayo, S. J. Blackband, J. Schoeniger, M. A. Mattingly, and M. Hintermann, "Nuclear magnetic resonance imaging of a single cell." *Nature*, vol. 322, no. 6075, pp. 190–1, 1986.

[106] J. French, N. Gingles, J. Stewart, and N. Woodhouse, "Use of magnetic resonance imaging (MRI) and micro-computed tomography (micro-CT) in the morphological examination of rat and rabbit fetuses from embryo-fetal development studies," *Reproductive Toxicology*, vol. 30, no. 2, pp. 292–300, 2010.

[107] D. P. Clark and C. T. Badea, "Micro-CT of rodents: State-of-the-art and future perspectives," *Physica Medica*, vol. 30, no. 6, pp. 619–634, 2014.

[108] C. Migliaresi and A. Motta, *Scaffolds for Tissue Engineering: Biological Design, Materials, and Fabrication*, 1st ed. CRC Press, 2014.

[109] E. L. Ritman, "Molecular imaging in small animals–roles for micro-CT." *Journal of Cellular Biochemistry.*, vol. 87, no. S39, pp. 116–124, 2002.

[110] J. T. Bushberg, J. A. Seibert, E. M. Leidholdt, and J. M. Boone, *The Essential Physics of Medical Imaging*, 3rd ed. Philadelphia, PA, USA: Lippincott Williams & Wilkins, 2012.

[111] R. N. Bryan, *Introduction to the Science of Medical Imaging.* Cambridge, UK: Cambridge University Press, 2010.

[112] N. M. Tole, *Basic Physics of Ultrasonographic Imaging*, H. Ostensen, Ed. Geneava, Switzerland: World Health Organisation, 2005.

[113] A. Fercher, W. Drexler, C. Hitzenberger, and T. Lasser, "Optical coherence tomography — principles and applications," *Reports on Progress in Physics*, vol. 66, pp. 239–303, 2003.

[114] L. E. Smith, R. Smallwood, and S. MacNeil, "A comparison of imaging methodologies for 3D tissue engineering," *Microscopy Research and Technique*, vol. 73, no. 12, pp. 1123–1133, 2010.

[115] R. M. Williams, W. R. Zipfel, and W. W. Webb, "Multiphoton microscopy in biological research," *Current Opinion in Chemical Biology*, vol. 5, pp. 603–608, 2001.

[116] J. R. Ferraro and K. Nakamoto, *Introductory Raman Spectroscopy*. San Diego CA, USA: Academic Press, 1994.

[117] K. F. Domke and B. Pettinger, "Studying surface chemistry beyond the diffraction limit: 10 years of TERS," *ChemPhysChem*, vol. 11, no. 7, pp. 1365–1373, 2010.

[118] I. Notingher, S. Verrier, H. Romanska, A. E. Bishop, J. M. Polak, and L. L. Hench, "In situ characterisation of living cells by Raman spectroscopy," *Journal of Spectroscopy*, vol. 16, pp. 43–51, 2002.

[119] M. J. Pelletier, "Quantitative Analysis Using Raman Spectrometry," *Applied Spectroscopy*, vol. 57, no. 1, pp. 20A–42A, 2003.

[120] K. W. Short, S. Carpenter, J. P. Freyer, and J. R. Mourant, "Raman Spectroscopy Detects Biochemical Changes Due to Proliferation in Mammalian Cell Cultures," *Biophysical Journal*, vol. 88, no. 6, pp. 4274–4288, 2005.

[121] K. Klein, A. M. Gigler, T. Aschenbrenner, R. Monetti, W. Bunk, F. Jamitzky, G. Morfill, R. W. Stark, and J. Schlegel, "Label-free live-cell imaging with confocal Raman microscopy," *Biophysical Journal*, vol. 102, no. 2, pp. 360–368, 2012.

[122] L. L. McManus, G. A. Burke, M. M. McCafferty, P. O'Hare, M. Modreanu, A. R. Boyd, and B. J. Meenan, "Raman spectroscopic monitoring of the osteogenic differentiation of human mesenchymal stem cells," *Analyst*, vol. 136, no. 12, pp. 2471–2481, 2011.

[123] G. Penel, G. Leroy, C. Rey, and E. Bres, "MicroRaman Spectral Study of the PO4 and CO3 Vibrational Modes in Synthetic and Biological Apatites," *Calcified Tissue International*, vol. 63, no. 6, pp. 475–481, 1998.

[124] R. Smith, K. L. Wright, and L. Ashton, "Raman spectroscopy: an evolving technique for live cell studies," *Analyst*, vol. 141, 2016.

[125] H. J. Byrne, G. D. Sockalingum, and N. Stone, "Raman Microscopy: Complement or Competitor?" in *Biomedical Applications of Synchrotron Infrared Microspectroscopy : A Practical Approach*, D. Moss, Ed. Cambridge: RSC Publishing, 2011, ch. 4, pp. 105–143.

[126] Hasegawa, Takeshi, Nishijo, Jujiro, and Umemura, Junzo, "Separation of Raman spectra from fluorescence emission background by principal component analysis," *Chemical Physics Letters*, vol. 317, no. 6, pp. 642–646, 2000.

[127] B. B. Praveen, P. C. Ashok, M. Mazilu, A. Riches, C. S. Herrington, and K. Dholakia, "Fluorescence suppression using wavelength modulated Raman spectroscopy in fiber-probe-based tissue analysis," *Journal of Biomedical Optics*, vol. 17, no. 7, p. 077006, 2012.

[128] K. Kong, C. Kendall, N. Stone, and I. Notingher, "Raman spectroscopy for medical diagnostics - From in-vitro biofluid assays to in-vivo cancer detection," *Advanced Drug Delivery Reviews*, vol. 89, pp. 121–134, 2015.

[129] E. Gentleman, R. J. Swain, N. D. Evans, S. Boonrungsiman, G. Jell, M. D. Ball, T. A. V. Shean, M. L. Oyen, A. Porter, and M. M. Stevens, "Comparative materials differences revealed in engineered bone as a function of cell-specific differentiation." *Nature materials*, vol. 8, no. 9, pp. 763–770, 2009.

[130] Z. Movasaghi, S. Rehman, and I. U. Rehman, "Raman Spectroscopy of Biological Tissues," *Applied Spectroscopy Reviews*, vol. 42, no. 5, pp. 493–541, 2007. [Online]. Available: http://www.informaworld.com/smpp/title{~}content=t713597229http://www.informaworld.com/smpp/title{~}content=t713597229http://www.informaworld.com/smpp/title{~}content=t713597229

[131] C. V. Raman and K. S. Krishnan, "A new type of secondary radiation," *Nature*, vol. 121, pp. 501–502, 1928.

[132] Nobel Media, "Nobelprize.org: Sir Venkata Raman - Facts [Date Accessed: 01.10.2014]," 2014. [Online]. Available: http://www.nobelprize.org/nobel_prizes/physics/laureates/1930/raman-facts.html

[133] P. A. Tipler and G. Mosca, *Physics for Scientists and Engineers : with modern physics*, 6th ed. New York, NY Houndmills, Basingstoke: W. H. Freeman, 2008.

[134] E. Smith and G. Dent, *Modern Raman Spectroscopy - A Practical Approach*. Chichester, West Sussex: John Wiley & Sons, Ltd, 2005.

[135] E. C. L. Ru and P. G. Etchegoin, *Principles of Surface-Enhanced Raman Spectroscopy: And Related Plasmonic Effects*, 1st ed. Oxford, UK: Elsevier B.V., 2009.

[136] E. B. Wilson, J. C. Decius, and P. C. Cross, *Molecular Vibrations: The Theory of Infrared and Raman Vibrational Spectra*, e-book ed. New York, USA: Dover Publications Inc, 2012.

[137] S. F. A. Kettle, *Symmetry and Structure: Readable Group Theory for Chemists*, 2nd ed. Chichester, West Sussex: John Wiley & Sons, 1995.

[138] H. Haken and H. C. Wolf, *Molecular Physics and Elements of Quantum Chemistry: Introduction to Experiments and Theory*. Springer Science & Business Media, 2004.

[139] J. Rosen, *Encyclopedia of Physics*. New York, USA: Facts on File Inc, 2004.

[140] P. J. Larkin, *Infrared and Raman Spectroscopy*. Elsevier, 2011.

[141] D. Long, *Raman Spectroscopy*, 1st ed. London: McGraw-Hill International Book Company, 1977.

[142] M. Tanaka and R. J. Young, "Review Polarised Raman spectroscopy for the study of molecular orientation distributions in polymers," *Journal of Materials Science*, vol. 41, no. 3, pp. 963–991, 2006.

[143] B. L. Sands, M. J. Welsh, S. Kin, R. Marhatta, J. D. Hinkle, and S. B. Bayram, "Raman scattering spectroscopy of liquid nitrogen molecules: An advanced undergraduate physics laboratory experiment," *American Journal of Physics*, vol. 75, no. 6, pp. 488–495, 2007.

[144] S. S. Mitra, "Vibration Spectra of Solids," in *Solid State Physics, Volume 13*, 1st ed., Frederick Seitz and David Turnbull, Eds. New York, USA: Academic Press Inc., 1962, ch. 4, p. 47.

[145] B. C. Smith, *Infrared Spectral Interpretation: A Systematic Approach*, 1st ed. CRC Press, 1998.

[146] W. Kutzner, "Das raman-spektrum an mono-, di- und trisacchariden," *Naturwissenschaften*, vol. 20, no. 19, pp. 331–332, 1932.

[147] A. Walton, M. Deveney, and J. Koenig, "Raman spectroscopy of calcified tissue," *Calcified Tissue Research*, vol. 6, no. 1, pp. 162–167, 1970.

[148] C. M. Perlaki, Q. Liu, and M. Lim, "Raman Spectroscopy Based Techniques in Tissue Engineering—An Overview," *Applied Spectroscopy Reviews*, vol. 49, no. 7, pp. 513–532, 2014.

[149] F. H. Spedding and R. F. Stamm, "The Raman Spectra of the Sugars in the Solid State and in Solution I. The Raman Spectra of α- and β-d-Glucose," *The Journal of Chemical Physics*, vol. 10, pp. 176–183, 1942.

[150] R. Lord and G. Thomas, "Raman spectral studies of nucleic acids and related molecules - I Ribonucleic acid derivatives," *Spectrochimica Acta Part A: Molecular and Biomolecular Spectroscopy*, vol. 23, no. 9, pp. 2551–2591, 1967.

[151] M. C. Tobin, "Raman Spectra of Crystalline Lysozyme , Pepsin , and Alpha Chymotrypsin," *Science*, vol. 161, no. 3836, pp. 68–69, 1968.

[152] M. Smith, A. G. Walton, and J. L. Koenig, "Raman Spectra of Polyglycines," *Biopolymers*, vol. 8, pp. 29–43, 1969.

[153] M. Smith, A. G. Walton, and J. L. Koenig, "Raman spectroscopy of poly-L-proline in aqueous solution," *Biopolymers*, vol. 8, pp. 173–179, 1969.

[154] S. Webb, "Effects of microwaves on normal and tumour cells as seen by laser raman spectroscopy," *Journal of Microwave Power*, vol. 11, no. 138, 1976.

[155] S. Webb, J. Montgomery, and M. Stoneham, "Effects af Microwaves on the Metabolic Time Clocks of Normal and Tumour Cells as Seen By Laser Raman Spectroscopy," *IRCS (International Research Communications System) Medical Science Library Compendium*, vol. 4, no. 1, p. 10, 1976.

[156] S. Webb, M. Stoneham, and J. Montgomery, "Identification of Bacterial, Normal and Tumour Mammalian Cells as Seen By Laser Raman Spectroscopy," *IRCS (International Research Communications System) Medical Science Library Compendium*, vol. 4, no. 1, pp. 8–9, 1976.

[157] S. J. Webb, R. Lee, and M. E. Stoneham, "Possible viral involvement in human mammary carcinoma: A microwave and laser-Raman study," *International Journal of Quantum Chemistry*, vol. 12, no. S4, pp. 277–284, 1977.

[158] P. Jeannesson, M. Manfait, and J.-C. Jardillier, "A technique for laser raman spectroscopic studies of isolated cell populations," *Analytical Biochemistry*, vol. 129, no. 2, pp. 305–309, 1983.

[159] I. Notingher, S. Verrier, S. Haque, J. M. Polak, and L. L. Hench, "Spectroscopic Study of Human Lung Epithelial Cells (A549) in Culture : Living Cells Versus Dead Cells," *Biopolymers*, vol. 72, no. 4, pp. 230–240, 2003.

[160] Y. S. Huang, T. Karashima, M. Yamamoto, and H. O. Hamaguchi, "Molecular-level investigation of the structure, transformation, and bioactivity of single living fission yeast cells by time- and space-resolved Raman spectroscopy," *Biochemistry*, vol. 44, no. 30, pp. 10 009–10 019, 2005.

[161] R. J. Swain, G. Jell, and M. M. Stevens, "Non-invasive analysis of cell cycle dynamics in single living cells with Raman micro-spectroscopy," *Journal of Cellular Biochemistry*, vol. 104, no. 4, pp. 1427–1438, 2008.

[162] T. Ichimura, L.-D. Chiu, K. Fujita, H. Machiyama, S. Kawata, T. M. Watanabe, and H. Fujita, "Visualizing the appearance and disappearance of the attractor of differentiation using Raman spectral imaging," *Scientific Reports*, vol. 5, p. 11358, 2015.

[163] L. Ashton, K. A. Hollywood, and R. Goodacre, "Making colourful sense of Raman images of single cells," *The Analyst*, pp. 1852–1858, 2015.

[164] S.-I. Morita, S. Takanezawa, M. Hiroshima, T. Mitsui, Y. Ozaki, and Y. Sako, "Raman and Autofluorescence Spectrum Dynamics along the HRG-Induced Differentiation Pathway of MCF-7 Cells," *Biophysical Journal*, vol. 107, no. 10, pp. 2221–2229, 2014.

[165] I. Notingher, G. Jell, P. L. Notingher, I. Bisson, O. Tsigkou, J. M. Polak, M. M. Stevens, and L. L. Hench, "Multivariate analysis of Raman spectra for in vitro non-invasive studies of living cells," *Journal of Molecular Structure*, vol. 744-747, no. Special Issue, pp. 179–185, 2005.

[166] M. E. Keating, H. Nawaz, F. Bonnier, and H. J. Byrne, "Multivariate statistical methodologies applied in biomedical Raman spectroscopy: assessing the validity of partial least squares regression using simulated model datasets," *Analyst*, vol. 140, no. 7, pp. 2482–2492, 2015. [Online]. Available: http://www.ncbi.nlm.nih.gov/pubmed/25558476{%}5Cnhttp://www.ncbi.nlm.nih.gov/entrez/query.fcgi?cmd=Retrieve{&}db=PubMed{&}dopt=Citation{&}list{_}uids=25558476

[167] A. Bonetti, A. Bonifacio, A. Della Mora, U. Livi, M. Marchini, and F. Ortolani, "Carotenoids co-localize with hydroxyapatite, cholesterol, and other lipids in calcified stenotic aortic valves. Ex vivo Raman maps compared to histological patterns," *European Journal of Histochemistry*, vol. 59, no. 2, 2015.

[168] R. Schmidt-Ullrich, S. Verma, and D. Wallach, "Anomalous side chain amidation in plasma membrane proteins of simian virus 40-transformed lymphocytes indicated by isoelectric focussing and laser raman spectroscopy," *Biochemical and biophysical research communications*, vol. 67, no. 3, pp. 1062–1069, 1975.

[169] S. P. Verma, R. Schmidtullrich, W. S. Thompson, and D. F. H. Wallach, "Differences between Structural Dynamics of Plasma-Membranes of Normal Hamster Lymphocytes and Lymphoid-Cells Neoplastically Transformed by Simian Virus-40 as Revealed by Laser Raman-Spectroscopy," *Cancer Research*, vol. 37, no. October, pp. 3490–3493, 1977.

[170] C. J. Frank, D. C. Redd, T. S. Gansler, and R. L. McCreery, "Characterization of human breast biopsy specimens with near-IR Raman spectroscopy." *Analytical chemistry*, vol. 66, no. 3, pp. 319–326, 1994.

[171] C. J. Frank, R. L. McCreery, and D. C. Redd, "Raman spectroscopy of normal and diseased human breast tissues." *Analytical chemistry*, vol. 67, no. 5, pp. 777–783, 1995.

[172] K. E. Shafer-Peltier, A. S. Haka, M. Fitzmaurice, J. Crowe, J. Myles, R. R. Dasari, and M. S. Feld, "Raman microspectroscopic model of human breast tissue: Implications for breast cancer diagnosis in vivo," *Journal of Raman Spectroscopy*, vol. 33, no. 7, pp. 552–563, 2002.

[173] S. Sigurdsson, P. A. Philipsen, L. K. Hansen, J. Larsen, M. Gniadecka, and H. Christian Wulf, "Detection of skin cancer by classification of Raman spectra," *IEEE Transactions on Biomedical Engineering*, vol. 51, no. 10, pp. 1784–1793, 2004.

[174] M. Gniadecka, P. A. Philipsen, S. Sigurdsson, S. Wessel, O. F. Nielsen, D. H. Christensen, J. Hercogova, K. Rossen, H. K. Thomsen, R. Gniadecki, L. K. Hansen, and H. C. Wulf, "Melanoma Diagnosis by Raman Spectroscopy and Neural Networks: Structure Alterations in Proteins and Lipids in Intact Cancer Tissue," *Journal of Investigative Dermatology*, vol. 122, no. 2, pp. 443–449, 2004.

[175] L. F. C. Carvalho, F. Bonnier, K. O'Callaghan, J. O'Sullivan, S. Flint, H. J. Byrne, and F. M. Lyng, "Raman micro-spectroscopy for rapid screening of oral squamous cell carcinoma," *Experimental and Molecular Pathology*, vol. 98, no. 3, pp. 502–509, 2015.

[176] N. Rashid, H. Nawaz, K. W. C. Poon, F. Bonnier, S. Bakhiet, C. Martin, J. J. O. Leary, H. J. Byrne, and F. M. Lyng, "Raman microspectroscopy for the early detection of pre-malignant changes in cervical tissue," *Experimental and Molecular Pathology*, vol. 97, no. 3, pp. 554–564, 2014.

[177] Y. Leung, M. A. Walters, N. C. Blumenthal, J. L. Ricci, and J. M. Spivak, "Determination of the mineral phases and structure of the bone-implant interface using Raman spectroscopy." *Journal of biomedical materials research*, vol. 29, no. 5, pp. 591–594, 1995.

[178] K. Ohsaki, S. Yamashita, S. Ueda, T. Sugiura, K. Tamura, and A. Shibata, "Mechanism of Bone Destruction Due to Middle Ear Cholesteatoma as Revealed by Laser-Raman Spectrometry," *American Journal of Otolaryngology*, vol. 9, pp. 117–126, 1988.

[179] M. Kozielski, T. Buchwald, M. Szybowicz, Z. Błaszczak, a. Piotrowski, and B. Ciesielczyk, "Determination of composition and structure of spongy bone tissue in human head of femur by Raman spectral mapping," *Journal of Materials Science: Materials in Medicine*, vol. 22, no. 7, pp. 1653–1661, 2011.

[180] A. Carden, R. M. Rajachar, M. D. Morris, and D. H. Kohn, "Ultrastructural changes accompanying the mechanical deformation of bone tissue: A Raman imaging study," *Calcified Tissue International*, vol. 72, no. 2, pp. 166–175, 2003.

[181] M. D. Morris and G. S. Mandair, "Raman assessment of bone quality," *Clinical Orthopaedics and Related Research*, vol. 469, no. 8, pp. 2160–2169, 2011.

[182] A. L. Boskey and R. Mendelsohn, "Infrared spectroscopic characterization of mineralized tissues," *Vibrational Spectroscopy*, vol. 38, no. 1-2, pp. 107–114, 2005.

[183] M. D. Morris, "Raman Spectroscopy of Bone and Cartilage," in *Emerging Raman Applications and Techniques in Biomedical and Pharmaceutical Fields*, 1st ed., P. Matousek and M. Morris, Eds. Springer-Verlag Berlin Heidelberg, 2010, pp. 347–364.

[184] D. Bazin, C. Chappard, C. Combes, X. Carpentier, S. Rouzière, G. André, G. Matzen, M. Allix, D. Thiaudière, S. Reguer, P. Jungers, and M. Daudon, "Diffraction techniques and vibrational spectroscopy opportunities to characterise bones," *Osteoporosis International*, vol. 20, no. 6, pp. 1065–1075, 2009.

[185] C. Silve, E. Lopez, B. Vidal, D. C. Smith, S. Camprasse, G. Camprasse, and G. Couly, "Nacre initiates biomineralization by human osteoblasts maintained in vitro," *Calcified Tissue International*, vol. 51, no. 5, pp. 363–369, 1992.

[186] L. L. McManus, F. Bonnier, G. A. Burke, B. J. Meenan, A. R. Boyd, and H. J. Byrne, "Assessment of an osteoblast-like cell line as a model for human primary osteoblasts using Raman spectroscopy," *The Analyst*, vol. 137, no. 7, p. 1559, 2012.

[187] I. Notingher, G. Jell, U. Lohbauer, V. Salih, and L. L. Hench, "In situ non-invasive spectral discrimination between bone cell phenotypes used in tissue engineering," *Journal of Cellular Biochemistry*, vol. 92, no. 6, pp. 1180–1192, 2004.

[188] P. S. Hung, Y. C. Kuo, H. G. Chen, H. H. K. Chiang, and O. K. S. Lee, "Detection of Osteogenic Differentiation by Differential Mineralized Matrix Production in Mesenchymal Stromal Cells by Raman Spectroscopy," *PLoS ONE*, vol. 8, no. 5, pp. 1–7, 2013.

[189] H. J. Byrne, M. Baranska, G. J. Puppels, N. Stone, B. Wood, K. M. Gough, P. Lasch, P. Heraud, J. Sulé-Suso, and G. D. Sockalingum, "Spectropathology for the next generation : Quo Vadis?" *Analyst*, vol. 140, no. 7, pp. 2066–2073, 2015.

[190] T. C. Bakker Schut, M. J. H. Witjes, H. J. C. M. Sterenborg, O. C. Speelman, J. L. N. Roodenburg, E. T. Marple, H. A. Bruining, and G. J. Puppels, "In vivo detection of dysplastic tissue by Raman spectroscopy," *Analytical Chemistry*, vol. 72, no. 24, pp. 6010–6018, 2000.

[191] G. Penel, C. Delfosse, M. Descamps, and G. Leroy, "Composition of bone and apatitic biomaterials as revealed by intravital Raman microspectroscopy," *Bone*, vol. 36, no. 5, pp. 893–901, 2005.

[192] E. Azrad, D. Zahor, R. Vago, Z. Nevo, R. Doron, D. Robinson, L. A. Gheber, S. Rosenwaks, and I. Bar, "Probing the effect of an extract of elk velvet antler powder on mesenchymal stem cells using Raman microspectroscopy: Enhanced differentiation toward osteogenic fate," *Journal of Raman Spectroscopy*, vol. 37, no. 4, pp. 480–486, 2006.

[193] G. Jell, I. Notingher, O. Tsigkou, P. Notingher, J. M. Polak, L. L. Hench, and M. M. Stevens, "Bioactive glass-induced osteoblast differentiation: A noninvasive spectroscopic study," *Journal of Biomedical Materials Research - Part A*, vol. 86, no. 1, pp. 31–40, 2008.

[194] R. Carretta, E. Stüssi, R. Müller, and S. Lorenzetti, "Prediction of Local Ultimate Strain and Toughness of Trabecular Bone Tissue by Raman Material Composition Analysis," *BioMed Research International*, vol. 2015, p. 457371, 2015.

[195] X. Ojanen, H. Isaksson, J. Töyräs, M. Turunen, M. Malo, a. Halvari, and J. Jurvelin, "Relationships between tissue composition and viscoelastic properties in human trabecular bone," *Journal of Biomechanics*, vol. 48, no. 2, pp. 269–275, 2015.

[196] N. J. Crane, V. Popescu, M. D. Morris, P. Steenhuis, and M. a. Ignelzi, "Raman spectroscopic evidence for octacalcium phosphate and other transient mineral species deposited during intramembranous mineralization," *Bone*, vol. 39, no. 3, pp. 434–442, 2006.

[197] N. Uzunbajakava, a. Lenferink, Y. Kraan, B. Willekens, G. Vrensen, J. Greve, and C. Otto, "Nonresonant Raman imaging of protein distribution in single human cells," *Biopolymers - Biospectroscopy Section*, vol. 72, no. 1, pp. 1–9, 2003.

[198] M. Mazilu, A. D. Luca, A. Riches, C. S. Herrington, and K. Dholakia, "Optimal algorithm for fluorescence suppression of modulated Raman spectroscopy," *Optics Express*, vol. 18, no. 11, pp. 11 382–11 395, 2010.

[199] C. M. Krishna, G. D. Sockalingum, G. Kegelaer, S. Rubin, V. B. Kartha, and M. Manfait, "Micro-Raman spectroscopy of mixed cancer cell populations," *Vibrational Spectroscopy*, vol. 38, no. 1-2, pp. 95–100, 2005.

[200] A. Khmaladze, S. Kuo, R. Y. Kim, R. V. Matthews, C. L. Marcelo, S. E. Feinberg, and M. D. Morris, "Human Oral Mucosa Tissue-Engineered Constructs Monitored by Raman Fiber-Optic Probe," *Tissue Engineering Part C: Methods*, vol. 21, no. 1, pp. 46–51, 2015.

[201] A. Khmaladze, A. Ganguly, S. Kuo, M. Raghavan, R. Kainkaryam, J. H. Cole, K. Izumi, C. Marcelo, S. Feinberg, and M. D. Morris, "Tissue Engineered Constructs of Human Oral Mucosa Examined by Raman Spectroscopy," *Tissue Engineering Part C: Methods*, vol. 19, no. 4, pp. 299–306, 2013.

[202] K. Kerney, N. Roki, M. Fenn, and C. Bashur, "Using Surface Enhanced Raman Spectroscopy to Assess the Calcification Potential of Engineered Vascular Grafts," *Tissue Engineering Part A*, vol. 20, no. S1, pp. S130–S131, 2014.

[203] W. L. Lo, J. Y. Lai, S. E. Feinberg, K. Izumi, S. Y. Kao, C. S. Chang, A. Lin, and H. K. Chiang, "Raman spectroscopy monitoring of the cellular activities of a tissue-engineered ex vivo produced oral mucosal equivalent," *Journal of Raman Spectroscopy*, vol. 42, no. 2, pp. 174–178, 2011.

[204] M. Leroy, J.-F. Labbé, M. Ouellet, J. Jean, T. Lefèvre, G. Laroche, M. Auger, and R. Pouliot, "A comparative study between human skin substitutes and normal human skin using Raman microspectroscopy." *Acta biomaterialia*, vol. 10, no. 6, pp. 2703–11, 2014.

[205] K. Hashimoto, S. N. Kudoh, and H. Sato, "Analysis of the developing neural system using an in vitro model by Raman spectroscopy," *The Analyst*, vol. 140, no. 7, pp. 2344–2349, 2015.

[206] M. Steinke, R. Gross, H. Walles, R. Gangnus, K. Schütze, and T. Walles, "Biomaterials An engineered 3D human airway mucosa model based on an SIS scaffold," *Biomaterials*, vol. 35, no. 26, pp. 7355–7362, 2014.

[207] M. Pudlas, D. A. C. Berrio, M. Votteler, S. Koch, S. Thude, H. Walles, and K. Schenke-Layland, "Non-contact discrimination of human bone marrow-derived mesenchymal stem cells and fibroblasts using Raman spectroscopy," *Medical Laser Application*, vol. 26, no. 3, pp. 119–125, 2011.

[208] I. Notingher, I. Bisson, J. M. Polak, and L. L. Hench, "In situ spectroscopic study of nucleic acids in differentiating embryonic stem cells," *Vibrational Spectroscopy*, vol. 35, no. 1-2, pp. 199–203, 2004.

[209] I. Notingher, I. Bisson, A. E. Bishop, W. L. Randle, J. M. P. Polak, and L. L. Hench, "In situ spectral monitoring of mRNA translation in embryonic stem cells during differentiation in vitro," *Analytical Chemistry*, vol. 76, no. 11, pp. 3185–3193, 2004.

[210] H. G. Schulze, S. S. O. Konorov, N. J. N. Caron, J. M. Piret, M. W. Blades, and R. F. B. Turner, "Assessing differentiation status of human embryonic stem cells noninvasively using Raman microspectroscopy." *Analytical chemistry*, vol. 82, no. 12, pp. 5020–7, 2010.

[211] C. H. Glover, M. Marin, C. J. Eaves, C. D. Helgason, J. M. Piret, and J. Bryan, "Meta-analysis of differentiating mouse embryonic stem cell gene expression kinetics reveals early change of a small gene set," *PLoS Computational Biology*, vol. 2, no. 11, p. e158, 2006.

[212] J. W. Chan, D. K. Lieu, T. Huser, and R. A. Li, "Label-free separation of human embryonic stem cells and their cardiac derivatives using Raman spectroscopy," *Analytical Chemistry*, vol. 81, no. 4, pp. 1324–1331, 2009.

[213] I. Notingher, J. Selvakumaran, and L. L. Hench, "New detection system for toxic agents based on continuous spectroscopic monitoring of living cells," *Biosensors and Bioelectronics*, vol. 20, no. 4, pp. 780–789, 2004.

[214] I. Notingher, C. Green, C. Dyer, E. Perkins, N. Hopkins, C. Lindsay, and L. L. Hench, "Discrimination between ricin and sulphur mustard toxicity in vitro using Raman spectroscopy." *Journal of the Royal Society, Interface*, vol. 1, no. 1, pp. 79–90, 2004.

[215] A. M. Alkilany and C. J. Murphy, "Toxicity and cellular uptake of gold nanoparticles: What we have learned so far?" *Journal of Nanoparticle Research*, vol. 12, no. 7, pp. 2313–2333, 2010.

[216] L. T. Kerr, H. J. Byrne, and B. M. Hennelly, "Optimal choice of sample substrate and laser wavelength for Raman spectroscopic analysis of biological specimen," *Analytical Methods*, vol. 7, no. 12, pp. 5041–5052, 2015.

[217] Y. Ilin and M. L. Kraft, "Secondary ion mass spectrometry and Raman spectroscopy for tissue engineering applications," *Current Opinion in Biotechnology*, vol. 31, pp. 108–116, 2015.

[218] J. Chaudhuri and M. Al-Rubeai, *Bioreactors for Tissue Engineering: Principles, Design and Operation*. Dordrect, Netherlands: Springer, 2005.

[219] K. J. M. Boonen, M. L. P. Langelaan, R. B. Polak, D. W. J. van der Schaft, F. P. T. Baaijens, and M. J. Post, "Effects of a combined mechanical stimulation protocol: Value for skeletal muscle tissue engineering," *Journal of Biomechanics*, vol. 43, no. 8, pp. 1514–1521, 2010.

[220] E. Schmelzer, A. Finoli, I. Nettleship, and J. Gerlach, "Long-term three-dimensional perfusion culture of human adult bone marrow mononuclear cells in bioreactors," *Biotechnology and Bioengineering*, vol. 112, no. 4, pp. 801–810, 2015.

[221] C.-F. Mandenius, *Bioreactors: Design, Operation and Novel Applications*. Wiley-VCH, 2016.

[222] Y. J. Xu, J. F. Ford, C. K. Mann, T. J. Vickers, J. M. Brackett, K. L. Cousineau, and W. G. Robey, "Raman measurement of glucose in bioreactor materials," *Biomedical Sensing, Imaging, And Tracking Technologies II*, vol. 2976, pp. 10–19, 1997.

[223] C. Cannizzaro, M. Rhiel, I. Marison, and U. von Stockar, "On-line monitoring of Phaffia rhodozyma fed-batch process with in situ dispersive raman spectroscopy," *Biotechnology and Bioengineering*, vol. 83, no. 6, pp. 668–680, 2003.

[224] S. Varma, "Simultaneous determination of multiple components in CHO cell culture using Raman spectroscopy," in *The 234th ACS National Meeting, Boston, MA, August 19-23, 2007*, 2007, p. BIOT 256.

[225] V. V. Pully, A. Lenferink, H.-J. van Manen, V. Subramaniam, C. A. van Blitterswijk, and C. Otto, "Microbioreactors for Raman microscopy of stromal cell differentiation." *Analytical chemistry*, vol. 82, no. 5, pp. 1844–1850, 2010.

[226] N. R. Abu-Absi, B. M. Kenty, M. E. Cuellar, M. C. Borys, S. Sakhamuri, D. J. Strachan, M. C. Hausladen, and Z. J. Li, "Real time monitoring of multiple parameters in mammalian cell culture bioreactors using an in-line Raman spectroscopy probe," *Biotechnology and Bioengineering*, vol. 108, no. 5, pp. 1215–1221, 2011.

[227] J. Whelan, S. Craven, and B. Glennon, "In situ Raman spectroscopy for simultaneous monitoring of multiple process parameters in mammalian cell culture bioreactors," *Biotechnology Progress*, vol. 28, no. 5, pp. 1355–1362, 2012.

[228] B. Berry, J. Moretto, T. Matthews, J. Smelko, and K. Wiltberger, "Cross-scale predictive modeling of CHO cell culture growth and metabolites using Raman spectroscopy and multivariate analysis," *Biotechnology Progress*, vol. 31, no. 2, pp. 566–576, 2015.

[229] F. C. Pascut, S. Kalra, V. George, N. Welch, C. Denning, and I. Notingher, "Non-invasive label-free monitoring the cardiac differentiation of human embryonic stem cells in-vitro by Raman spectroscopy." *Biochimica et biophysica acta*, vol. 1830, no. 6, pp. 3517–24, 2013.

[230] L. Knudsen, C. K. Johansson, P. A. Philipsen, M. Gniadecka, and H. C. Wulf, "Natural variations and reproducibility of in vivo near-infrared Fourier transform Raman spectroscopy of normal human skin," *Journal of Raman Spectroscopy*, vol. 33, no. 7, pp. 574–579, 2002.

[231] I. J. Pence, E. Vargis, and A. Mahadevan-Jansen, "Assessing variability of in vivo tissue Raman spectra," *Applied Spectroscopy*, vol. 67, no. 7, pp. 789–800, 2013.

[232] V. J. Cogliano, E. G. Luebeck, and G. A. Zapponi, *NATO Challenges of Modern Society Volume 23: Perspectives on Biologically Based Cancer Risk Assessment.* New York, USA: Springer Science & Business Media, 1997.

[233] H. L. Borges, R. Linden, and J. Y. Wang, "Dna damage-induced cell death: lessons from the central nervous system," *Cell Research*, vol. 18, no. 1, pp. 17–26, 2008.

[234] M. W. Hayman, K. H. Smith, N. R. Cameron, and S. A. Przyborski, "Enhanced neurite outgrowth by human neurons grown on solid three-dimensional scaffolds," *Biochemical and Biophysical Research Communications*, vol. 314, no. 2, pp. 483–488, 2004.

[235] M. E. S. Romero, "Electrospun Poly(Caprolactone) and Strontium-Substituted Bioactive Glass for Bone Tissue Engineering," Ph.D. dissertation, University of Sheffield, 2014.

[236] C. Maniatopoulos, J. Sodek, and A. H. Melcher, "Bone formation in vitro by stromal cells obtained from bone marrow of young adult rats." *Cell and tissue research*, vol. 254, no. 2, pp. 317–30, 1988.

[237] M. Soleimani and S. Nadri, "A protocol for isolation and culture of mesenchymal stem cells from mouse bone marrow." *Nature protocols*, vol. 4, no. 1, pp. 102–106, 2009.

[238] R. J. Deans and A. B. Moseley, "Mesenchymal stem cells: biology and potential clinical uses." *Experimental hematology*, vol. 28, no. 8, pp. 875–884, 2000.

[239] M. Dominici, K. Le Blanc, I. Mueller, I. Slaper-Cortenbach, F. Marini, D. Krause, R. Deans, A. Keating, D. Prockop, and E. Horwitz, "Minimal criteria for defining multipotent mesenchymal stromal cells. The International Society for Cellular Therapy position statement." *Cytotherapy*, vol. 8, no. 4, pp. 315–317, 2006.

[240] H. Puchtler, S. N. Meloan, and M. S. Terry, "On the history and mechanism of Alizarin and Alizarin Red S stains for calcium," *Journal of Histochemistry & Cytochemistry*, vol. 17, no. 2, pp. 110–124, 1969.

[241] J. N. Beresford, S. E. Graves, and C. A. Smoothy, "Formation of mineralized nodules by bone derived cells in vitro: A model of bone formation?" *American Journal of Medical Genetics*, vol. 45, no. 2, pp. 163–178, 1993.

[242] M. Balcerzak, E. Hamade, L. Zhang, S. Pikula, G. Azzar, J. Radisson, J. Bandorowicz-Pikula, and R. Buchet, "The roles of annexins and alkaline phosphatase in mineralization process," *Acta Biochimica Polonica*, vol. 50, no. 4, pp. 1019–1038, 2003.

[243] C. G. Bellows, J. E. Aubin, and J. N. M. Heersche, "Initiation and progression of mineralization of bone nodules formed in vitro: The role of alkaline phosphatase and organic phosphate," *Bone and Mineral*, vol. 14, no. 1, pp. 27–40, 1991.

[244] M. Peckham, A. Knibbs, and S. Paxton, "University of Leeds, The Histological Guide, What is Histology? What is H&E? [Date Accessed:31.08.2015]," 2003. [Online]. Available: http://www.histology.leeds.ac.uk/what-is-histology/H_and_E.php

[245] W. S. Rasband, *ImageJ*. Bethesda, Maryland, USA,: U. S. National Institutes of Health, 2004. [Online]. Available: http://imagej.nih.gov/ij/

[246] S. R. Peters, *A Practical Guide to Frozen Section Technique*. New York, USA: Springer, 2010.

[247] G. Sridharan and A. Shankar, "Toluidine blue: A review of its chemistry and clinical utility," *Journal of Oral and Maxillofacial Pathology*, vol. 16, no. 2, pp. 251–255, 2012.

[248] P. Nandakumar, A. Kovalev, and A. Volkmer, "Vibrational imaging based on stimulated Raman scattering microscopy," *New Journal of Physics*, vol. 11, p. 033026, 2009.

[249] C. Evans and X. Xie, "Coherent Anti-Stokes Raman Scattering Microscopy: Chemical Imaging for Biology and Chemistry," *Annual Review of Analytical Chemistry*, vol. 1, pp. 883–909, 2008.

[250] D. Fu, G. Holtom, C. Freudiger, X. Zhang, and X. Xie, "Hyperspectral Imaging with Stimulated Raman Scattering by Chirped Femtosecond Lasers," *The Journal of Physical Chemistry B*, vol. 117, pp. 4634–4640, 2013.

[251] Stanford Research Systems, "About Lock-In Amplifiers," *Application Note*, pp. 1–9, 2011. [Online]. Available: http://www.thinksrs.com/downloads/PDFs/ApplicationNotes/AboutLIAs.pdf

[252] P. Harms, J. Sipior, N. Ram, G. Carter, and G. Rao, "Low cost phase-modulation measurements of nanosecond fluorescence lifetimes using a lock-in amplifier," *Review of Scientific Instruments*, vol. 70, no. 2, pp. 1535–1539, 1999.

[253] J. Snoddy, Y. Li, F. Ravet, and X. Bao, "Stabilization of electro-optic modulator bias voltage drift using a lock-in amplifier and a proportional-integral-derivative controller in a distributed Brillouin sensor system," *Applied Optics*, vol. 46, no. 9, pp. 1482–1485, 2007.

[254] D. Meshulach and Y. Silberberg, "Coherent quantum control of multiphoton transitions by shaped ultrashort optical pulses," *Physical Review A*, vol. 60, no. 2, p. 1287, 1999.

[255] J. Scofield, "Frequency-Domain Description of a Lock-In Amplifier," *American Journal of Physics*, vol. 62, no. 2, pp. 129–133, 1994.

[256] P. Kromer, R. Robinett, R. Bengtson, and C. Hays, "PC-based digital lock-in detection of small signals in the presence of noise [Date Accessed: 12.09.2016]," 1999. [Online]. Available: http://www.science.unitn.it/{~}bassi/Signal/AAPTPaper.pdf

[257] G. M. Shamieh, *Electronics for Dummies*, 2nd ed. Indianapolis, USA: John Wiley & Sons Ltd, 2009.

[258] M. L. Meade, *Lock-in Amplifiers: Prinicples and Applications (IEE electrical measurement series)*. London, UK: Peter Peregrinus, 1983.

[259] M. L. Meade, "Advances in lock-in amplifiers," *Journal of Physics E: Scientific Instruments*, vol. 15, no. 4, pp. 395–403, 1982.

[260] R. Alfano and N. Ockman, "Methods for Detecting Weak Light Signals," *Journal of the Optical Society of America*, vol. 58, no. 1, p. 90, 1968.

[261] J. Cooper, K. Wise, and B. Jensen, "Modulated FT-Raman Fiber-Optic Spectroscopy: A Technique for Remotely Monitoring High-Temperature Reactions in Real-time," *Analytical Chemistry*, vol. 69, pp. 1973–1978, 1997.

[262] M. T. Gebrekidan, C. Knipfer, F. Stelzle, J. Popp, S. Will, and A. Braeuer, "A shifted-excitation Raman difference spectroscopy (SERDS) evaluation strategy for the efficient isolation of Raman spectra from extreme fluorescence interference," *Journal of Raman Spectroscopy*, vol. 47, no. 2, pp. 198–209, 2016.

[263] P. C. Ashok, A. C. De Luca, M. Mazilu, and K. Dholakia, "Enhanced bioanalyte detection in waveguide confined Raman spectroscopy using wavelength modulation," *Journal of Biophotonics*, vol. 4, no. 7-8, pp. 514–518, 2011.

[264] B. B. Praveen, M. Mazilu, R. F. Marchington, C. S. Herrington, A. Riches, and K. Dholakia, "Optimisation of Wavelength Modulated Raman Spectroscopy: Towards High Throughput Cell Screening," *PLoS ONE*, vol. 8, no. 6, p. e67211, 2013.

[265] E. Canetta, A. Riches, E. Borger, C. S. Herrington, K. Dholakia, and A. K. Adya, "Discrimination of bladder cancer cells from normal urothelial cells with high specificity and sensitivity: combined application of atomic force microscopy and modulated Raman spectroscopy." *Acta biomaterialia*, vol. 10, no. 5, pp. 2043–55, 2014.

[266] D. Craig, M. Mazilu, and K. Dholakia, "Quantitative Detection of Pharmaceuticals Using a Combination of Paper Microfluidics and Wavelength Modulated Raman Spectroscopy," *Plos One*, vol. 10, no. 5, p. e0123334, 2015.

[267] Thorlabs. (2017) Nir free-space isolators (690-1080 *nm*): Optical isolator tutorial. [Online]. Available: www.thorlabs.com/newgrouppage9.cfm?objectgroup_id=4914

[268] E. Hecht, *Optics*, 2nd ed. Addison-Wesley, 1987.

[269] I. S. Grant and W. R. Phillips, *Electromagnetism*, 2nd ed. Chichester, West Sussex: John Wiley & Sons, 1990.

[270] M. Hass, "Raman spectra of vitreous silica, germania and sodium silicate glasses," *Journal of Physics and Chemistry of Solids*, vol. 31, no. 3, pp. 415–422, 1970.

[271] J. B. Bates, R. W. Hendricks, and L. B. Shaffer, "Neutron irradiation effects and structure of noncrystalline SiO2," *The Journal of Chemical Physics*, vol. 61, no. 10, pp. 4163–4176, 1974.

[272] C. Palmer and E. Lowen, *Diffraction Grating Handbook*, 2005.

[273] J. Hunter, "Matplotlib: A 2D graphics environment," *Computing In Science and Engineering*, vol. 9, no. 3, pp. 90–95, 2007.

[274] J. Púčik, O. Ondráček, and E. Cocherová, "Observability of Spectral Components beyond Nyquist Limit in Nonuniformly Sampled Signals," *ISRN Signal Processing*, vol. 2012, p. 643563, 2012.

[275] W. Billotte, "Ceramic Biomaterials," in *The Handbook of Biomedical Engineering Handbook 1*, 2nd ed., J. Bronzino, Ed. Boca Raton, USA: CRC Press, 2000, ch. 38, pp. 38–1.

[276] M. A. Short, S. Lam, A. M. McWilliams, D. N. Ionescu, and H. Zeng, "Using laser raman spectroscopy to reduce false positives of autofluorescence bronchoscopies: A pilot study," *Journal of Thoracic Oncology*, vol. 6, no. 7, pp. 1206 – 1214, 2011. [Online]. Available: http://www.sciencedirect.com/science/article/pii/S1556086415310364

[277] M. A. Short, I. T. Tai, D. Owen, and H. Zeng, "Using high frequency raman spectra for colonic neoplasia detection," *Opt. Express*, vol. 21, no. 4, pp. 5025–5034, Feb 2013. [Online]. Available: http://www.opticsexpress.org/abstract.cfm?URI=oe-21-4-5025

[278] Z.-G. Ye, *Handbook of Advanced Dielectric, Piezoelectric and Ferroelectric Materials: Synthesis, Properties and Applications*. Cambridge, UK: Woodhead Publishing Limited, 2008.

[279] J. Kim and T. Ma, "Bioreactor Strategy in Bone Tissue Engineering : Under Two Flow Configurations," *Tissue Engineering Part A*, vol. 18, no. 21-22, pp. 2354–2364, 2012.

[280] A. A. Bharath, "Introductory Medical Imaging," *Synthesis Lectures on Biomedical Engineering*, vol. 3, no. 1, pp. 1–186, 2008.

[281] J. H. Hubbell and S. M. Seltzer, "NISTIR 5632: Tables of X-Ray Mass Attenuation Coefficients and Mass Energy-Absorption Coefficients from 1 keV to 20 MeV for Elements Z = 1 to 92 and 48 Additional Substances of Dosimetric Interest (Version 1.4) [Date Accessed: 2016-07-09]," 2004. [Online]. Available: http://physics.nist.gov/xaamdi

[282] R. Jonson, "Original Article Mass Attenuation Coefficients , Quantities and Units for Use in Bone Mineral Determinations," *Osteoporosis International*, vol. 3, no. 2, pp. 103–106, 1993.

[283] M. R. O'Rourke, A. Aggarwal, and B. Evans, "Late Complications and Managment," in *The Adult Hip*, 2nd ed., J. J. Callaghan, A. G. Rosenberg, and H. E. Rubash, Eds. Philadelphia, PA, USA: Lippincott Williams & Wilkins, 2007, ch. 77, pp. 1109–1123.

[284] T. L. Riss, R. A. Moravec, A. L. Niles, S. Duellman, H. A. Benink, T. J. Worzella, and L. Minor, "Cell Viability Assays," in *Assay Guidance Manual*, G. S. Sittampalam, N. P. Coussens, K. Brimacombe, A. Grossman, M. Arkin, D. Auld, C. Austin, B. Bejcek, M. Glicksman, J. Inglese, P. W. Iversen, Z. Li, J. McGee, O. McManus, L. Minor, A. Napper, J. M. Peltier, T. Riss, O. J. Trask Jr., and J. Weidner, Eds. Bethesda, Maryland, USA,: Eli Lilly

& Company and the National Center for Advancing Translational Sciences, 2013. [Online]. Available: https://www.ncbi.nlm.nih.gov/books/NBK53196/

[285] M. Hollins, *Medical Physics*, 2nd ed. Cheltenham, UK: Nelson Thornes, 2001.

[286] J. Beutel, H. Kundel, and R. Van Metter, *Handbook of Medial Imaging: Volume 1. Physics and Psychophysics.* Washington, USA: SPIE Press, 2000.

[287] S. Logunov and S. Kuchinsky, "Experimental and theoretical study of bulk light scattering in caf2 monocrystals," *Journal of Applied Physics*, vol. 98, no. 5, p. 053501, 2005.

[288] N. Shibata, M. Horigudhi, and T. Edahiro, "Raman spectra of binary high-silica glasses and fibres containing GeO2, P2O5 and B2O3," *Journal of Non-Crystalline Solids*, vol. 45, no. 1, pp. 115–126, 1981.

[289] S. K. Sharma, J. F. Mammone, and M. F. Nicol, "Raman investigation of Ring Configurations in Vitreous Silica," *Nature*, vol. 292, no. 5819, pp. 140–141, 1981.

[290] I. R. Lewis and H. G. Edwards, *Handbook of Raman Spectroscopy: From the Research Laboratory to the Process Line.* New York, USA: Marcel Dekker Inc., 2001.

[291] F. Lyng, E. Gazi, and P. Gardner, "Preparation of Tissues and Cells for Infrared and Raman Spectroscopy and Imaging," in *Biomedical Applications of Synchrotron Infrared Microspectroscopy: A Practical Approach*, D. Moss, Ed. RSC Publishing, 2011, ch. 5, pp. 145–191.

[292] M. Jastrzebska, R. Wrzalik, A. Kocot, J. Zalewska-Rejdak, and B. Cwalina, "Raman spectroscopic study of glutaraldehydestabilized collagen and pericardium tissue," *Journal of Biomaterials Science, Polymer Edition*, vol. 14, no. 2, pp. 185–197, 2003.

[293] M. Manfait, T. Theophanides, A. Alix, and P. Jeannesson, "Raman and FT-IR Spectroscopy of Drug-Biological Target Interactions In Vitro and In Vicvo," in *Spectroscopy of Biological Molecules: Theory and Applications — Chemistry, Physics, Biology and Medicine*, C. Sandorfy and T. Theophanides, Eds. Dordrect, Holland: D Reidel Publishing Company, 1984, pp. 113–137.

[294] M. Louviot, V. Boudon, D. Bermejo, R. Z. Martínez, and L. Manceron, "High-resolution stimulated Raman spectroscopy and analysis of the v1 band of osmium tetroxide," *Journal of Raman Spectroscopy*, vol. 44, no. 1, pp. 63–69, 2013.

[295] L. A. Nafie, "Infrared And Raman Vibrational Optical Activity : Theoretical and Experimental Aspects," *Annual Review of Physical Chemistry*, vol. 48:, pp. 357–86, 1997.

[296] L. D. Barron, "The development of biomolecular Raman optical activity spectroscopy," *Biomedical Spectroscopy and Imaging*, vol. 4, pp. 223–253, 2015.

[297] V. Parchansky, J. Kapitan, and P. Bour, "Inspecting chiral molecules by Raman optical activity spectroscopy," *RSC Advances*, vol. 4, pp. 57 125–57 136, 2014.

[298] J. D. Horvath and A. J. Gellman, "Naturally chiral surfaces," *Topics in Catalysis*, vol. 25, no. 1, pp. 9–15, 2003. [Online]. Available: http://dx.doi.org/10.1023/B:TOCA.0000003094.07345.d1

[299] M. Klein, M. Maier, and W. Prettl, "Raman optical activity and stimulated raman scattering along the c axis in α-quartz," *Phys. Rev. B*, vol. 28, pp. 6008–6021, Nov 1983. [Online]. Available: http://link.aps.org/doi/10.1103/PhysRevB.28.6008

[300] M. Klein and M. Maier, "Giant raman optical activity of the 128-cm-1 mode in α-quartz," *Optics Communications*, vol. 44, no. 6, pp. 411 – 414, 1983. [Online]. Available: http://www.sciencedirect.com/science/article/pii/0030401883902286

[301] K. Onuma and A. Ito, "Investigation of crystal growth mechanism for hydroxyapatite," *Journal of the Mineralogical Society of Japan*, vol. 29, no. 1, pp. 17–30, 2000.

[302] A. Oyane, K. Onuma, A. Ito, and T. Kokubo, *Bioceramics Volume 12*. World Scientific, 1999, ch. Clustering of Calcium Phosphate in SBF and in the System $CaCl_2$-H_3PO_4-KCl-H_2O, pp. 157–160.

[303] E. W. Blanch, L. Hecht, C. D. Syme, V. Volpetti, G. P. Lomonossoff, K. Nielsen, and L. D. Barron, "Molecular structures of viruses from Raman optical activity." *The Journal of general virology*, vol. 83, no. Pt 10, pp. 2593–2600, 2002. [Online]. Available: http://www.ncbi.nlm.nih.gov/pubmed/12237443{%}5Cnhttp://www.scopus.com/inward/record.url?eid=2-s2.0-0036787172{&}partnerID=40{&}md5=77cf7be58d3c71a4e8e32c5cc3635a6b{%}5Cnhttp://jgv.microbiologyresearch.org/content/journal/jgv/10.1099/0022-1317-83-10-2593

[304] A. Synytsya, M. Judexova, T. Hruby, M. Tatarkovic, M. Miskovicova, L. Petruzelka, and V. Setnicka, "Analysis of human blood plasma and hen egg white by chiroptical spectroscopic methods (ECD, VCD, ROA)," *Analytical and Bioanalytical Chemistry*, vol. 405, no. 16, pp. 5441–5453, 2013.

[305] N. R. Yaffe, A. Almond, and E. W. Blanch, "A New Route to Carbohydrate Secondary and Tertiary Structure Using Raman Spectroscopy and Raman Optical Activity," *Journal of the American Chemical Society*, vol. 132, pp. 10 654–10 655, 2010.

[306] Z. Q. Wen, L. D. Barron, and L. Hecht, "Vibrational Raman Optical Activity of Monosaccharides," *Journal of the American Chemical Society*, vol. 115, pp. 285–292, 1993.

[307] E. W. Blanch, L. A. Morozova-roche, D. A. Cochran, A. J. Doig, L. Hecht, and L. D. Barron, "Is Polyproline II Helix the Killer Conformation ? A Raman Optical Activity Study of the Amyloidogenic Prefibrillar Intermediate ...

Is Polyproline II Helix the Killer Conformation ? A Raman Optical Activity Study of the Amyloidogenic Prefibrillar Intermed," *Journal of Molecular Biology*, vol. 301, p. 553±563, 2000.

[308] S. Schlucker, "Surface-enhanced raman spectroscopy: Concepts and chemical applications," *Angewandte Chemie - International Edition*, vol. 53, no. 19, pp. 4756–4795, 2014.

Appendix A

Programs Developed to Support and Enable Lens Vibration Lock-in Amplified Raman Spectroscopy

A.1 LabView Programs for Spectral Collection

A.1.1 Basic Collection of Lock-In Amplified Raman Spectra

Spectral collection was automated through the use of a LabView program to control the photodiode stage and acquire the voltage from the lock-in amplifier and direct from the photodiode. A flow chart explaining operation of the LabView program for basic single point spectral collection is given in Figure A.1. The program is built to move the photodiode through a predefined number of steps and collect voltage data at each position through the lock-in amplifier. To do this the translation stage is initialised and provided with movement control parameters. The stage moves to its initial position, waits for a time period equal to the time constant then collects two sets of voltages. The first is always the lock-in amplified photodiode signal, with the second either being the raw photodiode voltage, or a phase measurement from the lock-in amplifier as required. The translation stage then move to the next position, waits the duration of the set time constant and collects the next set of measurement and repeats the process until a full spectrum is collected. The position of the photodiode and voltage measurements are written to a file using a comma delimited format for analysis.

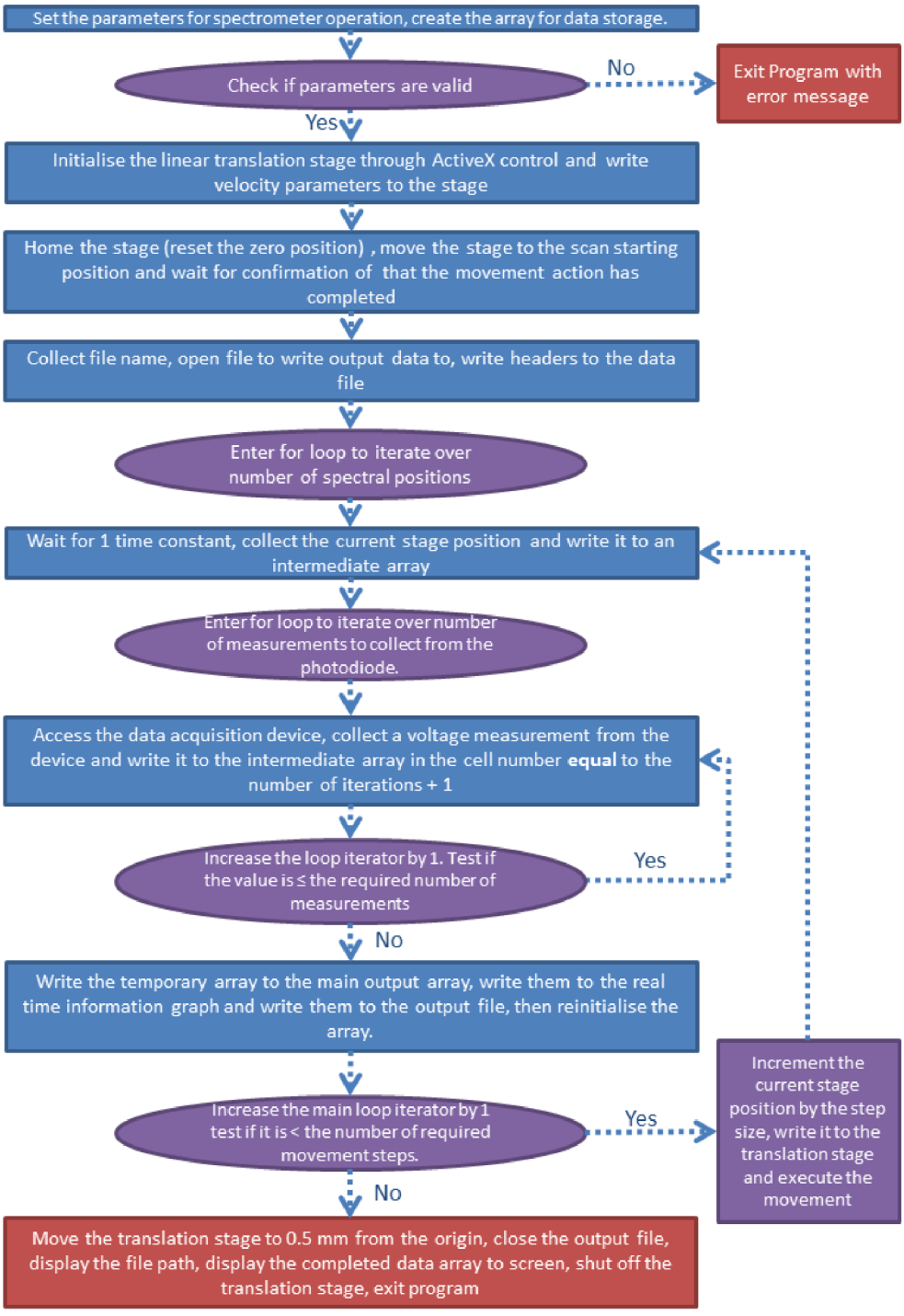

Fig. A.1 Block diagram of basic spectrometer Labview control code.

The block diagram forming the LabView code described in the figure above is given on the following pages below.

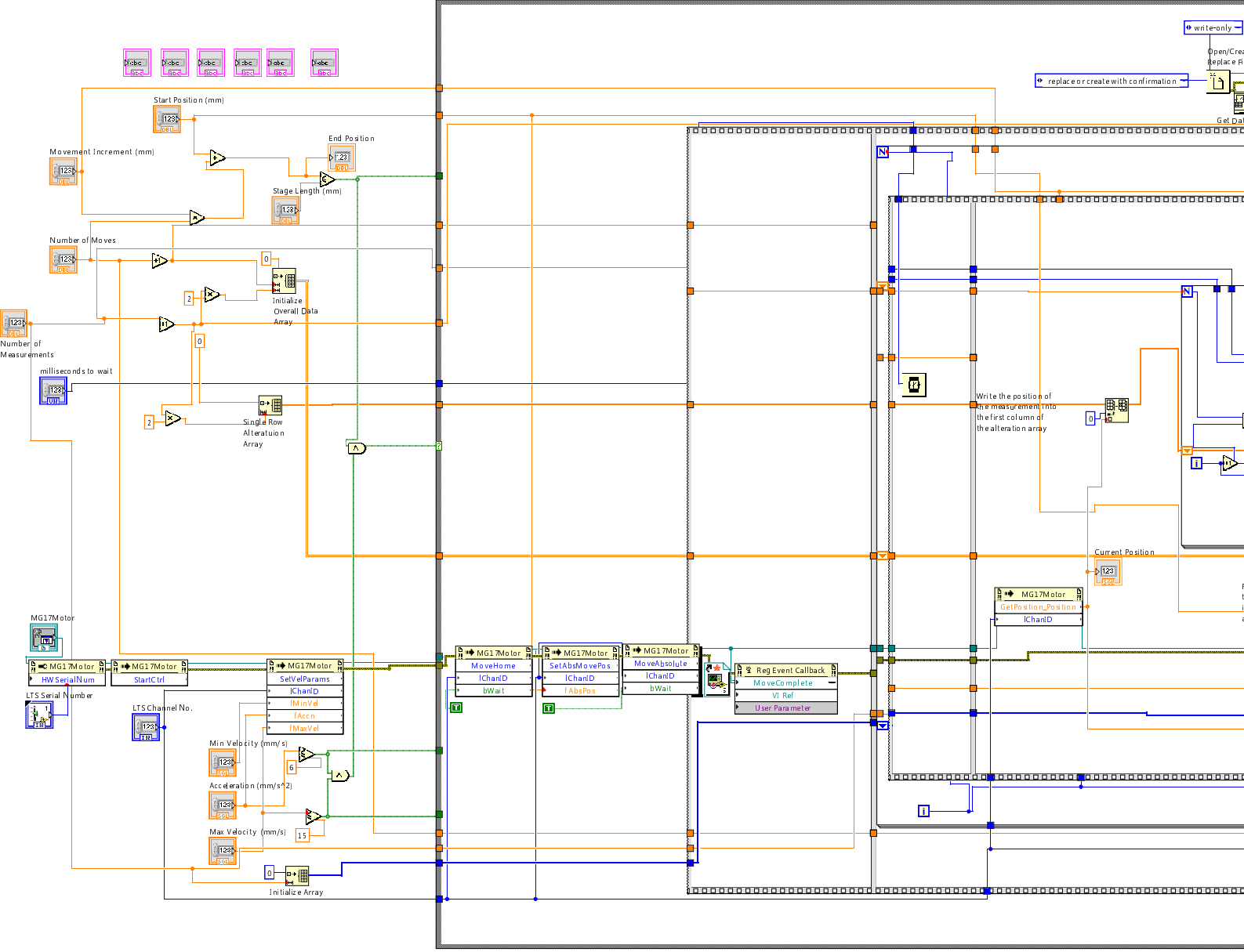
Start Position (mm)
End Position
Movement Increment (mm)
Stage Length (mm)
Number of Moves
Initialize Overall Data Array
Number of Measurements
milliseconds to wait
Single Row Alteration Array
Write the position of the measurement into the first column of the alteration array
Current Position
MG17Motor
HW SerialNum
StartCtrl
SetVelParams
lChanID
fMinVel
fAccn
fMaxVel
LTS Serial Number
LTS Channel No.
Min Velocity (mm/s)
Acceleration (mm/s^2)
Max Velocity (mm/s)
Initialize Array
MoveHome
bWait
SetAbsMovePos
fAbsPos
MoveAbsolute
Reg Event Callback
MoveComplete
VI Ref
User Parameter
GetPosition_Position
write-only
replace or create with confirmation

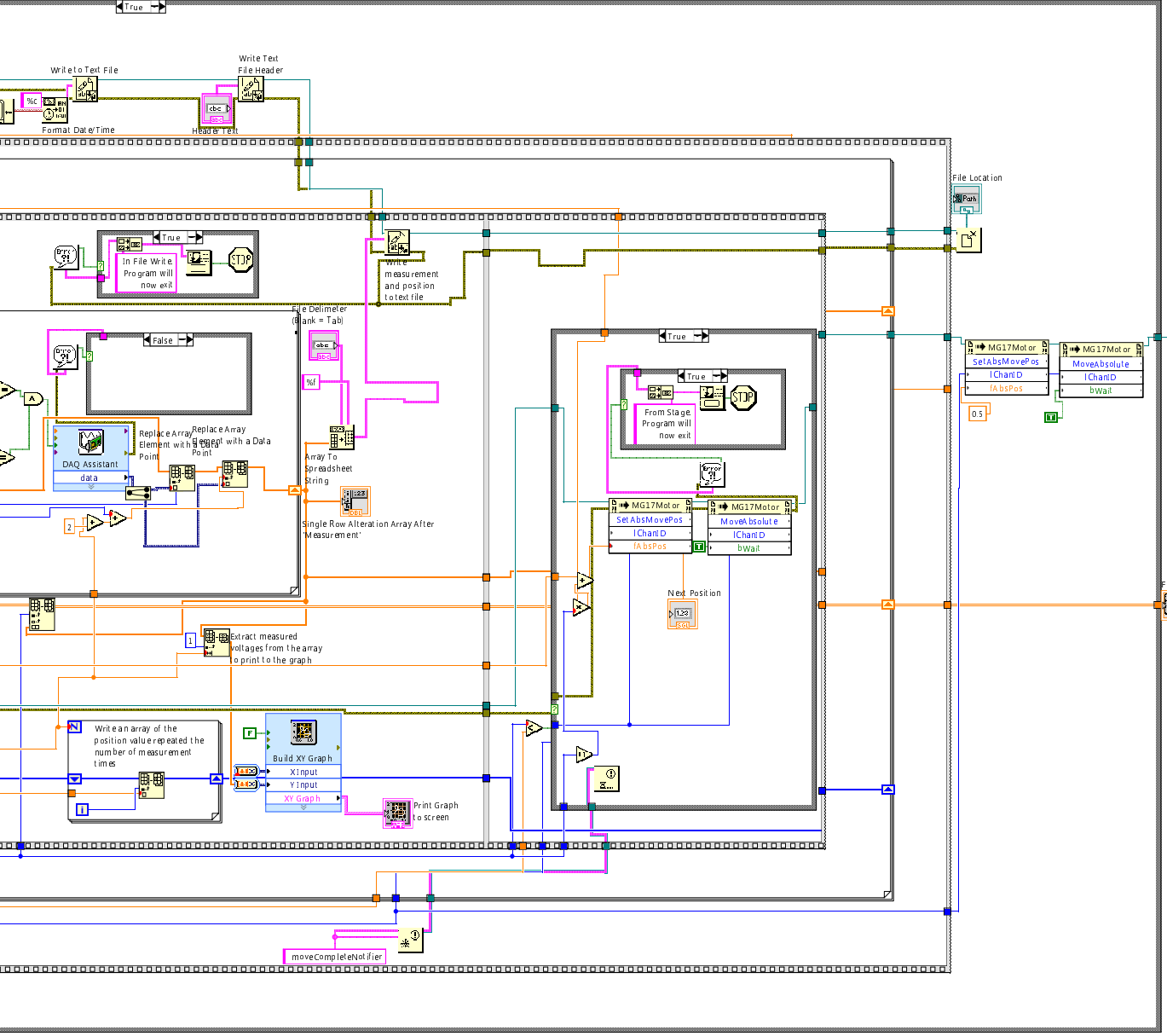
True
Write to Text File
Write Text File Header
%c
Format Date/Time
Header Text
File Location
Path
True
In File Write Program will now exit
STOP
Write measurement and position to text file
File Delimeter (Blank = Tab)
False
%f
DAQ Assistant
data
Replace Array Element with a Data Point
Replace Array Element with a Data Point
Array To Spreadsheet String
Single Row Alteration Array After 'Measurement'
Extract measured voltages from the array to print to the graph
Write an array of the position value repeated the number of measurement times
Build XY Graph
XInput
YInput
XY Graph
Print Graph to screen
moveCompleteNotifier
True
True
From Stage Program will now exit
MG17Motor
SetAbsMovePos
lChanID
fAbsPos
MG17Motor
MoveAbsolute
lChanID
bWait
Next Position
MG17Motor
SetAbsMovePos
lChanID
fAbsPos
MG17Motor
MoveAbsolute
lChanID
bWait
0.5
MG17Motor
StopCtrl
Final Output Array

A.1.2 Scanning System for the Collection of Spectral Data in 2D

The base spectral collection system was augmented in order to allow for spectra to be collected at multiple points across a 2D surface. In order to do this the sample under analysis was affixed to a translation stage moving vertically, which was in turn attached to a translation stage moving in the horizontal plane. The 2D scanning system operates by firstly initialising the translation stages, them system then waits for the user to position the sample at the required starting point in front of the laser. The system then collects the movement parameters for each translation stage and for spectral collection. When the user tells the program they are ready for the scan to start, a spectrum is collected in the same way as for a standard basic spectrum. Once the first spectrum has been collected the data from that position in printed to a comma delimited file with a header indicating the vertical and horizontal position of the sample with respect to the translation stages it is mounted on. The photodiode position is then reset and the sample is moved along horizontally by a user defined step size. This process is repeated until all spectra are collected along the horizontal, at which point the stage moves vertically and back to the beginning of the horizontal line. This process repeats until a full set of spectra are created. The block diagram for the program to perform this process is given on the following pages.

SpectralCollectionWith2DScan.vi
C:\Users\labuser\Desktop\LabviewForThesis\2D\SpectralCollectionWith2DScan.vi
Last modified on 09/09/2015 at 09:02
Printed on 09/09/2015 at 12:34

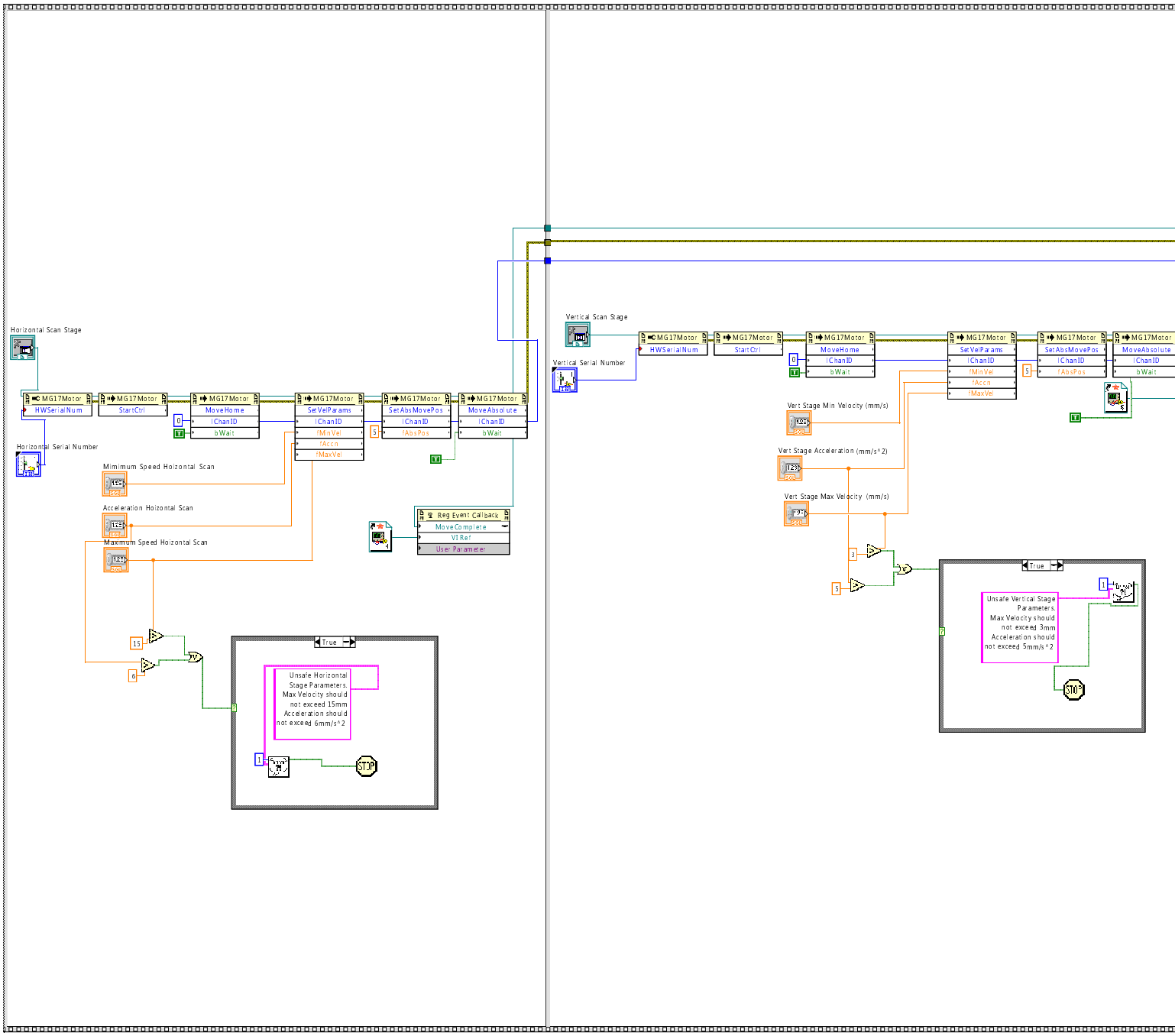

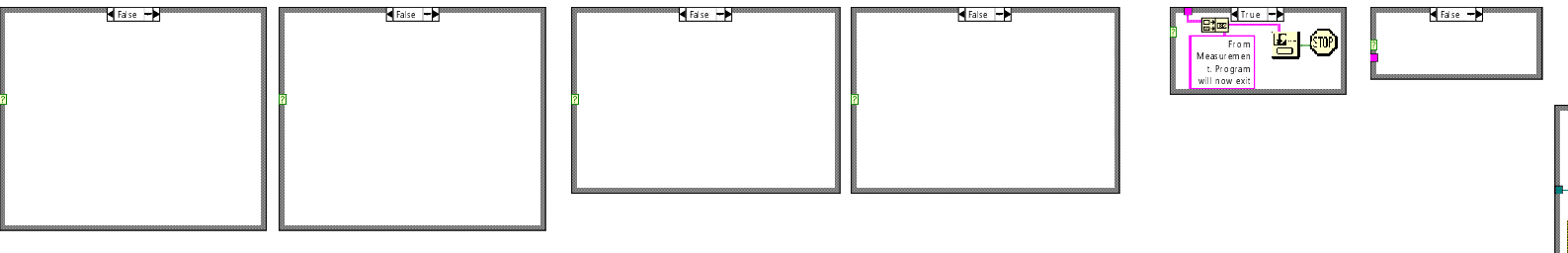

SpectralCollectionWith2DScan.vi
C:\Users\labuser\Desktop\LabviewForThesis\2D\SpectralCollectionWith2DScan.vi
Last modified on 09/09/2015 at 09:02
Printed on 09/09/2015 at 12:34

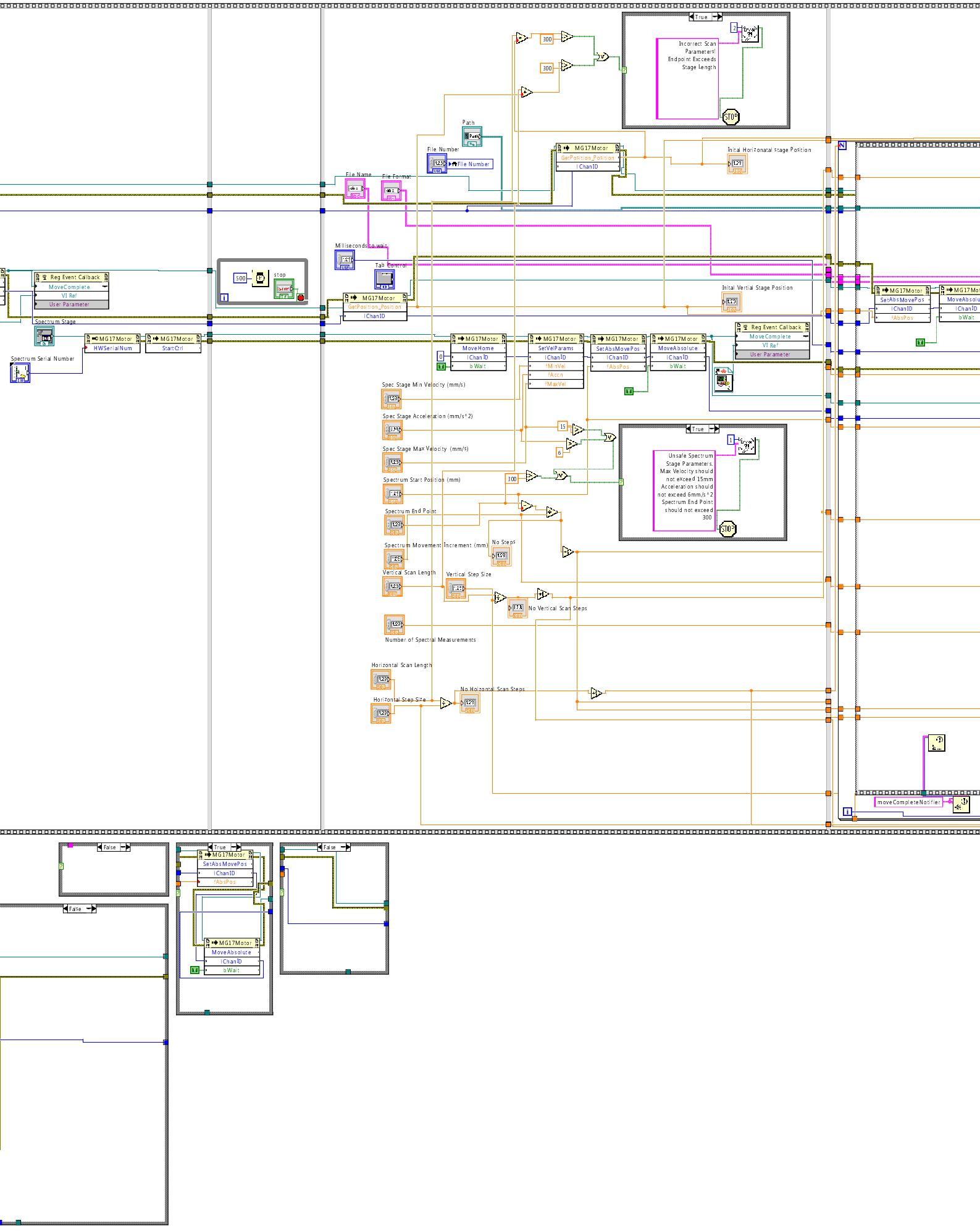

SpectralCollectionWith2DScan.vi
C:\Users\labuser\Desktop\LabviewForThesis\2D\SpectralCollectionWith2DScan.vi
Last modified on 09/09/2015 at 09:02
Printed on 09/09/2015 at 12:34

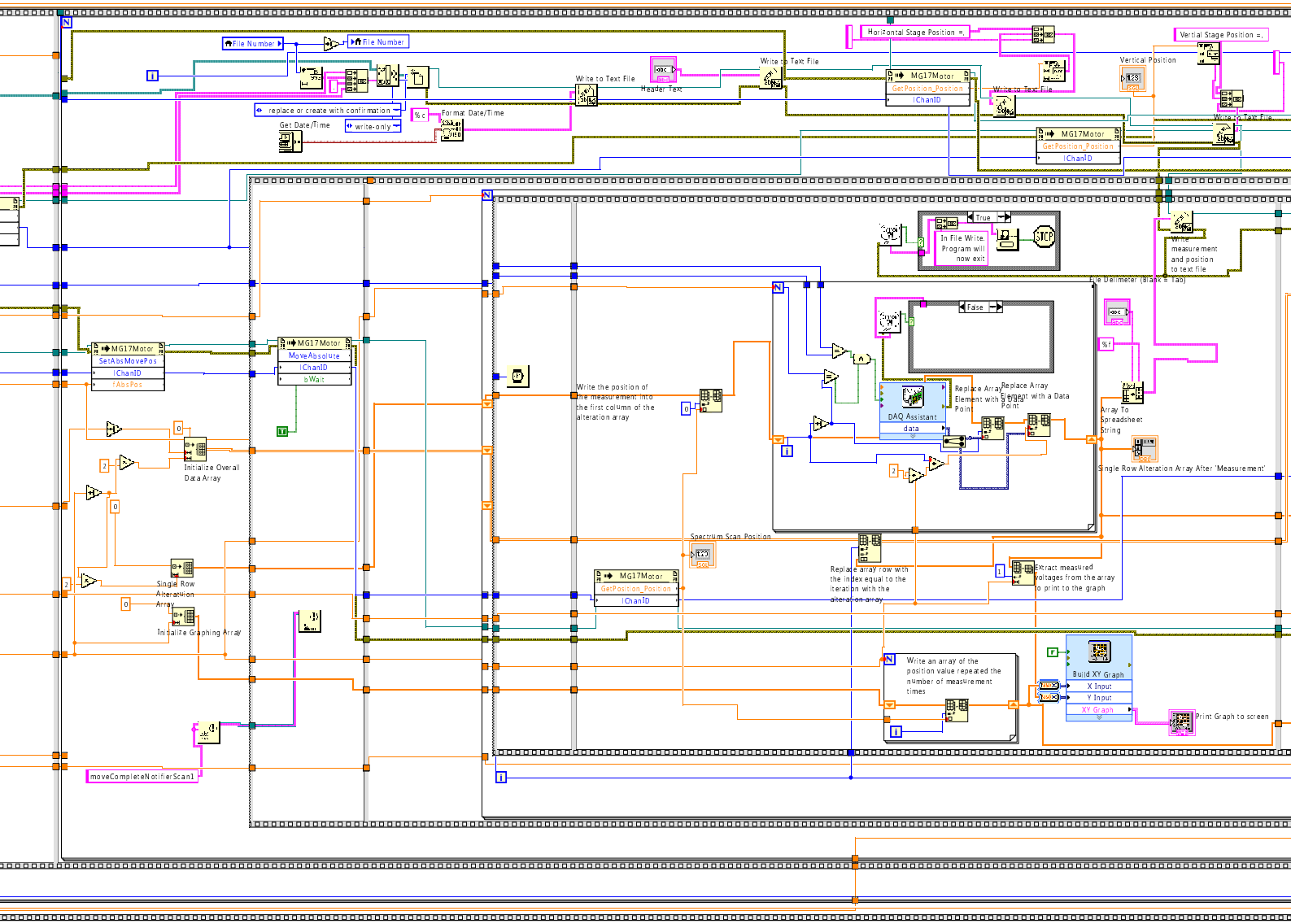

SpectralCollectionWith2DScan.vi
C:\Users\labuser\Desktop\LabviewForThesis\2D\SpectralCollectionWith2DScan.vi
Last modified on 09/09/2015 at 09:02
Printed on 09/09/2015 at 12:35

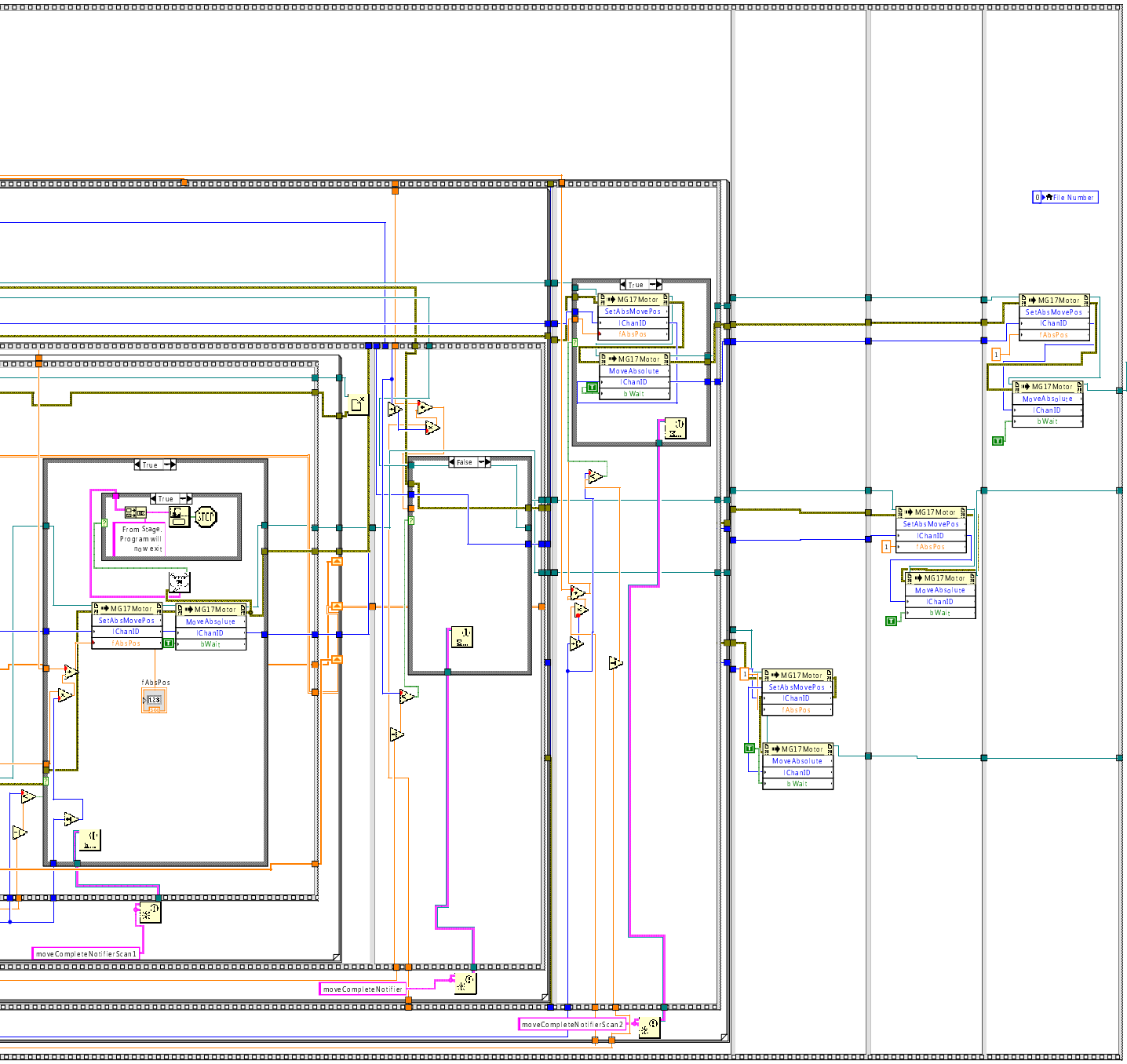

A.1.3 Single Spectral Point Raman Mapping

Single Raman spectral point mapping collects the voltage from a single photodiode position over a 2D surface of a sample. It allows for relatively fast mapping of the Raman signal intensity from a chemical group across the surface off a sample. The single spectral point mapping system operates by initialising the translation stages, then waiting for the user to position the required sample starting position, as in a 2D scan. The program also collects the position where the user would like to collect spectral data from. When the user confirms the initial parameters have been chosen the system moves the photodiode to the required position for data collection and collects multiple measurements. The sample is then translated horizontally and measurements are collect from the lock-in amplifier. This continues until the final horizontal position is reached. At this point, all the voltage measurements from the fixed photodiode across a line along the sample are saved to a comma delimited file with a file header providing the vertical stage position. The horizontal stage moves back to it's original position and the vertical stage will move one step and the horizontal collection process will begin repeat until data has been collected across all vertical lines.

The block diagram for the program to perform this process is given on the following pages.

SpectralCollectionWith2DScan.vi
C:\Users\labuser\Desktop\LabviewForThesis\2D\SpectralCollectionWith2DScan.vi
Last modified on 09/09/2015 at 09:02
Printed on 09/09/2015 at 12:34

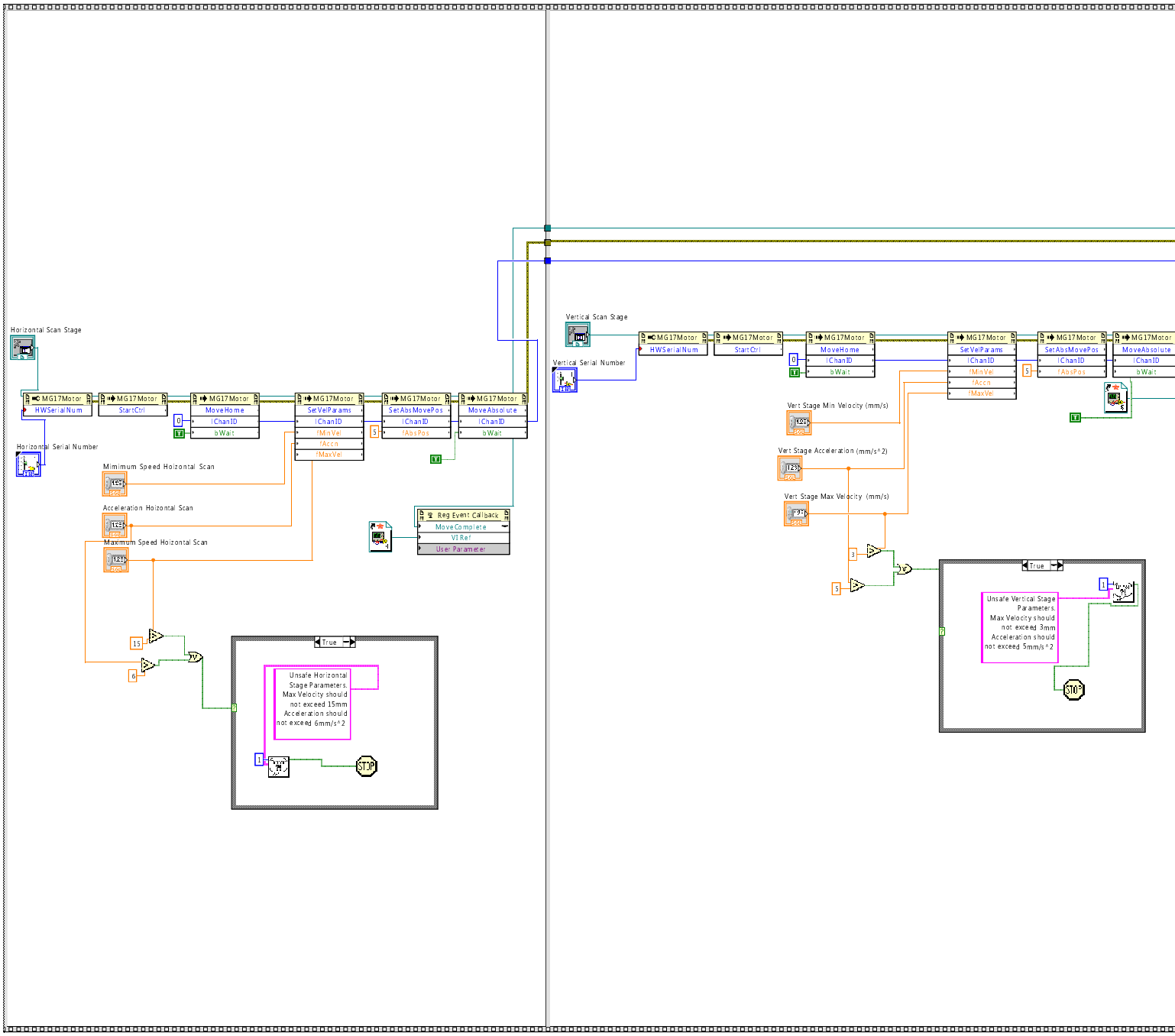

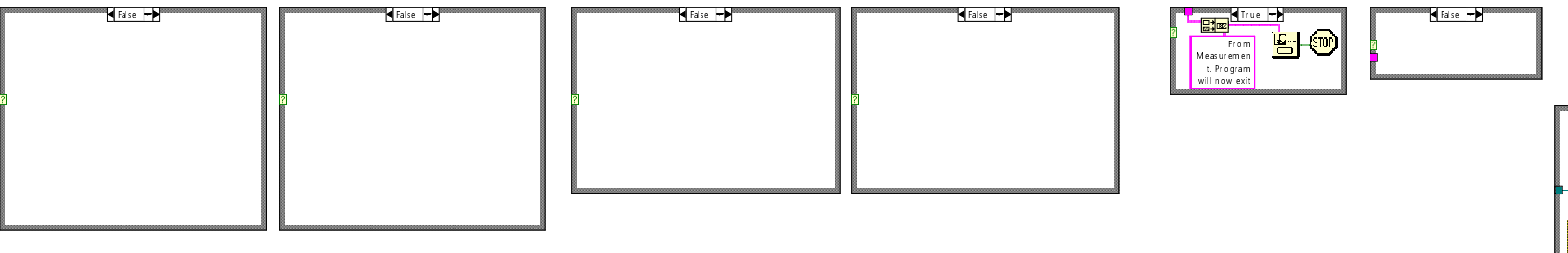

SpectralCollectionWith2DScan.vi
C:\Users\labuser\Desktop\LabviewForThesis\2D\SpectralCollectionWith2DScan.vi
Last modified on 09/09/2015 at 09:02
Printed on 09/09/2015 at 12:34

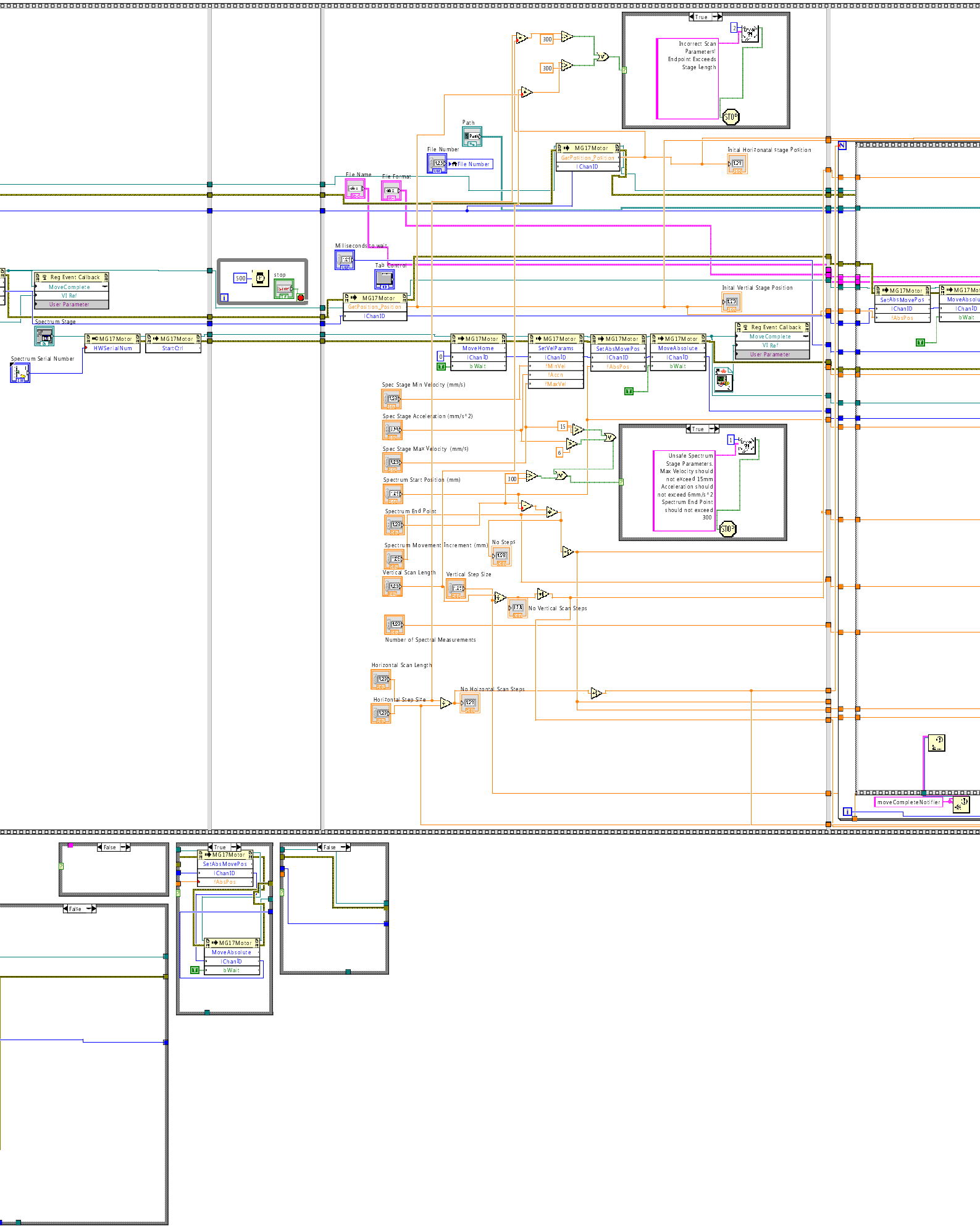

SpectralCollectionWith2DScan.vi
C:\Users\labuser\Desktop\LabviewForThesis\2D\SpectralCollectionWith2DScan.vi
Last modified on 09/09/2015 at 09:02
Printed on 09/09/2015 at 12:34

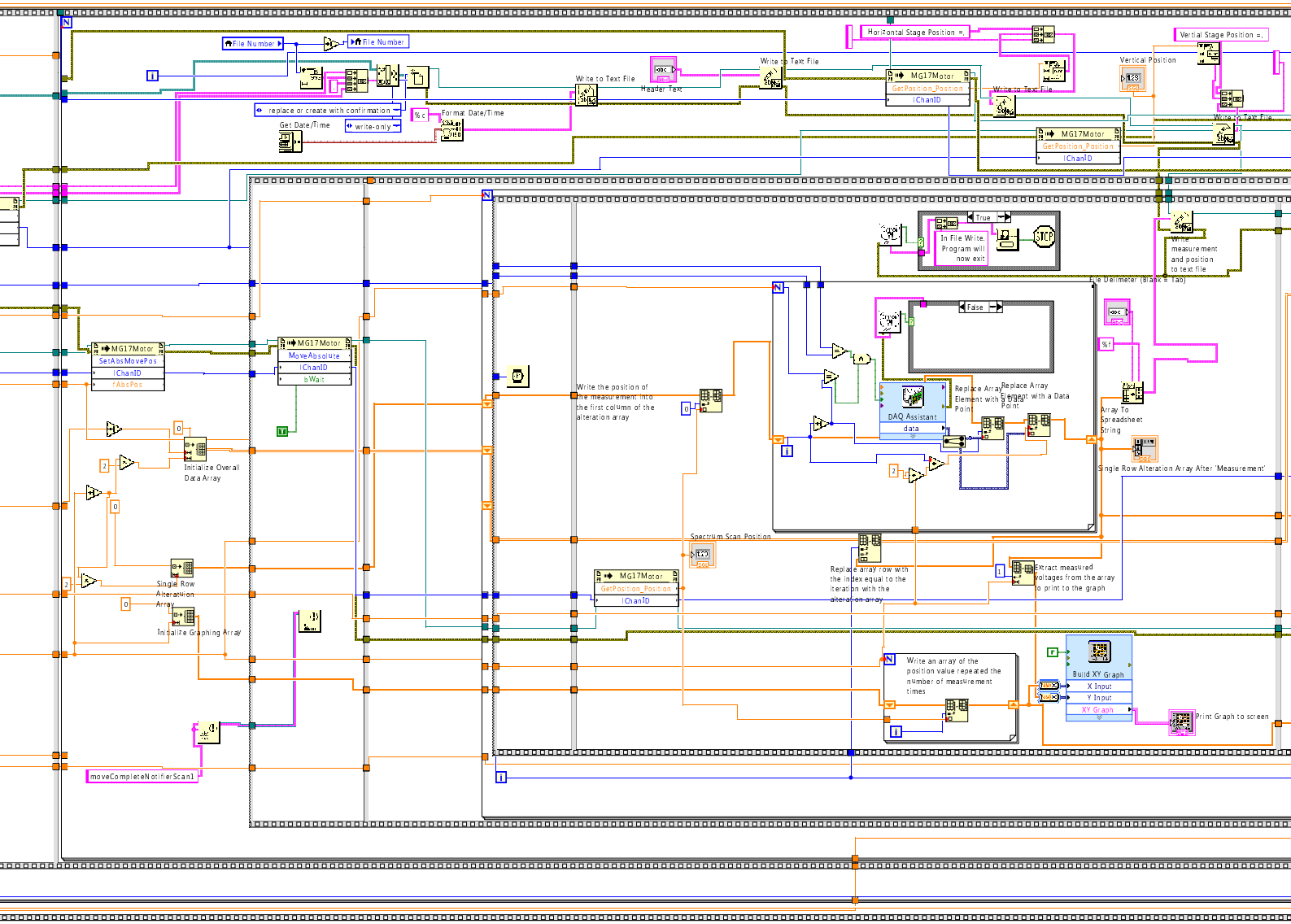

SpectralCollectionWith2DScan.vi
C:\Users\labuser\Desktop\LabviewForThesis\2D\SpectralCollectionWith2DScan.vi
Last modified on 09/09/2015 at 09:02
Printed on 09/09/2015 at 12:35

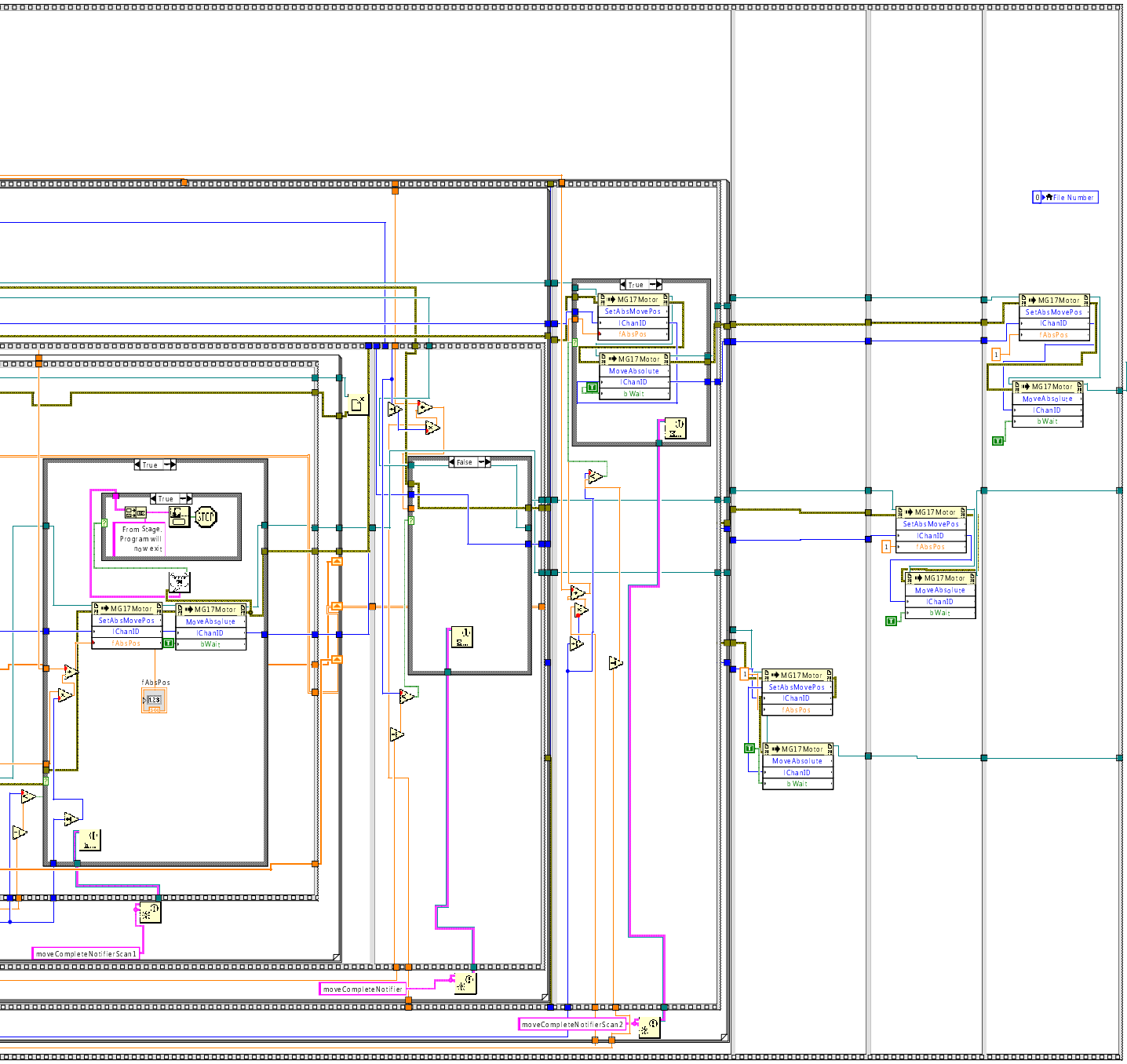

A.1.4 CCD Spectrometer Data Collection

A.1.5 Processing of CCD Spectra and Lock-In Amplification Data Construction, Output and Collection

A number of programs were developed in LabView in order to generate lock-in amplified Raman spectra using the CCD Spectrometer. Initially, multiple spectra were collected from the spectrometer with a user defined integration time and written into a single filed. This was done using the program given on the following page.

CCSMultiSPectra.vi
C:\Users\labuser\Desktop\LabviewForThesis\CCS Labview\CCSMultiSPectra.vi
Last modified on 09/09/2015 at 08:33
Printed on 09/09/2015 at 12:37

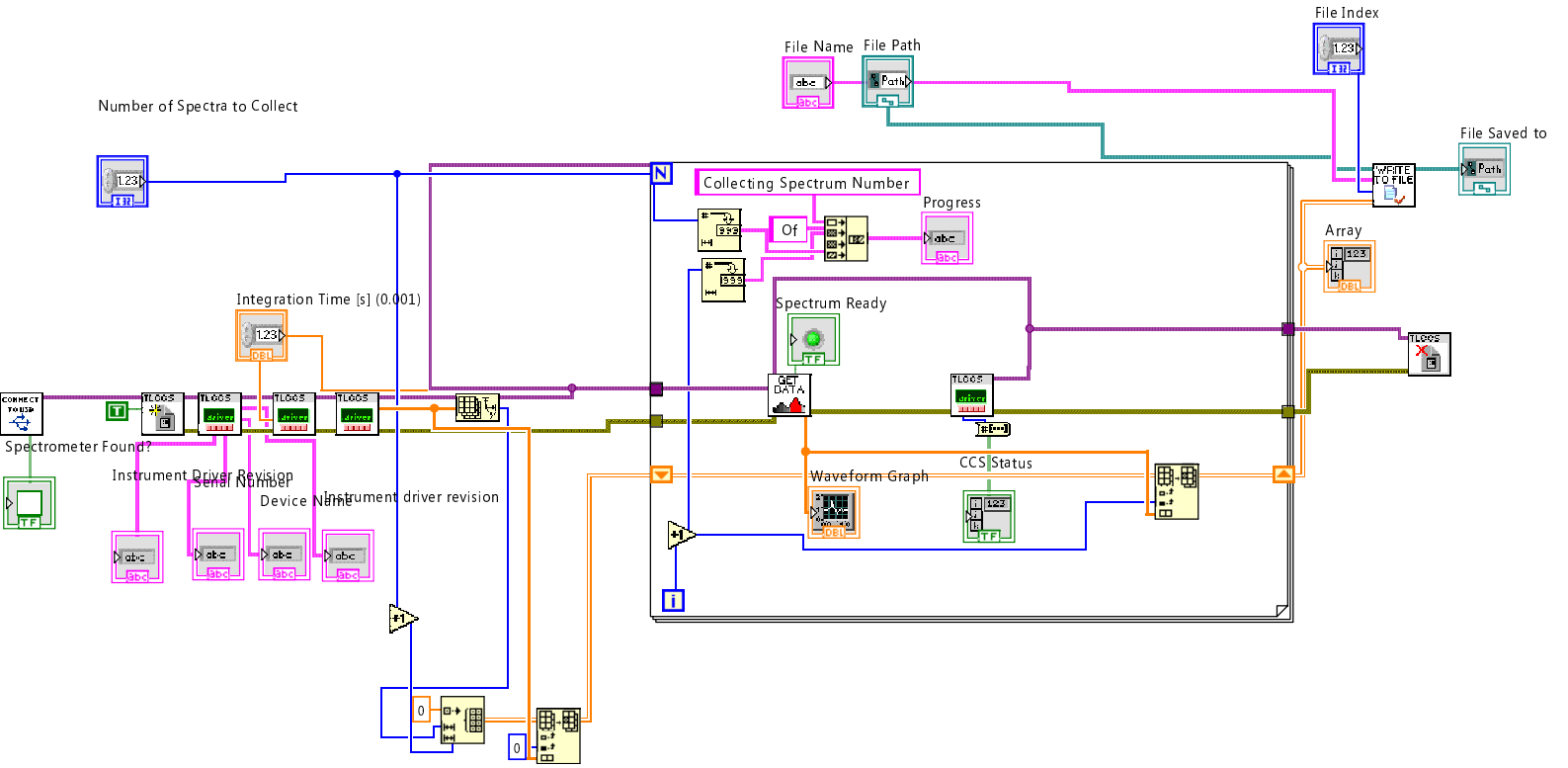

Once the required data sets had been required, the two files of spectral data (E.g. spectra with and without the laser on, or at two different voltages across the piezoelectric crystal) were constructed into an output waveform using an LabView program. In the program, the two data files required for the waveform are read in an formed into a new array as a square wave, according to the user defined parameters. At the same the reference spectrum is also computed. The block diagram for the program used to achieve this is given on the following page.

CreatingSignalFromFileChopShort.vi
C:\Users\labuser\Desktop\LabviewForThesis\CCS Labview\CreatingSignalFromFileChopShort.vi
Last modified on 09/09/2015 at 12:01
Printed on 09/09/2015 at 12:21

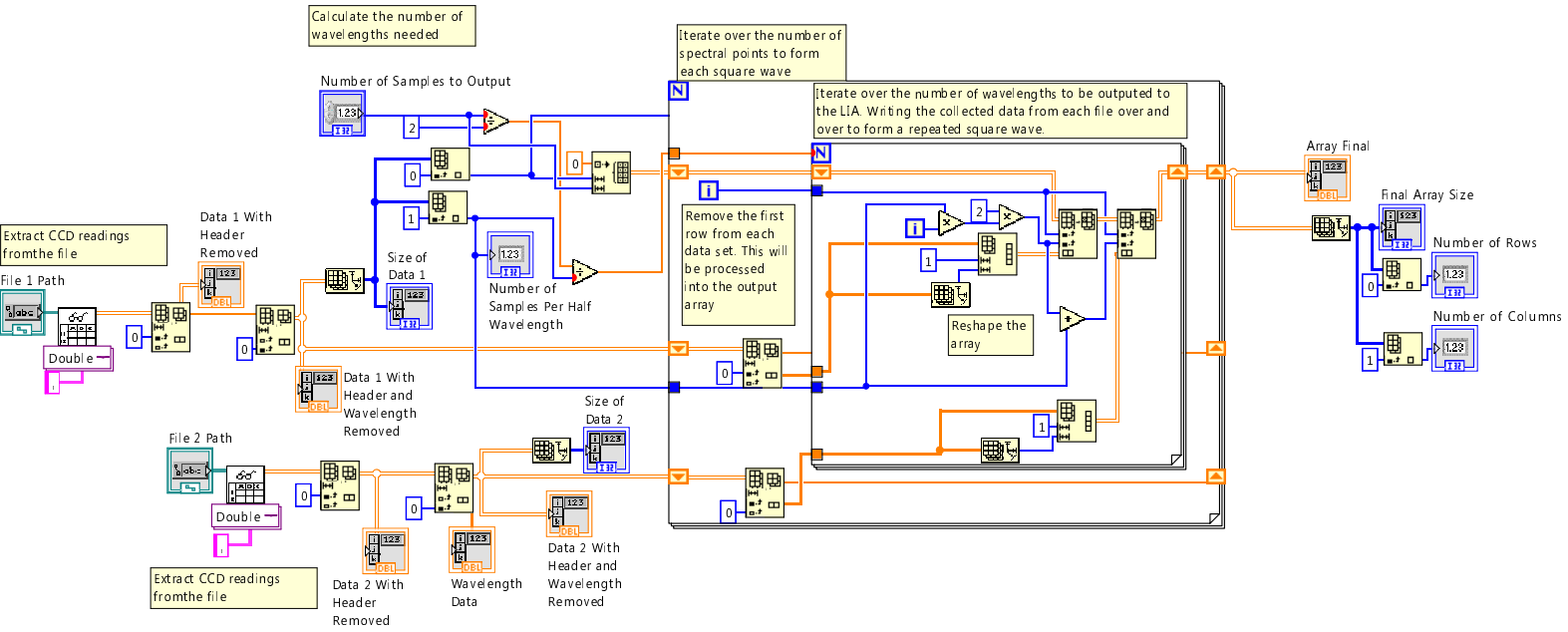

A final LabView program was developed to output the created waveform to the lock-in amplifier and collect the lock-in amplified output. The program initially gets the correct data waveform and reference signal from the previous lab view script. It then outputs the waveform and reference at the user defined frequency and will collect lock-in amplified data after a defined time period. The program which performs these operations is given on the following page.

CCSChopperLIASimulationV1.vi
C:\Users\labuser\Desktop\LabviewForThesis\CCS Labview\CCSChopperLIASimulationV1.vi
Last modified on 09/09/2015 at 11:55
Printed on 09/09/2015 at 11:55